Title

Characterizing SAPO-37-Supported Catalysts: From Rhodium and Platinum Single-Site Species to Rhodium and Platinum Clusters

Author

Perez-Aguilar, Jorge

Publication Date

2021

Peer reviewed|Thesis/dissertation

Characterizing SAPO-37-Supported Catalysts: From Rhodium and Platinum Single-Site Species to Rhodium and Platinum Clusters

By

JORGE ERNESTO PEREZ-AGUILAR

DISSERTATION

Submitted in partial satisfaction of the requirements for the degree of

DOCTOR OF PHILOSOPHY

in

Chemical Engineering

in the

OFFICE OF GRADUATE STUDIES

of the

UNIVERSITY OF CALIFORNIA

DAVIS

Approved:

Bruce C. Gates, Chair

Ron C. Runnebaum

Coleman X. Kronawitter

Committee in Charge

2021

Table of Contents

Characterizing SAPO-37-Supported Catalysts: From Rhodium and Platinum Single-Site Species to Rhodium and Platinum Clusters

Abstract

Supported single-site metal catalysts that have nearly uniform structures are drawing increasing attention because of prospects for increased application and elucidation of structure-catalytic activity relationships. The research summarized in this dissertation was carried out with the goal of fundamental understanding of the structures, reactivities, and catalytic properties of highly uniform solid catalysts with well-defined structures. Catalysts were synthesized by using organometallic complex precursors, $Rh(C_2H_4)_2(acac)$ or $Pt(acac)_2$ (where acac is acetylacetonato), and the porous crystalline material SAPO-37 as a support. The samples were characterized by infrared (IR) spectroscopy, X-ray absorption spectroscopy (including X-ray absorption near edge structure and extended X-ray absorption fine structure (EXAFS) analysis), X-ray diffraction (XRD) crystallography, N_2 adsorption, and thermogravimetric analysis (TGA). The catalytic performance was measured for ethylene hydrogenation.

SAPO-37-supported rhodium diethylene complexes formed in the synthesis were anchored by two Rh−O bonds at SAPO framework tetrahedral sites, as shown by IR and EXAFS spectra. The ethylene ligands were readily replaced with CO, giving sharp ν_{CO} bands indicating highly uniform supported species. Comparing the spectra with those of rhodium complexes on zeolite HY shows that the SAPO- and zeolite-supported complexes are isostructural. The two catalysts had similar initial room-temperature activities per Rh atom for ethylene conversion in the presence of H_2, but the SAPO-supported catalyst was selective for ethylene hydrogenation and the zeolite-supported catalyst selective for ethylene dimerization; correspondingly, the catalyst on the SAPO was more stable than that on the

zeolite during operation in a flow reactor. These results show how isostructural SAPO-37 and zeolite HY are similar in structure yet different in reactivity, corresponding to the different bonding environments for rhodium.

SAPO-37-supported rhodium clusters were synthesized by exposure of SAPO-37-supported rhodium diethylene complexes to H_2 at 373 K for 1 h. EXAFS data indicate an average Rh–Rh coordination number of 3.0 and an average Rh–Rh distance of 2.66 Å. XANES spectra show that the transformation of rhodium diethylene complexes to rhodium clusters is stoichiometrically simple. At 303 K, the SAPO-37-supported rhodium clusters are similar in selectivity for hydrogenation of ethylene (fed to a flow reactor with a H_2:C_2H_4 molar ratio of 1:4) to DAY zeolite-supported rhodium clusters but their initial room-temperature activity per rhodium atom was found to be substantially less than that of the zeolite-supported rhodium clusters.

Atomically dispersed supported platinum catalysts were synthesized by the reaction of $Pt(acac)_2$ with SAPO-37. EXAFS spectra show that, after heating in air to 623 K, each platinum atom on average was bonded to approximately four light scatterer atoms (such as support oxygen atoms), with no evidence of a Pt–Pt contribution that would have indicated platinum clusters. XANES data indicate a platinum formal oxidation state of +2. IR data show that, upon exposure of the sample to CO, the non-support ligands on the platinum were CO in various coordinations, with platinum in various oxidation states. The supported platinum was characterized as a catalyst for ethylene hydrogenation. Within a few minutes of the start of flow of ethylene + H_2, the EXAFS-determined Pt−Pt coordination number increased from essentially zero to 1.8 ± 0.4; the XANES white line intensity decreased; and, after 2 h of continuous reactant flow, the value had increased to 2.7 ± 0.5 as the XANES white line intensity slightly increased—with these data taken together indicating the almost instantaneous formation of platinum clusters of only a few atoms each (with average diameters in the range of about 0.4–0.8 nm). Subsequent exposure of the catalyst to flowing ethylene led to a decrease in the Pt−Pt coordination

number to 1.6 ± 0.3 and an increase in the XANES white line intensity, indicative of partial oxidative fragmentation of the clusters by ethylene. Platinum clusters in SAPO-37 that were formed by exposure to H_2 prior to catalysis were found to be catalytically active for ethylene hydrogenation, and a comparison of the activities of the catalyst initially containing atomically dispersed platinum versus that containing platinum clusters as a function of time on stream leads to the inference that the clusters are the catalytically active species, with no evidence of catalysis by the atomically dispersed platinum.

Acknowledgements

This work would not have been possible without the help and support of the people that have influenced my life. I would like to acknowledge those with substantial influence:

I thank Professor Bruce C. Gates for accepting me into his group and mentoring me into the researcher I am today. He has always had encouraging words and helpful analogies to help me reach my goals.

I thank DOE and Chevron for funding me during my time at UC Davis.

I thank Dr. Ryan Davis and the staff at Stanford Synchrotron Radiation Lightsource, as well as Dr. Adam S. Hoffman, Simon Bare, and the staff at Co-ACCESS for always being passionate and willing to adapt to make my experiments work.

I thank my co-authors Dr. C.Y. Chen for XRD measurements and Dr. Jim Hughes for making SAPO-37 and both for the helpful discussions on my research project.

I thank Professor Runnebaum and Kronawitter for being on my committee and their graduate students, for their enthusiastic collaborations using laboratory equipment, and times spent eating burritos.

I thank the older Gates' group students: Dr. Adam S. Hoffman, Dr. Louise Debefve, Dr. Erjia Guan, and Dr. Charlie Fang for being great mentors and friends. I also thank the rest of the Gates group, for always making me feel like I was part of a team, and helping me upgrade and maintain the lab especially Edward Conley, Kim Justl, Dr. Melike Babucci, Yizhen Chen, and all the visiting scholars.

I thank all the friends I have made during all my years as a graduate student for the countless happy hours, trivia nights, trinities, pool parties, and great memories.

I would like to thank my lifting group for helping me pick up weights and put them back down.

Finally, I thank my girlfriend and parents for all their love and support. I could not have completed this dissertation without the unwavering faith of my family.

List of Publications

1. Hoffman, A.S.; Debefve, L. M.; Zhang, S.; **Perez-Aguilar, J. E.**; Conley, E. T.; Justl, K. R.; Arslan, I.; Dixon, D. A.; Gates, B. C. *ACS Catalysis* **2018**, *8*, 3489.

2. Babucci, M.; Fang, C.-Y.; **Perez-Aguilar, J. E.**; Hoffman, A. S.; Boubnov, A.; Guan, E.; Bare, S. R.; Gates, B. C.; Uzun, A. *Chemical Science* **2019**, *10*, 2623.

3. Fang, C.-Y.; Zhang, S.; Hu, Y.; Vasiliu, M.; **Perez-Aguilar, J. E.**; Conley, E.T.; Dixon, D. A.; Chen, C. Y.; Gates, B. C. *ACS Catalysis* **2019**, *9*, 3311.

4. **Perez-Aguilar, J. E.**; Chen, C. Y.; Hughes J. T.; Fang, C.-Y.; Gates, B. C. *J. Am. Chem. Soc.* **2020**, *142*, 11474–11485.

Chapter 1: Introduction

1.1 INTRODUCTION

Molecular catalysts and solid catalysts are used in 90% of industrial process.[1] Solid catalysts are almost always favored over molecular catalysts for their ease or separation from fluid-phase products and their high thermal stability.[2] Common industrial catalysts are supported, and the supports are commonly porous metal oxides (exemplified by alumina) that are inexpensive and offer tailorable physical properties such as surface area and pore volume. But because of their surface heterogeneity (both in composition and structure), these metal oxides and the catalysts supported on them are challenging to understand fundamentally. Thus, researchers have been motivated to synthesize and investigate catalyst supports that are highly uniform and have structures that can be controlled and adjusted. When such supports are used for catalysts that have well-defined structures, the opportunity arises to observe how systematic changes in the support and catalyst structures influence catalytic properties and generate understanding that will ultimately provide guidance about how to make improved catalysts and tune their properties.

Zeolites are the most significant example of structurally well-defined supports—supports that are crystalline and porous and, when well made, highly uniform. In recent reports, isolated metals on non-zeolitic supports have been found to have uniformities approaching those of metals on zeolites such as (i) iridium cations on MgO treated to preferentially expose highly reactive sites for bonding of the iridium at low loadings[3] and (ii) iridium cations on reduced graphene aerogel.[4] Another class of material—silicoaluminophosphates (SAPOs)—are known to be isostructural to zeolites, but to differ in framework composion.[5] Characterizations of zeolites and SAPOs have been carried out by use of complementary physical characterization techniques, with a focus on advanced spectroscopic techniques. We extend the comparison between zeolites and SAPOs by using these materials as supports for metal complexes. Here we report and investigation of a class of solid catalysts that includes two isostructural supports —zeolites and SAPOs. We demonstrate synthesis methods to generate highly

uniform metal sites on the supports and show how changes in the support composition alter the activities of isostructural catalysts on these supports.

We chose to support rhodium species on a zeolite and on an isostructural silicoaluminophosphates (SAPO.). SAPOs differ from zeolites in composition; they incorporate phosphorus tetrahedral sites among silica and alumina tetrahedra, whereas zeolites do not. SAPOs offer many properties that are similar to those of zeolites, as follows: Si–OH–Al sites for metal bonding that are isostructural to their zeolite counterparts. Prospective advantages of SAPOs over zeolites are the following: the acid strength distributions are narrower; the densities of Si–OH–Al sites are different in the SAPO and the zeolite; and these sites potentially remain stable at higher temperatures than the ones in zeolites.[6] Thus, the SAPOs as a class offer the opportunity to expand the library of well-defined catalyst supports.

The zeolite that we chose was zeolite HY, and the SAPO that we chose was SAPO-37. This is an ideal pair for our purposes because they are isostructural, but different in framework composition. We chose a molecular organometallic precursor, $Rh(C_2H_4)_2(acac)$, which, after chemisorption on the support, without any additional treatments, maintains the $Rh(C_2H_4)_2$ structure.[7]

Chapter 2[8] provides a comparison of two isostructual catalyst precursors: SAPO-37-supported rhodium diethylene complexes and zeolite HY-supported rhodium diethylene complexes. They are compared in terms of structure and catalyst performance. IR spectra show that the rhodium complexes were anchored to nearly uniform Al sites of SAPO-37, and IR and EXAFS data show that the SAPO- and zeolite-supported rhodium diethylene species are isostructural. The rhodium diethylene complexes were converted into rhodium dicarbonyl complexes on each of the two supports, and these were also found to be Isostructural.

The isostructural supports are not identical in structure or in catalytic properties. IR spectra show that the supports as ligands harbor rhodium complexes that have different ν_{CO} frequencies. The differences in the supports as ligands account for the different selectivities of the two catalysts for

ethylene conversion in the presence of H_2 (with the zeolite-supported catalyst giving substantial butene product but the SAPO-supported catalysts not).

Chapter 3 is a comparison of structure and catalyst performance of species initially present as isolated platinum complexes on SAPO-37 and platinum clusters on SAPO-37. EXAFS spectra show that the atomically dispersed platinum complexes on average were bonded to two support oxygen atoms and other unidentified ligands. Under ethylene hydrogenation conditions, the atomically dispersed platinum rapidly transformed into clusters of only a few atoms each (with average diameters in the range of about 0.4–0.8 nm) upon exposure to H_2. The data all support the conclusion that the clusters are the catalytically active species, with no evidence of catalytic activity by the atomically dispersed platinum.

Chapter 4 is a report of rhodium clusters on SAPO-37 synthesized by exposure to H_2 at 373 K from SAPO-37-supported rhodium diethylene complexes. EXAFS data indicate an average Rh–Rh coordination number of 3.0 and an average Rh–Rh distance of 2.66 Å. XANES spectra show the transformation of rhodium diethylene complexes to clusters is stoichiometrically simple. The SAPO-37-supported rhodium clusters were found to have selectivity for hydrogenation (H_2:C_2H_4 molar ratio of 1:4) similar to that of DAY zeolite-supported rhodium clusters, but their initial room-temperature activity (per rhodium atom) for ethylene conversion in the presence of H_2 was substantially less than that of the zeolite-supported rhodium clusters.

1.2 REFERENCES

(1) Hagen, J. *Industrial Catalysis: A Practical Approach.*; Wiley-VCH Verlag Gmbh & Co. KGaA, Weinheim Germany, 2006.

(2) Gates, B. C. Models of Metal Catalysts: Beyond Single Crystals. *Top. Catal.* **2000**, *14*, 173–180.

(3) Hoffman, A. S.; Debefve, L. M.; Zhang, S.; Perez-Aguilar, J. E.; Conley, E. T.; Justl, K. R.; Arslan, I.; Dixon, D. A.; Gates, B. C. Beating Heterogeneity of Single-Site Catalysts: MgO-Supported Iridium Complexes. *ACS Catal.* **2018**, *8*, 3489–3498.

(4) Babucci, M.; Sarac Oztuna, F. E.; Debefve, L. M.; Boubnov, A.; Bare, S. R.; Gates, B. C.; Unal, U.; Uzun, A. Atomically Dispersed Reduced Graphene Aerogel-Supported Iridium Catalyst with an Iridium Loading of 14.8 Wt %. *ACS Catal.* **2019**, *9*, 9905–9913.

(5) Davis, M. E. Zeolites and Molecular Sieves: Not Just Ordinary Catalysts. *Ind. Eng. Chem. Res.* **1991**, *30*, 1675–1683.

(6) Briend, M.; Peltre, M. J.; Lamy, A.; Man, P. P.; Barthomeuf, D. Dependence of the Acidic Properties of SAPO-37 Molecular Sieve-on Si Content and Heat Treatment. *J. Catal.* **1992**, *138*, 90–100.

(7) Liang, A. J.; Bhirud, V. A.; Ehresmann, J. O.; Kletnieks, P. W.; Haw, J. F.; Gates, B. C. A Site-Isolated Rhodium–Diethylene Complex Supported on Highly Dealuminated Y Zeolite: Synthesis and Characterization. *J. Phys. Chem. B* **2005**, *109*, 24236–24243.

(8) Perez-Aguilar, J. E.; Chen, C. Y.; Hughes, J. T.; Fang, C. Y.; Gates, B. C. Isostructural Atomically Dispersed Rhodium Catalysts Supported on SAPO-37 and on HY Zeolite. *J. Am. Chem. Soc.* **2020**, *142*, 11474–11485.

Chapter 2

Isolated Atomically Dispersed Rhodium Catalysts Supported on SAPO-37 and on HY Zeolite[1]

[1] This chapter has been previously published in the Journal of American Chemical Society **2020**, *142*, 11474–11485 by J. E. Perez-Aguilar, C.-Y. Chen, J. T. Hughes, C.-Y. Fang, and B. C. Gates. The original manuscript has been reformatted to fit the requirements of the dissertation

2.1 ABSTRACT

Zeolites are widely applied supports for metal catalysts, but molecular sieves with comparable structures—silicoaluminophosphates (SAPOs)—have drawn much less attention and been overlooked as supports for atomically dispersed metals. Now, we report SAPO-37 as a support for atomically dispersed rhodium in rhodium diethylene complexes, made by the reaction of $Rh(\eta^2\text{-}C_2H_4)_2$(acetylacetonate) with the support and anchored by two Rh–O bonds at framework tetrahedral sites, as shown by infrared and extended X-ray absorption fine structure spectra. The ethylene ligands were readily replaced with CO, giving sharp ν_{CO} bands indicating highly uniform supported species. A comparison of the spectra with those of comparable rhodium complexes on zeolite HY shows that the SAPO- and zeolite- supported complexes are isostructural, providing an unmatched opportunity for determining support effects in catalysis. The two catalysts had similar initial room-temperature activities per Rh atom for ethylene conversion in the presence of H_2, but the SAPO-supported catalyst was selective for ethylene hydrogenation and the zeolite-supported catalyst selective for ethylene dimerization; correspondingly, the catalyst on the SAPO was more stable than that on the zeolite during operation in a flow reactor.

2.2 INTRODUCTION

Zeolites, especially those with acidic properties, find wide applications as catalysts and supports for metal catalysts. Examples are faujasites containing platinum used for processes such as alkane hydrocracking and hydroisomerization[1–3] and zeolite Beta and chabazite containing iron and copper, used for vehicle exhaust abatement.[4–6] The metals in these catalysts are typically highly dispersed, to maximize their accessibility to reactants. The most highly dispersed—atomically dispersed—metals are drawing wide attention because they maximize the number of metal atoms engaged in catalysis and have properties different from those of metals present in nanoparticles, the commonly applied form of supported metals.[7]

Zeolites, because they have microporous, crystalline aluminosilicate structures, are nearly ideal supports for atomically dispersed metals,[8–10] with well-prepared zeolite-supported metal complexes evidently being the most nearly uniform of any reported.[11,12] A straightforward method for assessing the degree of uniformity of supported metals involves measuring the infrared (IR) spectra of CO ligands bonded to them: when the ν_{CO} peaks are sharp (characterized by full width at half maximum (fwhm) values of about 5 cm^{-1}), they indicate nearly uniform bonding sites on the support. A few isolated metals on non-zeolitic supports have been found to have uniformities approaching those of metals on zeolites, without however meeting the highest standard of uniformity; these include (i) isolated palladium atoms on single-crystal Au(111);[13] (ii) iridium cations on MgO treated to preferentially expose highly reactive sites for bonding of the iridium at low loadings;[14] (iii) platinum cations at low loadings on TiO_2;[15] (iv) platinum cations on single-crystal Cu_2O(111)-like single-layer films mounted on single-crystal copper(111);[16] and (v) iridium cations on reduced graphene aerogel.[17]

We now consider another class of materials—silicoaluminophosphates (SAPOs)—that offer good prospects as supports for nearly uniform atomically dispersed supported metals. These microporous, crystalline materials offer many of the advantages of zeolites—potentially remaining stable at higher temperatures than zeolites.[18] Like zeolites, SAPOs are platforms for acidic OH groups on their interior surfaces, and correspondingly they find large-scale applications as acid catalysts.[19] They also find applications as supports for metal clusters, for example, in alkane hydroisomerization catalysts.[20–24] But SAPOs have not yet been explored as supports for atomically dispersed metal catalysts, and little is known about the structures and properties of highly dispersed metals in them. SAPO frameworks are constructed of alternating tetrahedral $[PO_{4/2}]^+$ and $[AlO_{4/2}]^-$ building units, for which some P^{5+} ions are isomorphously substituted by Si^{4+} ions in tetrahedral (T) sites. The pairing of the $[PO_{4/2}]^+$ and $[AlO_{4/2}]^-$ building units leads to the charge neutrality, but the pairing of the $[SiO_{4/2}]$ and $[AlO_{4/2}]^-$ building units generates $[Si\text{-}O\text{-}Al]^-H^+$ (also designated as Si–OH–Al) Brønsted acid sites with H^+ being attached to O^- in

them. These T sites are important in catalysis: OH groups bonded to them catalyze numerous reactions, as do metals bonded to them. The metals bonded at these Si–OH–Al Brønsted acid sites in a SAPO differ from those in a zeolite because they have different environments, and therefore they are expected to have different catalytic properties.

Our broad goals were to investigate a SAPO as a support for an atomically dispersed metal catalyst and to assess its degree of uniformity and catalytic properties and compare them with those characterizing isostructural zeolites. We chose SAPO-37[25,26] because it affords an excellent basis for comparison with a well-investigated isostructural zeolite, dealuminated HY (DAY, molar SiO_2/Al_2O_3 ratio = 30). SAPO-37 has acid strength distributions that are narrower than those of this DAY zeolite (with the mean acid strength less than that of this DAY zeolite), and this property might suggest a higher degree of uniformity of the SAPO sites than of the zeolite sites for bonding metals.[18] As a consequence of the differing framework compositions, the densities of Si–OH–Al sites are different in the SAPO and the zeolite.

We used atomically dispersed rhodium as the catalytic metal on the SAPO, because rhodium in many forms finds applications as a catalyst.[27] Acetylacetonato-diethylene rhodium(I), $Rh(C_2H_4)_2(acac)$, was chosen as the precursor to take advantage of its reactivity with support OH groups to form anchored rhodium complexes and afford a comparison with the reactivities of metal oxides and zeolites, with which this precursor reacts to form Hacac as the metal becomes bonded to support oxygen atoms.[28] Our specific goals were to prepare structurally well-defined rhodium complexes on SAPO-37, to determine the structures, reactivities, and catalytic properties of these species for a test reaction involving small molecules with identifiable spectral signatures—ethylene hydrogenation—and to make a comparison with an analogous DAY zeolite-supported catalyst.

2.3 MATERIALS AND METHODS

Synthesis of SAPO-37. SAPO-37 was prepared following a modification of the IZA-verified SAPO-37 synthesis.[29] A gel with a molar composition of 0.40 SiO_2:1.00 Al_2O_3:0.90 P_2O_5:0.05 TMAOH:2.00 TPAOH:100 H_2O (TMAOH is tetramethylammonium hydroxide; TPAOH is tetrapropylammonium hydroxide) was prepared by creating two separate mixtures. The first contained water, alumina, and phosphoric acid; the second contained structure-directing agents (SDAs, namely, TMAOH and TPAOH here) and silica. For the first mixture, a solution was made of deionized water and phosphoric acid (Sigma-Aldrich, 85% H_3PO_4) that was agitated with an overhead mixer. The deionized water that was added comprised all of the free water used in the synthesis. To this solution, the alumina source, Catapal B (Sasol N.A., Al_2O_3 75%), was slowly added to a gel that formed, with aggressive stirring. The rate of Catapal B addition was low enough to ensure the formation of a homogenous aluminophosphate gel that remained free flowing. This gel was covered to prevent evaporation and allowed to peptize for a minimum of 12 h under the influence of strong mixing. The initial pH of the gel was typically approximately 1.95 and the final pH approximately 2.20. As this alumina-phosphate gel was aging, a second solution consisting of TMAOH (Sigma-Aldrich, 25% TMAOH) and TPAOH (Sigma-Aldrich, 40% TPAOH) was prepared. Fumed silica (Aerosil 200, 90% SiO_2) was then slowly added to this SDA solution, dissolving readily. The resulting silica-SDA solution became transparent with a yellowish tint after all the silica had dissolved.

After aging of the aluminophosphate gel, the solution containing silica, TMAOH, and TMPOH was slowly combined with it. Then the resulting gel was covered and agitated for at least 24 h. The initial pH of the combined gel was approximately 8.2. As noted in several sources,[26,30] it was important that the gel be aged for at least 24 h and until a final pH of 7.5 was reached (and we confirmed that aging for at least 24 h was crucial to make pure SAPO-37). During the aging of the combined gel, the pH declined to 7.6 after only six hours of mixing, before reaching a pH of 7.4–7.5 after 24 h of aging. We observed that

if the pH of the gel after 24 h was still greater than the target pH, further aging with a goal of lowering the pH of the gel did not result in a pure SAPO-37 product.

Once the gel had been properly aged and a pH of 7.5 or less attained, parts of the gel were charged to a set of Teflon-lined 45-mL Parr autoclaves, each statically heated and held at a temperature of 463 K for five days. After this period, during which crystallization occurred, each of these autoclaves in a fume hood was allowed to cool to room temperature. The resulting slurry had a clear yellow layer of mother liquor with a layer of precipitated solids. The final pH of the liquid product was 7.2. The solid precipitate was readily recovered by filtration. The collected solids were washed with an excess of deionized water followed by drying at 393 K. We emphasize that, because of the susceptibility of the SAPO-37 framework to hydrolysis, it was handled in a water-free atmosphere after washing and drying. The as-synthesized SAPO-37 powder containing organic SDAs was calcined at 873 K for 6 h in flowing air (Praxair, 99.5%) followed by 6 h at the same temperature under dynamic vacuum in a once-through plug-flow reactor. Then the sample was cooled to room temperature under dynamic vacuum and transferred into an argon-filled oxygen-free glovebox.

Synthesis of $Rh(C_2H_4)_2$ on SAPO-37. Rhodium complexes were anchored to SAPO-37 by reaction of the rhodium-containing precursor with this support. Sample handling and treatments were carried out with standard air-exclusion techniques in an argon-filled glovebox. The precursor $Rh(C_2H_4)_2(acac)$ (99%, Strem) was mixed with the calcined SAPO-37 in dried, deoxygenated *n*-pentane (Fisher, 99%), and the slurry was stirred at 298 K under argon for 24 h. After the *n*-pentane had been removed by overnight evacuation, leaving all of the rhodium on the support, the resulting sample (containing 1.0 wt % rhodium) was recovered and stored in the glovebox. The supported samples were heated in flowing helium to 423 K at a ramp rate of 5 K min^{-1} and held for 10 min. Then the sample was cooled to room temperature in flowing helium.

Synthesis of HY zeolite-supported $Rh(C_2H_4)_2$. HY zeolite (Zeolyst CPV 600, molar SiO_2/Al_2O_3 ratio = 5.2) was calcined in flowing oxygen (Praxair, O_2 19.5–23.5%) at 773 K for 2 h followed by 14 h under dynamic vacuum in a once-through plug-flow reactor. HY zeolite-supported $Rh(C_2H_4)_2$ complexes formed by reaction of the zeolite with $Rh(C_2H_4)_2(acac)$.[31] The rhodium loading of the material was 1.0 wt %.

X-ray diffraction (XRD) characterization. The crystallinity and phase purity of all the SAPO-37 samples were characterized with a Panalytical X'pert Pro MRD diffractometer or with a Rigaku Miniflex600 with CuKα radiation, operating at 40 kV and 15 mA. The as-synthesized SAPO-37 powder, which still contained the organic structure-directing agent molecules occluded in its channels/cages, was analyzed in a conventional powder XRD sample holder in the ambient atmosphere. In contrast, a plastic domed sample holder from Panalytical/Malvern was used for characterizing a spent catalyst—in this holder the sample was sealed and protected in moisture-free and oxygen-free argon to prevent potential changes in the crystalline structure of SAPO-37 and the properties of supported rhodium complexes and carbonaceous deposits formed during catalysis that might have resulted if there had been any contact with moisture and/or oxygen. The spent catalyst in the plug-flow reactor was sealed under helium, then placed in an argon-filled glovebox where the catalyst sample was recovered and loaded into a plastic-domed sample holder and sealed to prevent exposure to moisture and air prior to and during the XRD measurement; this precaution was warranted because Briend *et al.*[18] reported that prolonged exposure of SAPO-37 to moisture in air caused the structure to collapse and become amorphous.

Infrared (IR) spectroscopy. A Bruker IFS 66v spectrometer with a liquid-nitrogen-cooled HgCdTe (MCT) detector and a spectral resolution of 2 cm^{-1} was used to collect transmission IR spectra of powder samples. In the glovebox, approximately 10 mg of powder was pressed between two KBr windows for optical optimization that allowed detection of minor peaks. IR spectra were recorded with samples at room temperature under vacuum, with each spectrum being an average of 128 scans. In some

experiments, the sample was present in a diffuse reflectance (DRIFTS) cell that also served as a reactor (Harrick Scientific) equipped with KBr windows, mounted in a Praying Mantis diffuse reflectance adapter (Harrick Scientific). This DRIFTS cell in the glovebox was loaded with approximately 50 mg of dry KBr powder (Crystal Labs, 7758-02-3), along with approximately 20 mg of sample. This cell was connected into a flow system that allowed recording of spectra as reactant gases (CO, ^{13}CO, D_2, H_2, and/or ethylene) flowed through the cell at the desired temperature.

X-ray absorption spectroscopy. X-ray absorption spectroscopy (XAS) of the solid samples was carried out at beam line 4-1 of the Stanford Synchrotron Radiation Lightsource (SSRL). The storage ring energy and current were 3 GeV and 500 mA, respectively. The double-crystal Si(220) monochromator was detuned by 20% at the Rh K edge. In an argon-filled glovebox at SSRL, 400 mg of SAPO-37-supported rhodium complex containing 1.0 wt % rhodium was loaded into a transmission and fluorescence X-ray absorption spectroscopy cell/flow reactor designed to accommodate powder samples under vacuum or in reactive atmospheres.[32] The cell window was aligned at a 45° angle relative to the X-ray beam. Transient fluorescence X-ray absorption near edge spectra (XANES) and extended X-ray absorption fine structure (EXAFS) spectra were collected with a Lytle detector for samples in flowing reactive gases. For energy calibration, measurement of the absorption of a rhodium foil mounted downbeam of the sample was carried out simultaneously.

Analysis of the EXAFS data was carried out with Athena of the software package Demeter and with the software XDAP. Athena was used for edge calibration and deglitching and XDAP for background removal, normalization, and conversion of the data into an EXAFS function file. Reference files used in the fitting, with backscattering amplitudes and phase shifts for Rh–Rh, Rh–O, Rh–C, and Rh–Al contributions, were calculated with the software FEFF7.0 from crystallographic coordinates of the unit cells of the reference compounds rhodium metal, $Rh(C_2H_4)_2(acac)$, RhO_2, and Rh-Al alloy.[33,34]

Our approach to data fitting, which is standard, involved selection of several plausible structural models that make good chemical sense and fitting to determine structure parameters that were required to have physically and chemically realistic values and appropriate values of goodness of fit—followed by selection of the best-fitting model for each sample. The number of parameters used in the fitting was always less than that justified statistically, calculated on the basis of the Nyquist theorem: $n = 2\Delta k \Delta r/\pi + 2$ (where Δk and Δr, respectively, are the ranges in the wave vector and distance in real space used in the fitting). Data fitting was done iteratively for the candidate models with a difference-file technique to determine how well each model compared with the data in terms of the overall fit and the fits of individual shells—the latter being especially important in our judgment for atomically dispersed samples.

The recommended model representing each sample was chosen as the best-fitting model when the k^1- and k^3-weighted EXAFS data, Fourier-transformed data, and Fourier-transformed data characterizing each shell contribution individually were all in good agreement with the calculated fits. The quality of each fit was evaluated by the value of goodness of fit, defined below:

$$Goodness\ of\ fit = \frac{\nu}{NPTS(\nu - N_{free})} \sum_{i=1}^{NPTS} \left(\frac{\chi_{exp,i} - \chi_{model,i}}{\sigma_{exp,i}} \right)^2$$

where χ_{exp} and χ_{model} are the experimental and calculated EXAFS functions, respectively; σ_{exp} the error in the experimental results; ν the number of independent data points in the fit range; N_{free} the number of free parameters; and NPTS the number of data points in the fit range. The estimates of the error bounds are based on the reported results and statistical analyses; the values are approximate. Complementary information is presented in the Supporting Information, SI.

Catalytic activity measurements. Catalyst performance was tested with samples in a once-through temperature-controlled plug-flow reactor. The reactant feed gases (H_2, ethylene, and helium) flowed through a bed of catalyst of known mass (usually in the range of 1.00–15.0 mg) mixed with 1.0 g

of inert particles of nonporous α−Al_2O_3 (Sigma-Aldrich, 100–200 mesh) at atmospheric pressure and a temperature of 303 K. A total feed flow rate of 100 mL(NTP) min^{-1} was used in each experiment, with the feed partial pressures (in mbar) being the following: H_2, 50; ethylene, 50; helium, 900. The effluent stream was analyzed periodically with an online gas chromatograph (Hewlett−Packard HP-6890) equipped with a capillary column (PLOT Alumina "M," 50 m × 0.53 mm) and a flame-ionization detector. The reported catalytic reaction rates per rhodium atom (turnover frequencies, TOF) were calculated from conversions <10%, which were shown to be differential on the basis of the essentially linear dependence of conversion on inverse space velocity (Figure 2A.1 in the SI).

Temperature-programmed oxidation of hydrocarbon deposits. A sample of used catalyst (13.0 mg) was characterized by temperature-programmed oxidation (TPO) in air (Praxair, 99.5%) flowing at 60 mL(NTP) min^{-1} in a Netzsch STA 449 F3 instrument, with the effluent gas flowing to a mass spectrometer. Samples were quickly transferred in air from an argon-filled glovebox to a crucible. A two-step treatment was used whereby (1) the sample temperature was raised at a rate of 5 K min^{-1} to 323 K and held for 1 h to remove any possible residual moisture and (2) the temperature was increased at a rate of 5 K min^{-1} to 973 K and held for 60 min. Baseline corrections for the mass signal were made by comparison with data collected with the same temperature program performed with an empty crucible.

Acidity measurement by temperature-programmed desorption. A sample of calcined SAPO-37 (32.2 mg) was characterized for acidity by temperature-programmed desorption (TPD) of isopropylamine in nitrogen (Praxair, 99.9999%) flowing at 50 mL(NTP) min^{-1} in a Netzsch STA 449 F3 instrument, with the effluent gas flowing to a mass spectrometer. A dehydration pretreatment was used with the sample in flowing nitrogen, whereby the temperature was raised at a rate of 2 K min^{-1} to 773 K and held for 1 h to remove any residual moisture. The sample was then cooled to room temperature, and isopropylamine (Sigma-Aldrich, 99%) was dosed (0.1 mL) into the flowing nitrogen for its adsorption on the SAPO-37 sample. Then a two-step treatment was used whereby (1) the sample temperature was

raised at a rate of 5 K min^{-1} to 453 K and held for 1 h to remove any physisorbed isopropylamine and (2) the temperature was increased at a rate of 5 K min^{-1} to 800 K and held for 15 min. The sample masses determined by the TGA results are reported in units of μmol of adsorbate per gram of catalyst and referenced to the initial mass of the sample before exposure to the amine.[35,36]

Scanning electron microscopy. Scanning electron microscopy (SEM) images were obtained using a Hitachi SU5000 instrument equipped with field emission SEM instrument at 5.0 kV. Each sample was coated with a thin layer of gold prior to imaging to minimize sample charging.

BET surface area measurements. Nitrogen physisorption measurements were made with a Micromeritics 3-Flex instrument. Oven-dried sample tubes capped with a Transeal cap (Micromeritics) were tared in the glovebox and then filled with approximately 50 mg of powder. Details of the experimental methods are as reported.[37] These data are presented for calibration purposes only; we recognize that they do not provide accurate values of internal surface areas for materials such as ours (Table 2A.1).

2.4 RESULTS AND DISCUSSION

Synthesis and characterization of SAPO-37. The XRD results (Figure 2A.2 in the SI) collected with the sample under ambient conditions indicate that the as-synthesized SAPO-37 sample is characterized by a pattern characteristic of SAPO-37, as reported by Briend *et al.* (details in the SI).[18,38,39] No peaks indicative of impurities were detected. The XRD results characterizing the spent SAPO-37-supported catalyst initially incorporating $Rh(C_2H_4)_2$ (Figure 2A.3 in the SI) show that the framework structure was maintained during the following steps: calcination of the as-synthesized SAPO, the treatments preceding the catalyst testing, and catalysis in the flow reactor (details in SI). SEM images (Figure 2A.4 in the SI) of the as-synthesized SAPO-37 show that it consisted of variously sized octahedral

crystals;[38] this was the only solid phase in the synthesis product as evidenced by the XRD results. The BET surface area of the calcined SAPO-37 matches well with literature.[38,40]

Synthesis of SAPO-37-supported $Rh(C_2H_4)_2$. The reaction of $Rh(C_2H_4)_2(acac)$ with SAPO-37 was accompanied by changes in the IR spectra of SAPO-37 indicating that OH groups on its surface were converted when the rhodium was anchored to the support, as discussed below. Spectrum A of Figure 2.1 characterizes bare SAPO-37 calcined at 873 K in air followed by evacuation, and spectrum B represents the sample after chemisorption of $Rh(C_2H_4)_2(acac)$. The intensities of the bands at 3640 and 3578 cm^{-1}, corresponding to OH groups at the Si–OH–Al sites of the SAPO,[20,41] decreased as the rhodium was chemisorbed, indicating that these groups were involved in the surface reaction and implying that the rhodium was bonded near the Si–OH–Al Brønsted acid sites. Supporting this inference are IR spectra indicative of Hacac on the support, formed as $Rh(C_2H_4)_2(acac)$ reacted with support OH groups and formed Rh–O bonds (as shown by EXAFS spectra, *vide infra*) (Figure 2A.5 in the SI). Ethylene ligands were still present on the rhodium after anchoring, indicated by IR bands in the C–H region (Figure 2A.6 in the SI). The band at 3745 cm^{-1}, corresponding to SAPO Si–OH groups,[42,43] is too low in intensity to justify any conclusion about whether reaction occurred at those sites. Moreover, the band corresponding to P-OH sites, which would have been expected at 3675 cm^{-1}, was not evident in the spectra, indicating negligible amounts of those species. The band at 3718 cm^{-1} is assigned to extra-framework silica on the basis of data characterizing the spectrum of the hydroxyl region of another SAPO, SAPO-34.[44,45] The growth of the band at 3718 cm^{-1} is attributed to slight moisture/air exposure that occurred between the measurements.

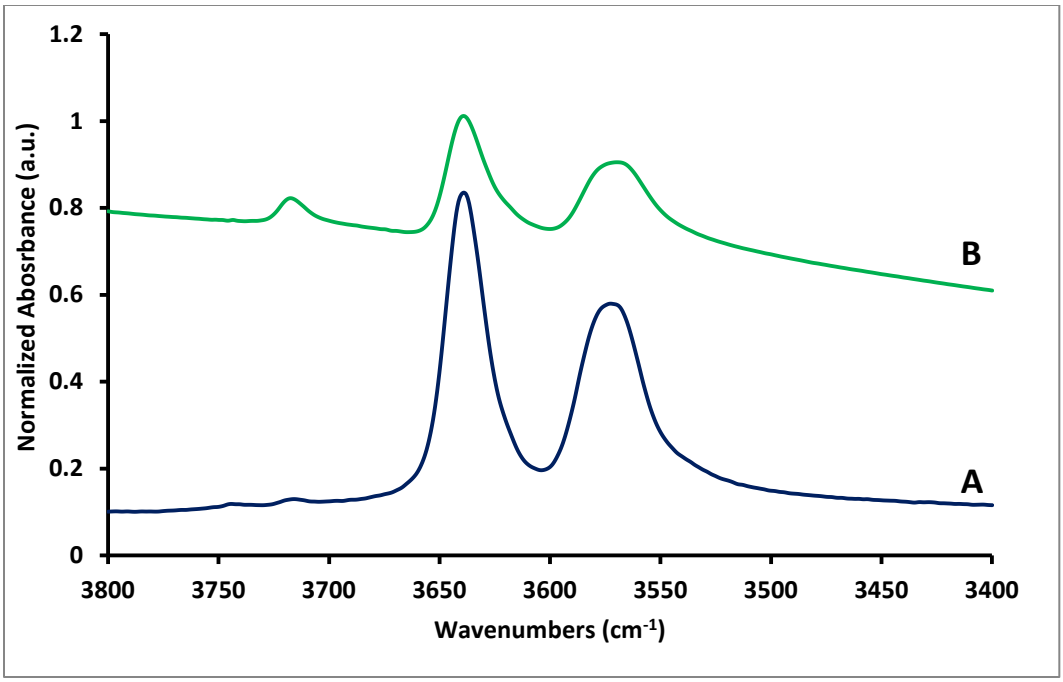

Figure 2.1. IR spectra in the ν_{OH} region characterizing the following samples: (A) bare calcined SAPO-37; (B) sample formed by reaction of SAPO-37 with $Rh(C_2H_4)_2(acac)$ in *n*-pentane after removal of this solvent.

XANES evidence of positively charged rhodium in rhodium diethylene complexes on SAPO-37. The XANES data characterizing the SAPO-37-supported rhodium complex are compared in Figure 2A.7 in the SI with the XANES spectrum of rhodium metal and that reported for the comparable rhodium diethylene complexes bonded to DAY zeolite. The white line characterizing rhodium in the SAPO-37-supported complex is centered at an energy 15 eV higher than that of the rhodium K edge (23220 eV). For comparison, XANES spectra characterizing rhodium on DAY zeolite (and rhodium foil) are characterized by white lines with maxima at 15 and 10 eV, respectively, above the rhodium K edge, implying that the rhodium supported on SAPO-37 and on DAY zeolite was positively charged (but, as expected, the XANES data are not sufficient to determine the exact rhodium oxidation states).

EXAFS evidence of structure of rhodium diethylene complexes on SAPO-37. The EXAFS results characterizing the supported rhodium complex are summarized in Table 2.1. Because the light backscatterers O and C are not readily distinguished from each other in the EXAFS data fitting, we

present the fitting results for a structural model that is verified by the IR data—that is, with each rhodium atom π-bonded to two ethylene ligands and anchored to the support by Rh–O bonds. Thus, the data determine a Rh–O coordination number of 2, within error, consistent with results for a comparable DAY zeolite- supported rhodium complex.[28] The Rh–O distance of 2.10 Å is a bonding distance.[12,46] The bonding distances of the Rh–C shells of the complexes on SAPO-37 and DAY zeolite are, within error, the same, but the Rh–O distances characterizing these complexes on the two supports differ slightly from each other (Table 2.1). In the fitting we could not distinguish the Rh–Al, Rh–Si, and Rh–P contributions, as expected. Details of other candidate models tested in the EXAFS fitting are presented in the SI (Figures 2A.19–21). On the basis of these results and the IR evidence that the rhodium precursor reacted at the Si–OH–Al sites, we infer the structural model shown in Scheme 2.1, which at this scale matches models for the rhodium complex on DAY zeolite.[9] This is a key result: it shows that the opportunity is presented to compare rhodium bonded at the SI–OH–Al Brønsted acid sites in SAPO-37 with those bonded at the corresponding sites in the isostructural DAY zeolite.

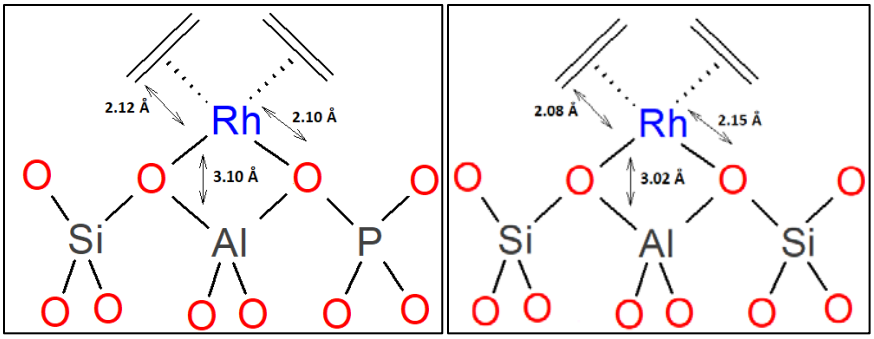

Scheme 2.1. Structural model of rhodium complex on SAPO-37 (left), and rhodium complex on DAY zeolite (right),[9] each with distances determined by the best-fit model determined by EXAFS spectroscopy.

Data reported for the comparable DAY zeolite-[9] and MgO-supported[47] rhodium species are presented in Table 2.1, showing that the DAY zeolite-supported species, within error, is isostructural with the SAPO-37 supported species. The rhodium species on MgO are also characterized by an average of two ethylene ligands per rhodium atom, but they are not isostructural with the SAPO-37- and DAY zeolite-

supported species because the data indicate a mixture of species—the number of oxygen atoms on MgO bonded to rhodium ranges from 1 to 2, depending on the treatment of the support and the sites to which the rhodium bonds.

Reactivity of SAPO-37-supported $Rh(C_2H_4)_2$. To investigate the reactivity of the supported rhodium diethylene complexes, samples in the DRIFTS cell were brought in contact with flowing CO in 15-min pulses (3115 CO molecules per rhodium atom) at atmospheric pressure and 298 K, followed by a temperature ramp to 423 K at a rate of 5 K min^{-1} with helium flowing through the cell. The spectra (Figure 2.2) show that the rhodium diethylene species reacted with CO to give supported species characterized by ν_{CO} bands at 2115 and 2052 cm^{-1}, assigned to the symmetric and asymmetric CO vibrations of rhodium *gem*-dicarbonyls (matching those of the DAY zeolite-supported sample[48]). During the treatment, there was a decrease in intensity of the bands at 3086, 3015, and 2980 cm^{-1} along with the disappearance of the ν_{CH} band at 3060 cm^{-1}, indicating that ethylene ligands had been removed from the rhodium (Figure 2A.8 in the SI). The bands at 2103 and 2021 cm^{-1} (Figure 2.2) correspond to ^{13}CO in natural abundance.[48] The shoulder at 2041 cm^{-1} (Figure 2.2) is assigned to rhodium dicarbonyls on the outer surfaces of SAPO-37 crystallites.[49,50] All these results support the inference that $Rh(C_2H_4)_2(acac)$ reacted with OH groups on SAPO-37 to give supported $Rh(C_2H_4)_2$ that upon further treatment reacted with CO to give the rhodium *gem*-dicarbonyl species bonded near Si–OH–Al sites in the SAPO-37.

Experiments with ^{13}CO confirmed that the bands shown in Figure 2.2 represent rhodium dicarbonyls, as the bands at 2115 and 2052 cm^{-1} decreased in intensity while the bands at 2066 and 2008 cm^{-1} grew in as ^{13}CO reacted with the sample (Figure 2A.9 in the SI). The ratio of frequencies of ^{12}CO and ^{13}CO corresponds to the harmonic approximation.[51]

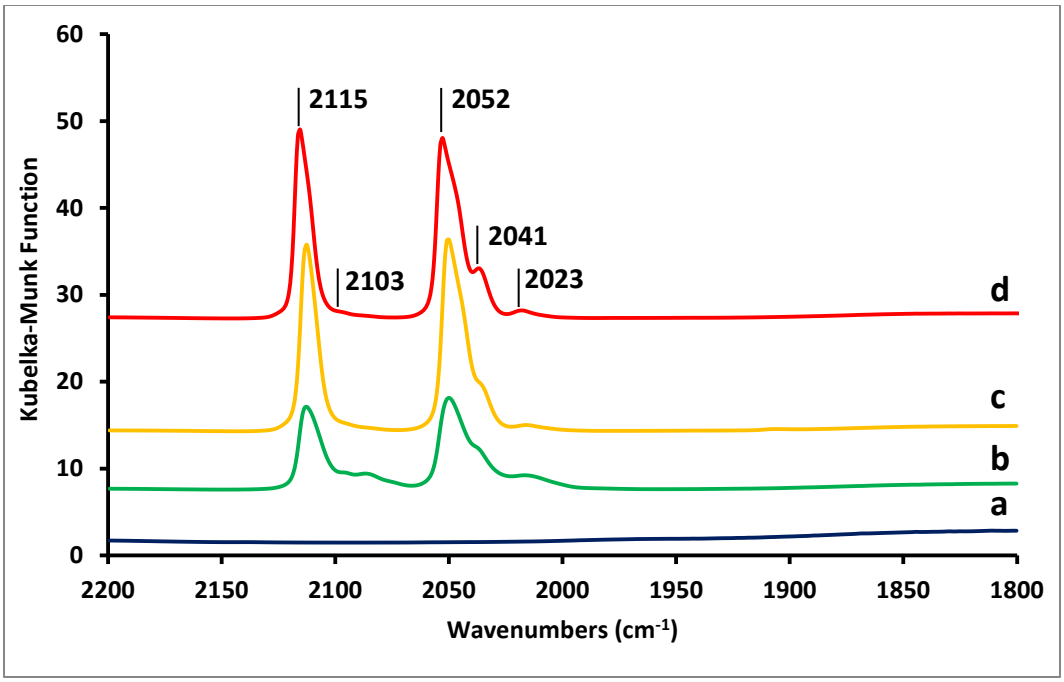

Figure 2.2. DRIFTS spectra in the υ_{CO} region characterizing the SAPO-37-supported $Rh(C_2H_4)_2$: spectrum **a** was recorded with the sample in helium flowing at 50 mL(NTP)/min, and spectrum **b** was recorded after the same sample had been in contact with flowing 10% CO in helium for 15 min, followed by a purge of the DRIFTS cell with helium for 30 min. Spectrum **c** is of the same sample at 423 K in flowing helium, and spectrum **d** was recorded at room temperature with the sample in flowing helium.

When the SAPO-37-supported $Rh(CO)_2$ was exposed to flowing ethylene at 298 K, the ν_{CO} bands at 2115 and 2052 cm^{-1}, assigned to the ν_s and ν_{as} vibrations, disappeared (Figure 2A.10 in the SI), and a new band appeared, at 2053 cm^{-1} (Figure 2A.10 in the SI), assigned on the basis of observations for zeolite DAY-supported species to $Rh(CO)(C_2H_4)$.[31] A weak band appeared at 2030 cm^{-1}, assigned tentatively to the species bonded to small amorphous regions of the support on the basis of observations with $Rh(CO)(C_2H_4)$ on SiO_2;[52,53] alternatively, it could be assigned to linear Rh(CO) on amorphous SiO_2.[54]

EXAFS data characterizing the SAPO-37-supported rhodium *gem*-dicarbonyls confirm the site-isolation of the rhodium and give evidence of the non-carbonyl ligands bonded to it—that is, the support itself. Structure parameters corresponding to the best-fit models (details in the SI) are given in Table 2.1, with data for rhodium carbonyls on other supports shown for comparison. The inference that each rhodium species was site-isolated is bolstered by the result that the EXAFS data give no evidence of any Rh–Rh contributions. The Rh–O distances are consistent with bonding of positively charged rhodium

atoms to oxygen atoms of the supports. The results are consistent with the structural model of the SAPO-37-supported species shown in Scheme 2.1.

Other comparable rhodium and iridium species have been reported for various metal oxide supports, with ν_{CO} values depending on the support; details are given in Table 2A.2 in the SI; the ν_{CO} values are a measure of the electron-donor properties of the supports as ligands.[55] The ν_{CO} values characterizing SAPO-37-supported rhodium dicarbonyl are slightly less than those characterizing the DAY zeolite-supported rhodium dicarbonyl. The support SAPO-37 is less electron withdrawing than DAY zeolite, but the difference is small—likely too small to distinguish within the error of our data. Correspondingly, the Rh–O and Rh–C distances determined by EXAFS spectroscopy are also nearly the same—and also likely too small to distinguish within the error of our data.

Table 2.1: Structural Models Based on EXAFS Spectra Characterizing Rhodium Diethylene and Rhodium *gem*-dicarbonyl Species Supported on SAPO-37, DAY Zeolite, and MgO and CO Vibrational Frequencies of the Rhodium Carbonyls.[a]

Initial form of catalyst	IR bands of carbonylated form of sample, ν_{CO} sym/asym (cm^{-1})	**fwhm of ν_{CO} band, sym/asym (cm^{-1})**	Shell	*N*	*R* (Å)	$10^3 \times \sigma^2$	ΔE_0	Refs
$Rh(C_2H_4)_2$/ SAPO-37, 1.0 wt % rhodium	2115/2052	**7/10**	Rh-C	4.0	2.12	7.5	-7.5	this work
			Rh- O	2.1	2.10	6.3	4.0	
			Rh-Al	1.1	3.10	6.4	-3.0	
$Rh(C_2H_4)_2$/ DAY, 1.0 wt % rhodium	2118/2053	**<8**	Rh-Rh	-[b]	-[b]	-[b]	-[b]	9,56
			Rh-C	3.7	2.08	3.4	-2.0	
			Rh-O	2.1	2.15	3.1	7.1	
			Rh-Al	1.1	3.02	6.7	-2.5	
$Rh(C_2H_4)_2$/ MgO, 1.0 wt % rhodium	2082/2004	**34/37**	Rh-Rh	-[b]	-[b]	-[b]	-[b]	47
			Rh-C	4.0	2.04	0.68	11.2	
			Rh- O_s[c]	1.4	2.18	0.86	-12.8	
			Rh-O_l[c]	1.7	2.79	6.62	-0.2	

[a]Notation: *N*, coordination number; *R*, distance between absorber and backscatterer atoms; $\Delta\sigma^2$, disorder term (Debye–Waller factor); ΔE_0, inner potential correction. Error bounds (accuracies) characterizing the structural parameters determined by EXAFS spectroscopy are estimated to be as follows: *N*, ±20%; *R*, ±0.02 Å; $\Delta\sigma^2$, ±20%; ΔE_0, ±20 %. [b]Contribution not detectable. Details of the EXAFS fitting are provided in the SI. [c]The subscripts s and l refer to short and long, respectively.

Uniformity of SAPO-37-supported $Rh(CO)_2$. The fwhm values of the carbonyl bands of the SAPO-37-supported rhodium species are < 10 cm^{-1} (Table 2.1), consistent with the inference that the sites to

which the rhodium was bonded were nearly uniform—but not quite as uniform as those in DAY zeolite incorporating analogous supported rhodium complexes (for which values of the fwhm are < 8 cm^{-1} (Table 2.1)).[57] The data are compared in Table 2A.2 in the SI with those of zeolite- and oxide-supported metal carbonyls—showing that the SAPO-37-supported species are among the most nearly uniform of any reported supported metal species. Thus, the results highlight the value of this support and these samples for fundamental investigations of the catalytic chemistry of the supported species and specifically for assessment of the effects of the support as a ligand.

Catalytic performance of SAPO-37-supported rhodium complexes. The rhodium diethylene complex supported on SAPO-37 was used as the precursor of a catalyst for ethylene hydrogenation in a flow reactor. We stress that the catalytic activity of the sample is not attributable to acidic OH groups as catalytic sites—this point is validated by the results of blank experiments confirming that the SAPO alone did not have measurable activity for hydrogenation and dimerization under our conditions. The same conclusion pertains to the HY zeolite-supported rhodium complexes (with zeolite molar SiO_2/Al_2O_3 ratios of 5 and 30): the results of blank experiments with the zeolites alone gave no evidence of activity for hydrogenation or dimerization under our conditions; that activity became measurable only when the temperature was raised to 433 K.[31]

Thus, the catalytic activity under our conditions is attributed to the rhodium species. Initial conversions were differential (Figure 2A.1 in the SI), determining TOF values directly. The catalyst lost activity in operation in the flow reactor (Figure 2.3); the initial TOF characterizing the SAPO-37-supported catalyst, determined by extrapolation of the TOF vs. time on stream data (Figure 2.3), was found to be approximately 0.1 s^{-1}. Comparable rhodium complexes supported on the aforementioned HY zeolites have been investigated at the same temperature and pressure used for the SAPO-37, but with different feed compositions,[31] as summarized in Figure 2.3.

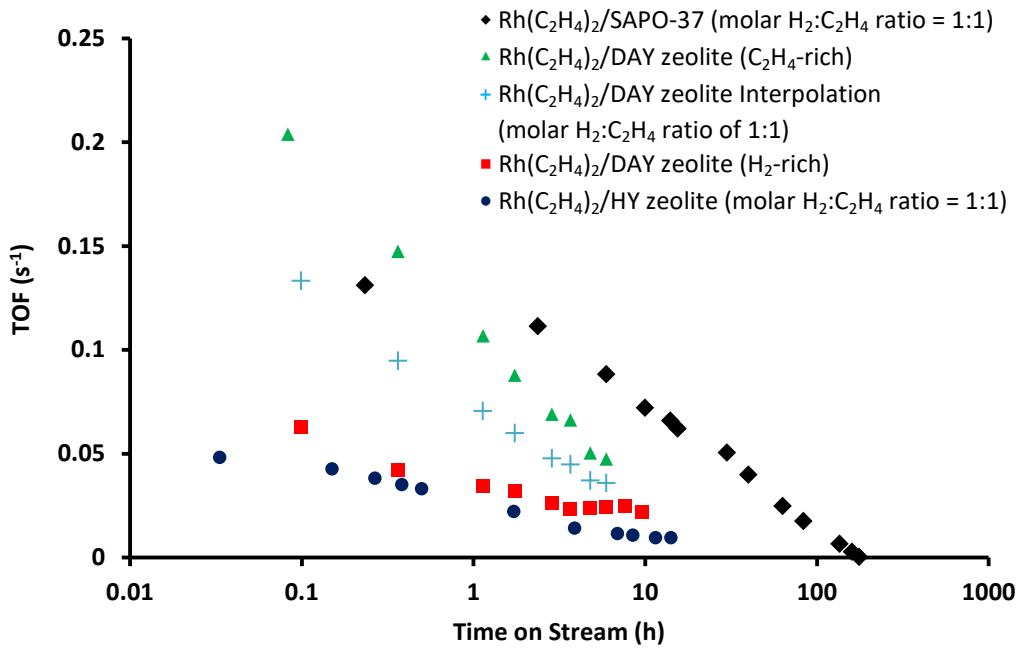

Figure 2.3. Comparison of SAPO-37 and HY zeolites as supports for rhodium complex catalysts for ethylene conversion. Performance of supported rhodium catalysts initially present as rhodium diethylene complexes for ethylene conversion in the presence of H_2 at 303 K and 1 bar (each catalyst contained 1.0 wt% rhodium). The catalyst samples (in their initial forms) are identified by symbols shown in the figure; details follow: ◆ SAPO-37-supported catalyst (this work, molar H_2:C_2H_4 ratio = 1:1); ● zeolite HY (molar SiO_2/Al_2O_3 ratio = 5.2) supported catalyst (this work, molar H_2:C_2H_4 ratio = 1:1). ■ zeolite DAY (molar SiO_2/Al_2O_3 ratio = 30) supported catalyst[31] (molar H_2:C_2H_4 ratio = 1:4); ▲ zeolite DAY (molar SiO_2/Al_2O_3 ratio = 30) supported catalyst[31] (molar H_2:C_2H_4 ratio = 4:1); + zeolite DAY (molar SiO_2/Al_2O_3 ratio = 30) supported catalyst[31] with points determined for molar H_2:C_2H_4 ratio = 1:1, by interpolation of data for the feed compositions stated above. Details are given in Figure 2A.11. A more direct comparison is afforded by considering the data for the SAPO-37 supported catalyst (◆) and the interpolated data for DAY zeolite supported catalyst (+), but we emphasize that the densities of metal bonding sites (OH groups bonded near Al sites) were not the same in these catalysts, being 160 µmol/g of DAY zeolite[35] and 900 µmol/g of SAPO-37, respectively, as determined by acidity measurements by TPD of isopropylamine (Figure 2A.12 in the SI).

Interpolated data provide a direct comparison with one of the zeolites (Figure 2.3). The products observed with the HY zeolite- and DAY zeolite-supported catalysts were predominantly butenes, along with ethane (Table 2.2). The data show that the SAPO-37-supported catalyst is more active than the comparable catalysts (Table 2.2), and the products formed with the SAPO-37-supported catalyst differ from those formed with the zeolite-supported catalysts, with the former being markedly more selective than the latter for hydrogenation rather than dimerization of the olefin (Table 2.2).

Table 2.2: Comparison of Activities of Catalysts Initially Incorporating Rhodium Diethylene Complexes Supported on SAPO-37, DAY, HY Zeolite, and MgO for Hydrogenation and Dimerization of Ethylene. Each catalyst contained 1.0 wt% rhodium.

Initial form of catalyst	Molar SiO_2/Al_2O_3 ratio in catalyst support	Initial TOF for ethylene conversion (s^{-1})	Initial selectivity in ethylene conversion (mol %)[I]					Deactivation time (h)[K]	Ref
			ethane	*n*-butane	*trans*-2-butene	1-butene	*cis*-2-butene		
$Rh(C_2H_4)_2$/SAPO-37	-[A]	0.13[C]	99.6	0.4				192	this work
$Rh(C_2H_4)_2$/HY zeolite	5.2	0.05[D]	61.3	< 0.4	26.6	2.7	9.0	59[L]	this work
$Rh(C_2H_4)_2$/DAY zeolite	30	0.10[E]	52.9	1.0	31.3	3.9	10.9	22[M]	58
$Rh(C_2H_4)_2$/DAY zeolite	30	0.26[F]	24	76[J]				20[L]	59
$Rh(C_2H_4)_2$/DAY zeolite	30	0.075[G]	18.9	1.9	78.2[J]			133[L]	31
$Rh(C_2H_4)_2$/MgO	-[B]	0.016[H]	100	No data reported				No data reported	47

[A]The molar SiO_2/Al_2O_3 ratio of a zeolite is used as a proxy for acid site density when the acidity stems from the amount of Al_2O_3 present in the neutral SiO_2. Because SAPOs and zeolites are two different classes of molecular sieves, with SAPOs incorporating Si, Al, and P and the zeolites Si and Al, the molar composition of SAPO-37 is reported here as 1.00 SiO_2: 1.67 Al_2O_3:1.06 P_2O_5. We recognize that the densities of metal bonding sites (SI–OH–Al) of SAPO-37 and zeolite are different and thus they are reported on the basis of TPD acidity measurements done with isopropylamine (900 µmol/g) for SAPO-37 (Figure 2A.12 in the SI) and elsewhere for DAY zeolite.[35]

[B]Not applicable.

[C]TOFs determined at 303 K and 1.0 bar; feed partial pressures (mbar): C_2H_4, 50; H_2, 50; helium, 900; total flow rate 100 mL(NTP)/min; catalyst mass, 8.4 mg.

[D]TOF determined at 303 K; 1 bar; feed partial pressures (mbar): C_2H_4, 50; H_2, 50; helium, 900; total flow rate 100 mL(NTP)/min; catalyst mass, 11 mg.

[E]TOFs determined from C_2H_4 conversions <5%; catalyst mass, 10−30 mg; feed partial pressures (mbar): C_2H_4, 50; H_2, 50; helium, 900; total flow rate, 100 mL(NTP)/min.

[F]TOF determined at 303 K; 1 bar; feed partial pressures (mbar): C_2H_4, 100; H_2, 400; helium, 500; total flow rate 100 mL(NTP)/min; catalyst mass, 21 mg.

[G]TOF determined at 303 K; 1 bar; feed partial pressures (mbar): C_2H_4, 400; H_2, 100; helium, 500; total flow rate 100 mL(NTP)/min; catalyst mass, 21 mg.

[H]TOF determined at 298 K; feed partial pressures (mbar): C_2H_4, 50; H_2, 50; balance helium; total flow rate 100 mL(NTP)/min.

[I]Selectivity as a function of time on stream remained essentially constant (Figure 2A.13 in the SI).

[J]Value reported in reference does not distinguish among the butenes.

[K]Deactivation time is defined as the time it takes for the catalytic activity (TOF) to decline to a value indistinguishable from zero in Figure 2.3 (details in SI).

[L]Value determined by extrapolation of trend line of TOF vs. time on stream plotted on a logarithmic scale.

[M]Value determined by extrapolation of trend line determined by interpolation of data for ethylene-rich and hydrogen-rich feeds plotted at TOF vs. logarithm of time on stream. Details are given in Figure 2A.11 in the SI.

To provide further understanding of the catalytic chemistry, experiments were done with D_2, ethylene, and mixtures of D_2 and ethylene as reactants. IR spectra of the SAPO-37-supported $Rh(C_2H_4)_2$ catalyst (20 mg) in D_2 flowing at 30 mL(NTP) min^{-1} show that the Si–OH–Al bands of SAPO-37 disappeared, but without the appearance of bands characterizing Si–OD–Al groups, which, had they formed, would have been expected in the range of 2550–2780 cm^{-1} (Figure 2A.14 in the SI).[60] To further probe the Si–OH–Al sites of SAPO-37, the SAPO-37 supported $Rh(C_2H_4)_2$ catalyst (20 mg) was exposed C_2H_4 flowing at 10 mL(NTP) min^{-1}. IR spectra show that the alkene interacted with the SAPO-37 through the acidic Si–OH–Al groups, as indicated by the reduced intensity of the OH stretching bands at 3640 and 3578 cm^{-1} (Figure 2A.15 in the SI). The C_2H_4–SAPO-37 interaction is inferred to be weak, with the C=C bond evidently maintained after adsorption, as indicated by the lack of evidence of C–C bond formation. This result is consistent with the observation that ethylene desorbed from the Si–OH–Al sites when helium flowed over the sample at room temperature, with full recovery of the initial Si–OH–Al bands at 3640 and 3578 cm^{-1} (Figure 2A.15 in the SI). The SAPO-37-supported rhodium complexes (20 mg) in a flowing mixture of C_2H_4 (5 mL(NTP) min^{-1} and D_2 (5 mL(NTP) min^{-1}) produced $C_2H_4D_2$ (m/z = 30), without monodeuterated ethane, as shown by mass spectra of the effluent gas (Figure 2A.16 in the SI) (the sensitivity of the mass spectrometer was not sufficient to determine whether deuterated butenes also formed). Thus, we infer that the Si–OH–Al sites did not exchange significantly with D_2 (or H_2) under our catalytic reactions conditions.

These results are contrasted with those reported for DAY zeolite-supported rhodium complexes, for which the Al–OH and Si–OH groups were observed to undergo exchange with D_2 to form Al–OD and Si–OD in the presence of flowing D_2 at 303 K and 1 bar.[9] When zeolite-supported rhodium complexes were exposed to a flowing mixture of C_2H_4 + D_2 under these conditions, mass spectra of the product stream demonstrated the formation of C_2H_5D and $C_2H_4D_2$ in low concentrations, along with nondeutrated

butenes characterized by C_3H_5 and C_4H_8 fragments (*m*/*z* 41 and 56, respectively, corresponding to the typical fragmentation of *n*-butenes).[9]

Characterization of deactivated catalyst. To characterize changes in the catalyst during operation, its performance was monitored by GC analysis of the reaction products. The data (Figure 2.3) show that the catalyst deactivated, becoming essentially inactive after about 192 h on stream. To gain insight into the activity loss, the experiment was repeated with the sample (20 mg for optimum spectra) in the DRIFTS cell under the same conditions. Spectra recorded as the catalytic reactions proceeded (Figure 2A.17 in the SI) show increasing intensities of peaks assigned to C–H vibrations (2964−2876 cm^{-1}), assigned to carbonaceous deposits in zeolite catalysts incorporating supported rhodium complexes.[9, 28, 31, 59,61] TPO data characterizing the used catalyst (Figure 2A.18 in the SI) show that it contained 2.0 wt% carbon after 143 h on stream, and correspondingly there had been a slight color change of the sample after this period of catalytic operation, from white to beige.

To check whether the catalyst deactivation was associated with structural changes of the SAPO-37 support, we used XRD to characterize a spent SAPO-37-supported that was initially in the form of $Rh(C_2H_4)_2$ after it had been tested as a catalyst at atmospheric pressure, 303 K, and a total flow rate of 100 mL(NTP) min^{-1}, with the partial pressures of H_2 and ethylene each being 50 mbar and that of helium 900 mbar. The catalyst (ca. 200 mg) was not mixed with inert particles in this experiment, to optimize the XRD data quality. A comparison of the XRD patterns of the as-synthesized SAPO-37 sample and the spent SAPO-37-supported catalyst sample is shown in Figure 2A.3 in the SI. The data show that the SAPO-37 structure was maintained during the calcination of the as-synthesized SAPO-37-supported sample and during the catalytic reactions, with the XRD pattern consistent with reported data for SAPO-37[38,62,63] and unchanged. The small differences in peak intensities relative to those of the parent (as-synthesized SAPO-37) are related to the following: (1) rhodium species bonded to the SAPO-37, consistent with reports of lanthanum atoms in zeolite HY;[64] (2) carbonaceous deposits occluded in the

channels/cages of SAPO-37, consistent with reports of coking of ZSM-5 during methanol to gasoline (MTG) conversion conditions;[65] (3) and the use of two different sample holders (a conventional sample holder for the as-synthesized SAPO-37 under ambient conditions) and a domed sample holder for the spent catalyst in which it was sealed and protected in a moisture- and oxygen-free argon atmosphere to prevent possible changes that might otherwise have affected the carbonaceous deposits and the crystal structure of the SAPO-37.

Thus, we infer that the catalyst deactivation resulted from the formation of large organics that accumulated in the pores, covering catalytic sites and/or blocking catalyst pores, as reported for zeolite-supported rhodium complexes;[9] reports characterizing the zeolite-supported catalysts (Table 2.2 and Figure 2.3) under both hydrogen-rich (molar feed H_2:C_2H_4 ratio = 4:1) and ethylene-rich conditions (molar feed H_2:C_2H_4 ratio = 1:4) show that the zeolite-supported rhodium complexes deactivated more rapidly than the SAPO-37-supported complexes (Figure 2.3). By interpolation of the reported results characterizing ethylene-rich and H_2-rich feeds that bracket our reaction conditions (molar H_2:C_2H_4 ratio = 1:1) (Table 2.2), we infer that DAY zeolite (molar SiO_2/Al_2O_3 ratio = 30)-supported rhodium complexes would have been almost completely deactivated after 22 h (Figure 2.3 and Figure 2A.11 in the SI).

We emphasize that although the densities of metal bonding sites (Si–OH–Al sites) are different for the two catalysts, the catalytic species in them are nearly equivalent in local structure, as shown by the EXAFS data, and the supported rhodium species are highly uniform, as shown by the ν_{CO} values determined by IR spectroscopy (Table 2A.2 in the SI).

Isostructural supported rhodium complexes on SAPO-37 and on HY zeolites: comparison of catalytic properties. To repeat a central result: when $Rh(C_2H_4)_2(acac)$ reacted with Si–OH–Al sites of SAPO-37, the rhodium became bonded to the support through Rh–O bonds, as shown by IR (Figure 2A.5) and EXAFS data (Table 2.1). These results match those for a family of oxide- and molecular sieve-supported rhodium complexes (Table 2A.2 in the SI).[9,28] The key result is therefore that the SAPO-37-

and DAY zeolite-supported rhodium complexes are isostructural—this statement pertains to both the rhodium diethylene complexes and to the rhodium *gem*-dicarbonyl complexes (Table 2.1, Table 2A.2 in the SI, and Figure 2.2). Thus, the EXAFS-determined bond distances characterizing the SAPO-37- and zeolite-supported species (Table 2.1) match within error, and the IR spectra indicate that the carbonylated species were rhodium *gem*-dicarbonyls, with all the results, specifically including the XANES data, being consistent with the identification of the rhodium complexes as Rh(I) species. The zeolite- and SAPO-37-supported rhodium complexes are the most closely related pair in any family of supported metals. However, the zeolite- and SAPO-37-supported rhodium *gem*-dicarbonyls are not the same, because the supports—as ligands—are different (Table 2A.2 in the SI), with the reactivities therefore expected to be different.

Thus, the catalyst performance data (Table 2.2, Figure 2.3) show that the rhodium complexes on SAPO-37 and on DAY zeolite are approximately the same in activity, as measured by the rate of product formation, with the measured initial TOF values being similar when the molar H_2 to ethylene ratio was 1:1 under our standard conditions. However, the product distributions characterizing the two catalysts are substantially different: the rhodium complexes on SAPO-37 are more selective for hydrogenation than those on the HY zeolite samples, with butenes formed only in trace amounts on the former but as the majority product on the latter (Table 2.2). This difference highlights the point that although the frameworks of SAPO-37 and zeolite Y (faujasite) are isostructural, the frameworks have different electronic properties.

All the data are consistent with the inference that both the SAPO-37-supported and zeolite-supported rhodium complexes were chemisorbed as the bidentate acac ligands in the precursor were replaced with a pair of oxygen atoms of the support, consistent with what was inferred before for DAY zeolite-supported rhodium diethylene.[66] All the data support this inference, with the IR and EXAFS data showing that the differences between the SAPO and zeolite supports as ligands are very small,

consistent with the differences between these supports as ligands being in the compositions at more than bonding distances away from the rhodium. The catalytic data are evidently a stronger indicator of these differences than the spectra.

If one were to suggest that the differences in ν_{CO} and Rh–O distances distinguishing the SAPO- and zeolite-supported samples were real—and we emphasize that the error estimates weigh against this suggestion, which must be considered hypothetical—then the differences in ν_{CO} values and shorter Rh–O distance (2.10 Å) characteristic of the SAPO-37-supported rhodium complex than of the zeolite-supported rhodium complex (2.15 Å) would imply that the electron-withdrawing properties increased in the order DAY zeolite > SAPO-37 (Table 2A.2 in the SI). We thus postulate that the different selectivities for dimerization are related to the different Rh–O distances in the working catalysts – consistent with the recent results of Vummaleti *et al.*,[67] who used density functional theory to investigate the mechanism of butene formation on a zeolite-supported rhodium complex catalyst closely comparable to ours. They inferred a new "three-ligand" mechanism proceeding through a metallacycle intermediate, whereby a Rh–zeolite oxygen bond is broken in the mechanism. To repeat, although the errors in our data leave the matter open to question, our data are consistent with the interpretation that the support properties affect the reactivities of the rhodium species so that the stronger electron-withdrawing tendency of zeolite DAY relative to SAPO-37 is reflected in a slight shift of ν_{CO} and weaker Rh–O bonds in the zeolite than in the SAPO-supported catalyst (the longer bond distance implies a weaker interaction between rhodium and oxygen and a more easily broken Rh–O bond, favoring the Vummaleti oligomerization mechanism on zeolite-supported rhodium over than on the SAPO-supported rhodium.

Consistent with this point, the strengths of the Si–OH–Al Brønsted acid sites on SAPO-37 are less than those of the Si–OH–Al Brønsted acid sites on DAY zeolite, [68] and the strengths of the Lewis acid sites on SAPO-37 and SAPOs in general are less than those of typical high-silica zeolites. These characteristics are important in determining the catalytic properties of these molecular sieves in large-scale

applications: the weaker acid strengths of the SAPOs correspond to fewer reaction pathways that lead to the formation of carbonaceous deposits and catalyst deactivation—and correspondingly to higher selectivities to desired products.[69] Specifically, the lower tendency for formation of carbonaceous deposits in SAPO-34 than in the isostructural chabazite in methanol-to-olefin (MTO) conversion catalysis (corresponding to the lower acid strength of SAPO-34) accounts for the important practical benefit of better maintenance of micropore volume in the SAPO during operation.[70]

Likewise, these support effects as ligand effects are evident in the catalytic data reported here, both in terms of catalyst selectivity and stability in operation. Our SAPO-supported catalyst is more stable than the isostructural zeolite-supported catalyst, as summarized in Table 2.2 and Figure 2.3. The formation of butenes on the zeolite-supported catalyst in contrast to the SAPO-supported catalyst reflects the differing effects of the supports as ligands, and this selectivity difference suggests that the olefins formed in the zeolite pores led to the formation of higher-molecular-weight products that would account for the observed accumulation of carbonaceous deposits and catalyst deactivation.

2.5 CONCLUSIONS

Well-defined SAPO-37-supported rhodium complexes were tested as catalysts for the conversion of H_2 with ethylene and compared with zeolite HY-supported rhodium complexes. IR spectra show that the rhodium complexes were anchored to nearly uniform Al sites of SAPO-37, and IR and EXAFS data show that the SAPO- and zeolite-supported rhodium diethylene and rhodium dicarbonyl complexes are isostructural—and thus unique in providing a comparison of two catalysts differing only in the support composition. Thus, the supports as ligands account for the different ν_{CO} frequencies of the CO ligands bonded to the rhodium in each molecular sieve. The differences in the supports as ligands account for the different selectivities of the two catalysts for ethylene conversion in the presence of H_2 (with the zeolite-supported catalyst giving substantial butene product but the SAPO-supported catalysts not) and

also for their differences in catalyst deactivation. We stress that the data and conclusions reported here were made possible by the near uniformity of the supports and the supported species, which allowed precise characterization of those species and a clear comparison of two isostructural catalysts.

2.6 ACKNOWLEDGEMENTS

We thank our University of California, Davis, colleagues N. W. Felvey and R. C. Runnebaum for help with the TGA measurements and A. J. Yeh for help with nitrogen physisorption measurements. We are grateful to D. Xie and M. Deldar of Chevron for the XRD measurements with the Panalytical domed sample holder. J. T. Hughes thanks Hong-Xin Li and Phillip Connolly of Zeolyst for their interest and support of this academic collaboration. The work was supported by the U.S. Department of Energy (DOE), Office of Science, Basic Energy Sciences (BES), Grant DE-FG02-04ER15513. We thank Chevron for a fellowship supporting JPA. We gratefully acknowledge beam time at Beamline 4-1 at the Stanford Synchrotron Radiation Lightsource supported by the DOE Division of Materials Sciences under Contract DE-AC02-76SF00515 and by the Co-ACCESS program supported by DOE BES Chemical Sciences, Geosciences, and Biosciences Division; we appreciate the help of Ryan Davis and Adam S. Hoffman at the synchrotron.

2.7 REFERENCES

(1) Vajglová, Z.; Kumar, N.; Peurla, M.; Hupa, L.; Semikin, K.; Sladkovskiy, D. A.; Murzin, D. Y. Effect of the Preparation of Pt-Modified Zeolite Beta-Bentonite Extrudates on Their Catalytic Behavior in *n*-Hexane Hydroisomerization. *Ind. Eng. Chem. Res.* **2019**, *58*, 10875–10885.

(2) Ning, Q.; Zhang, H.; He, Y.; Chen, Z.; Liu, S.; Ren, J. Suppression of platinum sintering on Pt–M/ZSM-22 (M = Ce, La, and Re) catalyst for *n*-dodecane isomerization. *New J. Chem.* **2019**, *43*, 13967–13978.

(3) Jalil, A. A.; Gambo, Y.; Ibrahim, M.; Abdulrasheed, A. A.; Hassan, N. S.; Nawawi, M. G. M.; Asli, U. A.; Hassim, M. H.; Ahmad, A. Platinum-Promoted Fibrous Silica Y Zeolite with Enhanced Mass Transfer as a Highly Selective Catalyst for *n*-Dodecane Hydroisomerization. *Int. J. Energy Res.* **2019**, *43*, 4201–4216.

(4) Li, H.-X.; Cormier, W. E.; Moden, B. NOVEL METAL-CONTAINING ZEOLITE BETA FOR NOX REDUCTION AND METHODS OF MAKING THE SAME. *US Patent Application* 20190054420 A1, 2019.

(5) Peterson, E. J.; DeLaRiva, A. T.; Lin, S.; Johnson, R. S.; Guo, H.; Miller, J. T.; Kwak, J. H.; Peden, C. H. F.; Kiefer, B.; Allard, L. F.; Ribeiro, F. H.; Datye, A. K. Low-temperature carbon oxidation catalysed by regenerable atomically dispersed palladium on alumina. *Nat. Commun.* **2014**, *5*.

(6) Wang, A.; Wang, Y.; Walter, E. D.; Kukkadapu, R. K.; Guo, Y.; Lu, G.; Weber, R. S.; Wang, Y.; Peden, C. H. F.; Gao, F. Catalytic N_2O decomposition and reduction by NH_3 over Fe/Beta and Fe/SSZ-13 catalysts. *J. Catal.* **2018**, *358*, 199–210.

(7) Avanesian, T.; Dai, S.; Kale, M. J.; Graham, G. W.; Pan, X.; Christopher, P. Quantitative and Atomic-Scale View of CO-Induced Pt Nanoparticle Surface Reconstruction at Saturation Coverage via DFT Calculations Coupled with *in Situ* TEM and IR. *J. Am. Chem. Soc.* **2017**, *139*, 4551–4558.

(8) Bordiga, S.; Lamberti, C.; Bonino, F.; Travert, A.; Thibault-Starzyk, F. Probing zeolites by vibrational spectroscopies. *Chem. Soc. Rev.* **2015**, *44*, 7262–7341.

(9) Serna, P.; Gates, B. C. A Bifunctional Mechanism for Ethene Dimerization: Catalysis by Rhodium Complexes on Zeolite HY in the Absence of Halides. *Angew. Chem. Int. Ed.* **2011**, *50*, 5528–5531.

(10) Lu, J.; Martinez-Macias, C.; Aydin, C.; Browning, N. D.; Gates, B. C. Zeolite-Supported Bimetallic Catalyst: Controlling Selectivity of Rhodium Complexes by Nearby Iridium Complexes. *Catal. Sci. Technol.* **2013**, *3*, 2199–2203.

(11) Guzman, J.; Gates, B. C. Supported molecular catalysts: metal complexes and clusters on oxides

and zeolites. *J. Chem. Soc. Dalt. Trans.* **2003**, *3*, 3303–3318.

(12) Goellner, J. F.; Gates, B. C.; Vayssilov, G. N.; Rösch, N. Structure and Bonding of a Site-Isolated Transition Metal Complex: Rhodium Dicarbonyl in Highly Dealuminated Zeolite Y. *J. Am. Chem. Soc.* **2000**, *122*, 8056–8066.

(13) Lucci, F. R.; Zhang, L.; Thuening, T.; Uhlman, M. B.; Schilling, A. C.; Henkelman, G.; Charles, E. The effect of single Pd atoms on the energetics of recombinative O_2 desorption from Au(111). *Surf. Sci.* **2018**, *677*, 296–300.

(14) Hoffman, A. S.; Debefve, L. M.; Zhang, S.; Perez-Aguilar, J. E.; Conley, E. T.; Justl, K. R.; Arslan, I.; Dixon, D. A.; Gates, B. C. Beating Heterogeneity of Single-site Catalysts: MgO-Supported Iridium Complexes. *ACS Catal.* **2018**, *8*, 3489–3498.

(15) DeRita, L.; Resasco, J.; Dai, S.; Boubnov, A.; Thang, H. V.; Hoffman, A. S.; Ro, I.; Graham, G. W.; Bare, S. R.; Pacchioni, G.; Pan, X.; Christopher, P. Structural Evolution of Atomically Dispersed Pt Catalysts Dictates Reactivity. *Nat. Mater.* **2019**, *18*, 746–751.

(16) Therrien, A. J.; Hensley, A. J. R.; Marcinkowski, M. D.; Zhang, R.; Lucci, F. R.; Coughlin, B.; Schilling, A. C.; McEwen, J. S.; Sykes, E. C. H. An atomic-scale view of single-site Pt catalysis for low-temperature CO oxidation. *Nat. Catal.* **2018**, *1*, 192–198.

(17) Babucci, M.; Sarac Oztuna, F. E.; Debefve, L. M.; Boubnov, A.; Bare, S. R.; Gates, B. C.; Unal, U.; Uzun, A. Atomically Dispersed Reduced Graphene Aerogel-Supported Iridium Catalyst with an Iridium Loading of 14.8 wt %. *ACS Catal.* **2019**, *9*, 9905–9913.

(18) Briend, M.; Peltre, M. J.; Lamy, A.; Man, P. P.; Barthomeuf, D. Dependence of the Acidic Properties of SAPO-37 Molecular Sieve-on Si Content and Heat Treatment. *J. Catal.* **1992**, *138*, 90–100.

(19) Zhong, J.; Han, J.; Wei, Y.; Tian, P.; Guo, X.; Song, C.; Liu, Z. Recent advances of the nano-hierarchical SAPO-34 in the methanol-to-olefin (MTO) reaction and other applications. *Catal. Sci.*

Technol. **2017**, *7*, 4905–4923.

(20) Corma, A.; Fornés, V.; Franco, M. J.; Mocholí, F. A.; Pérez-Pariente, J. Hydrothermal Stability and Cracking behavior of Silicoaluminophosphate Molecular Sieve-37 with Different Silicon Contents. *ACS Symp. Ser.* **1991**, *452*, 79–95.

(21) Su, B. L.; Lamy, A.; Dzwigaj, S.; Briend, M.; Barthomeuf, D. Oxidizing and Reducing Properties of SAPO-37 Molecular Sieve. Comparison with Acidity and Catalysis. *Appl. Catal.* **1991**, *75*, 311–320.

(22) Martens, J. A.; Grobet, P. J.; Jacobs, P. A. Catalytic Activity and Si, Al, P Ordering in Microporous Silicoaluminophosphates of the SAPO-5, SAPO-11, and SAPO-37 Type. *J. Catal.* **1990**, *126*, 299–305.

(23) Miller, S. J. New molecular sieve process for lube dewaxing by wax isomerization. *Micropor. Mater.* **1994**, *2*, 439–449.

(24) Miller, S. J.; Lacheen, H. S.; Chen, C. Y. Determining the Strength of Brønsted Acid Sites for Hydrodewaxing over Shape-Selective Catalysts. *Ind. Eng. Chem. Res.* **2016**, *55*, 6760–6767.

(25) Lok, B. M.; Messina, C. A.; Patton, R. L.; Gajek, R. T.; Cannan, T. R.; Flanigen, E. M. Silicoaluminophosphate Molecular Sieves: Another New Class of Microporous Crystalline Inorganic Solids. *J. Am. Chem. Soc.* **1984**, *106*, 6092–6093.

(26) Sierra de Saldarriaga, L. S.; Saldarriaga, C.; Davis, M. E. Investigations into the Nature of a Silicoaluminophosphate with the Faujasite Structure. *J. Am. Chem. Soc.* **1987**, *109*, 2686–2691.

(27) Claver, C. *Rhodium Catalysis*; Springer: Cham, 2017; Vol. 32.

(28) Liang, A. J.; Bhirud, V. A.; Ehresmann, J. O.; Kletnieks, P. W.; Haw, J. F.; Gates, B. C. A Site-Isolated Rhodium–Diethylene Complex Supported on Highly Dealuminated Y Zeolite: Synthesis and Characterization. *J. Phys. Chem. B* **2005**, *109*, 24236–24243.

(29) Franco, M. J.; Pérez-Pariente, J.; Misud, A.; Blasco, T.; Sanz, J. Crystallization kinetics of SAPO-37. *Zeolites* **1992**, *12*, 386–394.

(30) Hathaway, P. E.; Cox, D. F.; Davis, M. E.; Hasha, D.; Sierra de Saldarriaga, L.; Saldarriaga, C. Studies of Silicoaluminophosphates with the Sodalite Structure. *J. Am. Chem. Soc.* **1988**, *110*, 2127–2135.

(31) Serna, P.; Gates, B. C. Zeolite-Supported Rhodium Complexes and Clusters: Switching Catalytic Selectivity by Controlling Structures of Essentially Molecular Species. *J. Am. Chem. Soc.* **2011**, *133*, 4714–4717.

(32) Hoffman, A. S.; Debefve, L. M.; Bendjeriou-Sedjerari, A.; Ouldchikh, S.; Bare, S. R.; Basset, J. M.; Gates, B. C. Transmission and fluorescence X-ray absorption spectroscopy cell/flow reactor for powder samples under vacuum or in reactive atmospheres. *Rev. Sci. Instrum.* **2016**, *87*.

(33) Buhl, M.; Håkansson, M.; Mahmoudkhani, A. H.; Öhrström, L. X-ray Structures and DFT Calculations on Rhodium-Olefin Complexes: Comments on the ^{103}Rh NMR Shift–Stability Correlation. *Organometallics* **2000**, *19*, 5589–5596.

(34) Villars, P.; Calvert, L. D. *Pearson's Handbook of Crystallographic Data for Intermetallic Phases.*; Wiley: Metals Park, 1987, 1058-3094.

(35) Pereira, C.; Gorte, R. J. Method for distinguishing Brønsted-acid sites in mixtures of H-ZSM-5, H-Y and silica–alumina. *Top. Catal.* **1992**, *90*, 145–157.

(36) Gorte, R. J. What do we know about the acidity of solid acids? *Catal. Lett.* **1999**, *62*, 1–13.

(37) Debefve, L. M.; Hoffman, A. S.; Yeh, A. J.; Runnebaum, R. C.; Shulda, S.; Richards, R. M.; Arslan, I.; Gates, B. C. Iridium Atoms Bonded to Crystalline Powder MgO: Characterization by Imaging and Spectroscopy. *J. Phys. Chem. C* **2020,** *124*, 459–468.

(38) Ojo, A. F.; Dwyer, J.; Dewing, J.; Karim, K. Synthesis and Properties of SAPO-37. *J. Chem. Soc. Faraday Trans.* **1991**, *87*, 2679–2684.

(39) Peltre, M. J.; Briend, M.; Lamy, A.; Barthomeuf, D.; Taulelle, F. Interaction of SAPO-37 Molecular Sieves with Basic Molecules: Enhancement of Stability. *J. Chem. Soc. Faraday Trans.* **1990**, *86*, 3823–3826.

(40) Dang, T. T. H.; Bartoszek, M.; Schneider, M.; Hoang, D. L.; Bentrup, U.; Martin, A. Chloride-free Cu-modified SAPO-37 catalyst for the oxidative carbonylation of methanol in the gas phase. *Appl. Catal. B Environ.* **2012**, *121–122*, 115–122.

(41) Dzwigaj, S.; Briend, M.; Shikholeslami, A.; Peltre, M. J.; Barthomeuf, D. The acidic properties of SAPO-37 compared to faujasites and SAPO-5. *Zeolites* **1990**, *10*, 157–162.

(42) Makarova, M. A.; Ojo, A. F.; Karim, K.; Hunger, M.; Dwyer, J. FTIR Study of Weak Hydrogen Bonding of Brönsted Hydroxyls in Zeolites and Aluminophosphates. *J. Phys. Chem.* **1994**, *98*, 3619–3623.

(43) Corma, A.; Fornes, V.; Pérez-Pariente, J. SAPO-37: The Implications of Structure Flexibility on Acidity. *J. Chem. Soc. Chem. Commun.* **1993**, 676–678.

(44) Lin, L.; Zhang, X.; He, N.; Liu, J.; Xin, Q.; Guo, H. *Operando* Dual Beam FTIR Study of Hydroxyl Groups and Zn Species over Defective HZSM-5 Zeolite Supported Zinc Catalysts. *Catalysts* **2019**, *9*, 100.

(45) Halasz, I.; Moden, B.; Petushkov, A.; Liang, J. J.; Agarwal, M. Delicate Distinction between OH Groups on Proton-Exchanged H-Chabazite and H-SAPO-34 Molecular Sieves. *J. Phys. Chem. C* **2015**, *119*, 24046–24055.

(46) Koningsberger, D. C.; Gates, B. C. Nature of the Metal–Support Interface in Supported Metal Catalysts: Results from X-ray Absorption Spectroscopy. *Catal. Lett.* **1992**, *14*, 271–277.

(47) Bhirud, V. A.; Ehresmann, J. O.; Kletnieks, P. W.; Haw, J. F.; Gates, B. C. Rhodium Complex with Ethylene Ligands Supported on Highly Dehydroxylated MgO: Synthesis, Characterization, and Reactivity. *Langmuir* **2006**, *22*, 490–496.

(48) Miessner, H.; Burkhardt, I.; Gutschick, D.; Zecchina, A.; Morterra, C.; Spoto, G. The Formation of Well Defined Rhodium Dicarbonyl and Dinitrosyl with Rhodium Supported on Highly Dealuminated Zeolite Y by Interaction with CO. *Stud. Surf. Sci. Catal.* **1989**, *48*, 677–684.

(49) Burkhardt, I.; Gutschick, D.; Lohse, U.; Miessner, H. I.R. Spectroscopic Evidence of a Well Defined Rhodium Dicarbonyl in Highly Dealuminated Zeolite Y, Formed by Interaction of Carbon Monoxide with Exchanged Rhodium. *J. Chem. Soc. Chem. Commun.* **1987**, 291–292.

(50) Miessner, H.; Gutschick, D.; Ewald, H.; Müller, H. The Influence of Support on the Geminal Dicarbonyl Species $Rh^{I}(CO)_2$ on Supported Rhodium Catalysts: An IR Spectroscopic Study. *J. Mol. Catal.* **1986**, *36*, 359–373.

(51) Hadjiivanov, K. I.; Vayssilov, G. N. Characterization of Oxide Surfaces and Zeolites by Carbon Monoxide as an IR Probe Molecule. *Adv. Catal.* **2002**, *47*, 307–511.

(52) Chuang, E. J.; Srinivas, G.; Mukherjee, A. Infrared Studies of the Interactions of C_2H_4 and H_2 with $Rh^{+}(CO)_2$ and CO Adsorbed on $RhCl_3/SiO_2$ and $Rh(NO_3)_3/SiO_2$. *J. Catal.* **1993**, *193*, 490–503.

(53) Balakos, M. W.; Chuang, S. S. C. Transient Response of Propionaldehyde Formation during $CO/H_2/C_2H_4$ Reaction on Rh/SiO_2. *J. Catal.* **1995**, *151*, 253–265.

(54) Cannon, K. C.; Jo, S. K.; White, J. M. Reaction of Nitric Oxide and Silica-Attached Rhodium Carbonyl Complexes. *J. Am. Chem. Soc.* **1989**, *111*, 5064–5069.

(55) Yang, D.; Odoh, S. O.; Borycz, J.; Wang, T. C.; Farha, O. K.; Hupp, J. T.; Cramer, C. J.; Gagliardi, L.; Gates, B. C. Tuning Zr_6 Metal−Organic Framework (MOF) Nodes as Catalyst Supports: Site Densities and Electron-Donor Properties Influence Molecular Iridium Complexes as Ethylene Conversion Catalysts. *ACS Catal.* **2016**, *6*, 235–247.

(56) Liang, A. J.; Craciun, R.; Chen, M.; Kelly, T. G.; Kletnieks, P. W.; Haw, J. F.; Dixon, D. A.; Gates, B. C. Zeolite-Supported Organorhodium Fragments: Essentially Molecular Surface Chemistry Elucidated with Spectroscopy and Theory. *J. Am. Chem. Soc.* **2009**, *131*, 8460–8473.

(57) Liang, A. J.; Bhirud, V. A.; Ehresmann, J. O.; Kletnieks, P. W.; Haw, J. F.; Gates, B. C. A Site-Isolated Rhodium-Diethylene Complex Supported on Highly Dealuminated Y Zeolite: Synthesis and Characterization. *J. Phys. Chem. B* **2005**, *109*, 24236–24243.

(58) Bernales, V.; Yang, D.; Yu, J.; Gümüşlu, G.; Cramer, C. J.; Gates, B. C.; Gagliardi, L. Molecular Rhodium Complexes Supported on the Metal-Oxide-like Nodes of Metal Organic Frameworks and on Zeolite HY: Catalysts for Ethylene Hydrogenation and Dimerization. *ACS Appl. Mater. Interf.* **2017**, *9*, 33511–33520.

(59) Martinez-Macias, C.; Serna, P.; Gates, B. C. Isostructural Zeolite-Supported Rhodium and Iridium Complexes: Tuning Catalytic Activity and Selectivity by Ligand Modification. *ACS Catal.* **2015**, *5*, 5647–5656.

(60) Kondo, J. N.; Domen, K. IR Observation of adsorption and reactions of olefins on H-Form zeolites. *J. Mol. Catal. A Chem.* **2003**, *199*, 27–38.

(61) Lu, J.; Serna, P.; Aydin, C.; Browning, N. D.; Gates, B. C. Supported Molecular Iridium Catalysts: Resolving Effects of Metal Nuclearity and Supports as Ligands. *J. Am. Chem. Soc.* **2011**, *133*, 16186–16195.

(62) Fyfe, C. A.; Wong-Moon, K. C.; Huang, Y.; Grondey, H. Structural investigations of SAPO-37 molecular sieve by coherence-transfer and dipolar-dephasing solid-state nuclear magnetic resonance experiments. *Micropor. Mater.* **1995**, *5*, 29–37.

(63) Derewinski, M.; Peltre, M. J.; Briend, M.; Barthomeuf, D.; Man, P. P. Solid-state Transformation of SAPO-37 Molecular Sieve above 1100 K. *J. Chem. Soc. Faraday Trans.* **1993**, *89*, 1823–1828.

(64) Xu, P.; Lu, J.; Aydin, C.; Debefve, L. M.; Browning, N. D.; Chen, C. Y.; Gates, B. C. Imaging individual lanthanum atoms in zeolite Y by scanning transmission electron microscopy: evidence of lanthanum pair sites. *Micropor. Mesopor. Mater.* **2015**, *213*, 95–99.

(65) Rojo-Gama, D.; Mentel, L.; Kalantzopoulos, G. N.; Pappas, D. K.; Dovgaliuk, I.; Olsbye, U.; Lillerud, K. P.; Beato, P.; Lundegaard, L. F.; Wragg, D. S.; Svelle, S. Deactivation of Zeolite Catalyst H-ZSM-5 during Conversion of Methanol to Gasoline: Operando Time- and Space-Resolved X-ray Diffraction. *J. Phys. Chem. Lett.* **2018**, *9*, 1324–1328.

(66) Ogino, I.; Gates, B. C. Essentially Molecular Metal Complexes Anchored to Zeolite *β*: Synthesis and Characterization of Rhodium Complexes and Ruthenium Complexes Prepared from Rh(acac)(η^2-C_2H_4)$_2$ and *cis*-Ru(acac)$_2$(η^2-C_2H_4)$_2$. *J. Phys. Chem. C* **2010**, *114*, 2685–2693.

(67) Vummaleti, S. V. C.; Kuriakose, N.; Dinda, S.; Wu, Y.; Genest, A.; Rösch, N. C-C Coupling at a zeolite-supported Rh(I) complex. DFT search for the mechanism. *Catal. Sci. Technol.* **2019**, *9*, 2781–2793.

(68) Potter, M. E.; O'Malley, A. J.; Chapman, S.; Kezina, J.; Newland, S. H.; Silverwood, I. P.; Mukhopadhyay, S.; Carravetta, M.; Mezza, T. M.; Parker, S. F.; Catlow, C. R. A.; Raja, R. Understanding the Role of Molecular Diffusion and Catalytic Selectivity in Liquid-Phase Beckmann Rearrangement. *ACS Catal.* **2017**, *7*, 2926–2934.

(69) Ngamcharussrivichai, C.; Wu, P.; Tatsumi, T. Active and selective catalyst for liquid phase Beckmann rearrangement of cyclohexanone oxime. *J. Catal.* **2005**, *235*, 139–149.

(70) Wu, L.; Hensen, E. J. M. Comparison of mesoporous SSZ-13 and SAPO-34 zeolite catalysts for the methanol-to-olefins reaction. *Catal. Today* **2014**, *235*, 160–168.

Chapter 2A

SUPPORTING INFORMATION

for

Isolated Atomically Dispersed Rhodium Catalysts Supported on SAPO-37 and on HY Zeolite[1]

[1] This chapter has been previously published in the Journal of the American Chemical Society 2020, *142*, 11474–11485 by J. E. Perez-Aguilar, C.-Y. Chen, J. T. Hughes, C.-Y. Fang, and B. C. Gates. The original manuscript has been reformatted to fit the requirements of the dissertation

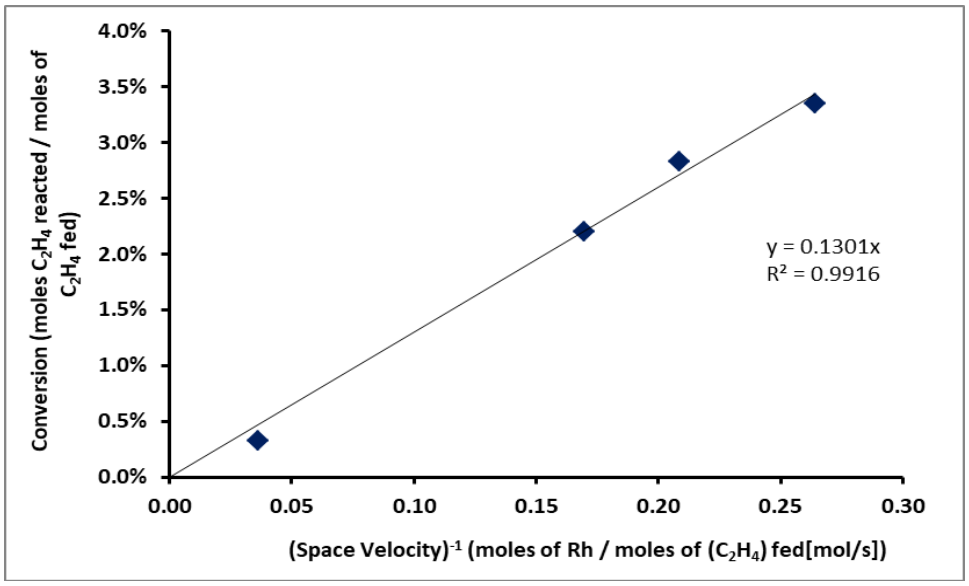

Figure 2A.1. Differential conversion of ethylene; the catalyst was initially present as $Rh(C_2H_4)_2$ supported on SAPO-37. Reaction conditions: H_2 + C_2H_4 at 1:1 molar ratio at 303 K at atmospheric pressure. The linearity of this plot that passes through the origin demonstrates that the data determine rates (TOF values) directly as the slope of the line.

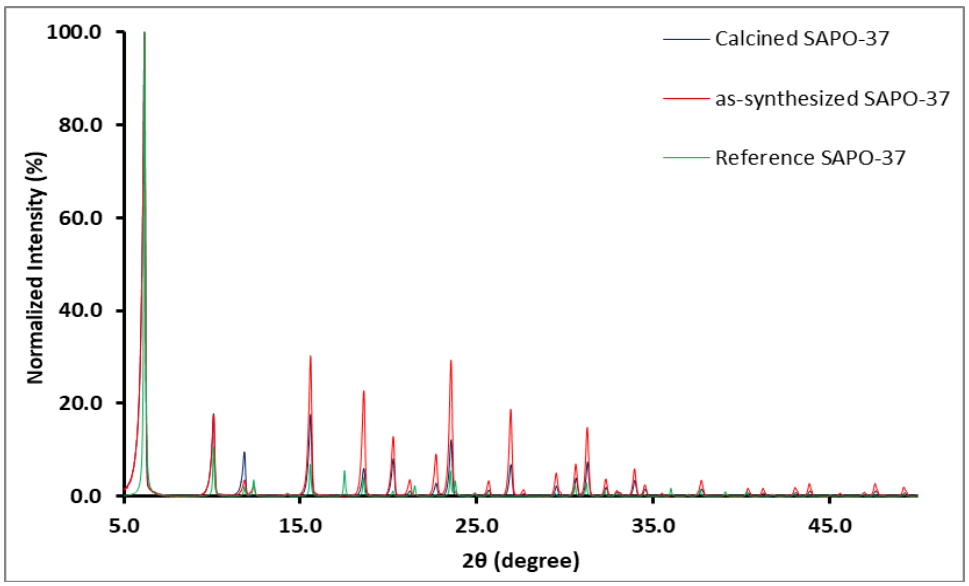

Figure 2A.2. Powder XRD pattern of freshly calcined SAPO-37 sample compared against as-synthesized SAPO-37 sample, and reference SAPO-37.[1] The peak intensity of the 100 reflection on both the samples and the reference pattern have been normalized.

The comparison of three XRD patterns clearly shows the presence of pure SAPO-37 (Figure 2A.1).

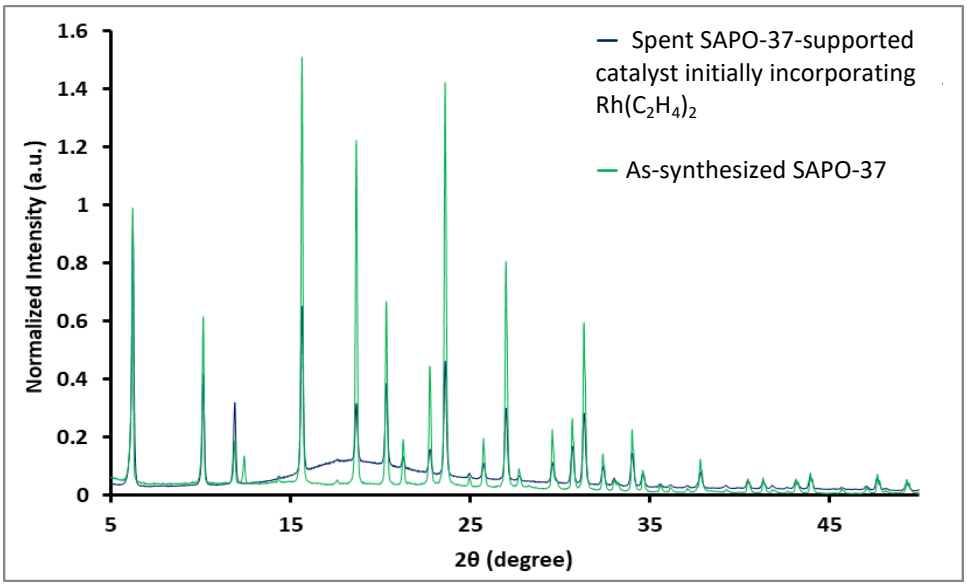

Figure 2A.3. XRD pattern of a SAPO-37-supported $Rh(C_2H_4)_2$ catalyst after 168 h of operation (details in main text); this spent catalyst was handled in the absence of air and moisture in a domed XRD sample holder as described in Chapter 2. Data characterizing the as-synthesized SAPO-37 material are shown for comparison. The baseline change characterizing the spent catalyst is attributed to the plastic window of the sample holder dome.

Table 2A.1. Catalyst Characterization Data: SAPO-37.

Sample	Molar Ratio[a]			A_{BET}[b] (m^2 g^{-1})	t-plot micropore volume[b] (cm^3 g^{-1})
	Al	P	Si		
SAPO-37	1.00	0.64	0.30	920	0.27

[a]Molar ratio determined by AA/ICP analysis. [b]Calculated from N_2 physisorption using BET equation.

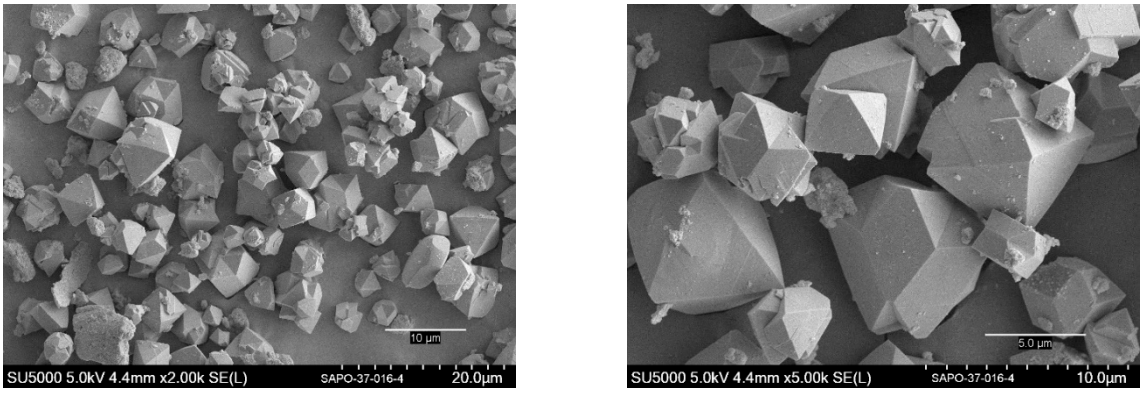

Figure 2A.4. SEM images of the as-synthesized SAPO-37 material.

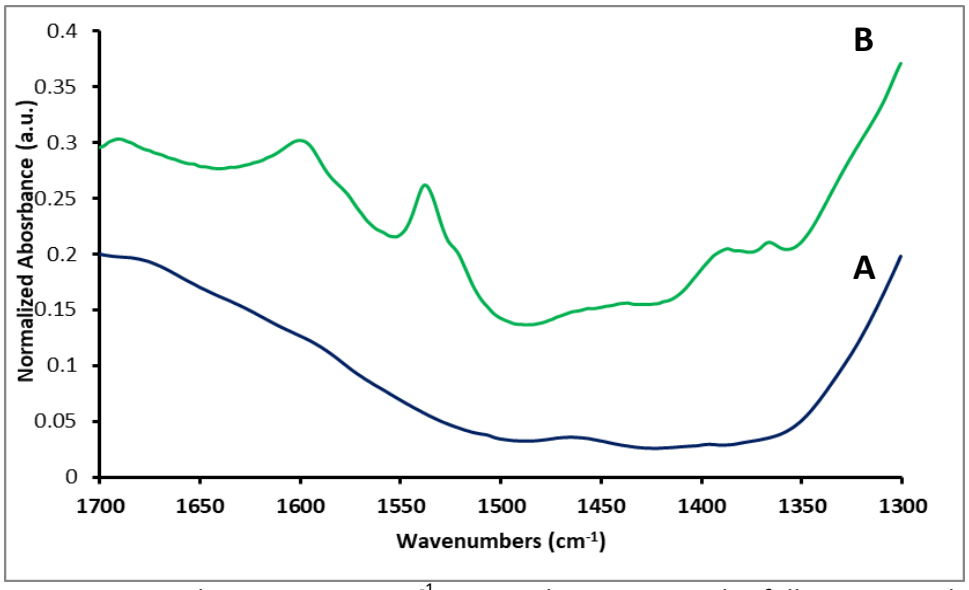

Figure 2A.5. IR spectra in the 1300–1700 cm^{-1} region characterizing the following samples: (**A**) bare, calcined SAPO-37; (**B**) sample formed by reaction of SAPO-37 with $Rh(C_2H_4)_2(acac)$ in *n*-pentane after removal of the solvent.

Figure 2A.5 shows the appearance of peaks after $Rh(C_2H_4)_2(acac)$ had been adsorbed on SAPO-37. Spectrum A is bare SAPO-37, and spectrum B represents the sample after reaction with the rhodium precursor. The bands appearing at 1370, 1539, and 1581 cm^{-1} are in good agreement with those attributed to Hacac adsorbed on isostructural dealuminated HY zeolite (DAY zeolite, molar SiO_2/Al_2O_3 ratio = 30) and are assigned to $\delta_{as}(CH)$, $\nu_{as}(CCC)_{ring}$, $\nu_s(CO)_{ring}$.[2] Moreover, no band at 1521 cm^{-1} assigned to acetylacetonate bonded to rhodium species was observed, demonstrating that the acac group was no longer bonded to the rhodium.[2] Further, no band at 2091 cm^{-1} (which would have been evidence of a Rh–H species) was observed.[3] The observed bands confirm the inference that acac ligands dissociated from $Rh(C_2H_4)_2(acac)$ as a result of the chemisorption on support SI–OH–Al groups.

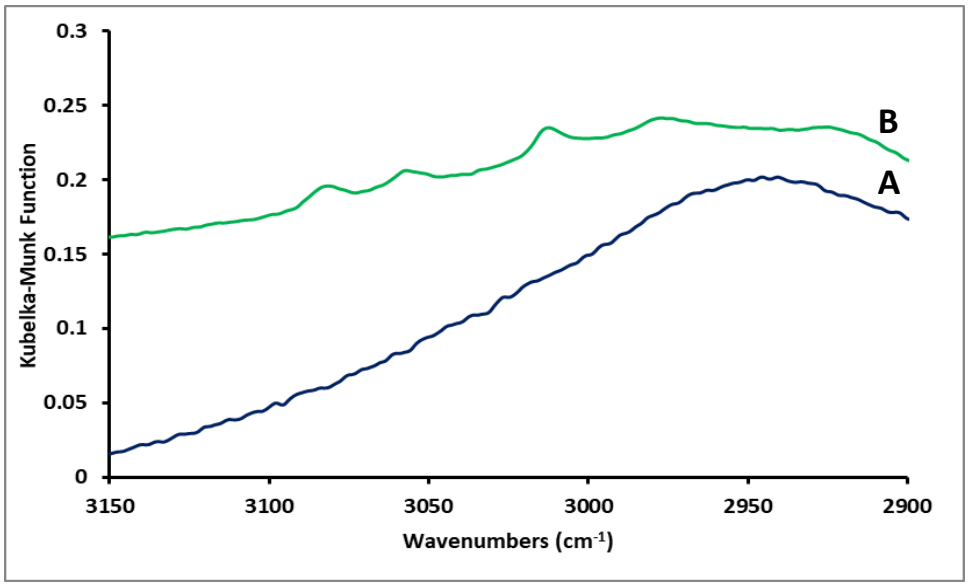

Figure 2A.6. DRIFTS spectra in ν_{C-H} region characterizing the following samples: (**A**) bare, calcined SAPO-37; (**B**) sample formed by reaction of SAPO-37 with $Rh(C_2H_4)_2(acac)$ in *n*-pentane after removal of solvent.

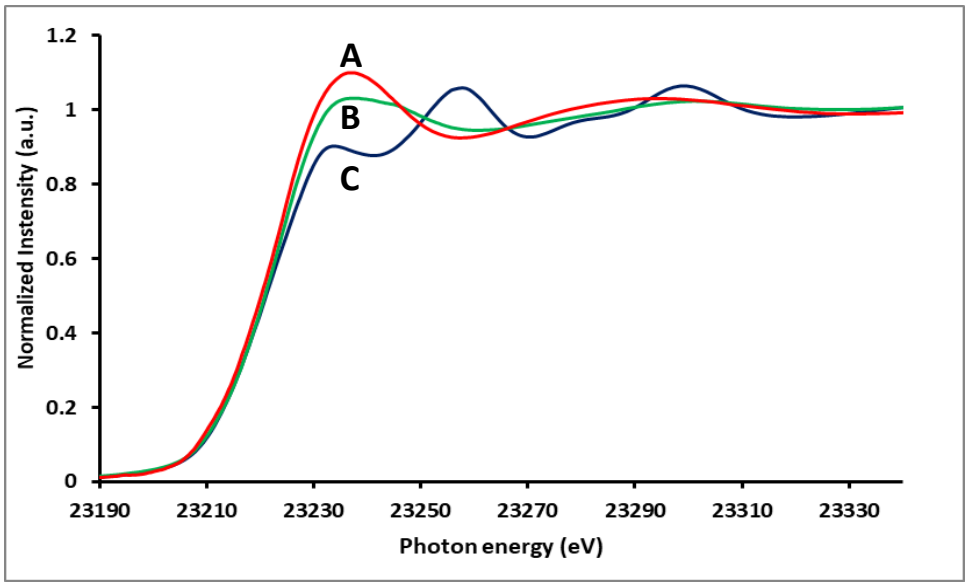

Figure 2A.7. Normalized XANES spectra near the Rh K edge (23220 eV) characterizing $Rh(C_2H_4)_2$ complexes on (**A**) DAY zeolite and on (**B**) SAPO-37 and (**C**) rhodium foil.

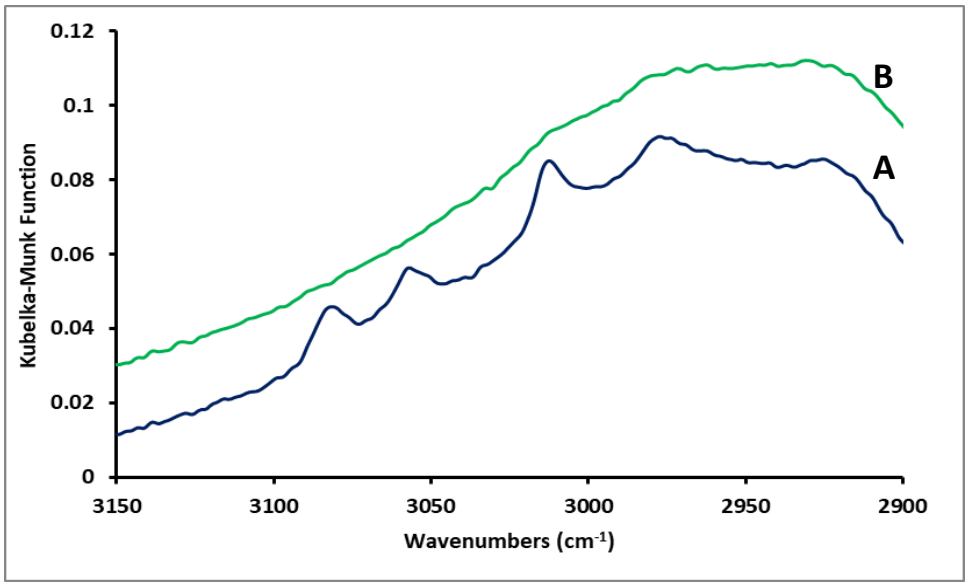

Figure 2A.8. DRIFTS spectra in the C–H region of species formed by adsorption of $Rh(C_2H_4)_2(acac)$ on SAPO-37. Spectrum **A** represents sample in flowing helium, characterized by bands at 3084, 3060, and 3016 cm^{-1} that are assigned to of π-bonded ethylene ligands on rhodium.[4] The peak at 2925 cm^{-1} is assigned to a C-H vibration from a weakly adsorbed species, traces of *n*-pentane solvent remaining from the synthesis, or remnants of acac ligands on the support that formed from the precursor $Rh(C_2H_4)_2(acac)$ in the synthesis.[2] Spectrum **B** shows that these bands disappeared as the ethylene ligands were replaced with carbonyl ligands after exposure of the sample to a pulse of CO.

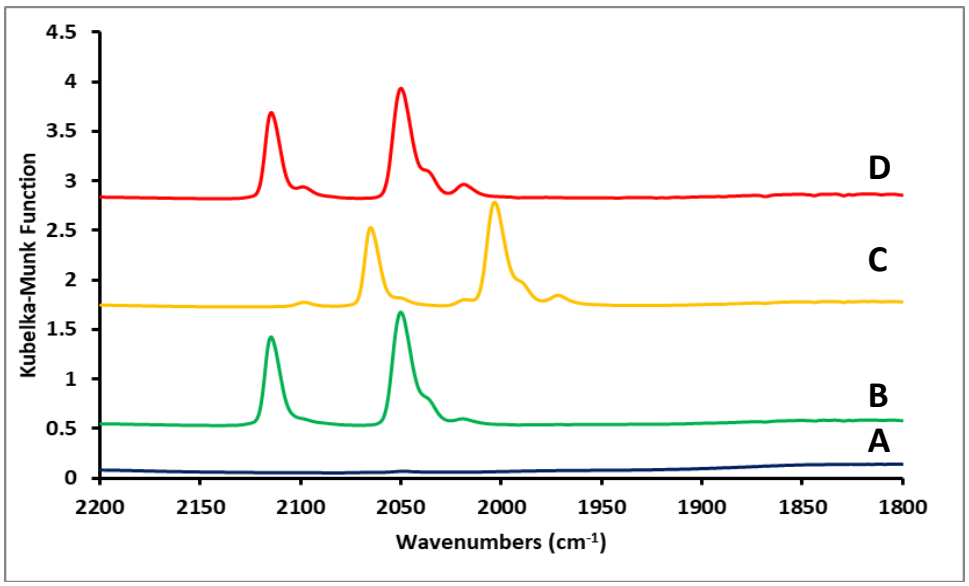

Figure 2A.9. DRIFTS spectra in the CO region of species formed by adsorption of $Rh(C_2H_4)_2(acac)$ on SAPO-37 after treatments. Spectrum **A** was recorded with the SAPO-37 supported $Rh(C_2H_4)_2$ in contact with flowing helium (50 mL(NTP)/min), and spectrum **B** was recorded after the sample had been in contact with 10% CO in helium for 15 min, followed by a purge of the IR cell with helium for 30 min. Spectrum **C** is of the same sample in helium after it had been in contact with a 2-min pulse of ^{13}CO, and spectrum **D** is that taken after the sample had been in contact with 10% CO in helium for 15 min, followed by a purge of the IR cell with helium for 30 min.

After the sample came into contact with CO, bands corresponding to the symmetric and asymmetric vibrations grew. Bands at 2115 and 2052 cm^{-1} are assigned to well-defined rhodium dicarbonyl species near the Si–OH–Al sites within the SAPO-37 pores. Bands at 2103 and 2021 cm^{-1} correspond to ^{13}CO in natural abundance. The shoulder at 2052 cm^{-1} is assigned to rhodium dicarbonyls on the outer surfaces of SAPO-37 crystallites.[6,7] Confirmation of the attribution of these bands to CO is provided by the observed shifts when ^{13}CO replaced ^{12}CO; see spectrum C, for which bands at 2115, 2103, 2052, 2021, and 2000 cm^{-1} are shifted to 2066, 2056, 2004, 1994, and 1976 cm^{-1}.[7]

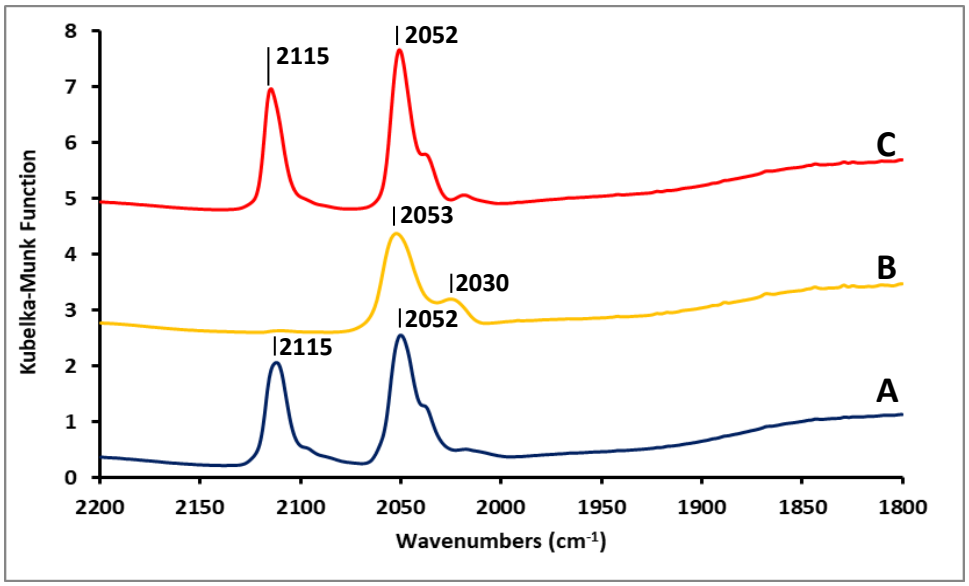

Figure 2A.10. DRIFTS spectra in υ_{CO} region characterizing SAPO-37-supported $Rh(CO)_2$: spectrum **A** of Figure 2A.4B recorded with the sample in helium flowing at 50 mL(NTP)/min; spectrum **B** recorded after the same sample was treated with flowing ethylene at 50 mL(NTP)/min at 298 K; spectrum **C** recorded after the same sample was treated with a pulse of CO at a pressure of 13 mbar at 298 K.

Table 2A.2. Vibrational Frequencies of Iridium and Rhodium *gem*-Dicarbonyls Supported on SAPO-37, Zeolites, MOFs, and Metal Oxides.

Initial form of catalyst	Molar SiO_2/Al_2O_3 ratio in catalyst support	IR spectra of carbonylated form of sample, ν_{CO} (cm^{-1})		fwhm of ν_{CO} (cm^{-1})		reference
		symmetric	asymmetric	symmetric	asymmetric	
Not applicable; sample is $(Rh(CO)_2(acac)$ in *n*-hexane)	–[a]	2084	2015	2.8	2.9	[8]
$Rh(C_2H_4)_2$/HY zeolite	5.2	2117	2053	7.1	9.3	[9]
$Rh(CO)_2$/DAY zeolite	30	2118	2053	<8	<8	[9]
$Rh(C_2H_4)_2$/ SAPO-37	-[b]	2115	2052	7	10	this work
$Rh(C_2H_4)_2$/H-Beta zeolite	38	2115	2048	9	9	[8]
$Rh(C_2H_4)_2$/H-SSZ-42 zeolite	30	2111; 2092	2045; 2020	Broad	Broad	[8]
$Rh(C_2H_4)_2$/H-mordenite zeolite	38	2111; 2092	2045; 2035	Broad	Broad	[8]
$Rh(C_2H_4)_2$/ZSM-5 zeolite	30	2116	2049	–[c]	–[c]	[10]
$Rh(C_2H_4)_2$/HY zeolite	190	2118	2052	≤5	≤5	[8]
$Rh(C_2H_4)_2/TiO_2$	–[a]	2102-2085	2038-2015	–[c]	–[c]	[11]
$Rh(C_2H_4)_2$/MgO	–[a]	2075	2000	Broad	Broad	[11]
$Rh(CO)_2/Al_2O_3$	–[a]	2090	2014	20	27.2	[9]
Not applicable; sample is $(Ir(CO)_2(acac)$ in hexanes)	–[a]	2074	2000	3.9	4	[8]
$Ir(C_2H_4)_2$/H-Beta zeolite	38	2105	2033	10.1	14.9	[8]
$Ir(C_2H_4)_2$/H-Beta zeolite	300	2105	2033	5.4	7.4	[8]
$Ir(C_2H_4)_2$/DAY zeolite	30	2109	2038	5	5	[8]
$Ir(C_2H_4)_2$/H-SSZ-42 zeolite	15	2102; 2086	2029; 2013	Broad	Broad	[8]
$Ir(C_2H_4)_2$/H-SSZ-53 zeolite	–[c]	2099	2027	10	10	[8]
$Ir(C_2H_4)_2$/NaY zeolite	5.2	2082	1995	Broad	Broad	[8]

$Ir(CO)_2$/NU-1000	–[a]	2066	1900	Broad	Broad	[8]
$Ir(CO)_2$/UiO-66	–[a]	2074	1996	Broad	Broad	[8]
$Ir(CO)_2/\gamma$-Al_2O_3	–[a]	2075	1996	30	30	[8]
$Ir(CO)_2$/MgO	–[a]	2066	1985	16.4	15.5	[8]
$Ir(CO)_2/SiO_2$	–[a]	2081	2008	–[c]	–[c]	[12]
$Ir(CO)_2/TIO_2$	–[a]	2076	1988	–[c]	–[c]	[12]
$Ir(CO)_2/Fe_2O_3$	–[a]	2073	1981	–[c]	–[c]	[12]
$Ir(CO)_2/CeO_2$	–[a]	2071	1982	–[c]	–[c]	[12]
$Ir(CO)_2/LaO_3$	–[a]	2066	1977	–[c]	–[c]	[12]

[a]Not applicable

[b]The molar SiO_2/Al_2O_3 ratio in zeolites is used as a proxy for acid site density where the acidity stems from the amount of Al_2O_3 present in the neutral SiO_2. Because SAPOs and zeolites are two different classes of molecular sieves, with SAPOs incorporating Si, Al, and P but zeolites SI and Al, the molar composition of SAPO-37 is reported here as 1.67 Al_2O_3:1.06 P_2O_5:1.00 SiO_2. We recognize that the densities of metal bonding sites (SI–OH–Al) in SAPO-37 and in zeolite are different from each other, and thus they are reported in terms of acidity measurements determined by TPD of isopropylamine (900 µmol/g) for SAPO-37 (Figure 2A.16 in the SI) and elsewhere for DAY zeolite.[13]

[c]Not reported.

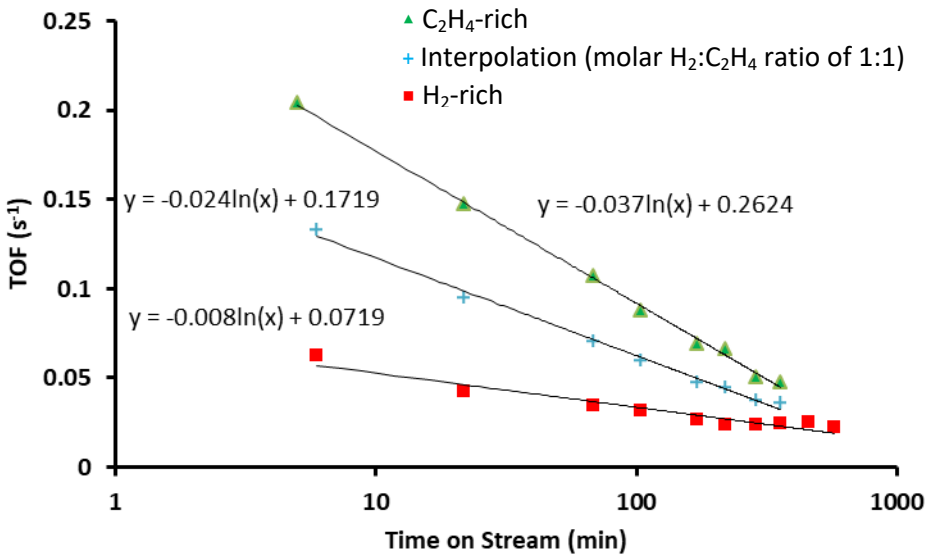

Figure 2A.11. Catalytic performance of rhodium complexes on zeolite HY (molar SiO_2/Al_2O_3 ratio = 30) for ethylene hydrogenation at 303 K and 1 bar. The meanings of the symbols are given in shorthand form in the figure; details follow: ■ 1 wt% rhodium complexes on zeolite HY under C_2H_4-rich reaction conditions (molar $H_2:C_2H_4$ ratio of 1:4) ; ▲ 1 wt% rhodium complexes on zeolite HY under H_2-rich reaction conditions (molar $H_2:C_2H_4$ ratio of 4:1); + Interpolation of C_2H_4-rich and H_2-rich reaction conditions in order to give a $H_2:C_2H_4$ ratio of 1:1.[4]

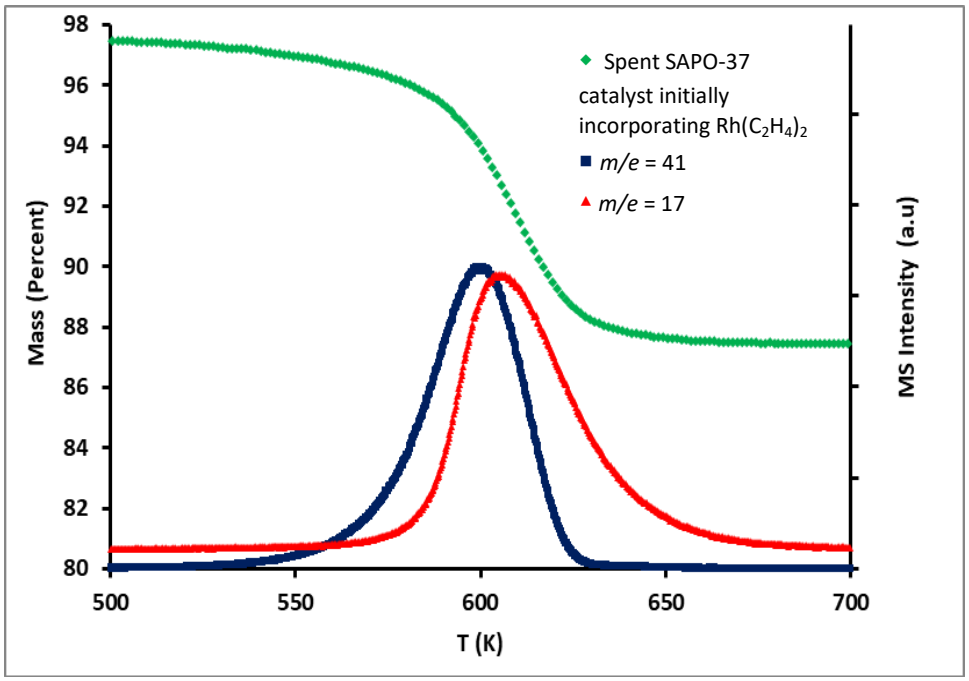

Figure 2A.12. Temperature programmed desorption (TPD) of isopropylamine on calcined SAPO-37 sample. The features correspond to ammonia (*m/e* = 17), and propene (*m/e* = 41).

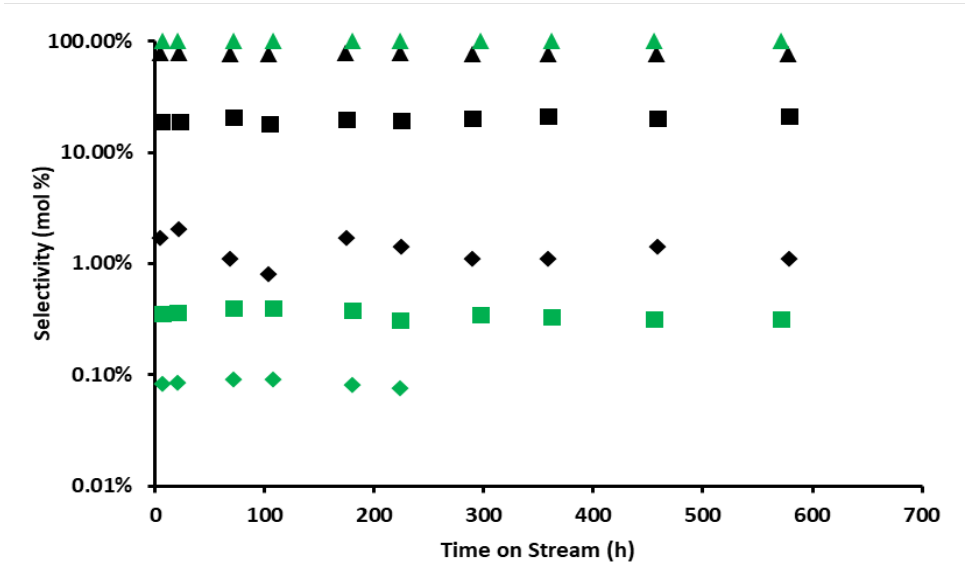

Figure 2A.13. Comparison of SAPO-37 and DAY zeolite as supports for rhodium complex catalysts for ethylene conversion. Selectivity of SAPO-37- supported catalyst (green) (molar H_2:C_2H_4 ratio = 1:1), and zeolite DAY- supported catalyst (black) (molar H_2:C_2H_4 ratio = 4:1).[4] The product selectivity is identified by symbols: ▲ ethane; ■ butane; ◆ *n*-butenes.

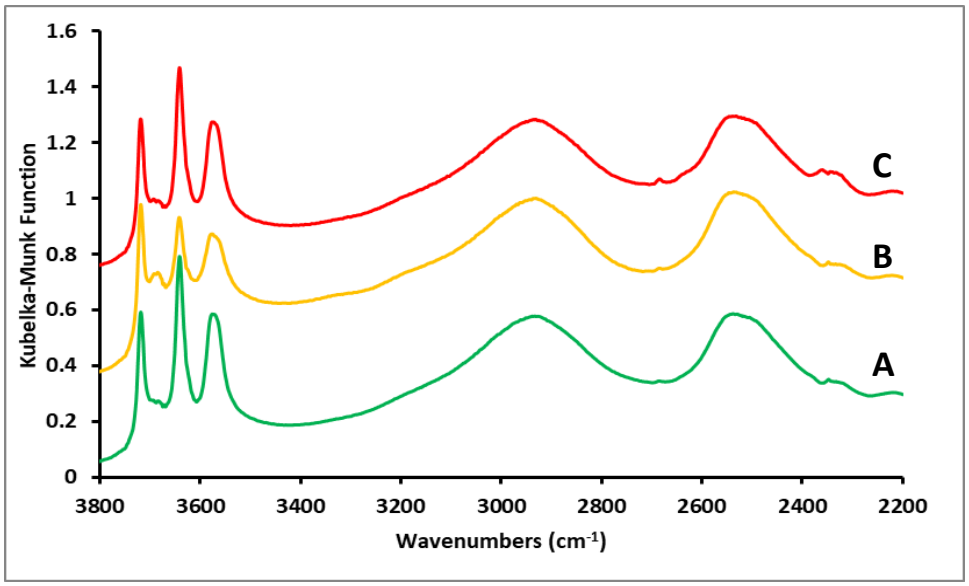

Figure 2A.14. DRIFTS spectra characterizing $Rh(C_2H_4)$ supported on SAPO-37 treated at 298 K and 1 bar in the following sequence: (**A**) $Rh(C_2H_4)_2$ on SAPO-37 in helium (flowing at 90 mL(NTP)/min); (**B**) D_2 (flowing at 30 mL(NTP)/min); (**C**) helium (flowing at 90 mL(NTP)/min).

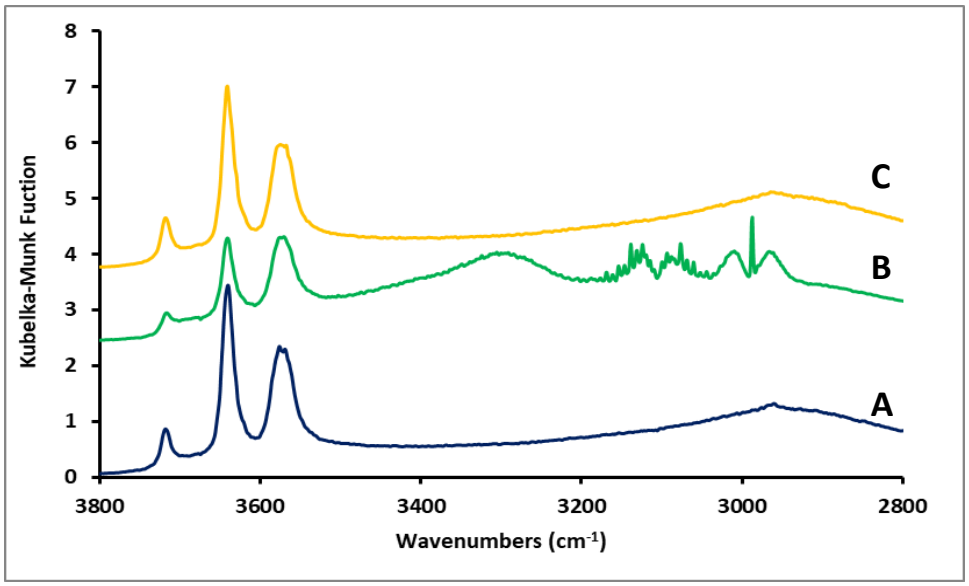

Figure 2A.15. DRIFTS spectra characterizing the following samples: Spectrum **A** represents $Rh(C_2H_4)_2$ on SAPO-37 in flowing helium (50 mL(NTP)/min); spectrum **B** the same sample in flowing C_2H_4 (50 mL(NTP)/min); spectrum **C** the same sample in flowing helium (50 mL(NTP)/min). The broad peak in spectrum **C** (at 3300 cm^{-1}) is assigned to either the extra-framework silica (3718 cm^{-1}) or the Si–OH–Al Brønsted acid sites (3640 cm^{-1}) interacting with absorbed ethylene, consistent with data characterizing the silanols or Brønsted acid sites on HZSM-5 zeolite shifting to 3300 cm^{-1} when ethylene is absorbed.[4]

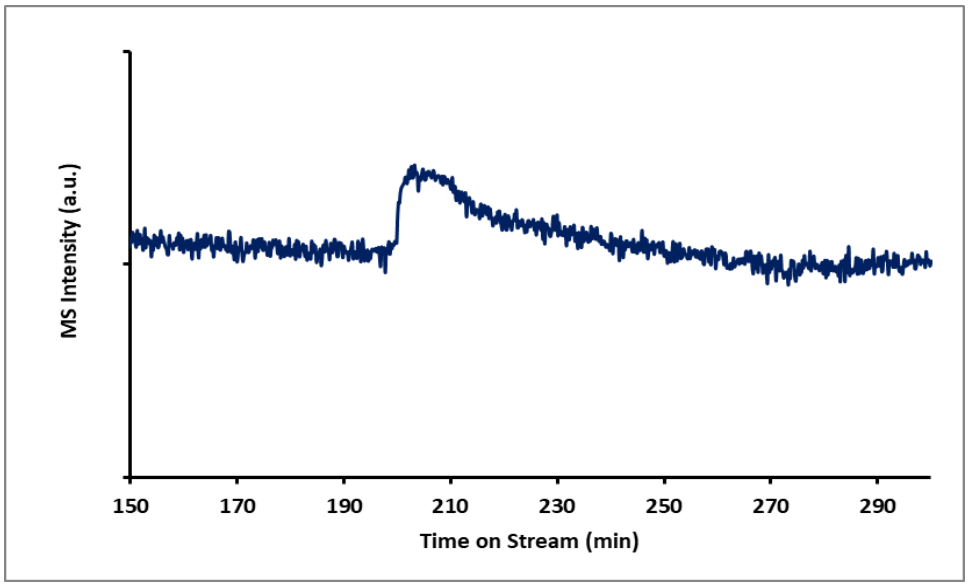

Figure 2A.16. Mass spectra of deuterated ethane (*m*/*e* = 30) in the effluent gas formed from SAPO-37-supported rhodium diethylene complex in contact with flowing D_2 (5 mL(NTP)/min) and C_2H_4 (5 mL(NTP)/ min) and helium (90 mL(NTP)/min); the sample mass was approximately 30 mg.

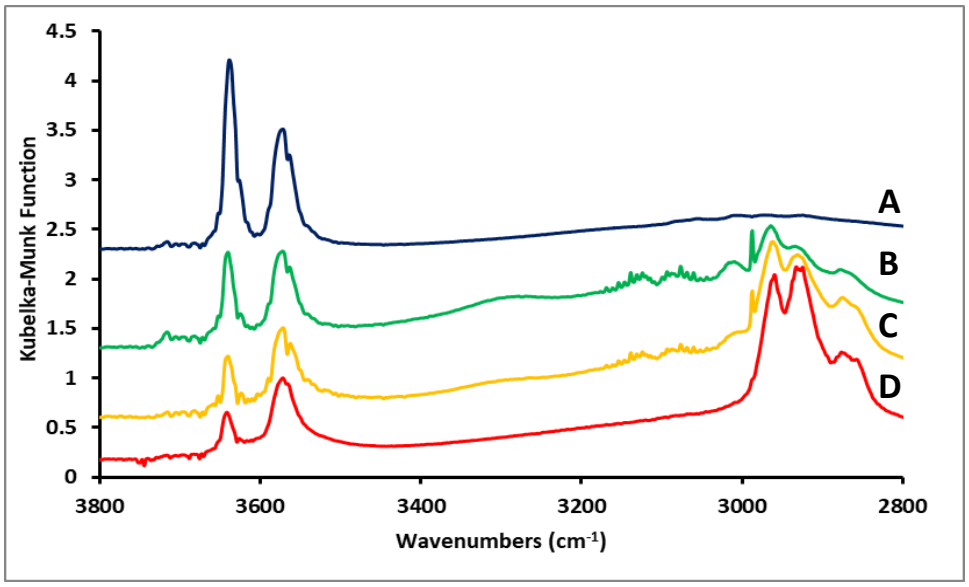

Figure 2A.17. DRIFTS spectra characterizing catalyst: **A**, SAPO-37 supported $Rh(C_2H_4)_2$ in flowing helium (50 mL(NTP)/min) at room temperature after a 5 K/min ramp to 393 K followed by a hold for 10 min; **B**, same sample under reaction conditions (flow rates of 5 mL(NTP)/min of C_2H_4 and of H_2, and 90 mL(NTP)/min of helium) after 9.3 h in contact with flowing reactants; **C**, after 73 h; **D**, after 143 h, after the sample had been purged with flowing helium (90 mL (NTP)/min) at 303 K. We infer that the peak at 3640 cm^{-1} (assigned to the Si–OH–Al Brønsted acid sites of SAPO-37) decreased in intensity as the carbonaceous deposits in the pores interacted with the Si–OH–Al Brønsted acid sites near the rhodium complexes; the result is similar to what has been reported for carbonaceous deposits on USHY zeolite[15] and H-mordenite.[16]

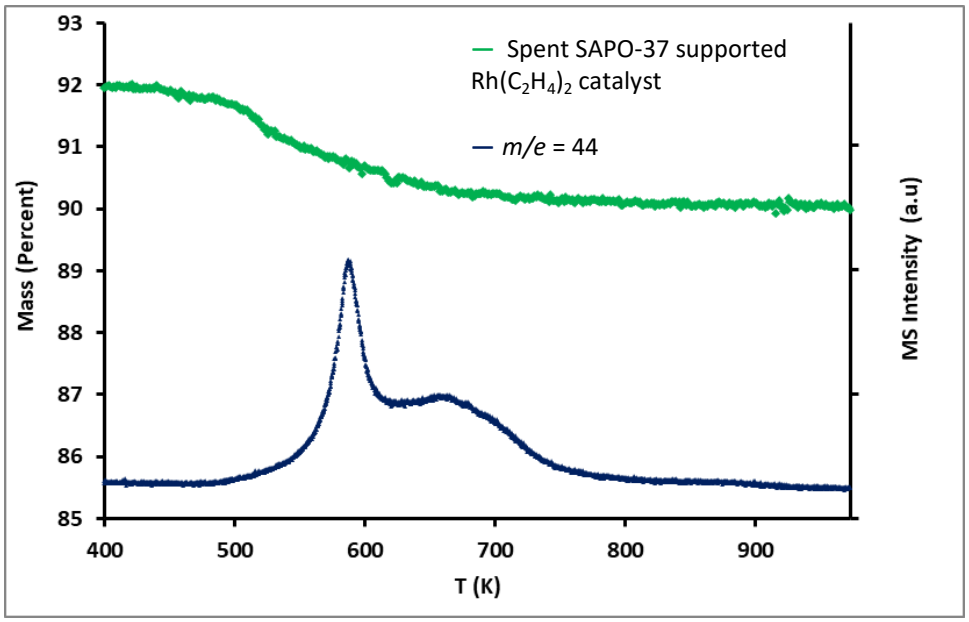

Figure 2A.18. Temperature-programmed oxidation (TPO) of SAPO-37-supported catalyst sample after 143 h on stream.

EXAFS data characterizing single-site rhodium containing 1.0 wt% rhodium and made from $Rh(C_2H_4)_2$(acac) on calcined SAPO-37.

An example illustrating the EXAFS fitting is as follows: Selection of the preferred model was based on satisfactory goodness of fit values less than 5 after the EXAFS analysis. Models that fit over the overall range in *k* (3.90 to 10.50 Å) at k^1- and k^3-weighting but failed in the fitting of individual contributions (amplitude and phase) and/or providing unrealistic values of the fit parameters were rejected. In all cases, the individual contributions were fitted using reference files that represent the bonding environment, and the best combination was chosen as summarized in the section entitled X-ray absorption spectroscopy.

Table 2A.3. Candidate EXAFS models representing the data at the Rh K edge characterizing SAPO-37-supported rhodium complexes formed by adsorption of $Rh(C_2H_4)_2$(acac) on SAPO-37 treated at 873 K to give a rhodium loading of 1.0 wt%. The range in *k* was from 3.90 to 10.50 Å; error = 0.00054; *Denotes best fit model.[a]

Model	Shell	N^a	$10^3 \times \Delta\sigma^2$ (Å^2)[a]	R (Å)[a]	ΔE_0 (eV)[a]	Goodness of Fit
1	Rh–C	4.0	7.5	2.12	-7.5	3.3181
	$Rh–O_{sup}$	2.1	6.3	2.10	4.0	
	Rh–Al	1.1	6.4	3.10	-3.0	
	$Rh–O_L$	-	-	-	-	
2	Rh–C	4.0	7.5	2.12	-7.5	3.2242
	$Rh–O_{sup}$	2.1	6.3	2.10	4.0	
	Rh–Si	1.0	6.3	3.10	-7.0	
	$Rh–O_L$	-	-	-	-	
3	Rh–C	4.0	7.5	2.12	-7.5	3.1576
	$Rh–O_{Sup}$	2.1	6.3	2.10	4.0	
	Rh–P	0.8	5.3	3.1	-9.5	
	$Rh–O_L$	-	-	-	-	

[a]Notation: *N*, coordination number; *R*, distance between absorber and backscatter atoms; $\Delta\sigma^2$, Debye-Waller/disorder term; ΔE_0, inner potential correction. Subscripts: Sup refers to an atom identified to be belonging to the support; L, refers to the longer contribution involving an atom in the support.

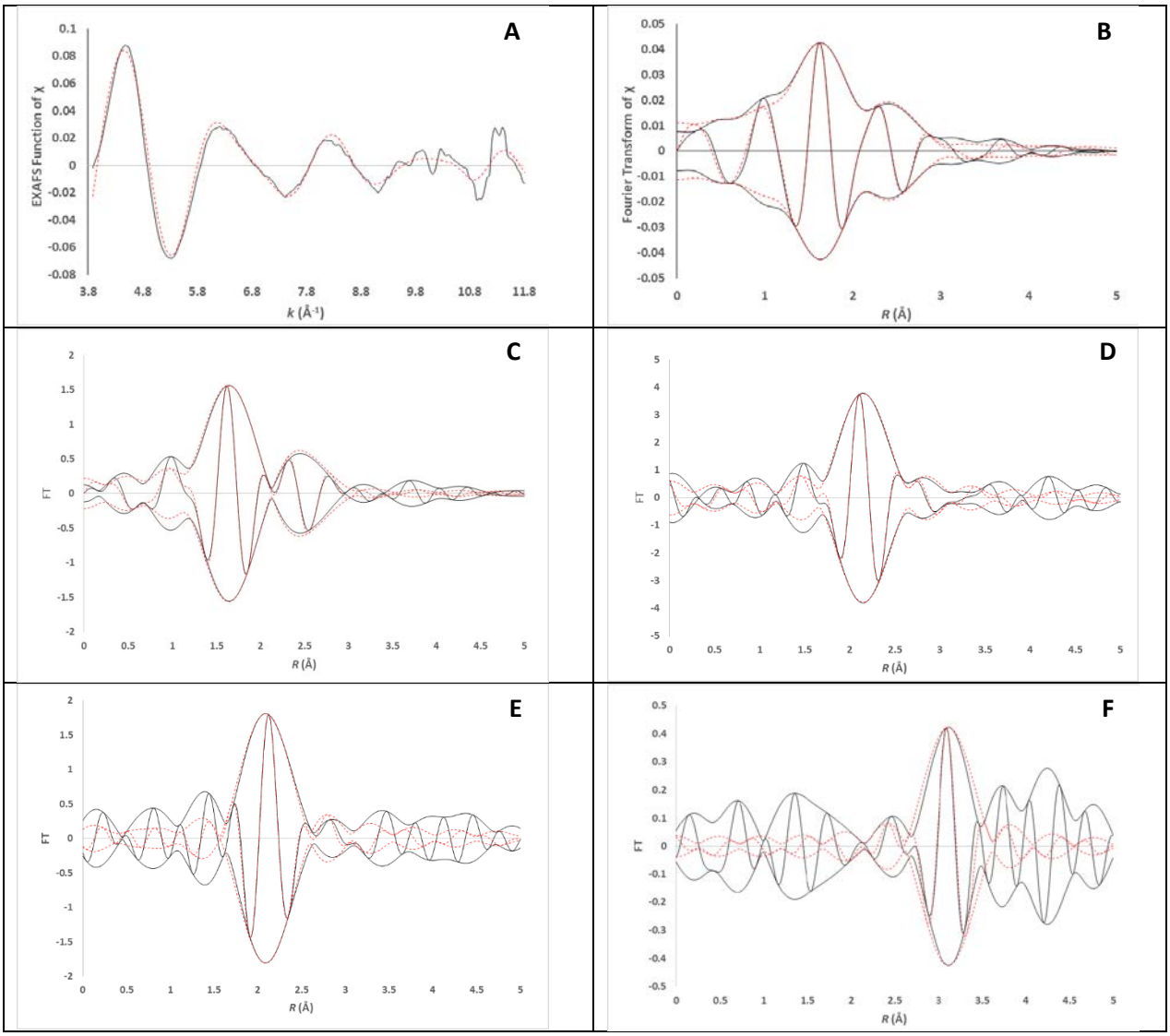

Figure 2A.19. EXAFS data recorded at Rh K edge characterizing the supported sample prepared by adsorption of $Rh(C_2H_4)_2(acac)$ on SAPO-37; sample was in flowing helium at 298 K and 1 bar: (A) k^1-weighted EXAFS function, $k^1(\chi)$ (solid line), and sum of the calculated contributions (dotted line). (B) k^1-Weighted imaginary part and magnitude of the Fourier transform of the data (solid line) and sum of the calculated contributions (dotted line). (C) k^3-Weighted imaginary part and magnitude of the Fourier transform of the data (solid line) and sum of the calculated contributions (dotted line). (D) k^2-Weighted, phase- and amplitude-corrected, imaginary part and magnitude of the Fourier Transform of the data (solid line) and calculated contributions (dotted line) of Rh–C shell. (E) k^2-Weighted, phase- and amplitude-corrected, imaginary part and magnitude of the Fourier transform of the data (solid line) and calculated contributions (dotted line) of Rh–O shell. (F) k^2-Weighted, phase- and amplitude-corrected, imaginary part and magnitude of the Fourier transform of the data (solid line) and calculated contributions (dotted line) of Rh–Al shell.

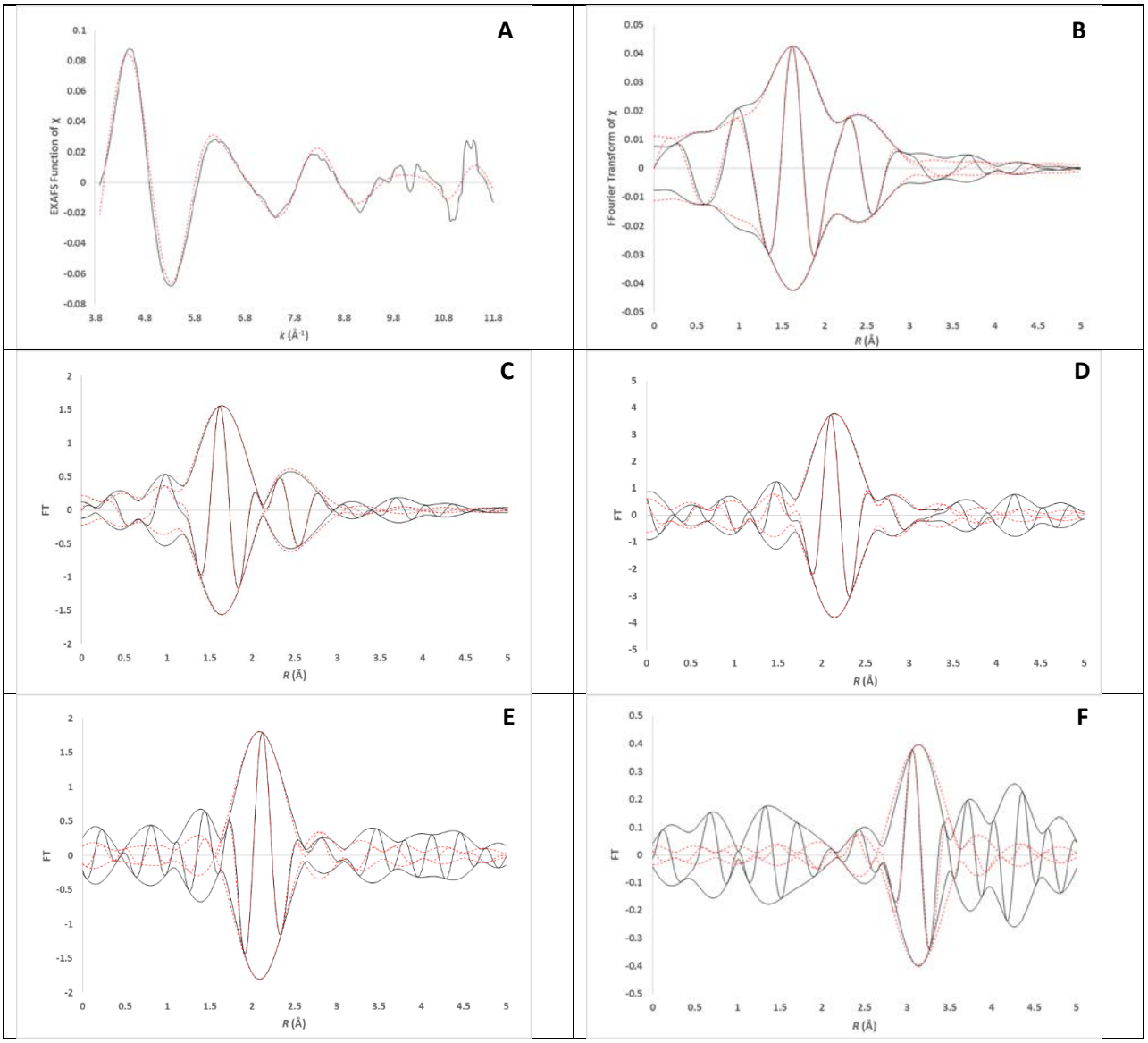

Figure 2A.20. EXAFS data recorded at Rh K edge characterizing the supported sample prepared by adsorption of $Rh(C_2H_4)_2(acac)$ on SAPO-37. Sample was in flowing helium at 298 K and 1 bar: (A) k^1-Weighted EXAFS function, $k^1(\chi)$ (solid line), and sum of the calculated contributions (dotted line). (B) k^1-Weighted imaginary part and magnitude of the Fourier transform of the data (solid line) and sum of the calculated contributions (dotted line). (C) k^3-Weighted imaginary part and magnitude of the Fourier transform of the data (solid line) and sum of the calculated contributions (dotted line). (D) k^2-Weighted, phase- and amplitude-corrected, imaginary part and magnitude of the Fourier Transform of the data (solid line) and calculated contributions (dotted line) of Rh–C shell. (E) k^2-Weighted, phase- and amplitude-corrected, imaginary part and magnitude of the Fourier transform of the data (solid line) and calculated contributions (dotted line) of Rh–O shell. (F) k^2-Weighted, phase- and amplitude-corrected, imaginary part and magnitude of the Fourier transform of the data (solid line) and calculated contributions (dotted line) of Rh–Si shell.

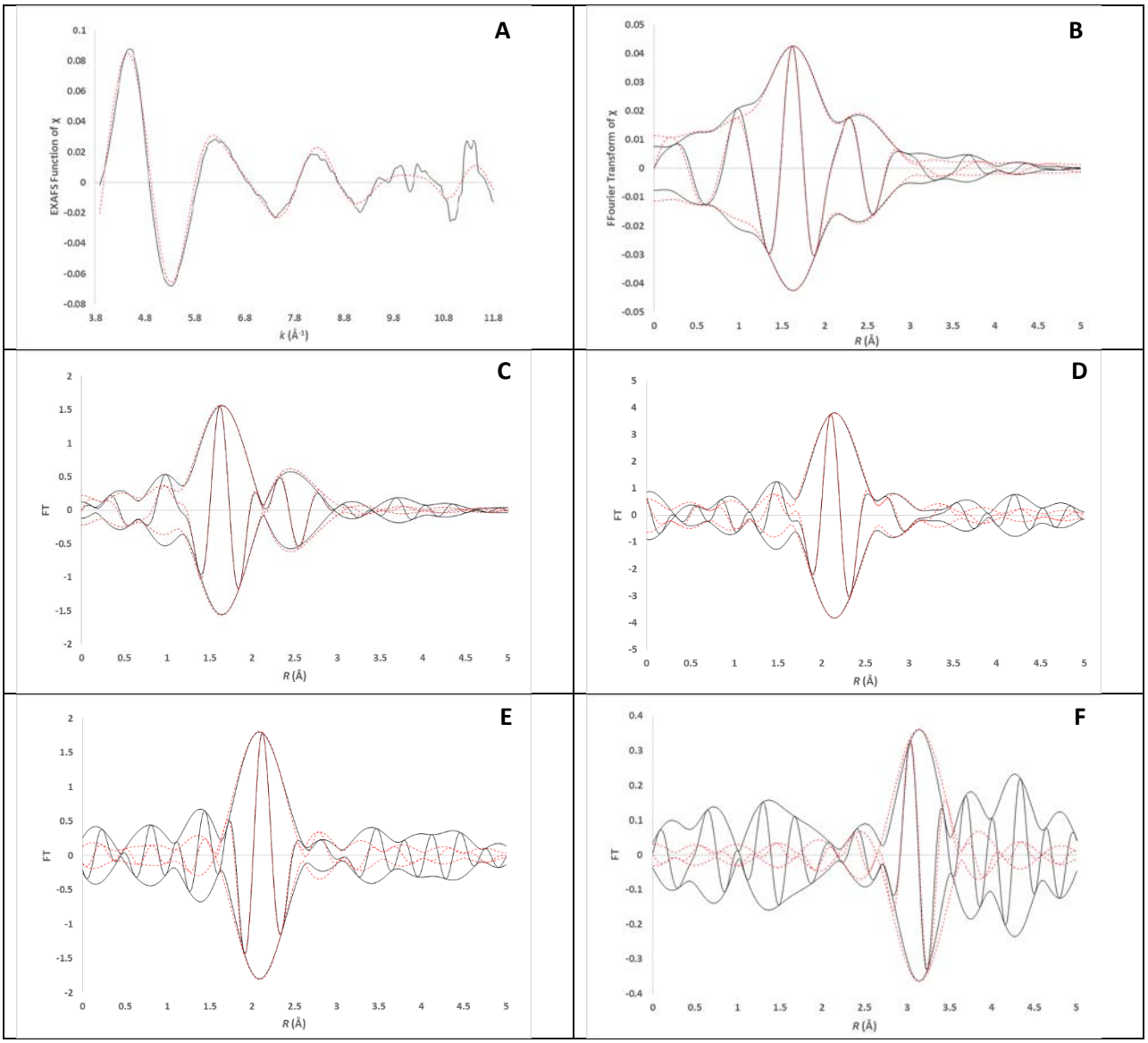

Figure 2A.21. EXAFS data recorded at Rh K edge characterizing the supported sample prepared from adsorption of $Rh(C_2H_4)_2(acac)$ on SAPO-37. Sample was in flowing helium at 298 K and 1 bar: (A) k^1-Weighted EXAFS function, $k^1(\chi)$ (solid line), and sum of the calculated contributions (dotted line). (B) k^1-Weighted imaginary part and magnitude of the Fourier transform of the data (solid line) and sum of the calculated contributions (dotted line). (C) k^3-Weighted imaginary part and magnitude of the Fourier transform of the data (solid line) and sum of the calculated contributions (dotted line). (D) k^2-Weighted, phase- and amplitude-corrected, imaginary part and magnitude of the Fourier Transform of the data (solid line) and calculated contributions (dotted line) of Rh–C shell. (E) k^2-Weighted, phase- and amplitude-corrected, imaginary part and magnitude of the Fourier transform of the data (solid line) and calculated contributions (dotted line) of Rh–O shell. (F) k^2-Weighted, phase- and amplitude-corrected, imaginary part and magnitude of the Fourier transform of the data (solid line) and calculated contributions (dotted line) of Rh–P shell.

References

(1) Bull, L. M.; Cheetham, A. K.; Powell, B. M.; Ripmeester, J. A.; Ratcliffe, C. I. The Interaction of Sorbates with Acid Sites in Zeolite Catalysts: A Powder Neutron Diffraction and ^{2}H NMR Study of Benzene in H-SAPO-37. *J. Am. Chem. Soc* **1995**, *117*, 4328–4332.

(2) Liang, A. J.; Bhirud, V. A.; Ehresmann, J. O.; Kletnieks, P. W.; Haw, J. F.; Gates, B. C. A Site-Isolated Rhodium–Diethylene Complex Supported on Highly Dealuminated Y Zeolite: Synthesis and Characterization. *J. Phys. Chem. B* **2005**, *109*, 24236–24243.

(3) Liang, A. J.; Craciun, R.; Chen, M.; Kelly, T. G.; Kletnieks, P. W.; Haw, J. F.; Dixon, D. A.; Gates, B. C. Zeolite-Supported Organorhodium Fragments: Essentially Molecular Surface Chemistry Elucidated with Spectroscopy and Theory. *J. Am. Chem. Soc.* **2009**, *131*, 8460–8473.

(4) Serna, P.; Gates, B. C. Zeolite-Supported Rhodium Complexes and Clusters: Switching Catalytic Selectivity by Controlling Structures of Essentially Molecular Species. *J. Am. Chem. Soc.* **2011**, *133*, 4714–4717.

(5) Uzun, A.; Bhirud, V. A.; Kletnieks, P. W.; Haw, J. F.; Gates, B. C. A Site-Isolated Iridium Diethylene Complex Supported on Highly Dealuminated Y Zeolite: Synthesis and Characterization. *J. Phys. Chem. C* **2007**, *111*, 15064–15073.

(6) Burkhardt, I.; Gutschick, D.; Lohse, U.; Miessner, H. I.R. Spectroscopic Evidence of a Well Defined Rhodium Dicarbonyl in Highly Dealuminated Zeolite Y, Formed by Interaction of Carbon Monoxide with Exchanged Rhodium. *J. Chem. Soc. Chem. Commun.* **1987**, 291–292.

(7) Miessner, H.; Gutschick, D.; Ewald, H.; Müller, H. The Influence of Support on the Geminal Dicarbonyl Species $Rh^{I}(CO)_2$ on Supported Rhodium Catalysts: An IR Spectroscopic Study. *J. Mol. Catal.* **1986**, *36*, 359–373.

(8) Hoffman, A. S.; Fang, C. Y.; Gates, B. C. Homogeneity of Surface Sites in Supported Single-Site

Metal Catalysts: Assessment with Band Widths of Metal Carbonyl Infrared Spectra. *J. Phys. Chem. Lett.* **2016**, *7*, 3854–3860.

(9) Vityuk, A. D. Synthesis and Reactivity of HY Zeolite-Supported Rhodium Complexes, *Ph.D. Dissertation*, University of South Carolina - Columbia, Columbia, SC, 2014.

(10) Shan, J.; Li, M.; Allard, L. F.; Lee, S.; Flytzani-Stephanopoulos, M. Mild oxidation of methane to methanol or acetic acid on supported isolated rhodium catalysts. *Nature* **2017**, *551*, 605–608.

(11) Ogino, I.; Gates, B. C. Reactions of Highly Uniform Zeolite H-β-Supported Rhodium Complexes: Transient Characterization by Infrared and X-ray Absorption Spectroscopies. *J. Phys. Chem. C* **2010**, *114*, 8405–8413.

(12) Babucci, M.; Fang, C. Y.; Perez-Aguilar, J. E.; Hoffman, A. S.; Boubnov, A.; Guan, E.; Bare, S. R.; Gates, B. C.; Uzun, A. Controlling catalytic activity and selectivity for partial hydrogenation by tuning the environment around active sites in iridium complexes bonded to supports. *Chem. Sci.* **2019**, *10*, 2623–2632.

(13) Pereira, C.; Gorte, R. J. Method for Distinguishing Brønsted-Acid Sites in Mixtures of H-ZSM-5, H-Y and Silica–Alumina. *Top. Catal.* **1992**, *90*, 145–157.

(14) Howard, J.; Lux, P. J.; Yarwood, J. A Fourier-Transform i.r. Study of Ethene Adsorbed on HZSM-5 Zeolite at Low Temperature (295 K). *Zeolites* **1988**, *8*, 427–431.

(15) Cerqueira, H. S.; Ayrault, P.; Datka, J.; Guisnet, M. Influence of coke on the acid properties of a USHY Zeolite. *Micropor. Mesopor. Mater.* **2000**, *38*, 197–205.

(16) Lange, J. P.; Gutsze, A.; Allgeier, J.; Karge, H. G. Coke Formation through the Reaction of Ethene over Hydrogen Mordenite III. IR and ^{13}C-NMR Studies. *Appl. Catal.* **1988**, *45*, 345–356.

Chapter 3

Atomically Dispersed Platinum in SAPO-37: Catalysis of Ethylene Hydrogenation and Transformation into Platinum Cluster[1]

[1] This chapter has been submitted to *ACS Catalysis* by J. E. Perez-Aguilar, J. T. Hughes, C.-Y. Chen, and B. C. Gates. The original manuscript has been reformatted to fit the requirements of the dissertation

3.1 ABSTRACT

Atomically dispersed supported platinum catalysts were synthesized by the reaction of $Pt(acac)_2$ (acac = acetylacetonato) with the silicoaluminophosphate molecular sieve SAPO-37. Extended X-ray absorption fine structure (EXAFS) spectra show that, after heating in air to 623 K, each platinum atom on average was bonded to approximately four light scatterer atoms (such as support oxygen atoms), with no evidence of a Pt–Pt contribution that would have indicated platinum clusters. X-ray absorption near edge spectra (XANES) indicate a platinum formal oxidation state of +2. Infrared spectra characterizing support OH groups show that $Pt(acac)_2$ reacted with them, as shown by the decreased intensities of the ν_{OH} bands and consistent with Pt–O bonds anchoring the platinum to the support. The supported species catalyzed ethylene hydrogenation at 1 bar and room temperature in a once-through flow reactor. The EXAFS-determined Pt–Pt coordination number (CN) increased from essentially zero to 1.8 ± 0.4 as the XANES white line intensity decreased, all within minutes, before recording of the first catalyst performance data. After 2 h of continuous reactant flow and catalysis, the CN had increased to 2.7 ± 0.5, and the white line intensity increased slightly. The data indicate the almost instantaneous formation of platinum clusters of only a few atoms each (with average diameters of about 0.4–0.8 nm). Subsequent exposure of the catalyst to ethylene led to a decrease in the Pt−Pt coordination number to 1.6 ± 0.3 and an increase in the white line intensity, indicating partial oxidative fragmentation of the clusters by ethylene. Platinum clusters in SAPO-37 formed in separate experiments by exposure to H_2 prior to catalysis were also catalytically active for ethylene hydrogenation. The data all support the conclusion that platinum clusters are the catalytically active species, with no evidence of catalysis by atomically dispersed platinum.

3.2 INTRODUCTION

Zeotype materials are widely used as acid-base catalysts for the production of fuels, petrochemicals, and fine chemicals,[1–3] and they find wide applications as supports for catalytic metals, with applications

including hydrocracking,[4] hydroisomerization,[5,6] reforming (aromatization),[7,8] and vehicle exhaust abatement.[9,10] Both support chemical properties such as acidity and physical properties such as aperture and cage dimensions affect the catalyst performance, as illustrated by data characterizing hydroisomerization and alkane reforming (e.g., in the Chevron Aromax process) catalyzed by platinum in zeolites.[11,12] The physical properties of the crystalline zeotype supports offer numerous advantages, including high surface areas for high metal dispersions, structures that stabilize the metals in highly dispersed states by encapsulation,[13] and pores that facilitate shape-selective catalysis.[14] The crystalline nature of these supports also offers the prospective advantages of structural uniformity of the supported species to facilitate fundamental understanding of the structure and function of the catalytic species.[15]

Zeolite-supported platinum catalysts are used on a large scale in some of the aforementioned applications.[16] Practical advantages include high hydrogenation selectivities observed for platinum nanoparticles encapsulated in MFI zeolites[17] and high selectivity for isomerization of alkanes (*n*-pentane and *n*-hexane) observed for platinum clusters supported on micro/mesoporous ZSM-5.[18] Recent work has been focused on highly dispersed (even atomically dispersed) platinum in zeolites,[19,20] with part of the motivation being the advantages of high metal utilization efficiency, maximized influence of the support, and new properties of noble metals in the most highly dispersed state, when they are positively charged.[21] Yet there are hardly any data allowing comparisons of zeolites with other zeotype materials as supports.

Our goal was fundamental understanding of the role of a non-zeolite support for an atomically dispersed noble metal catalyst. We chose platinum supported on the silicoaluminophosphate molecular sieve SAPO-37,[22,23] because platinum is of wide importance in catalysis and because SAPO-37 has the same framework structure as zeolite Y and thus provides the opportunity for comparisons with that zeolite to help elucidate the role of the support composition on catalyst performance. Because SAPOs

incorporate framework phosphorus atoms, they behave differently from their iso-structural zeolite counterparts as supports, as illustrated for atomically dispersed rhodium catalyzing the conversion of ethylene in the presence of H_2.[24]

Our specific goals were to investigate highly dispersed platinum supported on SAPO-37 as a catalyst for the reaction of ethylene with H_2; a working hypothesis was that the catalyst structures would be simple and uniform enough to yield to insights into the structure of the catalytic species.

The precursor used for catalyst synthesis was bis(acetylacetonato)platinum(II), $Pt(acac)_2$, chosen because it offers the prospect of making atomically dispersed platinum by reaction with support OH groups. Ethylene hydrogenation was chosen as the catalytic test reaction to take advantage of the identifiable spectroscopic signatures of the reactants and the adsorbed species derived from them.

3.3 MATERIALS AND METHODS

Preparation of Catalysts by Reaction of $Pt(acac)_2$ with SAPO-37. Platinum complexes were anchored to SAPO-37 that was synthesized by a reported method,[24] with the precursor $Pt(acac)_2$ reacting with SAPO powder that had been calcined at 873 K for 6 h in flowing air (Praxair, 99.5% purity) followed by 6 h under dynamic vacuum in a once-through plug-flow reactor. Sample handling and treatments were carried out with standard air-exclusion techniques. Under an argon atmosphere, the precursor $Pt(acac)_2$ (6.0 mg, 98 wt%, Strem) was mixed thoroughly with 300.0 mg of the calcined SAPO powder and placed in a once-through plug-flow reactor. The reactor tube was evacuated and then sealed under vacuum. The temperature was ramped up to 333 K at 1 K min^{-1} and held for 1 h, then ramped further to 353 K and held for 1 h, under vacuum (there was no flow through the reactor during this procedure). After further ramping to 373 K, the catalyst was held at this temperature for 1 h as the $Pt(acac)_2$ powder in the mixture with the SAPO particles sublimed and was deposited onto the SAPO.[25] If all the platinum in the precursor $Pt(acac)_2$ were deposited in the SAPO, the platinum loading would have been 1.1 wt%. The resultant catalyst was then exposed to air flowing at 45 mL(NTP) min^{-1}, and the temperature was

ramped to 403 K at a rate of 1 K min^{-1} and held for 15 min, followed by a further temperature ramp (1 K min^{-1}) to 623 K and a 2 h soak.[26] The resulting sample was recovered and stored in an argon-filled glovebox.

Elemental Analysis of the Supported Platinum Catalyst. The platinum content of the SAPO-37-supported platinum sample was determined at the UC Davis Interdisciplinary Center for Plasma Mass Spectrometry on an Agilent Model 7500a, quadrupole-type, inductively coupled plasma mass spectrometer (ICP-MS) (Agilent Technologies, Santa Clara, CA).

Infrared (IR) Spectroscopy. A Bruker IFS 66v spectrometer with a room-temperature DTGS detector and a spectral resolution of 2 cm^{-1} was used to collect transmission IR spectra of the catalyst samples. Approximately 10 mg of powder was pressed between two KBr windows for optical optimization that allowed detection of minor peaks. IR spectra were recorded with samples at room temperature under vacuum, with each spectrum being an average of 128 scans. In some experiments, the sample was placed in a diffuse reflectance (DRIFTS) reaction chamber (Harrick Scientific) equipped with KBr windows, mounted in a Praying Mantis diffuse reflectance adapter (Harrick Scientific). The cell in the argon-filled glovebox was loaded with approximately 50 mg of dry KBr powder (Crystal Labs, 7758-02-3), along with 15 mg of catalyst sample on top of the KBr powder. This cell was connected into a flow system without exposure of the sample to air, and it allowed recording of spectra as reactant gases (CO, ^{13}CO, O_2, D_2, H_2, and/or ethylene) flowed through the cell at the desired temperature.

X-Ray Absorption Spectroscopy (XAS). X-ray absorption spectroscopy (XAS) experiments characterizing the platinum-containing samples were carried out at beam lines 4-1 and 9-3 of the Stanford Synchrotron Radiation Lightsource (SSRL). In an argon-filled glovebox at SSRL, powder samples were loaded into a transmission fluorescence X-ray absorption spectroscopy cell/flow reactor[27] or a Kapton capillary (1.0 mm OD) cell and held in place with quartz wool.[28] The storage ring energies and currents were 3 GeV and 500 mA, respectively. X-ray energy scans from −250 to 1000 eV relative to the

Pt L_{III} edge (11564 eV) were obtained by using a double-crystal Si(220) monochromator at each beamline. For calibration purposes, measurement of the absorption of a platinum foil mounted downbeam of the sample was carried out simultaneously. Transient fluorescence X-ray absorption near edge spectra (XANES) and extended X-ray absorption fine structure (EXAFS) spectra were collected for samples in flowing reactive gases in a once-through flow system, with the effluent gases characterized with an online mass spectrometer (Hiden Analytical QGA) downstream of the cell. The following *m*/*z* values were used to identify the products: *m*/*z* = 28 for ethylene; 30 for ethane; and 41 for butenes.

Analysis of the EXAFS data was carried out with the Athena software of the Demeter package and with the software XDAP.[29] Athena was used for edge calibration and deglitching and XDAP for background removal, normalization, and conversion of the data into an EXAFS function file. Reference files used in the fitting, with backscattering amplitudes and phase shifts for Pt–Pt, Pt–O, Pt–C, and Pt–Al contributions, were calculated with the software FEFF7.0 from crystallographic coordinates of the unit cells of the reference compounds platinum metal, PtO_2, $Pt(acac)_2$, and Pt-Al alloy.[30,31] Each analyzed spectrum was the average of four spectra. Details of the data processing and analysis methodology are reported elsewhere.[24] The quality of each fit was evaluated by the goodness of fit, defined as follows:

$$Goodness\ of\ fit = \frac{\nu}{NPTS(\nu - N_{free})} \sum_{i=1}^{NPTS} \left(\frac{\chi_{exp,i} - \chi_{model,i}}{\sigma_{exp,i}} \right)^2$$

where χ_{exp} and χ_{model} are the experimental and calculated EXAFS functions, respectively; σ_{exp} the error in the experimental results; ν the number of independent data points in the fit range; N_{free} the number of free parameters; and NPTS the number of data points in the fit range. The estimates of the (approximate) error bounds are based on the reported results and statistical analyses. Best-fit models of each of EXAFS data set were fitted initially with various combinations of plausible absorber–scatterer contributions, which led to a list of candidate models. Then, a “difference-file” technique was applied to assess the candidate models, whereby the calculated EXAFS contribution from each individual Pt–

scatterer contribution was compared with the data in *R* (distance) space. This iterative fitting was continued in *R* space for both overall and individual contributions with the Fourier-transformed EXAFS data (χ data) until the best-fit model was obtained, which is the one providing optimum agreement between the calculated k_0-, k^1-, k^2-, and k^3-weighted EXAFS data and the model.

Catalytic Activity Measurements. Catalyst performance was tested with samples in a once-through temperature-controlled plug-flow reactor. The equipment and procedures have been described in detail.[24] The feed gases helium, H_2, and ethylene with the following partial pressures (in mbar) were as follows: 50 for ethylene, 50 for H_2, 900 for helium or 10 for ethylene, 100 for H_2, 890 for helium. The gas stream flowed through a bed of catalyst particles of mass typically 1.0–2.0 mg mixed with 0.5 g of particles of inert, nonporous α–Al_2O_3 (Sigma Aldrich, 100–200 mesh) at atmospheric pressure, a temperature of 303 K, and a total feed flow rate of 100 mL(NTP) min^{-1}. The effluent stream was analyzed periodically with an online gas chromatograph (Hewlett−Packard 6890N) equipped with a capillary column (PLOT Alumina "M," 50 m × 0.53 mm) and a flame ionization detector. All the reported catalytic reaction rates were determined from differential conversions and expressed per platinum atom (turnover frequencies, TOF) recorded at various times on stream. The maximum activity, following an induction period of typically 2.5 h, was observed before the onset of substantial catalyst deactivation. The conversions were <10% and shown to be differential on the basis of the essentially linear dependences of conversion on inverse space velocity (e.g., Figure 3A.1 in the Supporting Information, SI).

Summary of Characterization Experiments. Scheme 3A.1 in the SI is a summary of the characterization techniques that were used to investigate the samples, including experiments done after treatments of the SAPO-37-supported platinum in various gas atmospheres.

3.4 RESULTS

Synthesis of SAPO-37-Supported Platinum. During the first step of the catalyst synthesis, as $Pt(acac)_2$ (which is yellow) was thoroughly mixed with the SAPO and vaporized, there was no observable color change in the SAPO. The subsequent oxidation treatment during the synthesis led to a change in color of the material from white to green. These observations are consistent with the incorporation of platinum in the SAPO. The elemental analysis data show that the SAPO contained 1.1 ± 0.1 wt% platinum. This result is consistent with the masses of $Pt(acac)_2$ and SAPO used in the synthesis and the inference that all of the precursor $Pt(acac)_2$ reacted with the SAPO-37 support. The lack of observation of any deposits formed from the precursor during the synthesis and the color change of the SAPO bolster this conclusion. This platinum loading corresponds to approximately 1 platinum atom per 25 supercages.

Changes in the IR spectra of the samples indicate that SAPO Si–OH–Al sites (Brønsted acid sites) were converted by reaction with the platinum precursor. Spectrum A of Figure 3.1 represents bare SAPO-37 calcined at 873 K in air followed by evacuation; spectrum B represents the sample after the synthesis that involved chemisorption of $Pt(acac)_2$ and subsequent oxidation. The intensities of the bands at 3640 and 3578 cm^{-1} corresponding to the SAPO Si–OH–Al sites (in supercages and sodalite cages, respectively)[32,33] decreased as the platinum species evidently became bonded at these sites. IR spectra of the sample (Figure 3A.2 in SI) indicate that after the oxidation synthesis (details in Section 3.3), the acac ligands had been removed, presumably by the synthesis, as shown by the lack of ν_{COring}, ν_{C-C-Cs}, and δ_{CH} vibrations expected if Hacac had remained on the support as a product of the chemisorption.[24] Further, the data provide no evidence of acac ligands remaining on the platinum after this treatment. The bands corresponding to the SAPO Si–OH (3745 cm^{-1}) and P–OH (3675 cm^{-1}) sites and the hydroxyls in the minor extra-framework (3718 cm^{-1}) components of the support were too low in intensity to justify any conclusions about whether the precursor reacted with them.[34–37]

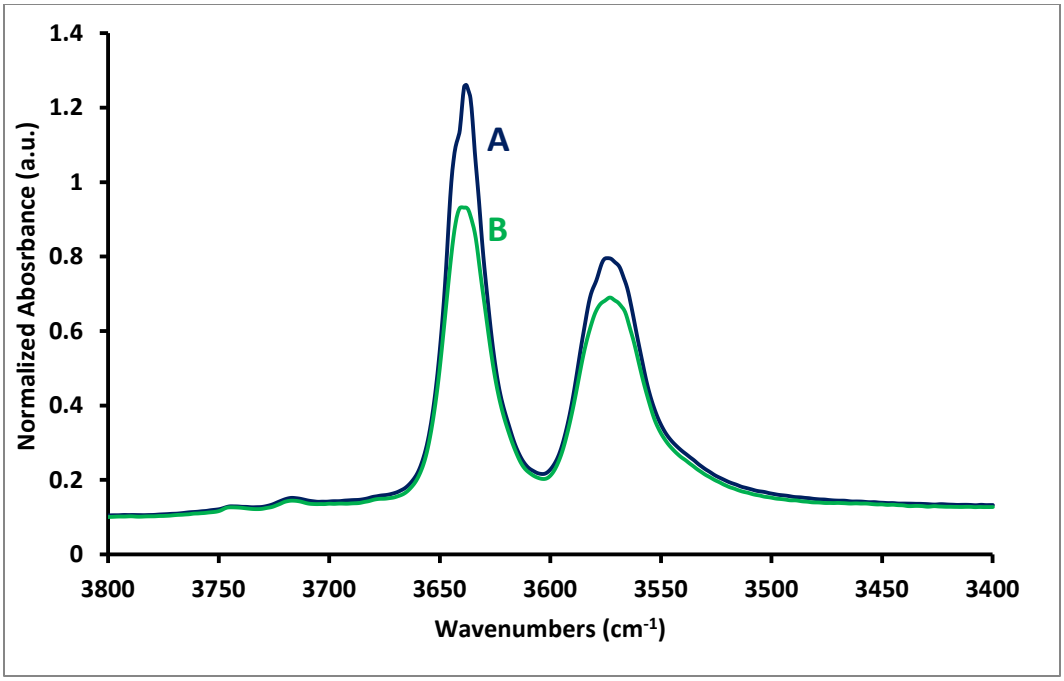

Figure 3.1. IR spectra in the ν_{OH} region characterizing (**A**) calcined SAPO-37 and (**B**) sample formed by reaction of $Pt(acac)_2$ with calcined SAPO-37.

EXAFS Spectra of Isolated Platinum Complexes and Clusters Formed from them on SAPO-37. EXAFS data recorded near the Pt L_{III} edge provide structural information about the platinum-containing SAPO-37 sample. A substantial Pt L_{III} absorption edge intensity confirmed the presence of platinum in the sample. Fitting of the data (Table 3.1, Figure 3.2a) demonstrated a lack of measurable Pt–Pt scattering, consistent with atomic dispersion of the platinum bonded to SAPO-37, and a Pt–light scatterer contribution, with a coordination number of nearly 4 at an average distance of 2.02 Å (a bonding distance, such as a Pt–O bonding distance), consistent with the bonding of the platinum to the support as, for example, a bidentate ligand. The IR data showing that support OH groups were converted in the synthesis when the $Pt(acac)_2$ was chemisorbed and the sample was subsequently oxidized imply that the platinum was bonded through $Pt–O_{support}$ bonds. The EXAFS data also give evidence of another Pt–light-scatterer contribution, with a coordination number of nearly 2 at a distance of 2.29 Å (longer than a typical Pt–O bonding distance) (Table 3.1). We suggest that the support provided two oxygen ligands for each platinum atom, comparable to HY zeolite as a support for

atomically dispersed cationic rhodium and iridium, and that the other scatterers represent ligands formed in the oxidation step of the synthesis that is expected to have removed the acac.[24,38]

EXAFS data recorded after the sample (150 mg) had been exposed to flowing H_2 (50 mL(NTP) min^{-1}) for 1 h demonstrate the formation of Pt–Pt bonds, implying the breaking of Pt–O bonds and unlinking of platinum from the support—that is, reduction, migration, and aggregation of platinum and the formation of platinum clusters. The EXAFS data characterizing the H_2-reduced sample (Table 3.1) demonstrate that the Pt–Pt coordination number increased from a value indistinguishable from zero to about 4, accompanied by a decrease in the Pt–light scatterer coordination number from about 4 to about 1 as more platinum atoms were unlinked from the support. These clusters, on average, are several-atom clusters (Table 3.1). Authors such as Torigoe *et al.*[39] and Moliner *et al.*[40] have observed CNs similar to ours after exposure of CHA zeolite-supported atomically dispersed platinum to H_2 at 773 K and suggested cluster diameters in the range of 1.0–1.3 nm.[40] We hypothesize that hydride ligands formed on platinum as clusters formed, but any gas-phase products formed in the reduction were evolved in concentrations too low to observe with the online mass spectrometer.

Species comparable to the atomically dispersed platinum species present initially on the SAPO support have been reported to exist on KLTL zeolite, NaY zeolite, and NaX zeolite, with these supports typically acting as bidentate ligands that provide two oxygen atoms to anchor each platinum atom.[19,41,42] A summary of the EXAFS data characterizing this family of samples is given in Table 3.1.

Table 3.1: Structural Models Based on EXAFS Spectra Characterizing Initial Platinum Complexes Supported on SAPO-37 and on Various Zeolites.[a]

Initial form of catalyst	Shell[b]	*N*	*R* (Å)	$10^3 \times \sigma^2$	ΔE_0 (eV)	Ref.
Pt/SAPO-37, 1.1 ± 0.1 wt% platinum	Pt–O_S	4.0	2.02	5.9	-8.0	this work
	Pt–O_I	2.0	2.29	2.4	-1.0	
	Pt–Al	1.0	2.70	1.8	-8.0	
	Pt–O_I	2.5	2.99	5.0	2.8	
Pt/SAPO-37, 1.1 ± 0.1 wt% platinum, after exposure to H_2 for 30 min	Pt–O_S	1.0	2.03	11.8	-8.0	
	Pt–Pt	4.0	2.71	3.8	-8.0	
	Pt–O_L	1.0	3.43	6.8	-1.7	
	Pt–Al	1.1	3.97	4.8	-4.0	

PtO_x/KLTL zeolite (oxidized), 1.0 wt% platinum	Pt–N	0.6	2.00	1.2	-1.8	[19]
	$Pt–O_s$	2.8	2.01	8.9	-3.8	
	$Pt–O_l$	5.9	2.64	10.5	8.0	
	Pt–Al	1.1	3.19	2.6	11.3	
0.2 wt% Pt/NaY zeolite	$Pt–O_s$	2.3	2.01	8.67	4.1	[41]
6 wt% Pt/NaY zeolite	$Pt–O_s$	3.9	2.03	7.4	-3.93	[42]
	$Pt–O_l$	0.9	3.03	3.9		
	Pt–Al/Si	0.6	3.52	5.9		
6 wt% Pt/NaX zeolite	$Pt–O_s$	3.8	2.04	7.4	-3.30	[42]
	$Pt–O_l$	2.1	3.07	3.2		
	Pt–Al/Si	0.7	3.20	4.5		
0.33 wt% Pt/CHA zeolite	$Pt–O_s$	3.22	2.01	1.6	12.4	[40]

[a]Notation: *N*, coordination number; *R*, distance between absorber and scatterer atoms; σ^2, disorder term; ΔE_0, inner potential correction. Error bounds (accuracies) characterizing the structural parameters determined by fitting the EXAFS spectra are estimated to be as follows: *N*, ±20%; *R*, ±0.02 Å; σ^2, ±20%; ΔE_0, ±20 %. Details of the EXAFS fitting are provided in the SI. [b]The subscripts s and l refer to short and long, respectively.

XANES of Platinum Complexes on SAPO-37 and Clusters formed by their Reduction in H_2.

XANES data recorded with the EXAFS data are compared with those of reference compounds: platinum metal foil (characterizing Pt^0); solid $Pt(acac)_2$ (characterizing Pt^{2+}); and solid PtO_2 (characterizing Pt^{4+}) (Figure 3.2b). The white-line intensity increased in the order of Pt foil < SAPO-37-supported platinum clusters < $Pt(acac)_2$ < SAPO-37-supported isolated platinum complexes < PtO_2, consistent with the trends in the platinum formal oxidation state (but we refrain from assigning values of formal oxidation states of the supported samples on the basis of XANES data alone, as these data also depend on the platinum coordination). The data (Figure 3.2) also indicate that the white line intensity characterizing each of the supported platinum complexes was slightly greater, and shifted to higher energy (eV), relative to that of the precursor $Pt(acac)_2$, demonstrating that the platinum in the initial SAPO-supported species was cationic. A comparison of the magnitude of the Fourier transform of the initial SAPO-37-supported platinum complexes with that of platinum foil (Figure 3.2b) shows a single major contribution at 2.0 Å and no evidence of Pt–Pt bonding, which would have been indicated by a contribution at 2.7 Å matching that in the spectrum of platinum foil. However, when the supported sample was exposed to H_2, the magnitude of the Fourier transform at 2.7 Å (indicating a Pt–Pt contribution) increased (Figure 3.2b,

Table 3.1). Thus, the initial platinum species on SAPO-37 were isolated cationic species that were reduced in H_2 and converted to platinum clusters.

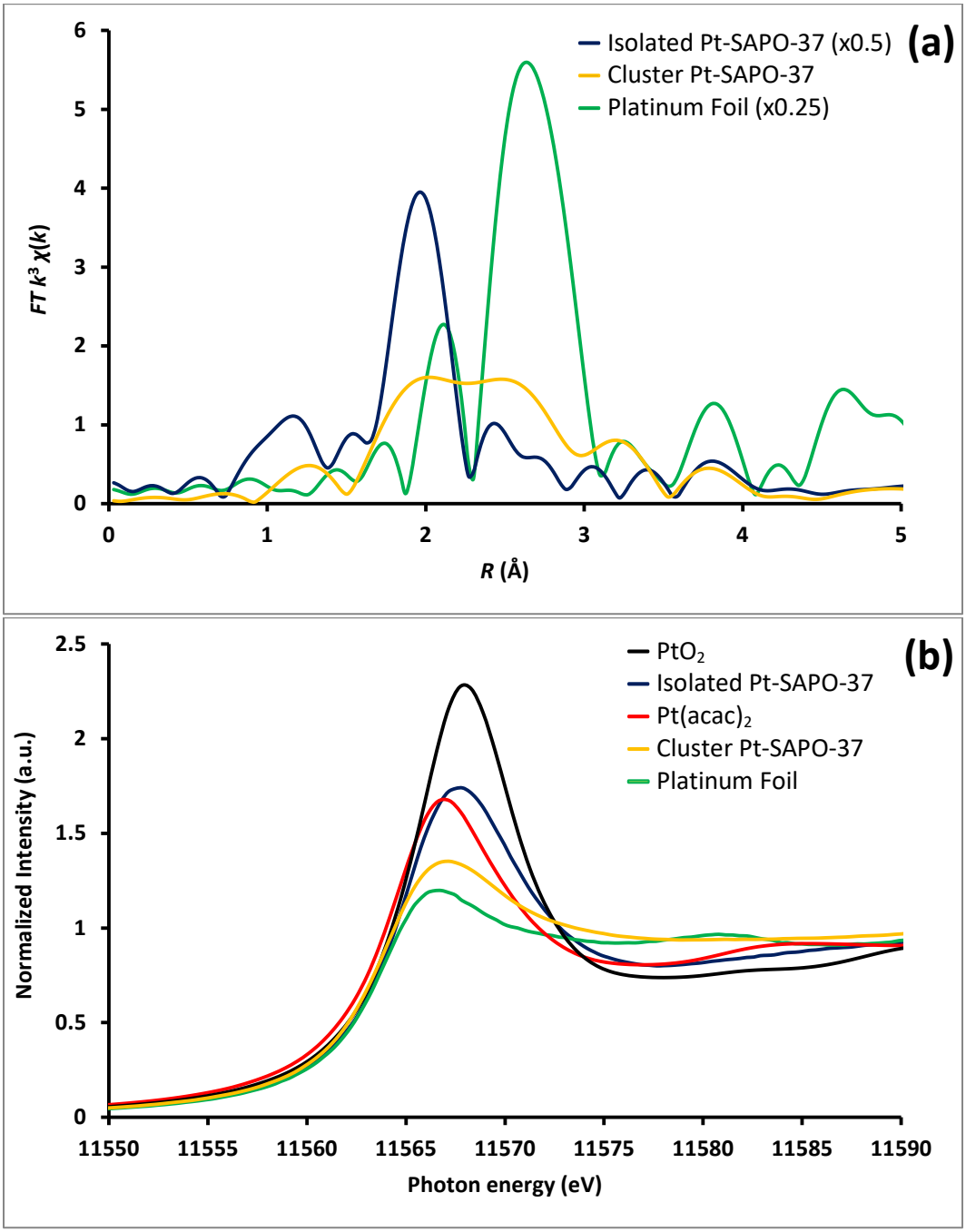

Figure 3.2. (**a**) k^3-Weighted magnitude of the Fourier transforms of EXAFS data recorded at Pt L_{III}-edge characterizing SAPO-37-supported isolated platinum (blue), platinum clusters made from the isolated platinum species by exposure to H_2 (orange), and platinum foil (green). (**b**) XANES data characterizing platinum oxide (PtO_2, black), SAPO-37-supported isolated platinum (blue), $Pt(acac)_2$ (red), platinum clusters supported on SAPO-37 (orange), and platinum foil (green).

Reactivity of Atomically Dispersed Supported Platinum Species Characterized by IR Spectroscopy. To further investigate the reactivity of the platinum species on SAPO-37, samples (20 mg) in the DRIFTS cell were brought in contact first with N_2 flowing at a rate of 50 mL(NTP) min^{-1} at atmospheric pressure and 298 K and then with a 12-min pulse of CO flowing at a rate of 50 mL(NTP) min^{-1} at atmospheric pressure and 298 K (2390 CO molecules per platinum atom). The sample in a flowing stream of 10% O_2 in helium (50 mL(NTP) min^{-1}) was then heated at a rate of 5 K min^{-1} to 473 K as spectra were recorded. Spectrum A, characterizing the sample in flowing N_2 prior to exposure to CO, includes two sets of ν_{CO} bands (at 2123 and 2090 cm^{-1}) characterizing the initially prepared sample (after the oxidation step). We infer that the CO present initially (Figure 3A.3 in the SI) had formed from the acac ligands in the $Pt(acac)_2$ precursor that reacted to form CO on the platinum species. But such species were minor components, as shown by the EXAFS data (Table 3.1) demonstrating that, on average, platinum was bonded predominantly to ligands that we suggest incorporated light scatterers, including two oxygen atoms of the support characterizing by the shorted Pt–O distance.[43–45] Spectrum B shows that the same sample in N_2 after exposure to a 15-min CO pulse included several new bands in the region of 2220–2090 cm^{-1}. The ν_{CO} bands in the 2220–2090 cm^{-1} region characterizing the sample after the CO pulse indicate isolated platinum species characterized by various CO coordinations and/or platinum in various formal oxidation states, as indicated by results reported for platinum carbonyls on zeolites.[42,46,47]

As the temperature subsequently increased with the sample in flowing O_2 at atmospheric pressure, the intensities of the bands initially evident in the 2220–2090 cm^{-1} region decreased. This result suggests that the CO ligands were removed by oxidation, but the mass spectrometer used to analyze the effluent stream was not sensitive enough to detect any evolved CO_2. Spectrum D, recorded after oxidation at 473 K with the sample in flowing N2 at room temperature, includes a remaining single νCO peak, at 2134 cm-1, indicating differing reactivities of the CO ligands.

Table 3A.2 in the SI is a summary of data characterizing carbonyls of platinum in various formal oxidation states (0 to +3) and with various coordination numbers (1 to 3) on various zeolites. These data show that both the local coordination and formal platinum oxidation state influence the ν_{CO} values. The IR data are not sufficient by themselves to identify the platinum species,[48] but the XANES spectra exclude the possibility that the initial supported species (after the oxidation step in the synthesis) incorporated zero-valent platinum (details in SI).

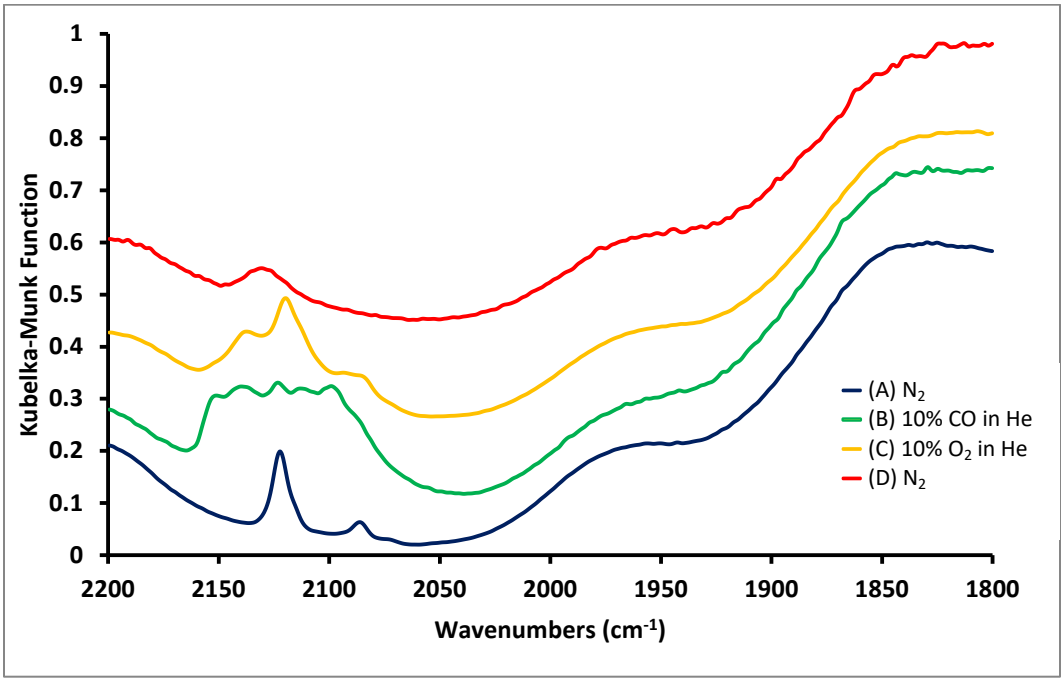

Figure 3.3. DRIFTS spectra in the ν_{CO} region: **(A)** recorded with the initially prepared sample (after the oxidation synthesis) in N_2 flowing at 50 mL(NTP)/min; **(B)** recorded after sample had been in contact with flowing 10% CO in helium for 15 min, followed by a purge of DRIFTS cell with helium for 30 min; **(C)** recorded after exposure to 10% O_2 at 473 K of sample in helium flowing at 50 mL(NTP)/min; and **(D)** recorded following these treatments with sample at room temperature in flowing N_2.

To further investigate the reactivity of the supported platinum and its local environment on SAPO-37, samples (20 mg) in the DRIFTS cell were brought in contact with helium flowing at 50 mL(NTP) min^{-1} at atmospheric pressure and 298 K. The sample was then exposed to H_2 flowing at 50 mL(NTP) min^{-1} at atmospheric pressure and 298 K for 30 min, and then the H_2 was purged out with helium and the sample exposed to a 12-min CO pulse (2392 CO molecules per platinum atom). The ν_{CO} region of the spectrum (Figure 3A.4 in SI) includes a single band at 2092 cm^{-1} in the range expected for CO on platinum

clusters.[46] The results thus verify the EXAFS data characterizing the sample after the H_2 exposure that show that platinum clusters had formed (Table 3.1, Table 3A.3 in SI). Correspondingly, they verify the XANES data demonstrating reduction of the platinum as cluster formed (Figure 3.2b).

The reduction was carried out separately with D_2 instead of H_2: the initially prepared sample was exposed to helium flowing at 50 mL(NTP) min^{-1} at atmospheric pressure and 298 K and then exposed to D_2 flowing at 10 mL(NTP) min^{-1} at atmospheric pressure and 298 K (Figure 3A.5 in the SI). The SAPO-37 OH group bands shifted from 3718, 3640, and 3578 cm^{-1} to 2766, 2686, and 2642 cm^{-1}, and, consistent with the harmonic oscillator approximation, the new bands are assigned to surface OD groups.[49] Thus, spillover occurred, with D_2 evidently activated on the platinum clusters and D migrating and undergoing exchange with support OH groups.[50,51]

When the sample containing OD groups was exposed to ethylene flowing at 10 mL(NTP) min^{-1} (Figure 3A.5 in the SI), ethylene adsorbed on the OD and OH groups, and, when the reactor was purged with helium, the ethylene desorbed, as shown by the full recovery of the OH and OD band intensities (Figure 3A.5 in the SI). These results indicate simple physisorption of ethylene on the OH or OD groups, consistent with reported results.[52]

Catalytic Performance of Supported Platinum: Evidence of Formation of Platinum Clusters as Catalytically Active Species. In experiments with a wide range of ethylene conversions in the presence of H_2, ethane was the only observed product. There was no detectable conversion when the SAPO-37 sample was present without platinum: the platinum was responsible for the catalysis.

The conversion initially increased with time on stream in the flow reactor, Figure 3.4 (the catalyst mass was 1.0 mg, the feed flow rate 100 mL(NTP) min^{-1}, and the C_2H_4 and H_2 partial pressures 10 and 100 mbar, respectively). Catalyst break-in such as this is commonly associated with changes in the metal-ligand environment resulting from reaction with the reactants, as illustrated by data of Martinez-Macias *et al.* ,[53] who observed changes in zeolite-supported iridium complexes during the break-in

period. These authors did not determine how the ligands changed during this period, but they systematically varied the ligands present initially (before catalysis) ($Ir(CO)(C_2H_4)$ and $Ir(C_2H_4)_2$ in HY zeolite) and demonstrated that the activity depended strongly on them, with the initial activities being in the order: $M(CO)_2 << M(CO)(C_2H_4) < M(C_2H_4)_2$ and the induction periods decreasing in the order ($M(CO)_2 > M(CO)(C_2H_4) > M(C_2H_4)_2$).[53]

Our results show that after an induction period of increasing activity (2.5 h), catalyst deactivation ensued, and, after about 172 h, the catalyst had lost essentially all of its activity (Figure 3.4). The number of turnovers during this period was approximately 913,000.

To test the hypothesis that the changes in the catalyst were associated with changes in the reactant-derived ligands—that might be expected to proceed faster at higher reactant partial pressures—we did an experiment with the same catalyst mass and feed flow rate but feed partial pressures of C_2H_4 and H_2 of 40 and 400 mbar, respectively (instead of 10 and 100 mbar). Correspondingly, the induction time was markedly reduced (Figure 3A.6 in the SI), and the catalyst deactivated more rapidly (in about 144 h), consistent with the expectation.

A summary comparison of the activities of these and related catalysts investigated under similar conditions is shown in Table 3.2.

Realizing that atomically dispersed platinum on numerous supports is easily reduced and aggregated and that platinum clusters and nanoparticles are active for our reaction,[40,54,55] we did complementary experiments with a catalyst incorporating preformed platinum clusters, made by pretreating the as-prepared sample in H_2 flowing at 50 mL(NTP) min^{-1} at room temperature for 1 h prior to the start of flow of ethylene + H_2 (Section 3.3). Thus, after a helium purge to remove H_2, the catalyst was tested under conditions matching those stated above (1.0 mg catalyst; feed flow rate 100 mL(NTP) min^{-1} ; and C_2H_4 and H_2 partial pressures of 40 and 400 mbar, respectively). The deactivation profile was similar to that observed with the catalyst that had not been pre-reduced, with the activities estimated by extrapolation

to zero time on stream (ignoring the induction period), being approximately the same and indistinguishable from each other within the estimated error (Table 3.2, Figure 3A.6 in the SI). Comparable activity data for platinum nanoparticles supported on SBA-15 silica, SiO_2, and Al_2O_3 are listed in Table 3.2. For comparison, data characterizing atomically dispersed rhodium and atomically dispersed iridium supported on DAY zeolite are shown with data characterizing SAPO-37 in Table 3.2.

Table 3.2: Comparison of Activities of Catalysts Incorporating Metal Complexes Supported on SAPO-37, Alumina, DAY Zeolite, and Silica for Hydrogenation of Ethylene.

Metal in catalyst	Support	Metal loading, wt%	initial form of catalyst	TOF (s^{-1})	ref.
Platinum	SAPO-37	1.1 ± 0.1 wt%	Atomically dispersed platinum species	0.12[a,b]	this work
				3.0[a,c]	
				4.5 ± 0.5[d]	
			Platinum clusters	6.6 ± 2.0[d]	
	SBA-15 silica	1.0	Platinum nanoparticles	0.64[e]	54
	SiO_2	0.05		1.3[f]	54
		0.5		17.5[f]	54
	Al_2O_3	9.2		53.4[f]	54
Iridium	DAY zeolite	1.0	$Ir(C_2H_4)_2$	0.71[g]	53
Rhodium			$Rh(C_2H_4)_2$	0.10[h]	24
	SAPO-37		$Rh(C_2H_4)_2$	0.13[h]	

[a]TOFs determined at maximum activity reached after induction period and before catalyst deactivation at respective conditions (Figure 3.4). The errors in the TOF values are estimated to be ± 10%, determined primarily by the error in the platinum content of the catalyst.
[b]TOFs determined at maximum activity at 303 K and 1.0 bar; feed partial pressures (mbar): C_2H_4, 50; H_2, 50; helium, 900; total flow rate 100 mL(NTP)/min; catalyst mass, 11.0 mg.
[c]TOFs determined at maximum activity at 303 K and 1.0 bar; feed partial pressures (mbar): C_2H_4, 10; H_2, 100; helium, 890; total flow rate 100 mL(NTP)/min; catalyst mass, 0.5–1.5 mg.
[d]Initial TOFs determined from C_2H_4 conversions <5%; catalyst mass, 1 mg; feed partial pressures (mbar): C_2H_4, 40; H_2, 400; helium, 560; total flow rate, 100 mL(NTP)/min.
[e]Steady-state TOF determined at 298 K; feed partial pressures (mbar): C_2H_4, 10; H_2, 100; inert, 890; catalyst mass, 1.1 mg.
[f]Rates reported as calculated from reference,[54] which are corrected to 10 mbar C_2H_4, 100 mbar H_2, and 298 K; see reference for details.
[g]Steady-state TOF determined at 303 K; feed partial pressures (mbar): C_2H_4, 100; H_2, 200; helium, 700.

[h]Initial TOFs determined from C_2H_4 conversions <5%; catalyst mass, 10−30 mg; feed partial pressures (mbar): C_2H_4, 50; H_2, 50; helium, 900; total flow rate, 100 mL(NTP)/min.

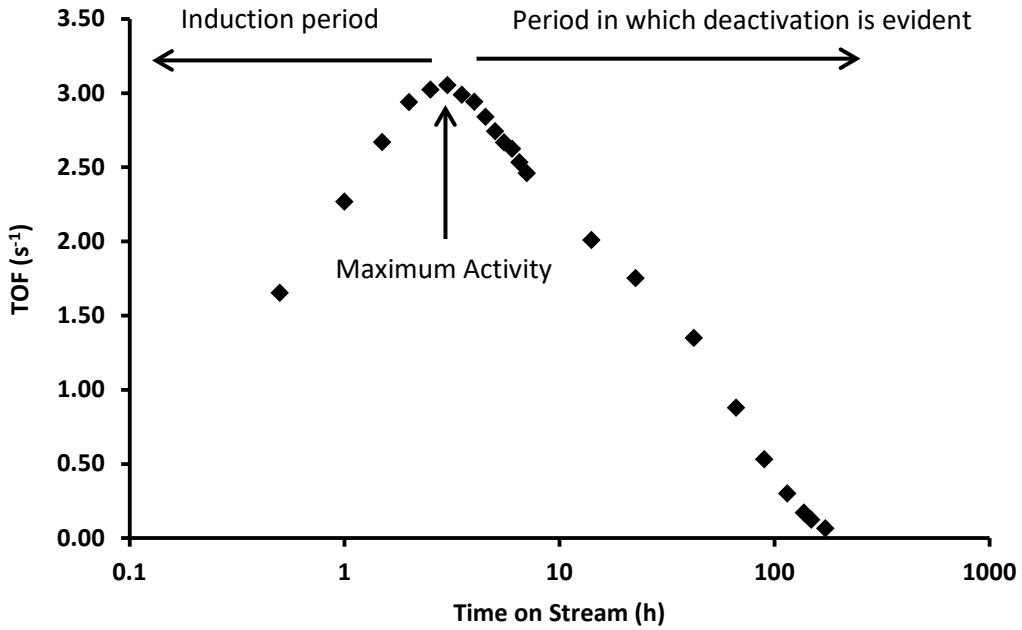

Figure 3.4. Performance of platinum supported on SAPO-37 for ethylene conversion catalysis in a once-through plug-flow reactor in the presence of H_2 at 303 K and 1 bar (molar H_2:C_2H_4 ratio = 10:1). The catalyst contained 1.1 ± 0.1 wt% platinum, and the TOF values were determined on the basis of the assumption that each platinum atom was exposed at each stage of the flow-reactor operation; see text for interpretation of how deactivation occurred and Table 3.2 for estimated error in TOF values.

XAS of Isolated Platinum Complexes and Platinum Clusters in Reactive Atmospheres. XAS experiments were done to characterize the SAPO-37-supported platinum in various atmospheres at various temperatures and during catalysis. XANES and k^3-weighted Fourier-transformed EXAFS data are shown in Figures 5a and b, respectively, recorded as the catalyst underwent changes in structure influenced by changes in the flowing gas atmosphere, with the products measured by on-line mass spectrometry: spectrum A represents the initial atomically dispersed platinum in flowing helium and spectrum B the sample after subsequent exposure to flowing ethylene—which evidently caused the white line to decrease in intensity and shift to a higher energy, accompanied by a decrease in magnitude of the Fourier transform at approximately 2.0 Å. Spectrum C represents the sample after the feed stream had subsequently been switched to a mixture of ethylene + H_2 (C_2H_4:H_2 ratio = 1:10, molar), with

catalysis occurring, and the data show a further decrease in the white line intensity and a slight shift of the white line to higher energy as well as a substantial increase in the magnitude of the Fourier transform at approximately 2.7 Å. Spectrum D was recorded after 2 h of exposure to catalytic reaction conditions followed by a switch of the feed back to ethylene, whereupon the white line increased in intensity and shifted to a lower energy; the Fourier-transformed data show maxima at approximately 2.1 and 2.6 Å.

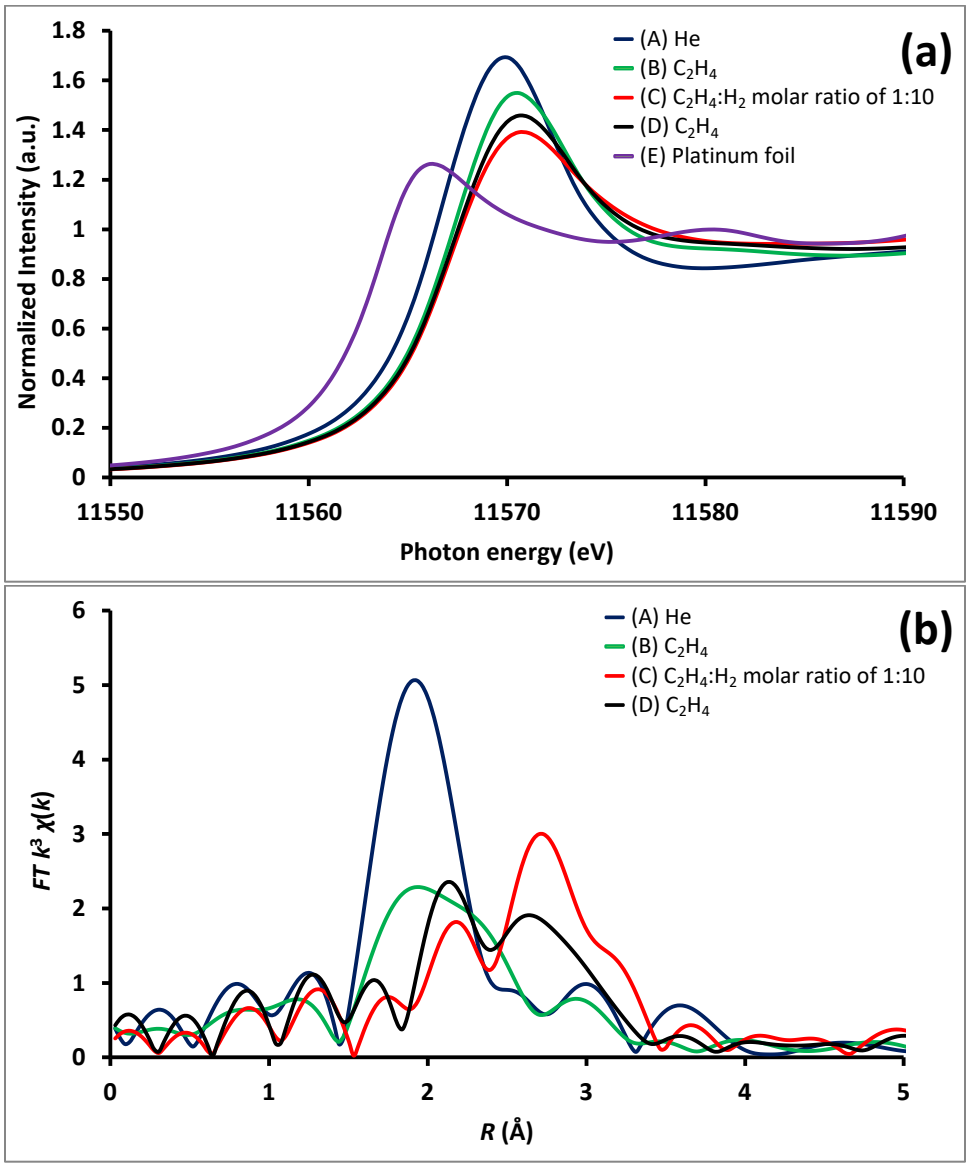

Figure 3.5. (a) XANES data characterizing SAPO-37-supported platinum complexes under the following conditions: (A) initial isolated platinum complexes (after oxidation synthesis) in flowing helium (30.0 mL(NTP) min^{-1}) (blue); (B) the sample subsequently exposed to flowing ethylene flowing at a rate of 2.4

mL(NTP) min^{-1} (green); (C) the sample subsequently under catalytic reaction condtions (C_2H_4:H_2 molar ratio = 1:10) (red); (D) the sample after a subsequent 2-h exposure to ethylene flowing at a rate of 2.4 mL(NTP) min^{-1} (black). Data characterizing platinum foil are shown for comparison (purple). (b) k^3-Weighted magnitude of the Fourier transforms of the EXAFS data recorded at the Pt L_{III}-edge characterizing SAPO-37-supported platinum complexes under conditions stated in (a).

In a continuation of the experimental sequence, transient data characterizing the transformation of the initial isolated platinum complexes into platinum clusters—and subsequent cluster breakup—were obtained with the catalyst in the XAS cell working as a flow reactor. Figure 3.6a shows the ethane signal from the online mass spectrometer downstream of the reactor along with XAS data recorded as a function of time on stream. Figure 3.6b shows transient white line and temperature data recorded during the experiments. Figure 3.6c shows the Pt−Pt distance and coordination number as a function of time onstream. When the sample was initially present in flowing helium, the magnitude of the Pt−light-scatterer contribution and the white line intensity were maximized, and no Pt−Pt contribution was observed. These data match the EXAFS data reported in Table 3.1. When the sample was later exposed to flowing ethylene at atmospheric pressure and room temperature (298 K), the magnitude of the Pt−light-scatterer contribution and the white line intensity decreased, and no Pt−Pt contribution was observed. We therefore conclude that the ligand sphere of the platinum had changed, consistent with the statements above and consistent with the adsorption of ethylene on the platinum. When the feed was then changed again to a reactive mixture of ethylene + H_2 (C_2H_4:H_2 ratio = 1:10, molar), the magnitude of the Pt−light-scatterer contribution decreased; the white line intensity decreased slightly; and a Pt−Pt contribution became evident and grew in intensity. The Pt−Pt coordination number jumped from 0 to 1.8, and the ethane signal in the mass spectrum increased, all within the period of the first scan (which required 5 min). These results show that platinum clusters formed in the reactive atmosphere that included H_2. As time progressed, the ethane signal in the mass spectrum increased and remained almost unchanged as the magnitude of the Pt−light-scatterer contribution decreased and the magnitude of the Pt−Pt contribution increased. We conclude from the increase in the Pt−Pt coordination

number (from 1.8 to 2.7) that—as the catalytic reaction occurred—the average size and/or number of platinum clusters increased (Figure 3.6c).

In a further continuation of the series of experiments with the same sample in the XAS cell, after 2 h of exposure to catalytic reaction conditions, the feed was switched back to ethylene. The data show that the magnitude of the Pt−light-scatterer contribution and the white line intensity both increased (the latter only slightly), but the values did not revert to the initial values—those observed before exposure of the catalyst to reaction conditions with ethylene + H_2 flowing. Concomitantly, the magnitude of the Pt−Pt contribution decreased, and the average Pt−Pt coordination number and distance also decreased, and—with H_2 being absent—the ethane signal decreased to noise level in the mass spectrum of the effluent.

This latter result indicates oxidative fragmentation of the platinum clusters by ethylene, which acts as an oxidizing agent[56] (ethylene has been shown to oxidatively fragment supported clusters of iridium[57] and of rhodium[58]). The inference is consistent with the slight increase in white line intensity (Figure 3.6c) and the decrease in Pt−Pt coordination number (2.7 to 1.6). These values indicate that, under our conditions, ethylene caused platinum cluster fragmentation but did not fragment these clusters entirely—that is, it did not cause the white line intensity to return to its initial value observed before catalytic reaction started. Further, the contraction of the average Pt−Pt bond distance from 2.74 to 2.64 Å, as H_2 was purged from the reactor and ethylene was present, matches results reported by Bus *et al.*[59] showing that platinum clusters losing hydrogen by desorption are characterized by decreasing Pt–Pt bond distances.

In the above-mentioned work,[57] it was shown that ethylene completely fragmented supported iridium clusters (consisting of approximately 4 atoms each) on a zeolite support when the sample was heated to at 353 K. To check whether ethylene could similarly completely fragment the platinum clusters,[60] the same sample mentioned above was heated to 353 K in flowing ethylene; then it was

cooled to room temperature in a period of 20 min, and the ethylene stream was replaced with helium. The white line intensity did not change during the temperature increase. Nor did purging of ethylene from the cell with helium lead to a change in the white line intensity. Consistent with these results, the average Pt−Pt coordination number was within error the same as that observed prior to the exposure of the sample to flowing ethylene as the temperature was increased and as the ethylene was later purged (Figure 3.6c). We thus conclude the platinum clusters remained stable as the temperature increased 353 K with the sample in ethylene and did not undergo complete fragmentation comparable to that observed for the zeolite-supported iridium clusters.[60]

We emphasize that the platinum clusters that formed in the partial fragmentation in ethylene were smaller than the ones formed by reduction of the initially formed catalyst in flowing H_2 (Table 3.1), with average cluster diameters that we infer on the basis of earlier estimates[40] to be in the range of 0.4–0.8 nm—characterizing extremely small clusters, with Pt−Pt coordination numbers ranging from about 1 to 4.

In summary, the EXAFS data (Table 3.1 and Table 3A.2 in SI) show that the platinum complexes present initially in the catalyst were converted into clusters within the period of the first scan under catalytic reaction conditions with H_2. As catalytic hydrogenation continued in the flow reactor, the average cluster size and/or number of clusters increased. When these clusters were later exposed to ethylene in the absence of H_2, they fragmented, and the products included smaller clusters but, within our ability to determine the structures, not atomically dispersed platinum (Figure 3.6c). During subsequent heating in the presence of flowing ethylene, the clusters were stable and not fragmented further.

Thus, all the data are consistent with the hypothesis that the observed catalytic activity is associated with the platinum clusters.

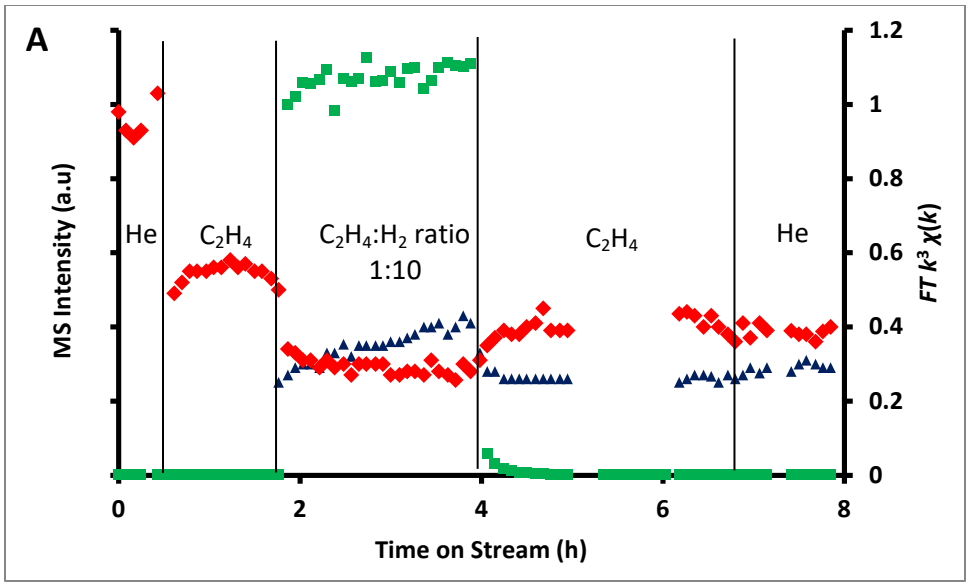
A
MS Intensity (a.u)
He
C_2H_4
C_2H_4:H_2 ratio
1:10
C_2H_4
He
FT k^3 $\chi(k)$
Time on Stream (h)

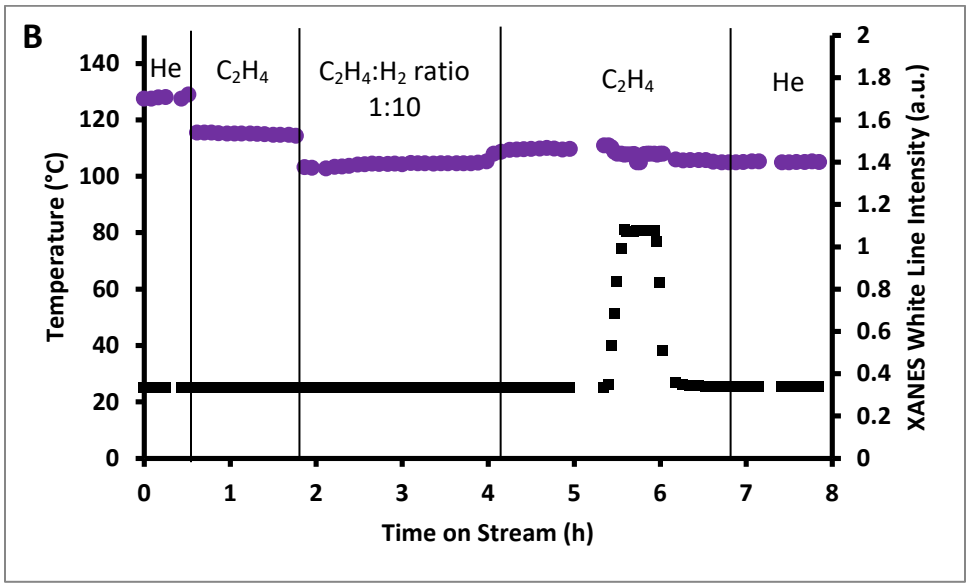
B
Temperature (°C)
He
C_2H_4
C_2H_4:H_2 ratio
1:10
C_2H_4
He
XANES White Line Intensity (a.u.)
Time on Stream (h)

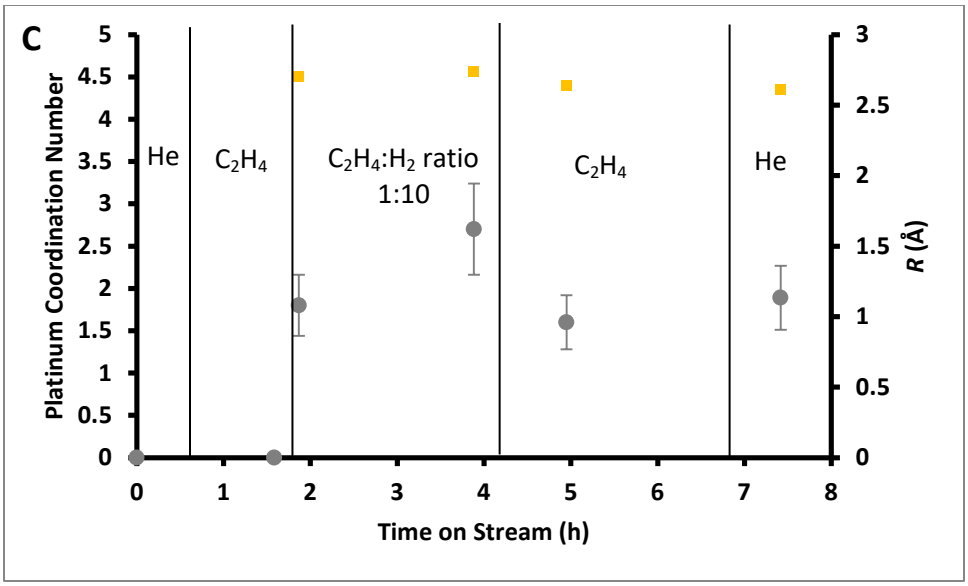

Figure 3.6. (a) Changes in k^3-weighted magnitude of the Fourier transforms of the EXAFS data and ethane signal observed during operation of the catalyst (1.1 ± 0.1 wt% platinum supported on SAPO-37) under ethylene hydrogenation conditions (molar H_2:C_2H_4 ratio = 10:1) in the EXAFS cell at 303 K and 1 bar. Symbols: red ◆, Pt−light-scatterer contribution at 2 Å; blue ▲, Pt−Pt contribution 2.5−2.8 Å; green ■, mass spectra of ethane (m/z = 30) in the effluent gas. (b) Changes in the white line intensity and temperature in various reactive gases. Symbols: purple ●, white line intensity; black ■, temperature. **(c)** Changes in the Pt−Pt distance and coordination number with sample in various reactive gases. Symbols: gray ●, platinum coordination number; orange ■, Pt−Pt distance. Details are presented in the text.

Characterization of Deactivated Catalyst. To gain insight into the catalyst activity loss, 20 mg of the catalyst following operation at room temperature, during which deactivation was essentially complete, were packed into the DRIFTS cell and exposed at 303 K and 1 bar to flowing C_2H_4 + H_2 at a molar ratio of 1:10. IR spectra recorded in separate experiments as the catalytic reaction proceeded (Figure 3A.7 in SI) show increasing intensities of peaks assigned to C−H vibrations (2970−2860 cm^{-1}), indicating carbonaceous deposits in the SAPO (and, in related work, in zeolite catalysts incorporating supported rhodium complexes[24]). We infer from the similar spectra that essentially the same carbonaceous deposits formed and interacted with the platinum centers, causing catalyst deactivation. Under these conditions, the initial CO peak observed at 2123 cm^{-1} declined in intensity during operation at a C_2H_4:H_2 molar ratio of 1:10, and the catalyst color changed from green to beige. After 24 h onstream, the reactants were purged from the cell with helium, and a CO pulse (50 mL(NTP)/min, 2390

CO molecules per platinum atom) was injected to provide IR evidence of whether the platinum nuclearity had changed. Figure 3A.8 in SI includes the ν_{CO} region of the spectrum, showing that the initial platinum species characterized by bands at 2123 and 2090 cm^{-1} (assigned to isolated platinum complexes and clusters, respectively) reappeared in greater intensity after the CO pulse. The results imply that the catalyst had begun to undergo aggregation under the catalytic reaction conditions (C_2H_4:H_2 molar ratio of 1:10), caused by the reduction by H_2.

The experiment was essentially repeated with the catalyst in the DRIFTS cell, but with D_2 instead of H_2, with a C_2H_4:D_2 ratio of 1:10. Again, during catalytic reaction, the Si−OH−Al groups of the SAPO-37 exchanged were replaced with Si−OD−Al groups. The rate of formation of Si−OD−Al groups under catalytic reaction conditions (C_2H_4:D_2 ratio of 1:10) was lower than that observed when pure D_2 flowed through the cell, corresponding to the lower D_2 partial pressure (165 vs. 35 min, when the Si−OD−Al absorbance stopped changing).

3.5 DISSCUSION

Reactivity of $Pt(acac)_2$ with Hydroxyl Groups of SAPO-37. When the precursor $Pt(acac)_2$ reacted with the Si-OH-Al Brønsted acid sites of SAPO-37, the platinum became bonded through Pt–O bonds, as shown by the decreased intensities of the ν_{OH} bands (Figure 3.1) and the EXAFS data indicating bonding of platinum atoms to light scatterer atoms such as support oxygen atoms (Table 3.1). The bond distances characterizing the SAPO- and analogous zeolite-supported species (Table 3.1) match, within error, reported values characterizing atomically dispersed platinum species on metal oxides—and give no evidence of Pt–Pt contributions—that is, no clusters (Figure 3.2a and Figure 3.5). The EXAFS data (Table 3.1) thus support the conclusion that the platinum in the initially prepared catalyst incorporated atomically dispersed platinum. Estimates of the formal oxidation states of platinum in the initial sample and following the various treatments based on the measured white line intensities and comparisons with reference compound data are summarized in Table 3A.1 in the SI and Figure 3.2b. The possibility

that the initial platinum (after the oxidation step in the synthesis) was Pt^{4+} is ruled out because white line of the initial supported platinum compared with that of PtO_2 is lower in intensity (Figure 3.2b). The lack of an observed Pt–Pt shell supports the inference of atomically dispersed platinum, which would be expected to be cationic.[61] The EXAFS data (Table 3.1) are consistent with an average structure in which each platinum atom is coordinated with four Pt–light scatterer atoms at an average distance of approximately 2 Å—in contrast to what would be expected for Pt^{4+} species with platinum coordinated to six oxygen atoms, at a bonding distance of about 2.0 Å.[39,42] The XANES data indicate a formal platinum oxidation state near +2 (but we realize that assignments of formal oxidation states on the basis of XANES data are limited in validity; for example, the suggestion of a linear relationship between platinum formal oxidation state and white line intensity is complicated by the dependence of the absorption probability on the density of states above the metal Fermi level as well as the platinum cluster size[15]).

In summary, the XANES, EXAFS, and IR data all point to the initial supported species as atomically dispersed platinum (after oxidation synthesis) is bonded near sites that were initially Si–OH–Al sites of SAPO-37 and coordinated to oxygen, whereby the support provides two oxygen ligands for each platinum atom. Equivalent statements pertain to a number of atomically dispersed metal complexes on zeolites, including zeolite HY. [40,62,63]

A remaining question is what ligands were bonded to the supported platinum in addition to the support. We postulate that the unidentified light scatterers could have been oxygen, with the results being similar to those reported for similarly treated atomically dispersed platinum on zeolites NaY,[41,42] NaX,[5] and CHA,[40] but the data are not sufficient to identify them. Ligands that might have be suggested to have formed on the atomically dispersed platinum in the oxidation step of the synthesis (Scheme 1 in the SI) could be postulated to be peroxo, OH, acac, and CO, but the IR spectra rule out acac and CO; a discussion of these possibilities is presented in the SI.

Reactivity of Platinum Complexes with CO. The IR spectra of Figure 3.3 give evidence of a mixture of platinum-containing species formed when CO reacts with the initial supported platinum complexes (after oxidation synthesis). By comparing the spectra with those of platinum species on various zeolites (H-MOR, NaY, NaX, ZSM-5), we infer that these bands indicate the presence of atomically dispersed platinum species.[34,38,49] However, because CO can be a reducing agent and might have reduced platinum from its initial cationic state at room temperature, we lack sufficient information to assign all the bands in the 2220–2090 cm^{-1} region (Figure 3.3). Further interpretation of the CO region along with a comparison of the XANES spectra would benefit from simulations, which are beyond the scope of this work.

Reactivity of Platinum Complexes with H_2. The XANES and EXAFS data (Figure 3.2, Table 3.1) showing that H_2 reacted with the SAPO-37-supported platinum species at room temperature to reduce the platinum and form clusters is broadly consistent with extensive literature demonstrating such behavior of platinum on numerous zeolite[40,65] and metal oxide supports.[66] IR spectra in the ν_{CO} region characterizing these clusters after exposure to CO (Figure 3A.4 in SI), consistent with the XANES and EXAFS data shown in Figure 3.2 and Table 3A.3 in the SI, agree well with data characterizing platinum clusters on H-MOR and on Al_2O_3, with a single ν_{CO} band near 2095 cm^{-1} assigned to CO ligands on platinum clusters.[64,67] Thus, we assign the 2090 cm^{-1} band (Figure 3A.4 in SI) to CO on these clusters.

The spectra of the SAPO-37 supported platinum clusters are characterized by significantly higher white line intensities than bulk platinum metal (Figure 3.2b and Figure 3.5a), indicating that the supported platinum species are small enough to have electronic properties significantly different from those of bulk platinum. This statement is consistent with the smallness of the clusters demonstrated by the EXAFS data.

Reactivity of Platinum Complexes with Ethylene. When the SAPO-supported platinum complexes were exposed to ethylene, a result of the ensuing reaction was a decrease in intensity of the

white line and a slight shift to higher energy (Figure 3.5a), accompanied by a decrease in magnitude of the Fourier transform at approximately 2.0 Å. However, there was no increase in the magnitude of the Fourier transform at approximately 2.7 Å. We suggest that the platinum adsorbed ethylene but did not form Pt–Pt bonds (clusters), but the data are not sufficient to determine the structures.

Reactivity of Platinum Complexes under Conditions of Ethylene Hydrogenation Catalysis. Under catalytic reaction conditions (with the sample in the presence of ethylene + H_2 or D_2), the ligands on the platinum changed, consistent with the change in conversion in the flow reactor. The occurrence of catalysis points to the incorporation of hydrogen and ethylene ligands on the platinum, suggesting replacement of the Pt–light-scatterer ligands. When D_2 was present, Si–OH–Al groups on the support were converted into Si–OD–Al groups, implying deuterium spillover and the formation of deuteride ligands on the platinum.[59,68] The formation of Si–OD–Al groups took longer when the ethylene + D_2 mixture was flowing than when just deuterium was flowing, consistent with a competition between ethylene and deuterium ligands on the platinum—deuteride ligands evidently reacted either to form deuterated ethane or Si–OD–Al groups.

After the initial break-in period during catalysis (Figure 3.4), when the ligands on platinum were evidently undergoing changes, the catalytic activity decreased, consistent with the catalyst color change and with the formation of relatively large, low-volatility organics bonded to the platinum and restricting access of reactive ethylene and hydrogen ligands (Figure 3A.7 in SI).

The data are not sufficient to determine whether deactivation was occurring during the break-in period when the data suggest that platinum clusters were forming. After about 24 h of operation, the formation of platinum clusters became evident, as shown by the increased intensity of the IR band at 2092 cm^{-1} assigned to CO on the clusters (Figure 3A.4, 3A.8, 3A.9 in SI), and the cluster formation occurred under both ethylene- and H_2-rich conditions (Figure 3A.10 in the SI), consistent with the role of H_2 as a reducing agent triggering the cluster formation. Bolstering the inference of platinum cluster

formation are the observed changes in the XANES white line intensity after exposure of the catalyst to reaction conditions; the EXAFS data of Figure 3.5b show the decrease in intensity of the contribution at 2.0 Å (indicating a loss of the Pt–O or Pt–C contribution) and the concomitant increase in intensity of the Pt–Pt contribution (at 2.7 Å) that confirms the cluster formation.

The cluster formation evidently started immediately upon exposure of the sample to H_2.[59,69] The data are consistent with results of Bus *et al.*,[59] who reported that when platinum clusters on Al_2O_3 were exposed to ethylene + H_2, their EXAFS results showed an increase in the Pt–Pt coordination number and a changed Pt–Pt bond distance attributed to (co)adsorbed hydrogen. But there is a lack of data characterizing the very first steps of platinum cluster formation on a support.

As summarized above, the data demonstrate that the clusters are catalytically active for ethylene hydrogenation, and there is no evidence that the initially present atomically dispersed platinum is active—although the data do not rule out the possibility. The only catalytic reaction product was ethane, so that there is no selectivity information for contrasting the isolated platinum sites and the platinum clusters—in contrast to what has been observed for supported rhodium[70] and supported iridium[71] catalysts.

This result is contrasted with observations for other noble metals on supports. For example, both atomically dispersed rhodium and rhodium clusters on HY zeolite catalyze ethylene hydrogenation,[38,70] and an equivalent statement pertains to iridium.[72] However, gold is evidently different; Guzman *et al.*[73] reported that MgO-supported mononuclear gold was active for ethylene hydrogenation and observed that gold clusters that formed under catalytic reaction conditions were inactive. Similar results were observed for hydrogenation of 1,3-butdiene.[74]

But observations for an oxidation reaction, CO oxidation, are markedly different from those characterizing olefin hydrogenation; Aguilar-Guerrero *et al.*[75] found that atomically dispersed gold on

CeO_2 catalyzed CO oxidation, but as gold clusters formed during catalysis, the activity increased, demonstrating that both species are active, with clusters being more active.[75]

3.6 CONCLUSIONS

IR and EXAFS spectra characterizing samples formed by the reaction of $Pt(acac)_2$ with SAPO-37 (after oxidation synthesis) show that the supported platinum was atomically dispersed, with each platinum atom initially bonded on average to two support oxygen atoms and other unidentified ligands. The atomically dispersed platinum rapidly transformed into clusters of only a few atoms each (with average diameters in the range of about 0.4–0.8 nm) upon exposure to H_2. These platinum clusters catalyzed ethylene hydrogenation with 100% selectivity at 303 K. Subsequent exposure of the clusters to ethylene led to their partial oxidative fragmentation, and these were stable at elevated temperatures. The data all support the conclusion that the clusters are the catalytically active species, with no evidence of catalytic activity by the atomically dispersed platinum. The results are the first to provide a detailed picture of the structures SAPO-37-supported metal complexes and clusters and show that the SAPO has properties markedly different from those of the isostructural HY zeolite.

3.7 ACKNOWLEDGEMENTS

J.T.H. thanks Hong-Xin Li and Phillip Connolly of Zeolyst for their interest and support of this industry-university collaboration. The work was supported by the U.S. Department of Energy (DOE), Office of Science, Basic Energy Sciences (BES), Grant DE-FG02-04ER15513. We thank Chevron for a fellowship supporting J.P.A. We gratefully acknowledge beam time at Beamlines 4-1 and 9-3 at the Stanford Synchrotron Radiation Lightsource, supported by the DOE Division of Materials Sciences under Contract DE-AC02-76SF00515 and by the Co-ACCESS program supported by the DOE BES Chemical Sciences, Geosciences, and Biosciences Division; we appreciate the help of Ryan Davis, Adam S. Hoffman, and Simon R. Bare at the synchrotron.

3.8 REFERENCES

(1) Naber, J. E.; de Jong, K. P.; Stork, W. H. J.; Kuipers, H. P. C. E.; Post, M. F. M. Industrial Applications of Zeolite Catalysis. *Stud. Surf. Sci. Catal.* **1994**, *84*, 2197–2219.

(2) Vermeiren, W.; Gilson, J. P. Impact of Zeolites on the Petroleum and Petrochemical Industry. *Top. Catal.* **2009**, *52*, 1131–1161.

(3) Robinson, P. R.; Hsu, C. S. *Practical Advances in Petroleum Processing*; Springer: New York, 2006; pp 564.

(4) Alvarez, F.; Ribeiro, F. R.; Perot, G.; Thomazeau, C.; Guisnet, M. Hydroisomerization and Hydrocracking of Alkanes. 7. Influence of the Balance between Acid and Hydrogenating Functions on the Transformation of *n*-Decane on PtHY Catalysts. *J. Catal.* **1996**, *162*, 179–189.

(5) Vajglová, Z.; Kumar, N.; Peurla, M.; Hupa, L.; Semikin, K.; Sladkovskiy, D. A.; Murzin, D. Y. Effect of the Preparation of Pt-Modified Zeolite Beta-Bentonite Extrudates on Their Catalytic Behavior in *n*-Hexane Hydroisomerization. *Ind. Eng. Chem. Res.* **2019**, *58*, 10875–10885.

(6) Gerasimov, D. N.; Fadeev, V. V.; Loginova, A. N.; Lysenko, S. V. Hydroisomerization of Long-Chain Paraffins: Mechanism and Catalysts. Part I. *Catal. Ind.* **2015**, *7*, 128–154.

(7) Steinberg, K. H.; Mroczek, U.; Roessner, F. Aromatization of Ethane on Platinum Containing ZSM-5 Zeolites. *Appl. Catal.* **1990**, *66*, 37–44.

(8) Perego, C.; Carati, A. *Zeolites: From Model Materials to Industrial Catalysts*; Transworld Research Network: India Kerala, 2008; pp 357–389.

(9) Li, H.-X.; Cormier, W. E.; Moden, B. Novel Metal-Containing Zeolite Beta for NO_X Reduction and Methods of Making the Same. US Patent Application 20190054420 A1, 2019.

(10) Wang, A.; Wang, Y.; Walter, E. D.; Kukkadapu, R. K.; Guo, Y.; Lu, G.; Weber, R. S.; Wang, Y.; Peden, C. H. F.; Gao, F. Catalytic N_2O Decomposition and Reduction by NH_3 over Fe/Beta and Fe/SSZ-13

Catalysts. *J. Catal.* **2018**, *358*, 199–210.

(11) M'Kombe, C. M.; Dry, M. E.; O'Connor, C. T. Influence of Preparation Variables on the Dispersion of Platinum on Zeolite KL. *Zeolites* **1997**, *19*, 175–179.

(12) Martens, J. A.; Verboekend, D.; Thomas, K.; Vanbutsele, G.; Pérez-Ramírez, J.; Gilson, J. P. Hydroisomerization and Hydrocracking of Linear and Multibranched Long Model Alkanes on Hierarchical Pt/ZSM-22 Zeolite. *Catal. Today* **2013**, *218–219*, 135–142.

(13) Chen, Y.; Ji, S.; Chen, C.; Peng, Q.; Wang, D.; Li, Y. Single-Atom Catalysts: Synthetic Strategies and Electrochemical Applications. *Joule* **2018**, *2*, 1242–1264.

(14) Liu, L.; Corma, A. Confining Isolated Atoms and Clusters in Crystalline Porous Materials for Catalysis. *Nat. Rev. Mater.* **2020,** 1− 20.

(15) DeRita, L.; Resasco, J.; Dai, S.; Boubnov, A.; Thang, H. V.; Hoffman, A. S.; Ro, I.; Graham, G. W.; Bare, S. R.; Pacchioni, G.; Pan, X.; Christopher, P. Structural Evolution of Atomically Dispersed Pt Catalysts Dictates Reactivity. *Nat. Mater.* **2019**, *18*, 746–751.

(16) Weitkamp, J.; Puppe, L. *Catalysis and Zeolites - Fundamentals and Applications*; Springer Berlin Heidelberg, 1999; pp 564.

(17) Gu, J.; Zhang, Z.; Hu, P.; Ding, L.; Xue, N.; Peng, L.; Guo, X.; Lin, M.; Ding, W. Platinum Nanoparticles Encapsulated in MFI Zeolite Crystals by a Two-Step Dry Gel Conversion Method as a Highly Selective Hydrogenation Catalyst. *ACS Catal.* **2015**, *5*, 6893–6901.

(18) Tamizhdurai, P.; Krishnan, P. S.; Ramesh, A.; Shanthi, K. Isomerization of Hydrocarbons over Pt Supported on Micro-Mesoporous ZSM-5. *Polyhedron* **2018**, *154*, 314–324.

(19) Kistler, J. D.; Chotigkrai, N.; Xu, P.; Enderle, B.; Praserthdam, P.; Chen, C. Y.; Browning, N. D.; Gates, B. C. A Single-Site Platinum CO Oxidation Catalyst in Zeolite KLTL: Microscopic and Spectroscopic Determination of the Locations of the Platinum Atoms. *Angew. Chem. Int. Ed.* **2014**, *53*, 8904–8907.

(20) Guo, J.; Ding, C.; Ma, Z.; Ma, L.; Wang, J.; Shangguan, J.; Yuan, Q.; Zhao, M.; Li, Y.; Wang, M.; Zhang, K. Highly Dispersed and Stable Pt Clusters Encapsulated within ZSM-5 with Aid of Sodium Ion for Partial Oxidation of Methane. *Fuel* **2021**, *289*, 119839.

(21) Liu, L.; Meira, D. M.; Arenal, R.; Concepcion, P.; Puga, A. V.; Corma, A. Determination of the Evolution of Heterogeneous Single Metal Atoms and Nanoclusters under Reaction Conditions: Which Are the Working Catalytic Sites? *ACS Catal.* **2019**, *9*, 10626–10639.

(22) Lok, B. M.; Messina, C. A.; Patton, R. L.; Gajek, R. T.; Cannan, T. R.; Flanigen, E. M. Silicoaluminophosphate Molecular Sieves: Another New Class of Microporous Crystalline Inorganic Solids. *J. Am. Chem. Soc.* **1984**, *106*, 6092–6093.

(23) Sierra de Saldarriaga, L. S.; Saldarriaga, C.; Davis, M. E. Investigations into the Nature of a Silicoaluminophosphate with the Faujasite Structure. *J. Am. Chem. Soc.* **1987**, *109*, 2686–2691.

(24) Perez-Aguilar, J. E.; Chen, C. Y.; Hughes, J. T.; Fang, C. Y.; Gates, B. C. Isostructural Atomically Dispersed Rhodium Catalysts Supported on SAPO-37 and on HY Zeolite. *J. Am. Chem. Soc.* **2020**, *142*, 11474–11485.

(25) Hong, S. B.; Mielczarski, E.; Davis, M. E. Aromatization of *N*-Hexane by Platinum-Containing Molecular Sieves I. Catalyst Preparation by the Vapor Phase Impregnation Method. *J. Catal.* **1992**, *134*, 349–358.

(26) Jacobs, G.; Ghadiali, F.; Pisanu, A.; Borgna, A.; Alvarez, W. E.; Resasco, D. E. Characterization of the Morphology of Pt Clusters Incorporated in a KL Zeolite by Vapor Phase and Incipient Wetness Impregnation. Influence of Pt Particle Morphology on Aromatization Activity and Deactivation. *Appl. Catal. A Gen.* **1999**, *188*, 79–98.

(27) Hoffman, A. S.; Debefve, L. M.; Bendjeriou-Sedjerari, A.; Ouldchikh, S.; Bare, S. R.; Basset, J. M.; Gates, B. C. Transmission and Fluorescence X-ray Absorption Spectroscopy Cell/Flow Reactor for Powder Samples under Vacuum or in Reactive Atmospheres. *Rev. Sci. Instrum.* **2016**, *87*, 073108.

(28) Hoffman, A. S.; Singh, J. A.; Bent, S. F.; Bare, S. R. In Situ Observation of Phase Changes of a Silica-Supported Cobalt Catalyst for the Fischer–Tropsch Process by the Development of a Synchrotron-Compatible in Situ/Operando Powder X-Ray Diffraction Cell. *J. Synchrotron Radiat.* **2018**, *25*, 1673–1682.

(29) Vaarkamp, M.; Linders, J. C.; Koningsberger, D. C. A New Method for Parameterization of Phase Shift and Backscattering Amplitude. *Phys. B Phys. Condens. Matter* **1995**, *208–209*, 159–160.

(30) Villars, P.; Calvert, L. D. *Pearson's Handbook of Crystallographic Data for Intermetallic Phases.*; Wiley: Metals Park, 1987.

(31) Ha, K. Crystal Structure of Bis(Pentane-2,4-Dionato-K^2O,O') Platinum(II), $Pt(C_5H_7O_2)_2$. *Z. Kristallogr. New Cryst. Struct.* **2011**, *226*, 329–330.

(32) Corma, A.; Fornés, V.; Franco, M. J.; Mocholí, F. A.; Pérez-Pariente, J. Hydrothermal Stability and Cracking Behavior of Silicoaluminophosphate Molecular Sieve-37 with Different Silicon Contents. *ACS Symp. Ser.* **1991**, *452*, 79–95.

(33) Dzwigaj, S.; Briend, M.; Shikholeslami, A.; Peltre, M. J.; Barthomeuf, D. The Acidic Properties of SAPO-37 Compared to Faujasites and SAPO-5. *Zeolites* **1990**, *10*, 157–162.

(34) Makarova, M. A.; Ojo, A. F.; Karim, K.; Hunger, M.; Dwyer, J. FTIR Study of Weak Hydrogen Bonding of Brönsted Hydroxyls in Zeolites and Aluminophosphates. *J. Phys. Chem.* **1994**, *98*, 3619–3623.

(35) Corma, A.; Fornes, V.; Pérez-Pariente, J. SAPO-37: The Implications of Structure Flexibility on Acidity. *J. Chem. Soc. Chem. Commun.* **1993**, No. 8, 676–678.

(36) Lin, L.; Zhang, X.; He, N.; Liu, J.; Xin, Q.; Guo, H. Operando Dual Beam FTIR Study of Hydroxyl Groups and Zn Species over Defective HZSM-5 Zeolite Supported Zinc Catalysts. *Catalysts* **2019**, *9*, 100.

(37) Halasz, I.; Moden, B.; Petushkov, A.; Liang, J. J.; Agarwal, M. Delicate Distinction between OH

Groups on Proton-Exchanged H-Chabazite and H-SAPO-34 Molecular Sieves. *J. Phys. Chem. C* **2015**, *119*, 24046–24055.

(38) Liang, A. J.; Gates, B. C. Time-Resolved Structural Characterization of Formation and Break-up of Rhodium Clusters Supported in Highly Dealuminated Y Zeolite. *J. Phys. Chem. C* **2008**, *112*, 18039–18049.

(39) Torigoe, K.; Remita, H.; Picq, G.; Belloni, J.; Bazin, D. Structural Characterization of Supported Platinum Carbonyl Clusters by X-ray Absorption Spectroscopy. *J. Phys. Chem. B* **2000**, *104*, 7050–7056.

(40) Moliner, M.; Gabay, J. E.; Kliewer, C. E.; Carr, R. T.; Guzman, J.; Casty, G. L.; Serna, P.; Corma, A. Reversible Transformation of Pt Nanoparticles into Single Atoms inside High-Silica Chabazite Zeolite. *J. Am. Chem. Soc.* **2016**, *138*, 15743–15750.

(41) Liu, Y.; Li, Z.; Yu, Q.; Chen, Y.; Chai, Z.; Zhao, G.; Liu, S.; Cheong, W. C.; Pan, Y.; Zhang, Q.; Gu, L.; Zheng, L.; Wang, Y.; Lu, Y.; Wang, D.; Chen, C.; Peng, Q.; et al. A General Strategy for Fabricating Isolated Single Metal Atomic Site Catalysts in y Zeolite. *J. Am. Chem. Soc.* **2019**, *141*, 9305–9311.

(42) Akdogan, Y.; Vogt, C.; Bauer, M.; Bertagnolli, H.; Giurgiu, L.; Roduner, E. Platinum Species in the Pores of NaX, NaY and NaA Zeolites Studied Using EPR, XAS and FTIR Spectroscopies. *Phys. Chem. Chem. Phys.* **2008**, *10*, 2952–2963.

(43) We infer that the CO present initially formed from the acac ligands in the $Pt(acac)_2$ precursor. Similar to reports of work with supported species formed from $Rh(C_2H_4)_2(acac)$, we suggest that the SAPO OH groups might have reacted with the surface acac species, leading to the formation of acetates on the support and acetone in the gas phase. The small amount of acetone supposedly generated in-situ could then undergo decomposition on the platinum similar to that of reported to occur on rhodium to form a small amount of CO bonded to the platinum. Any gas-phase products such as acetone were evidently formed in amounts too low for detection with

our on-line mass spectrometer.

(44) Bhirud, V. A.; Ehresmann, J. O.; Kletnieks, P. W.; Haw, J. F.; Gates, B. C. Rhodium Complex with Ethylene Ligands Supported on Highly Dehydroxylated MgO: Synthesis, Characterization, and Reactivity. *Langmuir* **2006**, *22*, 490–496.

(45) Anderson, J. A.; Rochester, C. H. Infrared Study of the Adsorption of Acetone, Acrolein, Ethanoic Acid and Propene-NO Mixtures on Rh/Al_2O_3 Catalysts. *J. Chem. Soc. Faraday Trans. 1* **1989**, *85*, 1117–1128.

(46) Ding, K.; Gulec, A.; Johnson, A. M.; Schweitzer, N. M.; Stucky, G. D.; Marks, L. D.; Stair, P. C. Identification of Active Sites in CO Oxidation and Water-Gas Shift over Supported Pt Catalysts. *Science.* **2015**, *350*, 189–192.

(47) Chakarova, K.; Mihaylov, M.; Hadjiivanov, K. FTIR Spectroscopic Study of CO Adsorption on Pt-H-ZSM-5. *Micropor.Mesopor.Mater.* **2005**, *81*, 305–312.

(48) Aleksandrov, H. A.; Neyman, K. M.; Hadjiivanov, K. I.; Vayssilov, G. N. Can the State of Platinum Species Be Unambiguously Determined by the Stretching Frequency of an Adsorbed CO Probe Molecule? *Phys. Chem. Chem. Phys.* **2016**, *18*, 22108–22121.

(49) Hadjiivanov, K. I.; Vayssilov, G. N. Characterization of Oxide Surfaces and Zeolites by Carbon Monoxide as an IR Probe Molecule. *Adv. Catal.* **2002**, *47*, 307–511.

(50) Conner, W. C.; Falconer, J. L. Spillover in Heterogeneous Catalysis. *Chem. Rev.* **1995**, *95*, 759–788.

(51) Bettahar, M. M. The Hydrogen Spillover Effect. A Misunderstanding Story. *Catal. Rev. Sci. Eng.* **2020**, 1–39.

(52) Serna, P.; Gates, B. C. A Bifunctional Mechanism for Ethene Dimerization: Catalysis by Rhodium Complexes on Zeolite HY in the Absence of Halides. *Angew. Chem.Int. Ed.* **2011**, *50*, 5528–5531.

(53) Martinez-Macias, C.; Serna, P.; Gates, B. C. Isostructural Zeolite-Supported Rhodium and Iridium Complexes: Tuning Catalytic Activity and Selectivity by Ligand Modification. *ACS Catal.* **2015**, *5*,

5647–5656.

(54) Rioux, R. M.; Song, H.; Hoefelmeyer, J. D.; Yang, P.; Somorjai, G. A. High-Surface-Area Catalyst Design: Synthesis, Characterization, and Reaction Studies of Platinum Nanoparticles in Mesoporous SBA-15 Silica. *J. Phys. Chem. B* **2005**, *109*, 2192–2202.

(55) Gallezot, P. The State and Catalytic Properties of Platinum and Palladium in Faujasite-Type Zeolites. *Catal. Rev.* **1979**, *20*, 121–154.

(56) Uzun, A.; Gates, B. C. Dynamic Structural Changes in a Molecular Zeolite-Supported Iridium Catalyst for Ethene Hydrogenation. *J. Am. Chem. Soc.* **2009**, *131*, 15887–15894.

(57) Uzun, A.; Gates, B. C. Dynamic Structural Changes in a Molecular Zeolite-Supported Iridium Catalyst for Ethene Hydrogenation. *J. Am. Chem. Soc.* **2009**, *131*, 15887–15894.

(58) Serna, P.; Gates, B. C. Zeolite- and MgO-Supported Rhodium Complexes and Rhodium Clusters: Tuning Catalytic Properties to Control Carbon-Carbon vs. Carbon-Hydrogen Bond Formation Reactions of Ethene in the Presence of H_2. *J. Catal.* **2013**, *308*, 201–212.

(59) Bus, E.; Ramaker, D. E.; Van Bokhoven, J. A. Structure of Ethene Adsorption Sites on Supported Metal Catalysts from in Situ XANES Analysis. *J. Am. Chem. Soc.* **2007**, *129*, 8094–8102.

(60) Uzun, A.; Gates, B. C. Real-Time Characterization of Formation and Breakup of Iridium Clusters in Highly Dealuminated Zeolite Y. *Angew. Chem. Int. Ed.* **2008**, *47*, 9245–9248.

(61) Tzou, M. S.; Teo, B. K.; Sachtler, W. M. H. Formation of Pt Particles in Y-Type Zeolites. *J. Catal.* **1988**, *235*, 220–235.

(62) DeRita, L.; Resasco, J.; Dai, S.; Boubnov, A.; Thang, H. V.; Hoffman, A. S.; Ro, I.; Graham, G. W.; Bare, S. R.; Pacchioni, G.; Pan, X.; Christopher, P. Structural Evolution of Atomically Dispersed Pt Catalysts Dictates Reactivity. *Nat. Mater.* **2019**, *18*, 746–751.

(63) Tzou, M. S.; Teo, B. K.; Sachtler, W. M. H. Formation of Pt Particles in Y-Type Zeolites. The Influence of Coexchanged Metal Cations. *J. Catal.* **1988**, *113*, 220–235.

(64) Zholobenko, V. L.; Lei, G. D.; Carvill, B. T.; Lerner, B. A.; Sachtler, W. M. H. Identification of Isolated Pt Atoms in H-Mordenite. *J. Chem. Soc. Faraday Trans.* **1994**, *90*, 233–238.

(65) De Graaf, J.; Van Dillen, A. J.; De Jong, K. P.; Koningsberger, D. C. Preparation of Highly Dispersed Pt Particles in Zeolite Y with a Narrow Particle Size Distribution: Characterization by Hydrogen Chemisorption, TEM, EXAFS Spectroscopy, and Particle Modeling. *J. Catal.* **2001**, *203*, 307–321.

(66) Resasco, J.; Derita, L.; Dai, S.; Chada, J. P.; Xu, M.; Yan, X.; Finzel, J.; Hanukovich, S.; Hoffman, A. S.; Graham, G. W.; Bare, S. R.; Pan, X.; Christopher, P. Uniformity Is Key in Defining Structure-Function Relationships for Atomically Dispersed Metal Catalysts: The Case of Pt/CeO_2. *J. Am. Chem. Soc.* **2020**, *142*, 169–184.

(67) Mendes, P. S. F.; Gregório, A. F. C.; Daudin, A.; Bouchy, C.; Silva, J. M.; Ribeiro, M. F. Elucidation of the Zeolite Role on the Hydrogenating Activity of Pt-Catalysts. *Catal. Commun.* **2017**, *89*, 152–155.

(68) Karim, W.; Spreafico, C.; Kleibert, A.; Gobrecht, J.; Vandevondele, J.; Ekinci, Y.; Van Bokhoven, J. A. Catalyst Support Effects on Hydrogen Spillover. *Nature* **2017**, *541*, 68–71.

(69) Dessal, C.; Len, T.; Morfin, F.; Rousset, J. L.; Aouine, M.; Afanasiev, P.; Piccolo, L. Dynamics of Single Pt Atoms on Alumina during CO Oxidation Monitored by Operando X-ray and Infrared Spectroscopies. *ACS Catal.* **2019**, *9*, 5752–5759.

(70) Yang, D.; Xu, P.; Browning, N. D.; Gates, B. C. Tracking Rh Atoms in Zeolite HY: First Steps of Metal Cluster Formation and Influence of Metal Nuclearity on Catalysis of Ethylene Hydrogenation and Ethylene Dimerization. *J. Phys. Chem. Lett.* **2016**, *7*, 2537–2543.

(71) Lu, J.; Serna, P.; Aydin, C.; Browning, N. D.; Gates, B. C. Supported Molecular Iridium Catalysts: Resolving Effects of Metal Nuclearity and Supports as Ligands. *J. Am. Chem. Soc.* **2011**, *133*, 16186–16195.

(72) Lu, J.; Aydin, C.; Browning, N. D.; Gates, B. C. Hydrogen Activation and Metal Hydride Formation

Trigger Cluster Formation from Supported Iridium Complexes. *J. Am. Chem. Soc.* **2012**, *134*, 5022–5025.

(73) Guzman, J.; Gates, B. C. Structure and Reactivity of a Mononuclear Gold- Complex Catalyst Supported on Magnesium Oxide. *Angew. Chem. Int. Ed.* **2003**, *42*, 2001–2004.

(74) Zhang, X.; Shi, H.; Xu, B. Q. Catalysis by Gold: Isolated Surface Au^{3+} Ions Are Active Sites for Selective Hydrogenation of 1,3-Butadiene over Au/ZrO_2 Catalysts. *Angew. Chem. Int. Ed.* **2005**, *44*, 7132–7135.

(75) Aguilar-Guerrero, V.; Lobo-Lapidus, R. J.; Gates, B. C. Genesis of a Cerium Oxide Supported Gold Catalyst for Co Oxidation: Transformation of Mononuclear Gold Complexes into Clusters as Characterized by X-ray Absorption Spectroscopy. *J. Phys. Chem. C* **2009**, *113*, 3259–3269.

Chapter 3A

SUPPORTING INFORMATION

for

Atomically Dispersed Platinum in SAPO-37: Catalysis of Ethylene Hydrogenation and Transformation into Platinum Clusters[1]

[1] This chapter has been submitted to *ACS Catalysis* by J. E. Perez-Aguilar, J. T. Hughes, C.-Y. Chen, and B. C. Gates. The original manuscript has been reformatted to fit the requirements of the dissertation

SUPPORTING INFORMATION

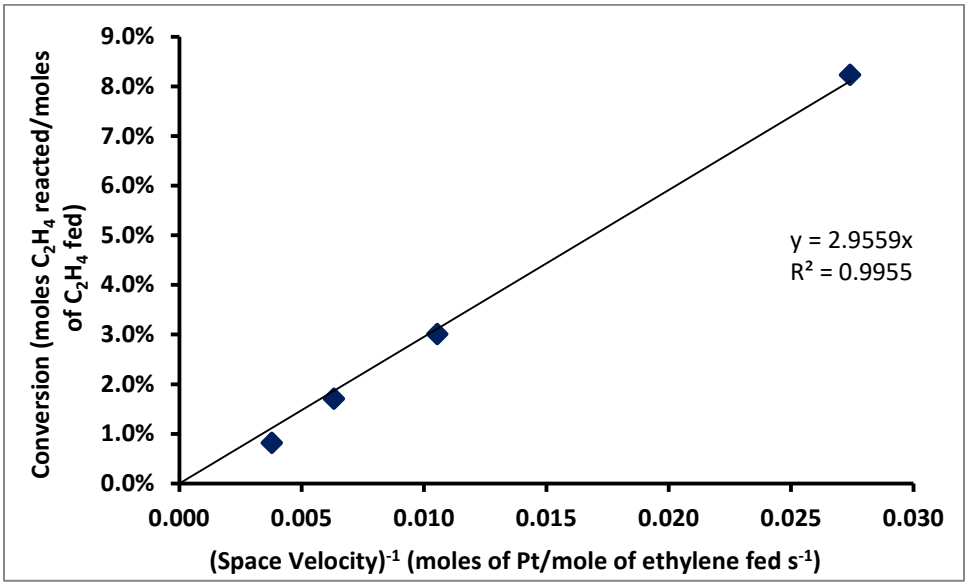

Figure 3A.1. Differential conversion of ethylene; the catalyst was initially present as platinum complexes supported on SAPO-37. Reaction conditions: H_2 + C_2H_4 at 10:1 molar ratio at 303 K at atmospheric pressure. The linearity of this plot that passes through the origin demonstrates that the data determine rates (TOF values) directly as the slope of the line.

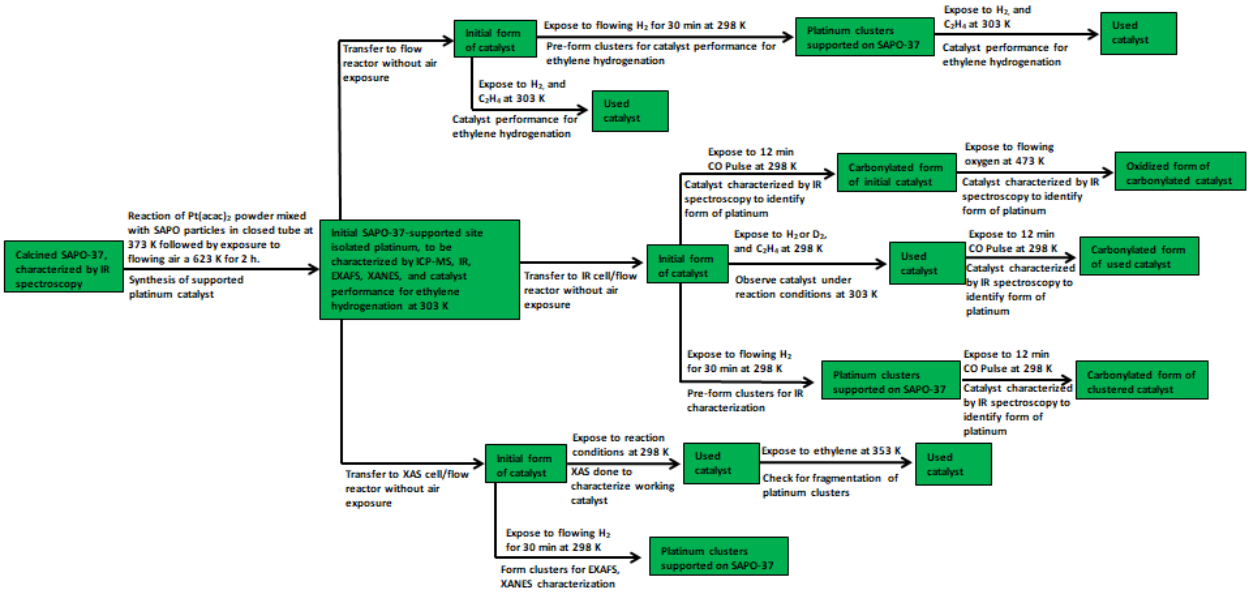

Scheme 1. Summary of treatment steps and methods of characterization of SAPO-37-supported platinum.

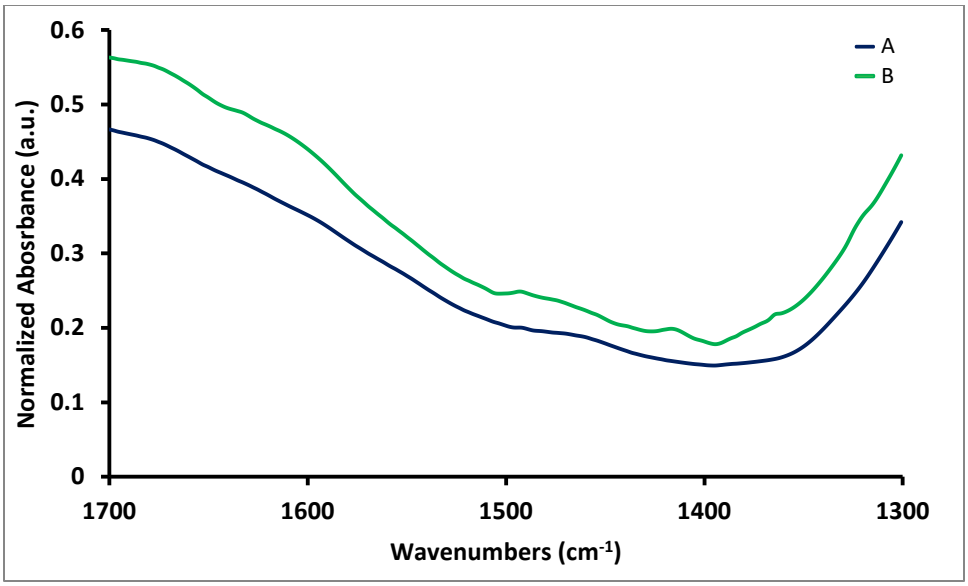

Figure 3A.2. IR spectra in the 1300–1700 cm^{-1} region characterizing the following samples: **A,** bare calcined SAPO-37; **B**, sample formed by reaction of SAPO-37 with $Pt(acac)_2$.

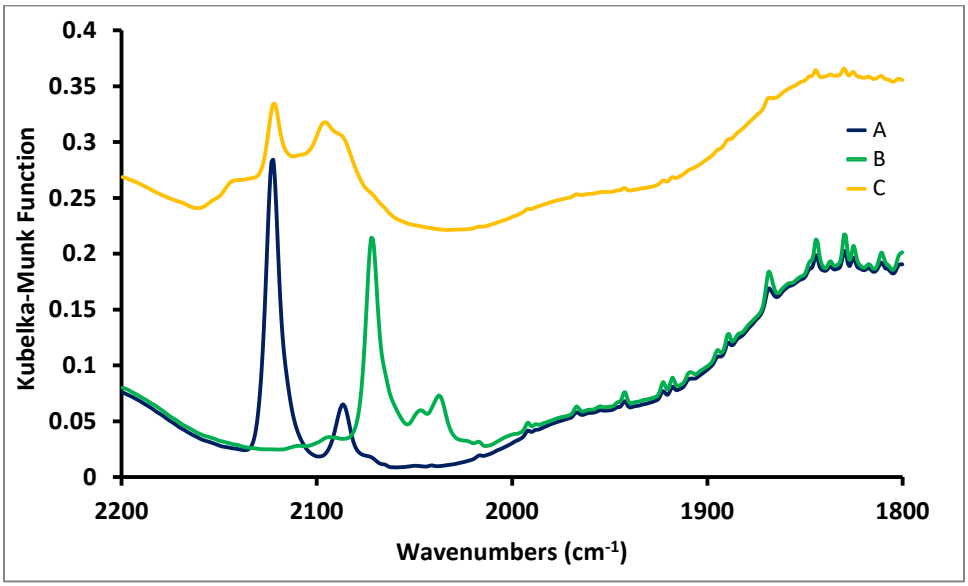

Figure 3A.3. DRIFTS spectra in the CO region of species formed by adsorption of isolated platinum on SAPO-37 after treatments. Spectrum **A** was recorded with the sample in contact with flowing helium (50 mL(NTP)/min), and Spectrum **B** is of the same sample in helium after it had been in contact with a 2 min pulse of ^{13}CO. Spectrum **C** is of the same sample under helium after a ^{12}CO pulse.

Bands at 2123 and 2090 cm^{-1} decreased in intensity while the bands at 2071 and 2039 cm^{-1} grew in as the ^{13}CO reacted with the sample (Figure 3A.3). The ratio of frequencies of ^{12}CO and ^{13}CO corresponds to the harmonic approximation.[1] Thus, bands at 2123 and 2088 cm^{-1} indicate the presence of CO on

platinum species in different locations and/or oxidation states, with the inferencebased on reported results characterizing platinum species on various zeolites,[2–4] and the shifts to 2071 and 2039 cm^{-1} confirm that ^{13}CO replaced ^{12}CO.[5] After a single ^{12}CO pulse to the same sample, the exchange to the initial CO bands was not reversed.

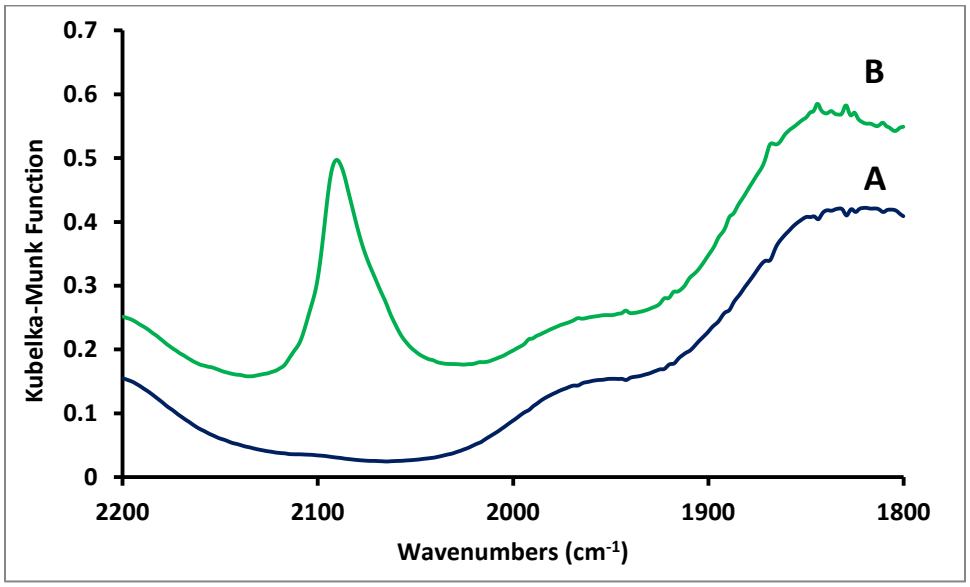

Figure 3A.4. DRIFTS spectra characterizing catalyst: **A**, SAPO-37 supported platinum complexes in flowing helium (50 mL(NTP)/min) at room temperature; **B**, same sample in helium(50 mL(NTP)/min) after a 12 minute CO(50 mL(NTP)/min) pulse and a 30 minute H_2 (50 mL(NTP)/min) treatment at room temperature.

Figure 3A.4 displays a single band as 2092 cm^{-1} that is expected for CO on platinum clusters.[2] EXAFS data given in Table 3A.4 confirms the platinum clusters formed.

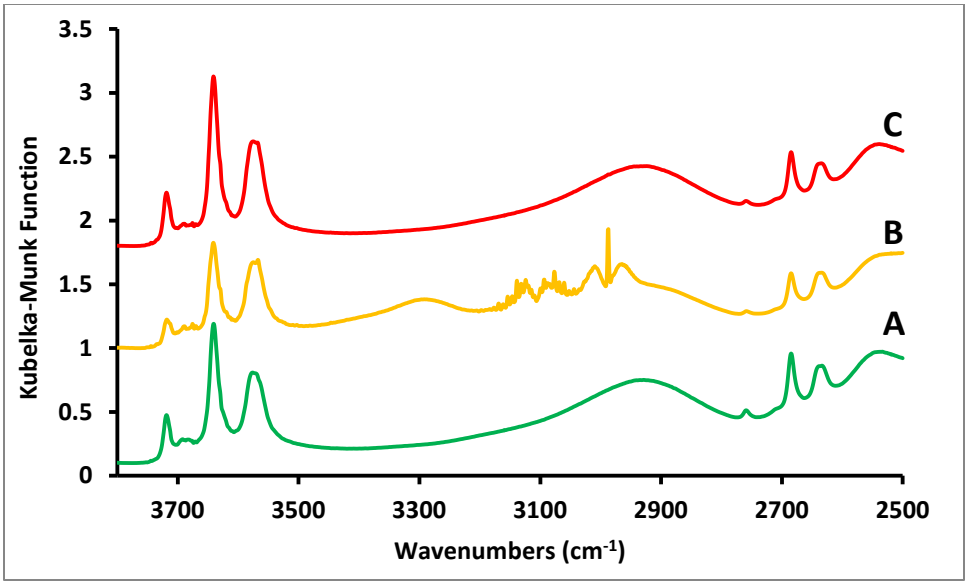

Figure 3A.5. DRIFTS spectra in the ν_{OH} and ν_{OD} regions characterizing (**A**) Platinum complexes on SAPO-37 in flowing D_2 and He (10 and 50 mL(NTP) min^{-1}) at 298 K and 1 bar, (**B**) the same sample in flowing C_2H_4 and He (10 and 50 mL(NTP) min^{-1}), (**C**) the same sample in flowing He (50 mL(NTP) min^{-1}). The broad peak in spectrum **B** (at 3300 cm^{-1}) is assigned to either the extra-framework silica (3718 cm^{-1}) or the Si–OH–Al Brønsted acid sites (3640 cm^{-1}) interacting with absorbed ethylene, consistent with data characterizing the silanols or Brønsted acid sites on HZSM-5 zeolite shifting to 3300 cm^{-1} when ethylene is absorbed.[6]

Figure 3A.5 displays the SAPO-37-supported platinum complexes after exposure to D_2 where the sample formed OD groups. This sample was then subsequently exposed to ethylene and a spectrum B shows that ethylene adsorbed on the OD and OH groups, when the reactor was purged with helium, the ethylene desorbed, as shown by the full recovery of the OH and OD band intensities.

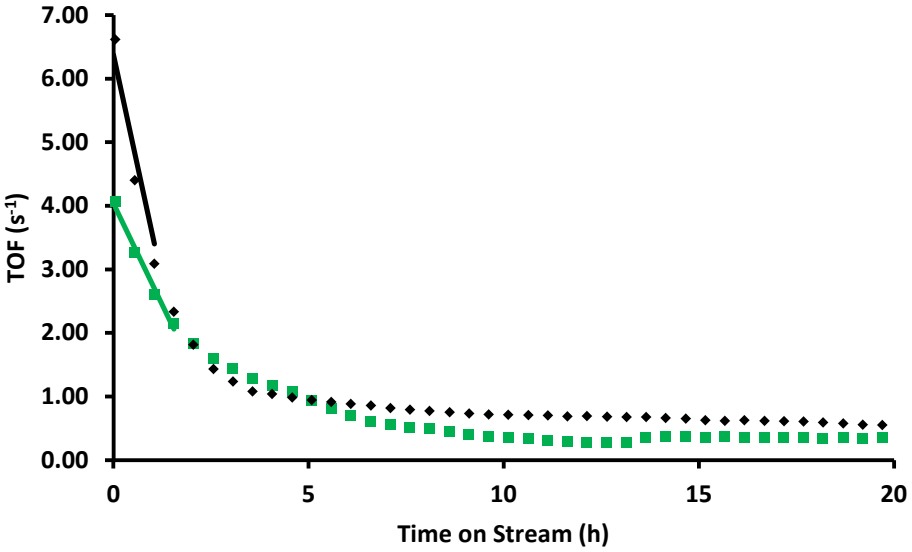

Figure 3A.6. Comparison of platinum supported SAPO-37 for ethylene conversion: performance of 1.4 ± 0.2 wt% platinum supported on SAPO-37 initially present as platinum clusters or atomically dispersed platinum for ethylene conversion catalysis in a once-through plug-flow reactor in the presence of H_2 at 303 K and 1 bar (molar H_2:C_2H_4 ratio = 4:1). The catalyst samples (in their initial forms) are identified by symbols shown in the figure: black ◆, SAPO-37-supported platinum clusters (molar H_2:C_2H_4 ratio = 1:10); green ■, atomically dispersed platinum supported on SAPO-37.

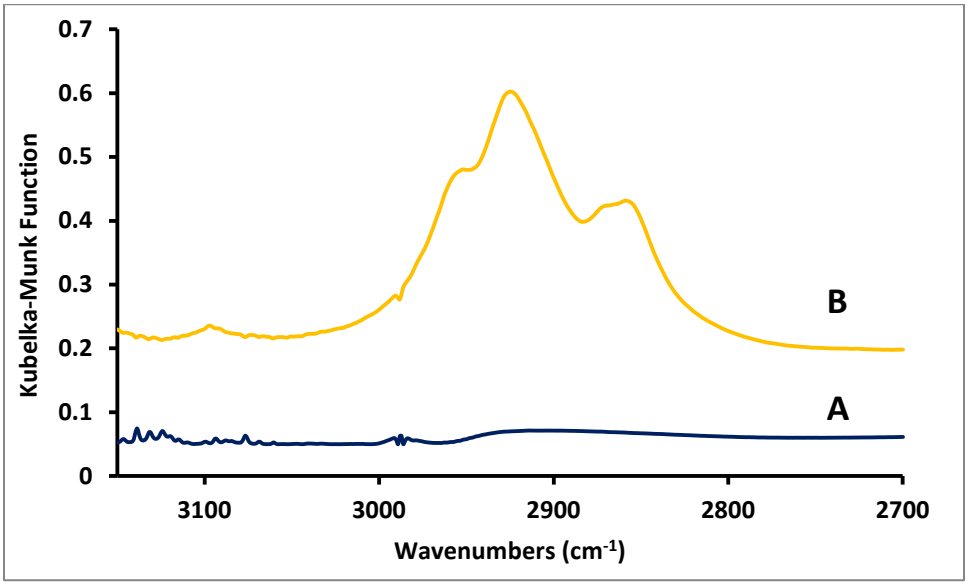

Figure 3A.7. DRIFTS spectra characterizing catalyst: **A**, SAPO-37 supported platinum complexes in flowing helium (50 mL(NTP)/min) at room temperature; **B**, same sample under reaction conditions (flow rates of 10 mL(NTP)/min of C_2H_4 and of H_2, and 90 mL(NTP)/min of helium) after 25 h in contact with flowing reactants at 303 K.

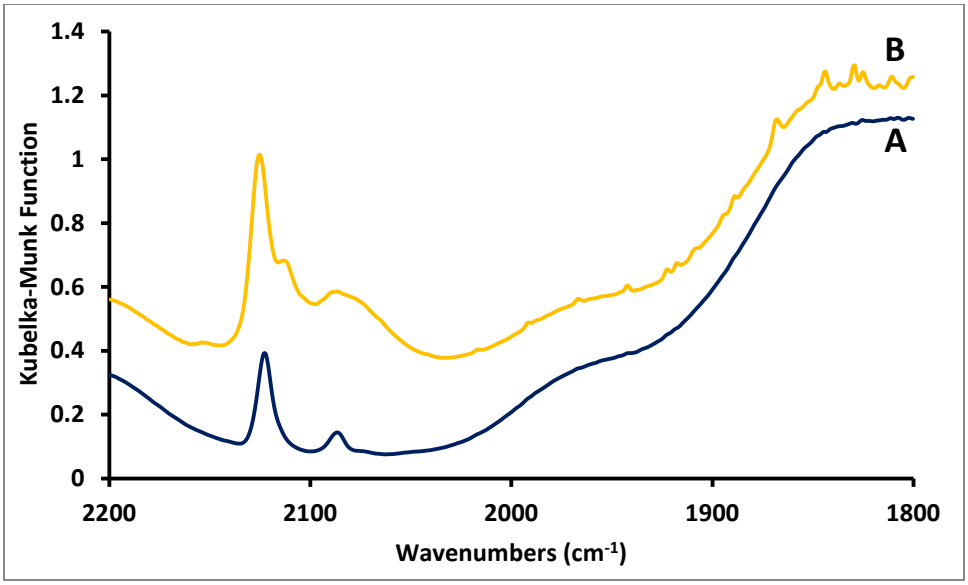

Figure 3A.8. DRIFTS spectra characterizing catalyst: **A**, SAPO-37 supported platinum complexes in flowing helium (50 mL(NTP)/min) at room temperature; **B**, same sample in flowing helium after a 12 min pulse of 10% CO in helium (50 mL(NTP)/min) and 24 h exposure of reactants at 303 K (4 and 40 mL(NTP)/min of C_2H_4 and H_2, and 56 mL(NTP)/min of helium.

Figure 3A.8 displays a change in the CO peaks after 24 h exposure to reaction conditions. There is an increase in intensity of the 2092 cm^{-1} peak that has been assigned to platinum clusters on SAPO-37.

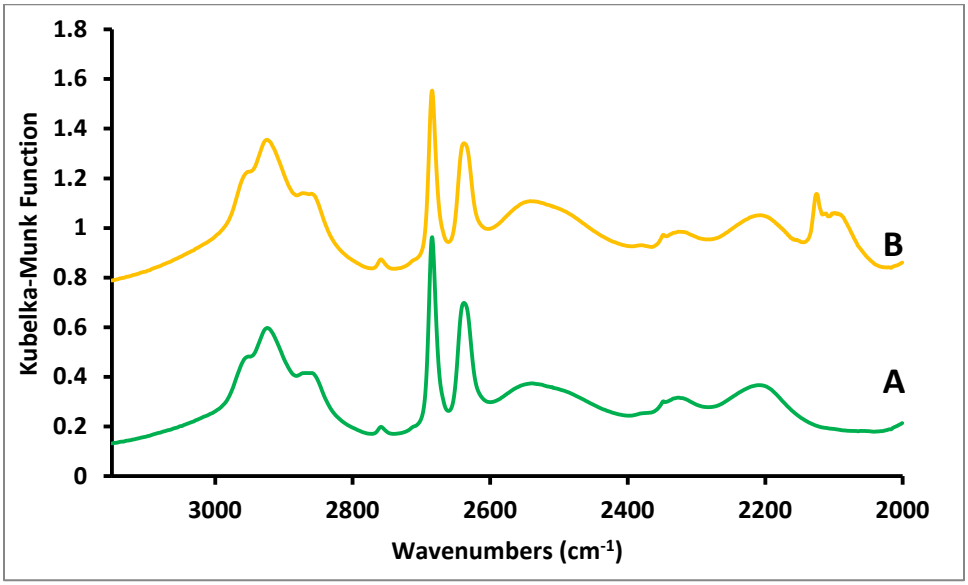

Figure 3A.9. DRIFTS spectra characterizing catalyst: **A**, SAPO-37 supported platinum complexes in flowing helium (50 mL(NTP)/min) at room temperature after a 24 h exposure of reactants at 303 K (2 and 20 mL(NTP)/min of C_2H_4 and D_2, and 78 mL(NTP)/min of helium; **B**, same sample in flowing helium after a 12 min pulse of 10% CO in helium (50 mL(NTP)/min). Bands at 2970−2860 cm^{-1} are assigned to C−H vibrations to carbonaceous deposits, as before.[7]

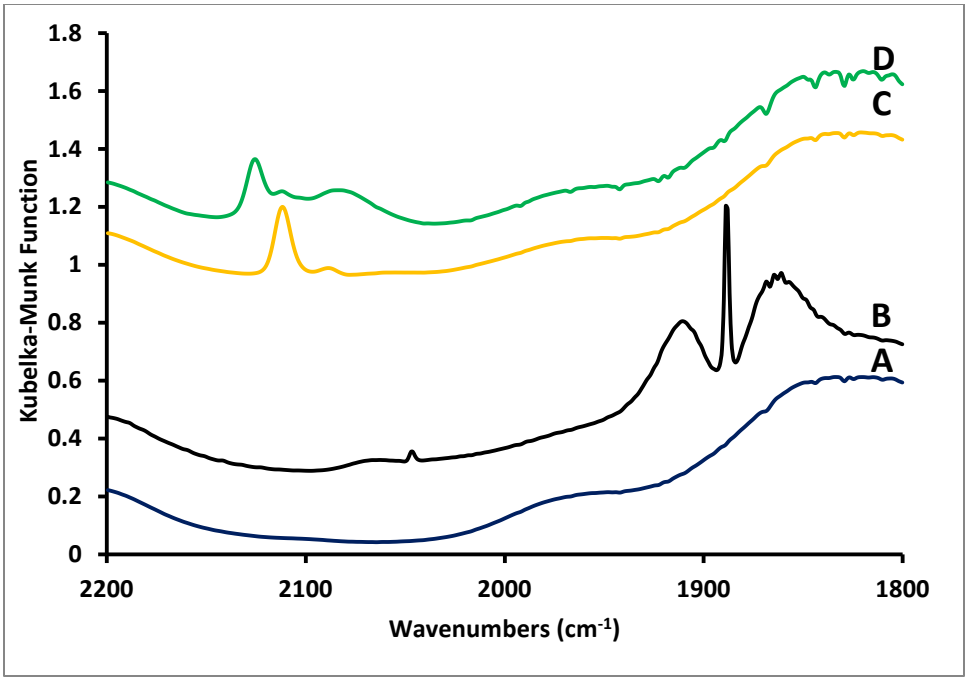

Figure 3A.10. DRIFTS spectra characterizing catalyst: **A**, SAPO-37 supported platinum complexes in flowing helium (50 mL(NTP)/min) at room temperature; **B** after a 24 h exposure of reactants at 303 K (40 and 4 mL(NTP)/min of C_2H_4 and H_2, and 56 mL(NTP)/min of helium; **C**, same sample in flowing helium; **D**, the same sample in flowing helium after a 12 min pulse of 10% CO in helium (50 mL(NTP)/min).

Table 3A.1. Oxidation state estimation based on XAS white line intensities. Correspondence between white line intensity and oxidation state made based on reference compounds of known oxidation state. This relationship was used to estimate oxidation states for Pt/SAPO-37 following exposure to ethylene and reaction conditions.

Reference compound	**Normalized white line height, arbitrary units**	**Formal Pt oxidation state**
PtO_2	2.27	4
$Pt(acac)_2$	1.67	2
Pt foil	1.20	0
	Normalized white line height	**Estimated Pt oxidation state**
Pt/SAPO-37, 1.4 ± 0.2 wt%	1.74	2.2
Pt/SAPO-37, 1.4 ± 0.2 wt% platinum, after exposure to H_2 for 30 min	1.35	0.6

Ligands that might have been formed on the supported atomically dispersed platinum in the oxidation step of the synthesis could be thought to be acac ligands, but that this possibility is ruled out, as follows: The IR spectra (Figure 3A.2) indicate the complete removal of the acac ligands present in the

precursor $Pt(acac)_2$ during the synthesis (including oxidation) at 623 K. Similar results were observed by Guzman *et al.*,[8] who found that temperatures above 573 K were needed for total removal of the acac ligands on from alumina-supported atomically dispersed gold made from $Au(CH_3)_2(acac)$.[8]

The ligands might also be thought to be peroxo ligands, but the XANES data weigh against this possibility, showing that the average platinum oxidation state was only slightly greater than +2 and not +4, which is common for platinum-group metal peroxo species.[9,10]

One might also suggest that CO ligands formed from the acac ligands during oxidation were present on the Pt, but the IR data rule out this possibility: in Spectrum A of Figure 3A.4, it is evident that there are no bands characterizing platinum carbonyls.

One might also suggest that OH ligands from the support migrated onto the Pt, but one would expect them to be more strongly bonded to the Al sites on the SAPO than to the platinum because of the negative formal charge of the alumina tetrahedra.

In summary, on the basis of our IR, XANES, and EXAFS data, we postulate that each platinum atom, on average, was bonded to two oxygen ligands of the SAPO support and to two other light scatterers, which could have been oxygen, but the data are not sufficient to identify these ligands.

Table 3A.2. Examples of CO bonded to platinum species including IR band locations in the ν_{CO} region.

Initial form of catalyst	IR bands of carbonylated form of various platinum oxidation states, ν_{CO} (cm^{-1})								Refs
	$Pt^0(CO)$	$Pt^{\delta+}(CO)$	$Pt^+(CO)_2$	$Pt^+(CO)_3$	$Pt^{2+}(CO)$	$Pt^{2+}(CO)_2$	$Pt^{3+}(CO)$	$Pt^{3+}(CO)_2$	
1.1 ± 0.1 wt % Pt/SAPO-37					2123				this work
1.1 ± 0.1 wt % Pt/SAPO-37, after exposure to H_2 for 30 min		2092							this work
PtO_x/KLTL zeolite (oxidized)	–[a]	–[a]	–[a]	–[a]	2100	–[a]	–[a]	–[a]	11
3.0 wt% Pt/H-ZSM-5	–[a]	–[a]	2120, 2091	2162, 2150, 2110	2113	2165, 2150	2195	2211, 2175, or 2195	3
0.5 wt% Pt/H-mordenite	2123	–[a]	–[a]	–[a]	–[a]	–[a]	–[a]	–[a]	12
4.0 wt% Pt/NaY zeolite	–[a]	–[a]	–[a]	–[a]	2110	–[a]	–[a]	–[a]	13
0.2 wt% Pt/NaY zeolite	–[a]	2116	–[a]	–[a]	–[a]	–[a]	–[a]	–[a]	14
6 wt% Pt/NaY zeolite	–[a]	2100-2120	–[a]	–[a]	–[a]	–[a]	–[a]	–[a]	4
6 wt% Pt/NaX z	2069	–[a]	2120, 2091	–[a]	2106	–[a]	2200	2216, 2188	4

[a]Not reported.

Table 3A.3 below shows the change of the isolated platinum species (initial species) supported on SAPO-37 under helium as they were exposed to ethylene, ethylene and hydrogen (reaction conditions), ethylene at 353 K, and lastly helium.

Table 3A.3. Summary of EXAFS fits parameters characterizing the structure of isolated platinum complexes supported on SAPO-37 at the Pt L_3 edge as the feed composition is varied at room temperature and atmospheric pressure. *Denotes best fit model.

C_2H_4/H_2/He (molar ratio)	Model	Shell	N^a	$10^3 \times \Delta\sigma^2$ ($Å^2$)[a]	R (Å)[a]	ΔE_0 (eV)[a]	Goodness of Fit	Notes
0:0:1	1*	O_s	4.0	5.9	2.02	-8.0	1.9876	Figure 3A.11 to 3A.13; *k* range was from 5.0 to 13.0 Å; Error = 0.00063.
		O	2.0	2.4	2.29	-1.0		
		Al	1.0	1.8	2.70	-8.0		
		O_l	2.5	5.0	2.99	2.8		
	2	O_s	4	9.1	2.02	-8.0	2.4893	
		O	3	2.1	2.30	-4.0		
		Al	1.1	1.9	2.70	-10.0		
		O_l	2.4	4.8	3.00	1.0		
	3	O_s	4.0	2.6	2.02	-8.0	2.0500	
		O	2.1	5.3	2.30	-3.5		
		P	1.0	2.6	2.67	2.8		
		O_l	2.5	5.5	3.00	1.0		
1:10:1.5	1*	C	1.1	4.0	1.97	3.0	2.3616	Figure 3A.14; *k* range was from 3.0 to 10.0 Å; Error = 0.00174.
		O	1.6	5.0	2.12	-5.0		
		Pt	1.8	7.6	2.70	1.0		
1:10:1.5	1*	C	0.4	4.0	2.20	-1.8	1.3635	Figure 3A.15 to 3A.17; *k* range was from 3.5 to 11.0 Å; Error = 0.00094.
		Pt	2.7	8.1	2.74	-2.5		
		O_l	1.5	4.0	2.97	-8.0		
	2	O	0.3	5.2	2.17	-8.0	1.5241	
		Pt	2.7	8.1	2.74	-4.0		
		O_l	1.5	3.7	2.97	-10.0		
	3	C	0.5	4.4	2.22	-4.6	1.4440	
		Pt	3.0	9.4	2.74	-3.5		
		C_l	1.1	3.8	2.78	-2.0		
		O_l	1.7	4.0	2.98	1.9		
1:0:1.5	1*	C	1.0	4.5	2.21	-8.0	2.1113	Figure 3A.18 to 3A.20; *k* range was from 4.0 to 10.8 Å; Error = 0.00089.
		Pt	1.6	3.4	2.64	8.0		
		O_l	2.0	4.0	3.0	6.0		
		C_l	1.6	3.1	3.4	0.5		
	2	C	1.2	5.0	2.21	-8.0	2.8148	
		Pt	1.4	3.4	2.64	8.0		
		O_l	2.0	4.2	3.00	5.0		
		O_l	1.0	3.2	3.39	1.5		
	3	C	1.0	4.7	2.20	-6.0	2.5405	
		Pt	2.0	5.4	2.62	8.0		

		C_l	2.0	4.2	2.99	7.5		
		O_l	1.0	4.7	3.40	2.0		
0:0:1	1*	C	0.9	5.0	2.19	-8.0	0.88204	Figure 3A.21; *k* range was from 4.0 to 11.0 Å; Error = 0.00131.
		Pt	1.9	6.0	2.61	8.0		
		O_s	2.9	4.8	2.98	7.0		
		O_l	1.2	4.0	3.31	6.0		

[a]Notation: *N*, coordination number; *R*, distance between absorber and backscatter atoms; $\Delta\sigma^2$, Debye-Waller/disorder term; ΔE_0, inner potential. Subscripts: S, refers to an atom identified to be belonging to a short distance L, refers to the long contribution of an atom in the support.

Table 3A.4. EXAFS models representing the data at the Pt L3 edge characterizing 1.1 ± 0.1 wt% platinum supported on SAPO-37 after exposure to hydrogen for 30 min at 298 K. The range in *k* was from 3.5 to 10.5 Å; error = 0.00075; *Denotes best fit model.

$C_2H_4/H_2/He$ (molar ratio)	Model	Shell	N^a	10^3 x $\Delta\sigma^2$ ($Å^2$)[a]	R (Å)[a]	ΔE_0 (eV)[a]	Goodness of Fit	Notes
0:0:1	1	O_s	1.0	9.0	2.02	-7.0	2.3760	Figure 3A.22 to 3A.24.
		Pt	4.9	14.3	2.71	-8.0		
		O_l	1.0	4.7	3.44	-5.5		
		Al	1.1	9.3	3.94	-1.0		
	2*	O_s	1.0	11.8	2.03	-8.0	3.8995	
		Pt	4.0	3.8	2.71	-8.0		
		O_l	1.0	6.8	3.43	-1.7		
		Al	1.1	4.8	3.97	-4.0		
	3	O_s	1.0	9.0	2.03	-9.0	5.8575	
		Pt	3.9	12.7	2.71	-8.0		

[a]Notation: *N*, coordination number; *R*, distance between absorber and backscatter atoms; $\Delta\sigma^2$, Debye-Waller/disorder term; ΔE_0, inner potential. Subscripts: s, refers to an atom identified as belonging to the support; l, refers to the long Pt-scatterer contribution involving an atom in the support.

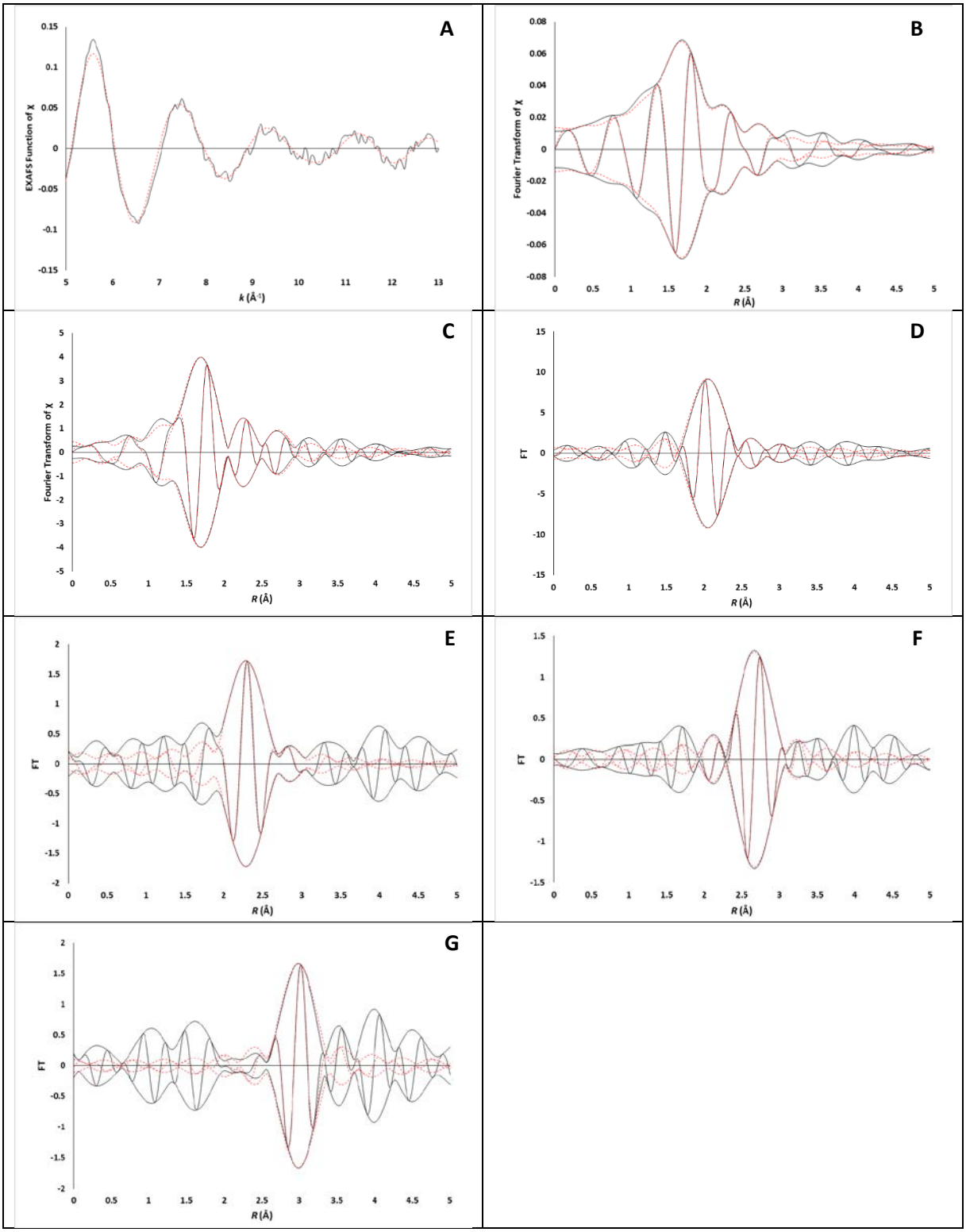

Figure 3A.11. EXAFS data recorded at Pt L3 edge characterizing the supported sample prepared from adsorption of $Pt(acac)_2$ on SAPO-37 in flowing helium at 298 K and 1 bar: (A) k^1-Weighted EXAFS function, $k^1(\chi)$ (solid line), and sum of the calculated contributions (dotted line). (B) k^1-Weighted imaginary part and magnitude of the Fourier transform of data (solid line) and sum of the calculated

contributions (dotted line). (C) k^3-Weighted imaginary part and magnitude of the Fourier transform of data (solid line) and sum of the calculated contributions (dotted line). (D) k^2-Weighted, phase- and amplitude-corrected, imaginary part and magnitude of the Fourier transform of data (solid line) and calculated contributions (dotted line) of Pt–O_{sup} shell. (E) k^2-Weighted, phase- and amplitude-corrected, imaginary part and magnitude of the Fourier transform of data (solid line) and calculated contributions (dotted line) of Pt–O shell. (F) k^2-Weighted, phase- and amplitude-corrected, imaginary part and magnitude of the Fourier transform of data (solid line) and calculated contributions (dotted line) of Pt–Al shell; (G) k^2-Weighted, phase- and amplitude-corrected, imaginary part and magnitude of the Fourier transform of data (solid line) and calculated contributions (dotted line) of Pt–O_l shell.

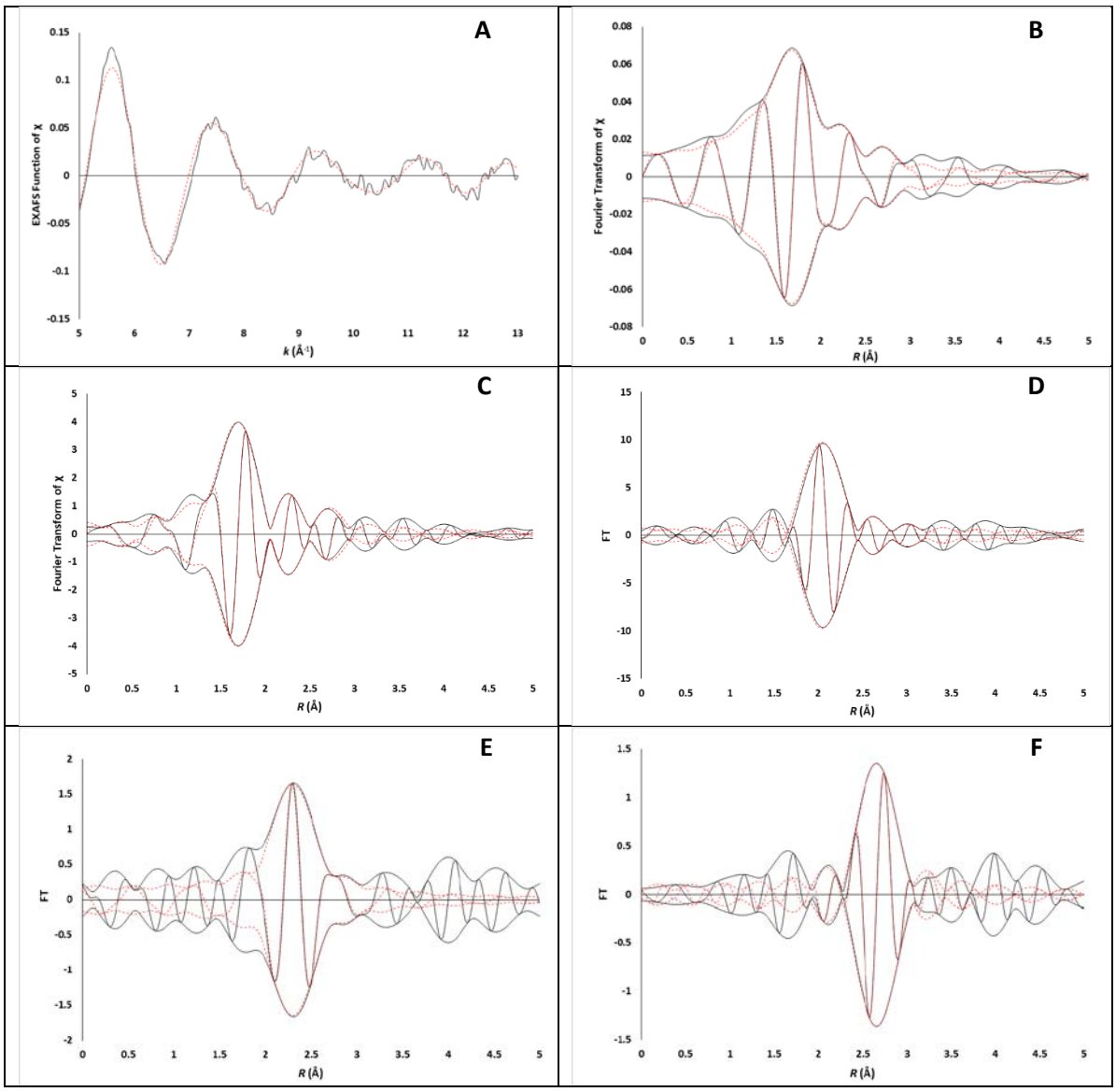

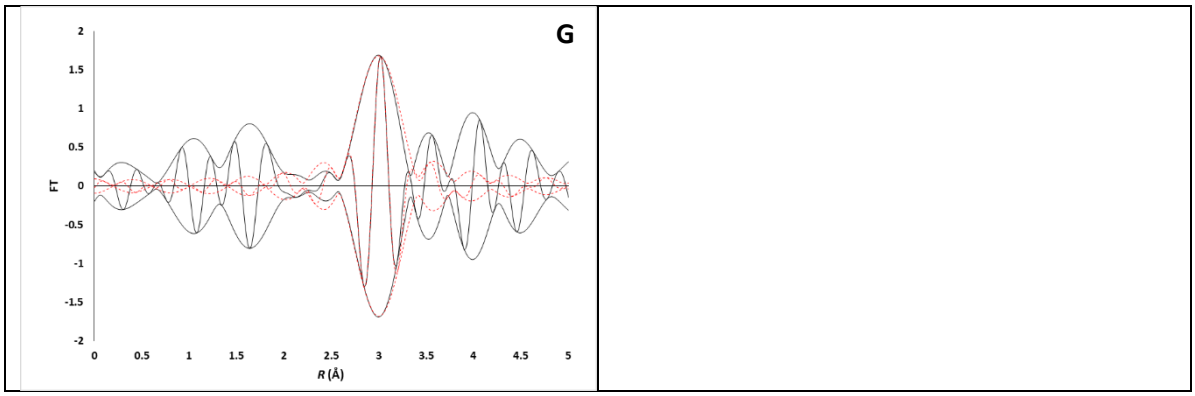

Figure 3A.12. EXAFS data recorded at Pt L3 edge characterizing the supported sample prepared from adsorption of $Pt(acac)_2$ on SAPO-37 in flowing helium at 298 K and 1 bar: (A) k^1-Weighted EXAFS function, $k^1(\chi)$ (solid line), and sum of the calculated contributions (dotted line). (B) k^1-Weighted imaginary part and magnitude of the Fourier transform of data (solid line) and sum of the calculated contributions (dotted line). (C) k^3-Weighted imaginary part and magnitude of the Fourier transform of data (solid line) and sum of the calculated contributions (dotted line). (D) k^2-Weighted, phase- and amplitude-corrected, imaginary part and magnitude of the Fourier transform of data (solid line) and calculated contributions (dotted line) of $Pt–O_{sup}$ shell. (E) k^2-Weighted, phase- and amplitude-corrected, imaginary part and magnitude of the Fourier transform of data (solid line) and calculated contributions (dotted line) of Pt–O shell. (F) k^2-Weighted, phase- and amplitude-corrected, imaginary part and magnitude of the Fourier transform of data (solid line) and calculated contributions (dotted line) of Pt–Al shell; (G) k^2-Weighted, phase- and amplitude-corrected, imaginary part and magnitude of the Fourier transform of data (solid line) and calculated contributions (dotted line) of $Pt–O_l$ shell.

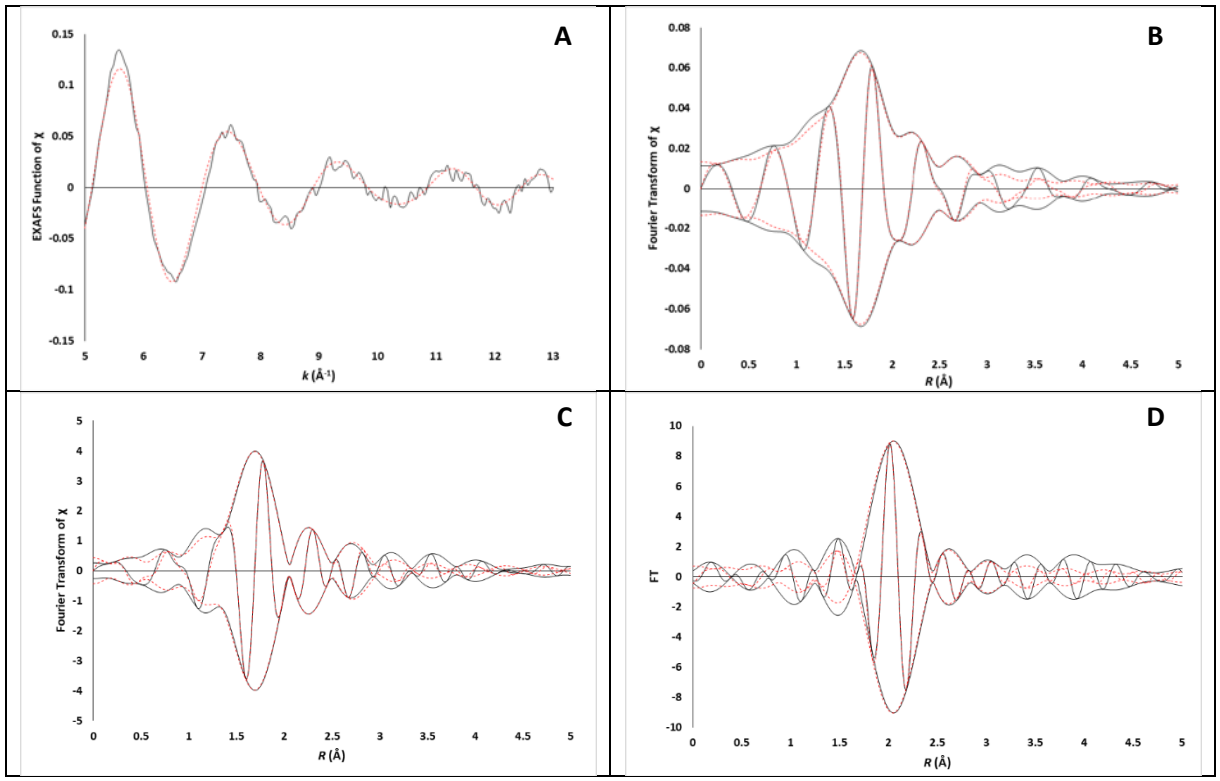

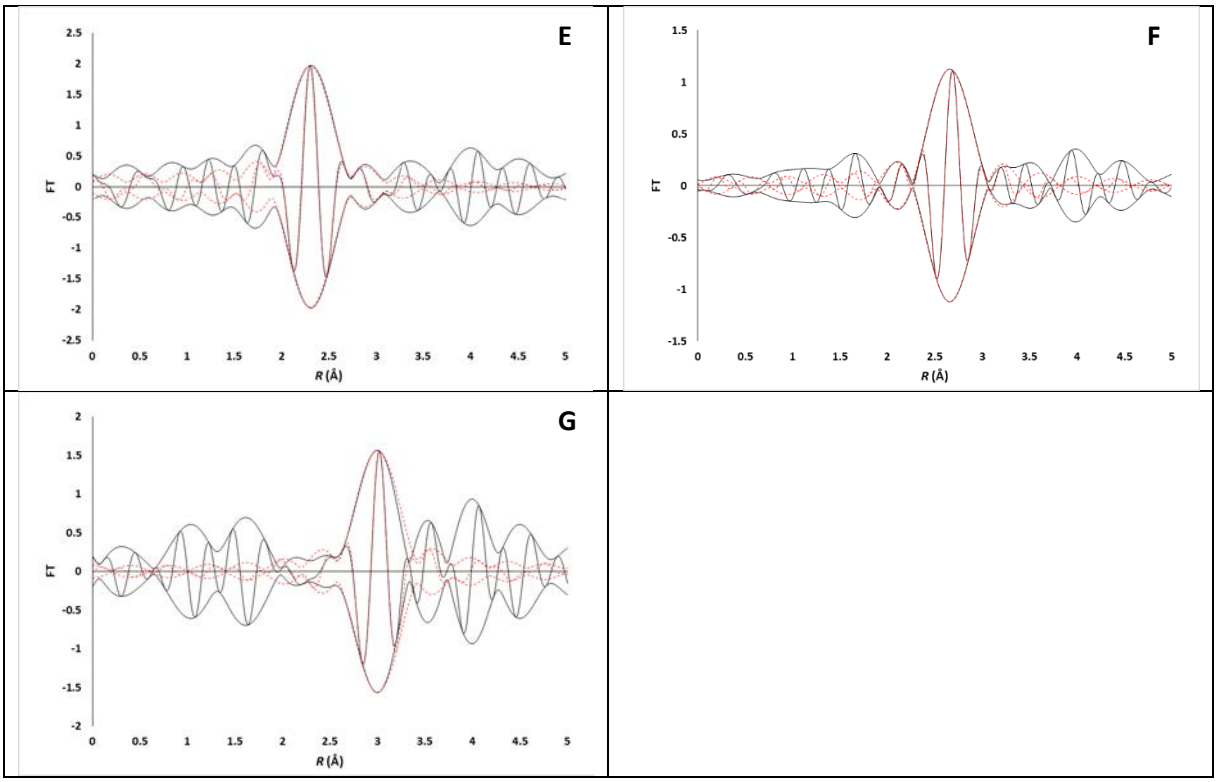

Figure 3A.13. EXAFS data recorded at Pt L3 edge characterizing the supported sample prepared from adsorption of $Pt(acac)_2$ on SAPO-37 in flowing helium at 298 K and 1 bar: (A) k^1-Weighted EXAFS function, $k^1(\chi)$ (solid line), and sum of the calculated contributions (dotted line). (B) k^1-Weighted imaginary part and magnitude of the Fourier transform of data (solid line) and sum of the calculated contributions (dotted line). (C) k^3-Weighted imaginary part and magnitude of the Fourier transform of data (solid line) and sum of the calculated contributions (dotted line). (D) k^2-Weighted, phase- and amplitude-corrected, imaginary part and magnitude of the Fourier transform of data (solid line) and calculated contributions (dotted line) of $Pt–O_{sup}$ shell. (E) k^2-Weighted, phase- and amplitude-corrected, imaginary part and magnitude of the Fourier transform of data (solid line) and calculated contributions (dotted line) of Pt–O shell; (F) k^2-Weighted, phase- and amplitude-corrected, imaginary part and magnitude of the Fourier transform of data (solid line) and calculated contributions (dotted line) of Pt–P shell. (G) k^2-Weighted, phase- and amplitude-corrected, imaginary part and magnitude of the Fourier transform of data (solid line) and calculated contributions (dotted line) of $Pt–O_l$ shell.

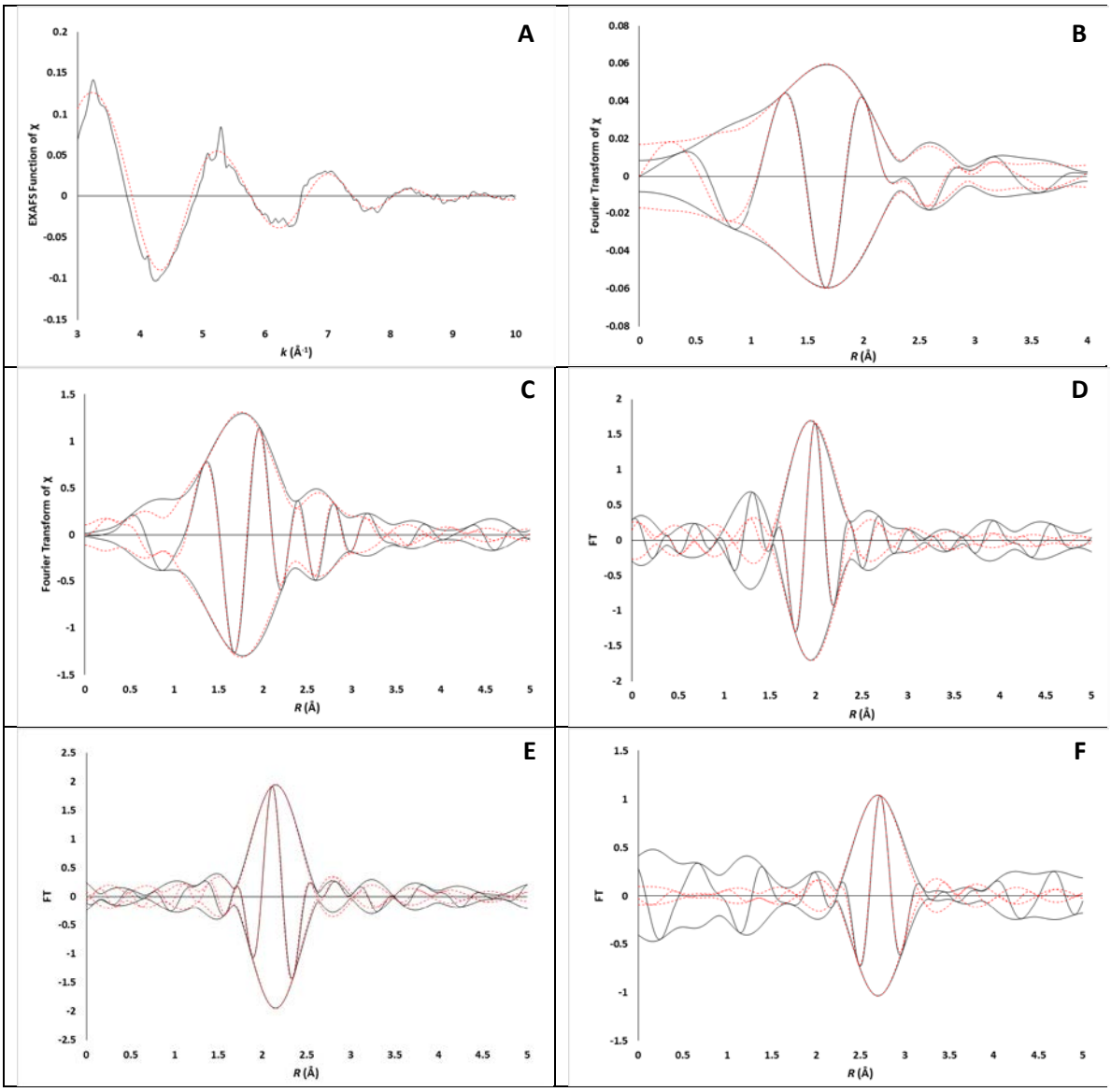

Figure 3A.14. EXAFS data recorded at Pt L3 edge characterizing the supported sample prepared from adsorption of $Pt(acac)_2$ on SAPO-37 in flowing ethylene and hydrogen at 298 K and 1 bar: (A) k^1-Weighted EXAFS function, $k^1(\chi)$ (solid line), and sum of the calculated contributions (dotted line). (B) k^1-Weighted imaginary part and magnitude of the Fourier transform of data (solid line) and sum of the calculated contributions (dotted line). (C) k^3-Weighted imaginary part and magnitude of the Fourier transform of data (solid line) and sum of the calculated contributions (dotted line). (D) k^2-Weighted, phase- and amplitude-corrected, imaginary part and magnitude of the Fourier transform of data (solid line) and calculated contributions (dotted line) of Pt–C shell. (E) k^2-Weighted, phase- and amplitude-corrected, imaginary part and magnitude of the Fourier transform of data (solid line) and calculated contributions (dotted line) of Pt–O shell. (F) k^2-Weighted, phase- and amplitude-corrected, imaginary part and magnitude of the Fourier transform of data (solid line) and calculated contributions (dotted line) of Pt–Pt shell.

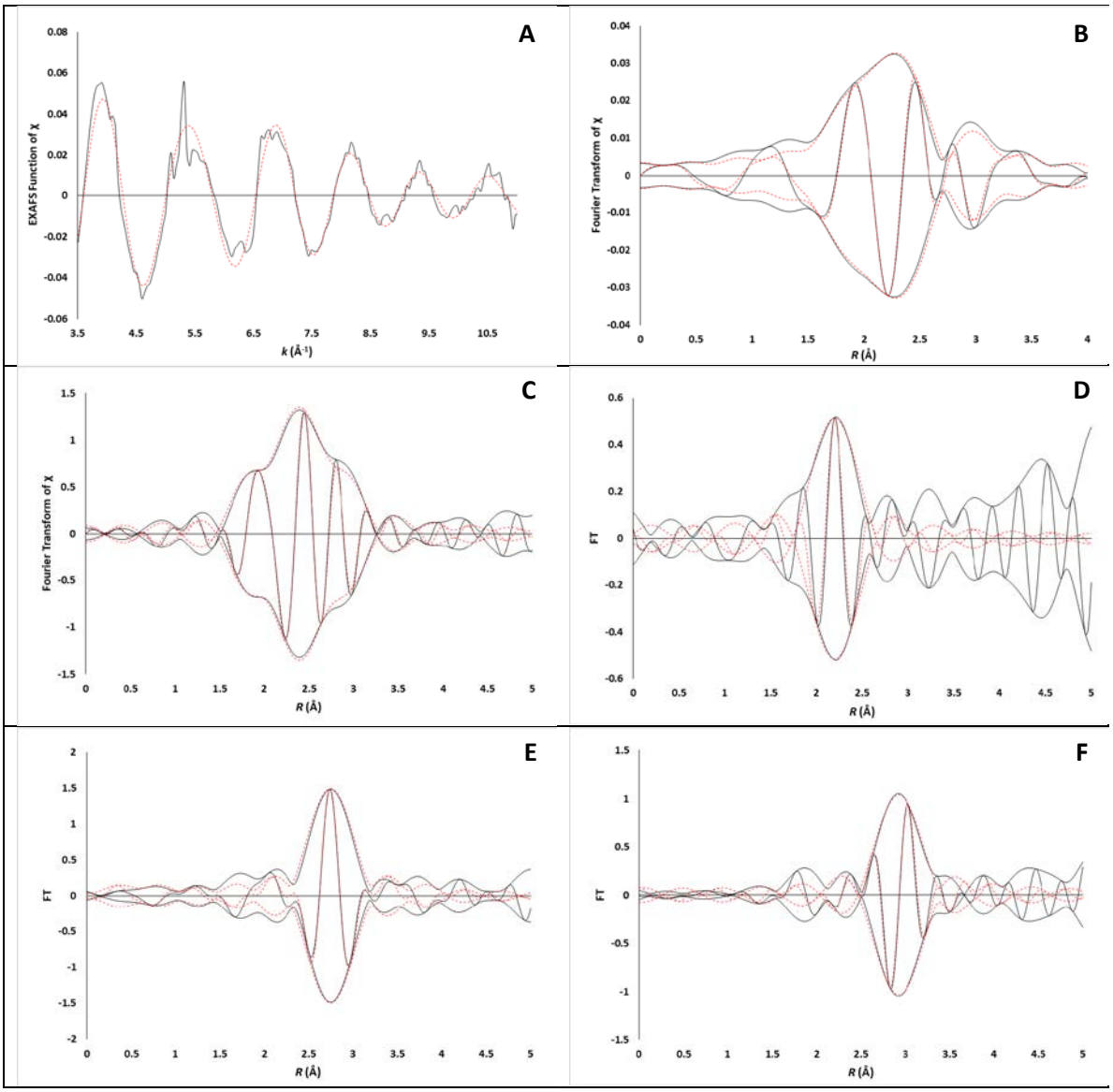

Figure 3A.15. EXAFS data recorded at Pt L3 edge characterizing the supported sample prepared from adsorption of $Pt(acac)_2$ on SAPO-37 in flowing ethylene and hydrogen at 298 K and 1 bar: (A) k^1-Weighted EXAFS function, $k^1(\chi)$ (solid line), and sum of the calculated contributions (dotted line). (B) k^1-Weighted imaginary part and magnitude of the Fourier transform of data (solid line) and sum of the calculated contributions (dotted line). (C) k^3-Weighted imaginary part and magnitude of the Fourier transform of data (solid line) and sum of the calculated contributions (dotted line). (D) k^2-Weighted, phase- and amplitude-corrected, imaginary part and magnitude of the Fourier Transform of data (solid line) and calculated contributions (dotted line) of Pt–C shell. (E) k^2-Weighted, phase- and amplitude-corrected, imaginary part and magnitude of the Fourier transform of data (solid line) and calculated contributions (dotted line) of Pt–Pt shell. (F) k^2-Weighted, phase- and amplitude-corrected, imaginary part and magnitude of the Fourier transform of data (solid line) and calculated contributions (dotted line) of Pt–O_l shell.

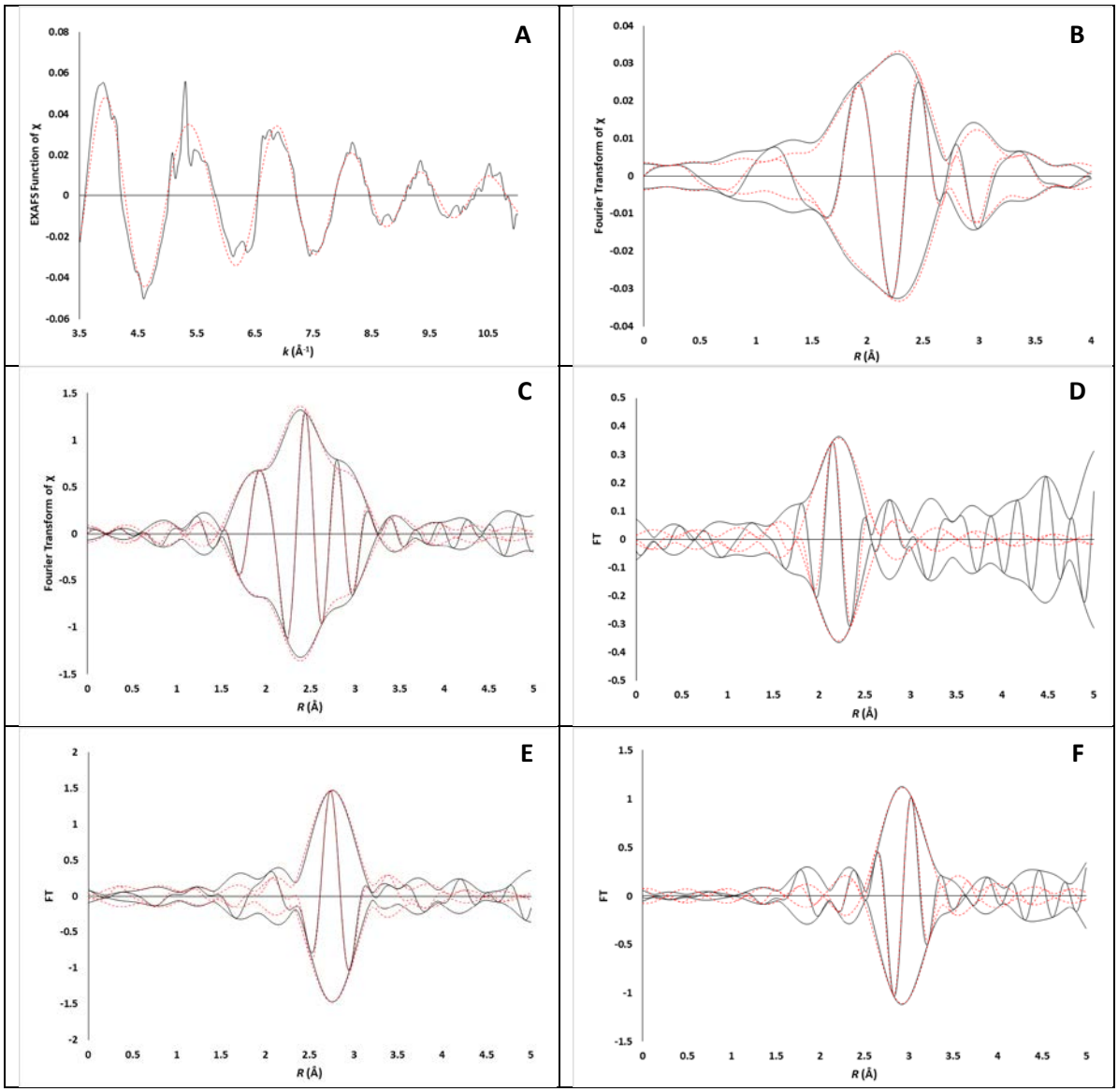

Figure 3A.16. EXAFS data recorded at Pt L3 edge characterizing the supported sample prepared from adsorption of $Pt(acac)_2$ on SAPO-37 in flowing ethylene and hydrogen at 298 K and 1 bar: (A) k^1-Weighted EXAFS function, $k^1(\chi)$ (solid line), and sum of the calculated contributions (dotted line). (B) k^1-Weighted imaginary part and magnitude of the Fourier transform of data (solid line) and sum of the calculated contributions (dotted line). (C) k^3-Weighted imaginary part and magnitude of the Fourier transform of data (solid line) and sum of the calculated contributions (dotted line). (D) k^2-Weighted, phase- and amplitude-corrected, imaginary part and magnitude of the Fourier Transform of data (solid line) and calculated contributions (dotted line) of Pt–O shell; (E) k^2-Weighted, phase- and amplitude-corrected, imaginary part and magnitude of the Fourier transform of data (solid line) and calculated contributions (dotted line) of Pt–Pt shell; (F) k^2-Weighted, phase- and amplitude-corrected, imaginary part and magnitude of the Fourier transform of data (solid line) and calculated contributions (dotted line) of $Pt–O_l$ shell.

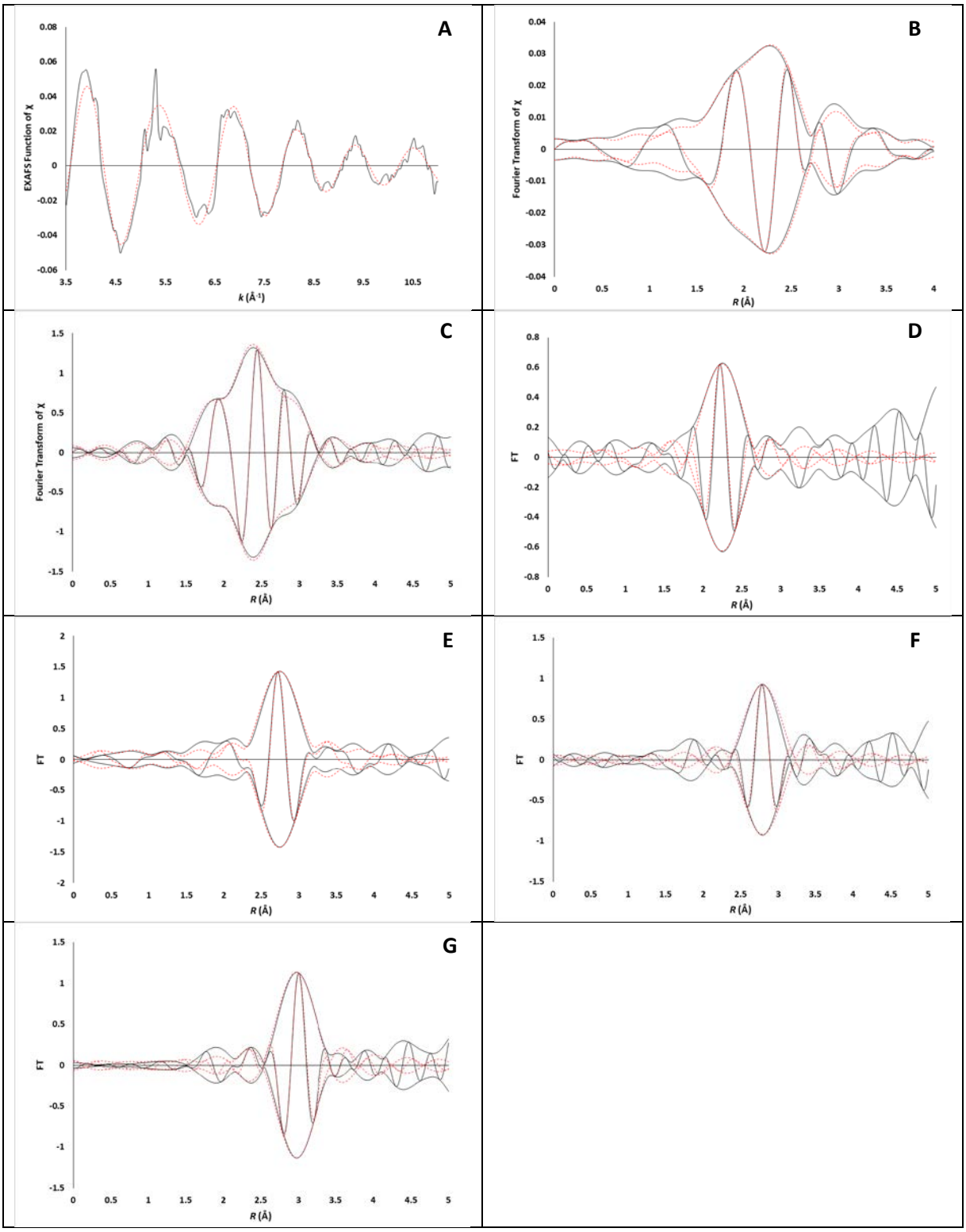

Figure 3A.17. EXAFS data recorded at Pt L3 edge characterizing the supported sample prepared from adsorption of $Pt(acac)_2$ on SAPO-37 in flowing ethylene and hydrogen at 298 K and 1 bar: (A) k^1-Weighted EXAFS function, $k^1(\chi)$ (solid line), and sum of the calculated contributions (dotted line). (B) k^1-Weighted imaginary part and magnitude of the Fourier transform of data (solid line) and sum of the calculated contributions (dotted line). (C) k^3-Weighted imaginary part and magnitude of the Fourier

transform of data (solid line) and sum of the calculated contributions (dotted line). (D) k^2-Weighted, phase- and amplitude-corrected, imaginary part and magnitude of the Fourier Transform of data (solid line) and calculated contributions (dotted line) of Pt–C shell; (E) k^2-Weighted, phase- and amplitude-corrected, imaginary part and magnitude of the Fourier transform of data (solid line) and calculated contributions (dotted line) of Pt–Pt shell; (F) k^2-Weighted, phase- and amplitude-corrected, imaginary part and magnitude of the Fourier transform of data (solid line) and calculated contributions (dotted line) of Pt–C_l shell; (G) k^2-Weighted, phase- and amplitude-corrected, imaginary part and magnitude of the Fourier transform of data (solid line) and calculated contributions (dotted line) of Pt–O_l shell.

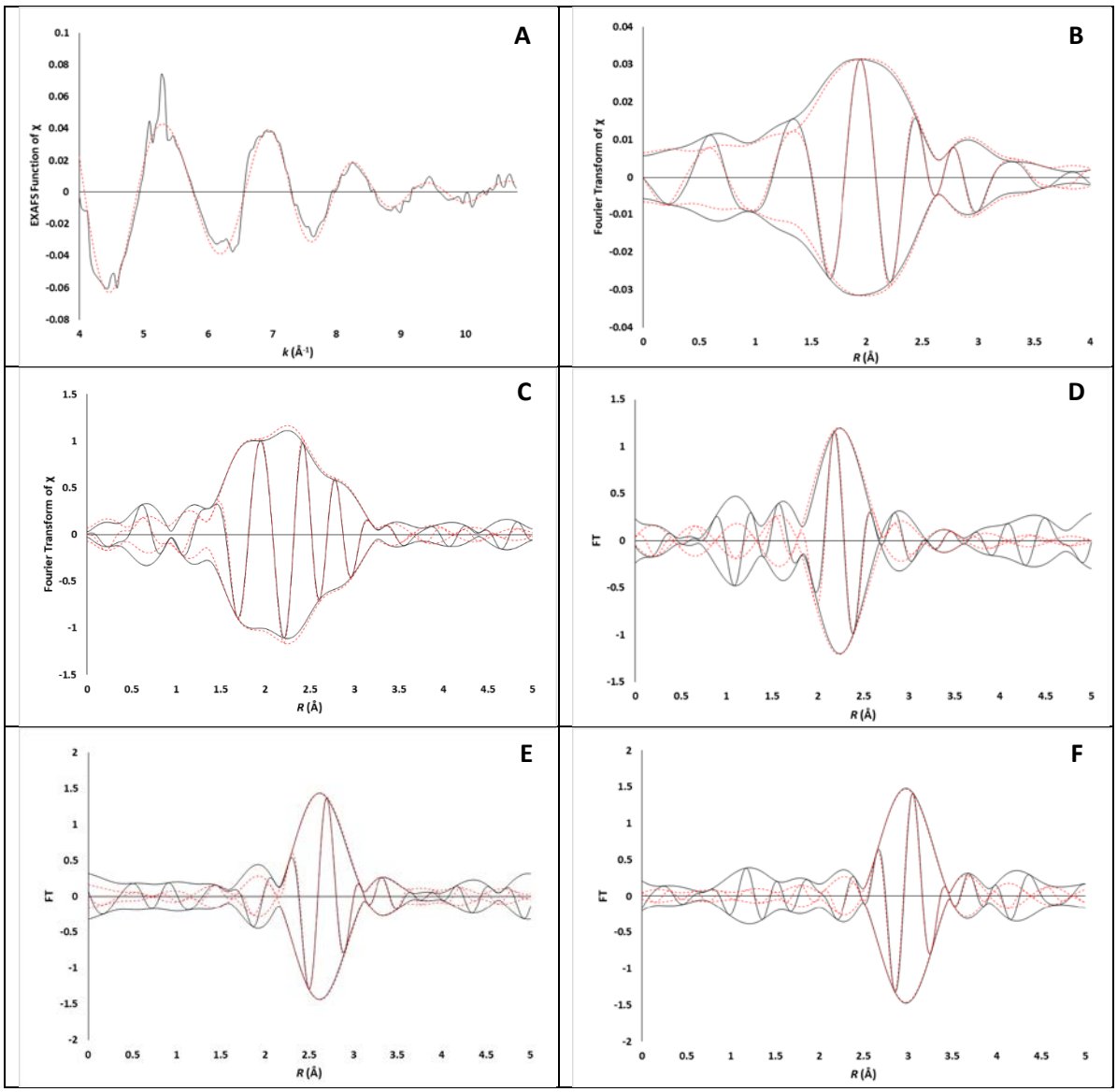

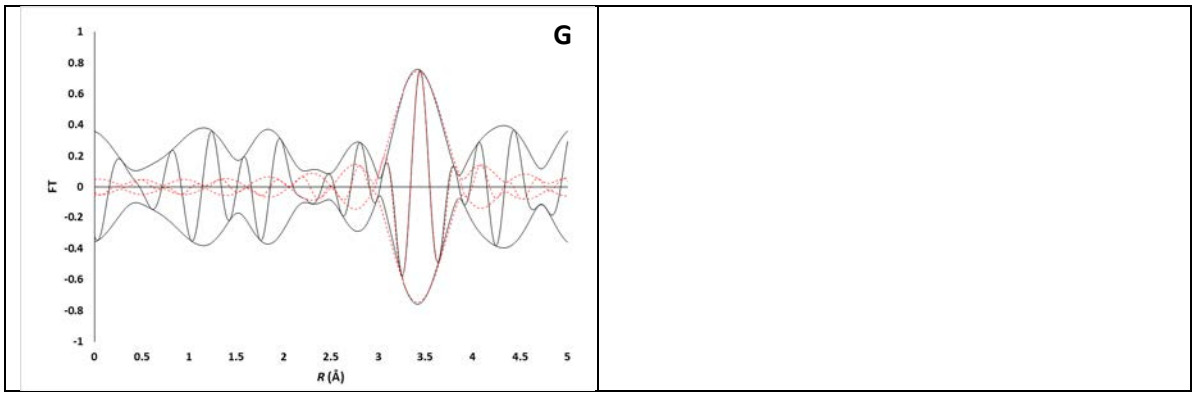

Figure 3A.18. EXAFS data recorded at Pt L3 edge characterizing the supported sample prepared from adsorption of $Pt(acac)_2$ on SAPO-37 in flowing ethylene after reaction conditions at 298 K and 1 bar: (A) k^1-Weighted EXAFS function, $k^1(\chi)$ (solid line), and sum of the calculated contributions (dotted line). (B) k^1-Weighted imaginary part and magnitude of the Fourier transform of data (solid line) and sum of the calculated contributions (dotted line). (C) k^3-Weighted imaginary part and magnitude of the Fourier transform of data (solid line) and sum of the calculated contributions (dotted line). (D) k^2-Weighted, phase- and amplitude-corrected, imaginary part and magnitude of the Fourier Transform of data (solid line) and calculated contributions (dotted line) of Pt–C shell; (E) k^2-Weighted, phase- and amplitude-corrected, imaginary part and magnitude of the Fourier transform of data (solid line) and calculated contributions (dotted line) of Pt–Pt shell; (F) k^2-Weighted, phase- and amplitude-corrected, imaginary part and magnitude of the Fourier transform of data (solid line) and calculated contributions (dotted line) of Pt–O shell (G) k^2-Weighted, phase- and amplitude-corrected, imaginary part and magnitude of the Fourier transform of data (solid line) and calculated contributions (dotted line) of Pt–C_I shell.

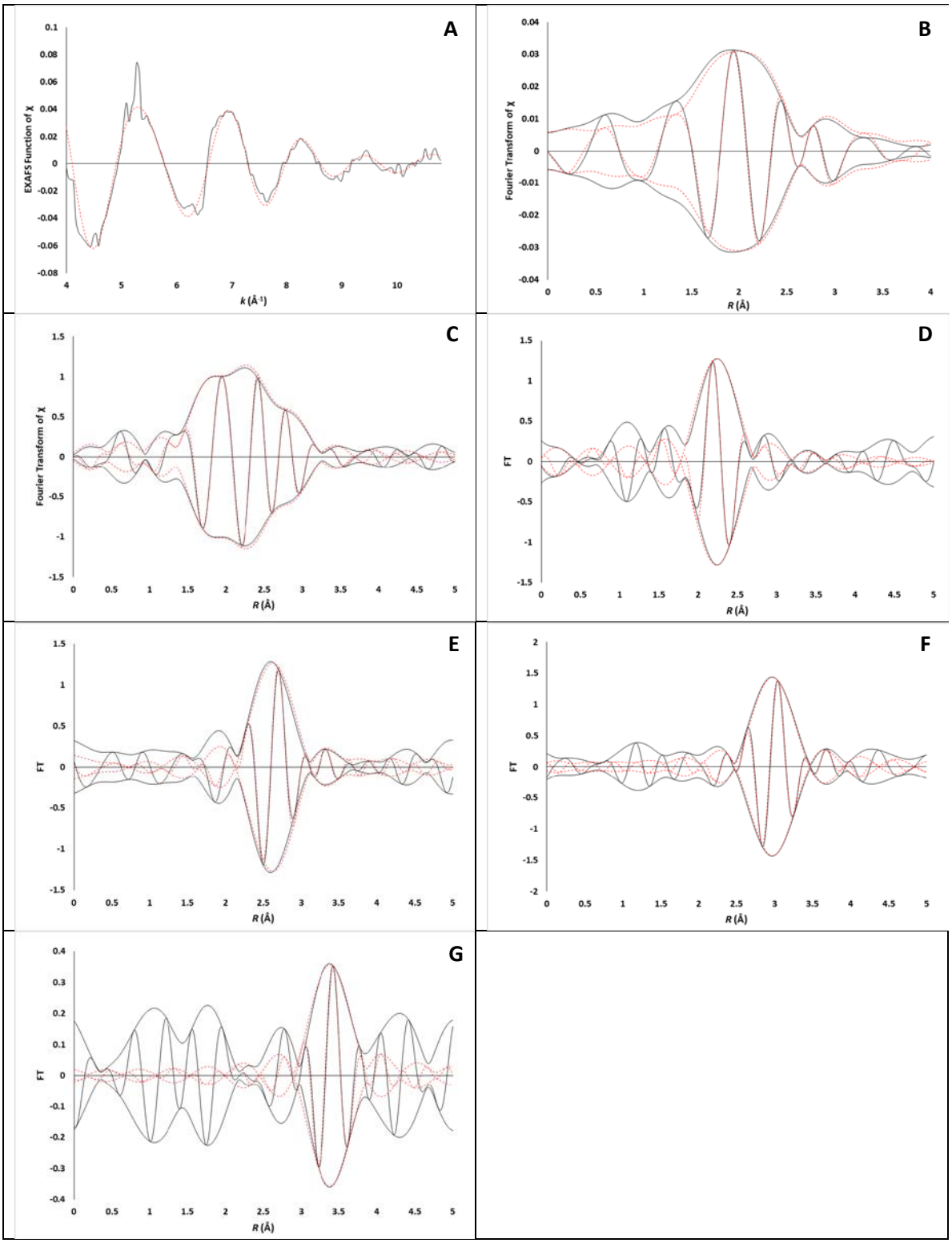

Figure 3A.19. EXAFS data recorded at Pt L3 edge characterizing the supported sample prepared from adsorption of $Pt(acac)_2$ on SAPO-37 in flowing ethylene after reaction conditions at 298 K and 1 bar: (A) k^1-Weighted EXAFS function, $k^1(\chi)$ (solid line), and sum of the calculated contributions (dotted line). (B) k^1-Weighted imaginary part and magnitude of the Fourier transform of data (solid line) and sum of the calculated contributions (dotted line). (C) k^3-Weighted imaginary part and magnitude of the Fourier

transform of data (solid line) and sum of the calculated contributions (dotted line). (D) k^2-Weighted, phase- and amplitude-corrected, imaginary part and magnitude of the Fourier Transform of data (solid line) and calculated contributions (dotted line) of Pt–C shell; (E) k^2-Weighted, phase- and amplitude-corrected, imaginary part and magnitude of the Fourier transform of data (solid line) and calculated contributions (dotted line) of Pt–Pt shell; (F) k^2-Weighted, phase- and amplitude-corrected, imaginary part and magnitude of the Fourier transform of data (solid line) and calculated contributions (dotted line) of Pt–O shell (G) k^2-Weighted, phase- and amplitude-corrected, imaginary part and magnitude of the Fourier transform of data (solid line) and calculated contributions (dotted line) of Pt–O_I shell.

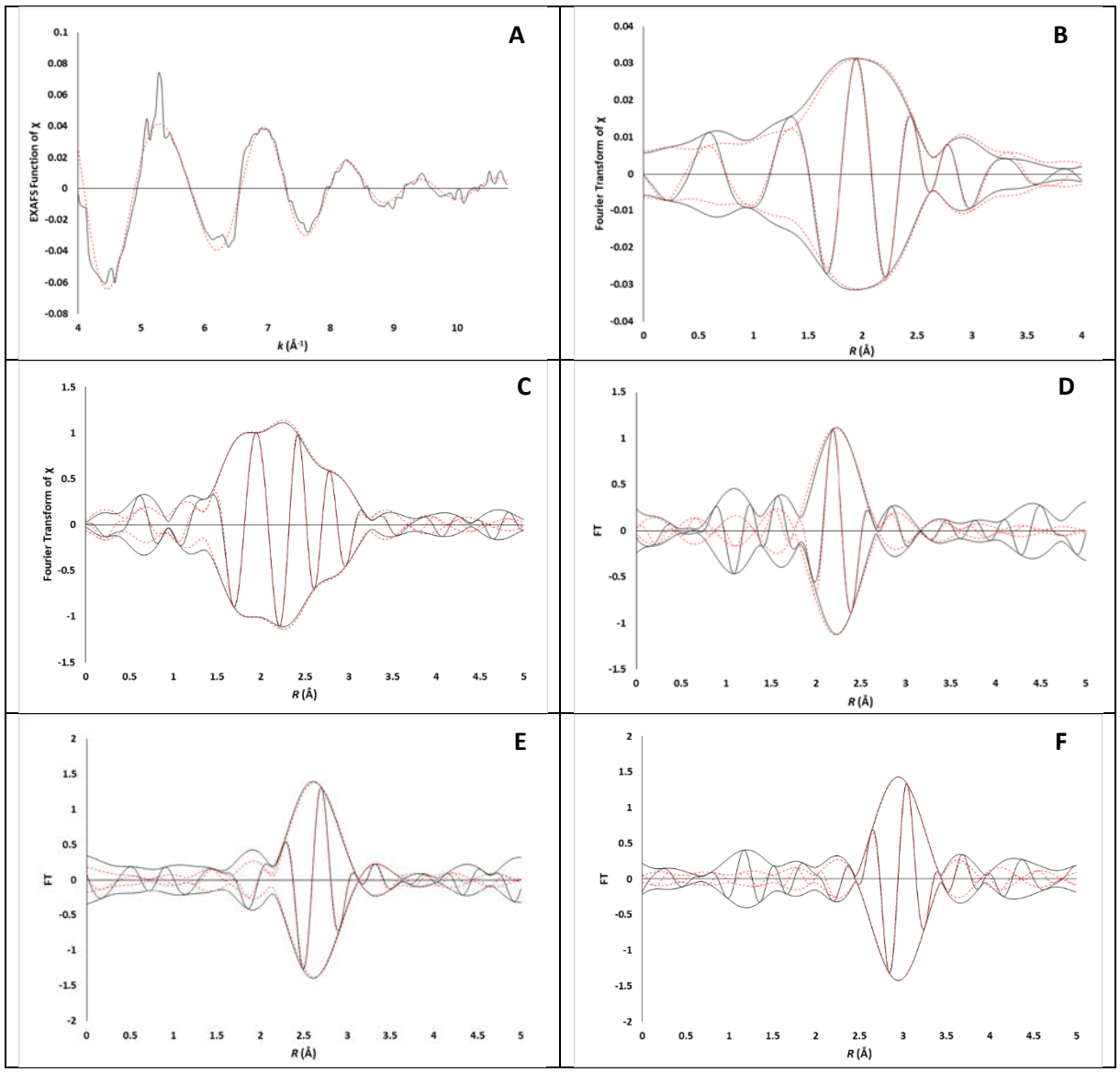

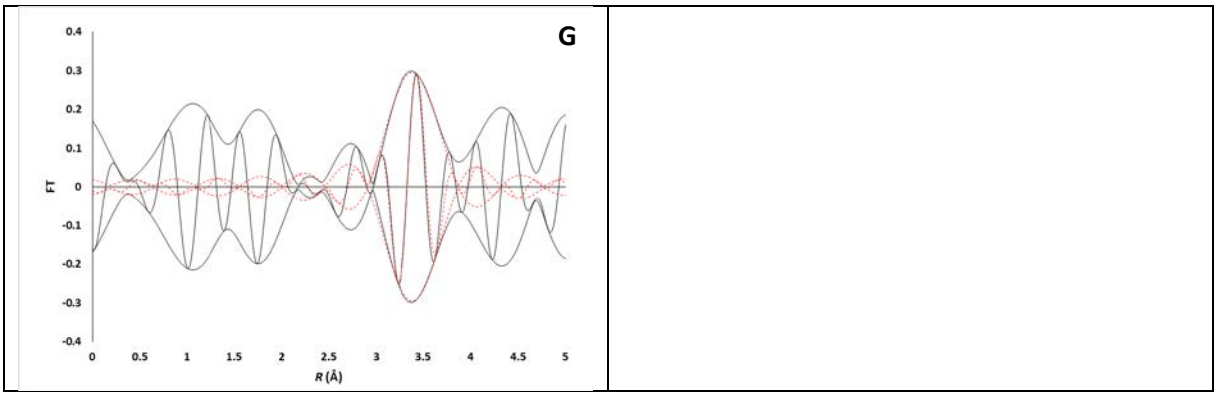

Figure 3A.20. EXAFS data recorded at Pt L3 edge characterizing the supported sample prepared from adsorption of $Pt(acac)_2$ on SAPO-37 in flowing ethylene after reaction conditions at 298 K and 1 bar: (A) k^1-Weighted EXAFS function, $k^1(\chi)$ (solid line), and sum of the calculated contributions (dotted line). (B) k^1-Weighted imaginary part and magnitude of the Fourier transform of data (solid line) and sum of the calculated contributions (dotted line). (C) k^3-Weighted imaginary part and magnitude of the Fourier transform of data (solid line) and sum of the calculated contributions (dotted line). (D) k^2-Weighted, phase- and amplitude-corrected, imaginary part and magnitude of the Fourier Transform of data (solid line) and calculated contributions (dotted line) of Pt–C shell; (E) k^2-Weighted, phase- and amplitude-corrected, imaginary part and magnitude of the Fourier transform of data (solid line) and calculated contributions (dotted line) of Pt–Pt shell; (F) k^2-Weighted, phase- and amplitude-corrected, imaginary part and magnitude of the Fourier transform of data (solid line) and calculated contributions (dotted line) of Pt–O shell (G) k^2-Weighted, phase- and amplitude-corrected, imaginary part and magnitude of the Fourier transform of data (solid line) and calculated contributions (dotted line) of $Pt–O_l$ shell.

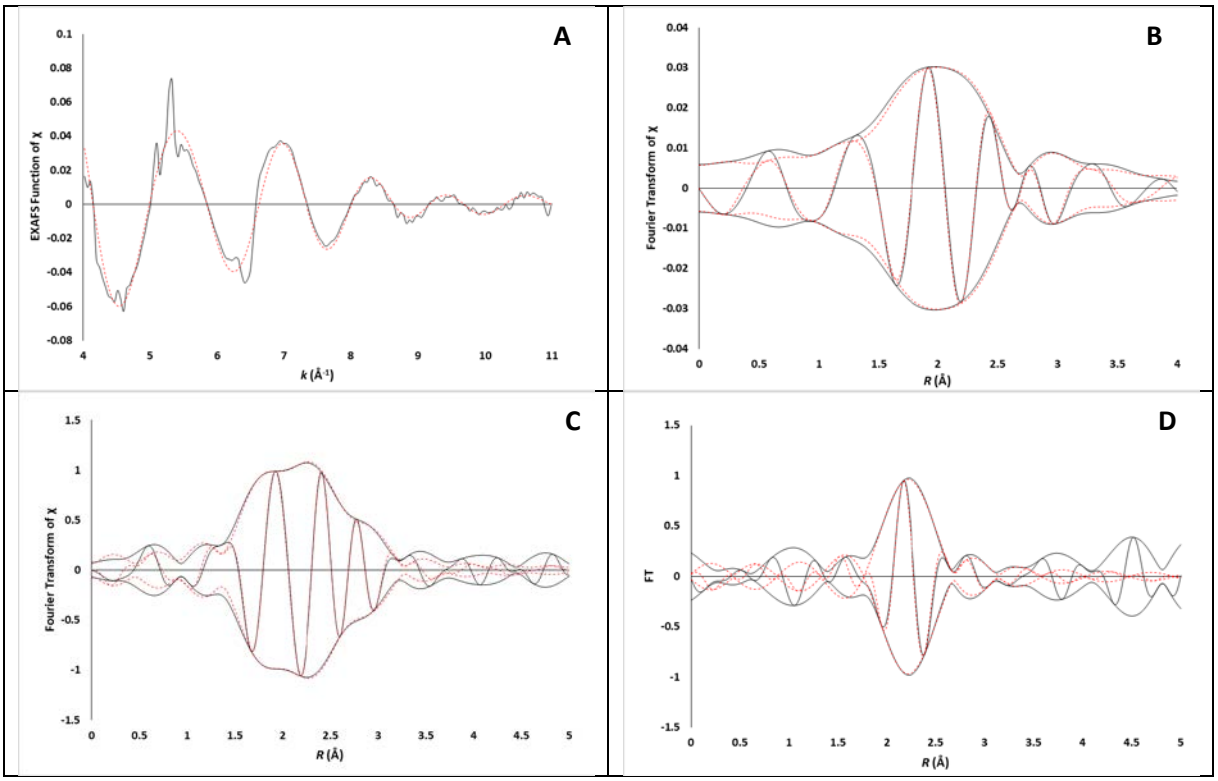

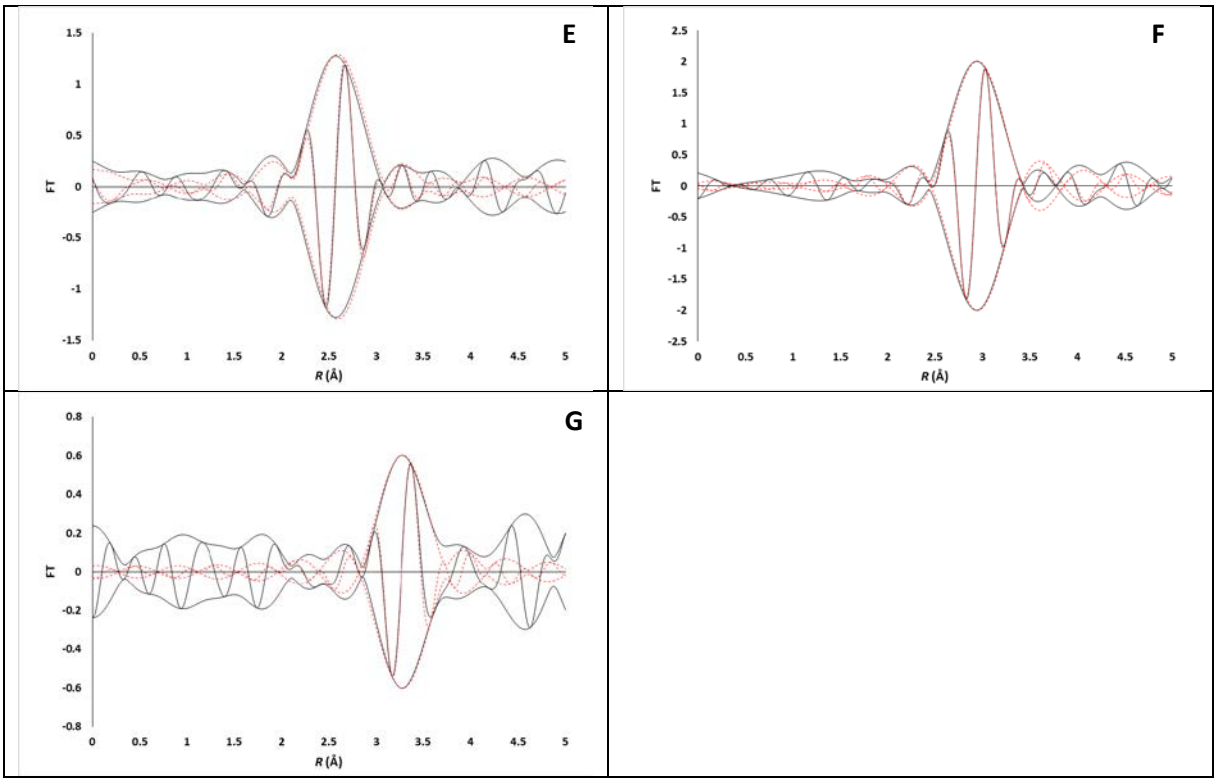

Figure 3A.21. EXAFS data recorded at Pt L3 edge characterizing the supported sample prepared from adsorption of $Pt(acac)_2$ on SAPO-37 in flowing helium at 298 K and 1 bar after exposure to reaction conditions and an ethylene treatment at 353 K: (A) k^1-Weighted EXAFS function, $k^1(\chi)$ (solid line), and sum of the calculated contributions (dotted line). (B) k^1-Weighted imaginary part and magnitude of the Fourier transform of data (solid line) and sum of the calculated contributions (dotted line). (C) k^3-Weighted imaginary part and magnitude of the Fourier transform of data (solid line) and sum of the calculated contributions (dotted line). (D) k^2-Weighted, phase- and amplitude-corrected, imaginary part and magnitude of the Fourier Transform of data (solid line) and calculated contributions (dotted line) of Pt–C shell; (E) k^2-Weighted, phase- and amplitude-corrected, imaginary part and magnitude of the Fourier transform of data (solid line) and calculated contributions (dotted line) of Pt–Pt shell; (F) k^2-Weighted, phase- and amplitude-corrected, imaginary part and magnitude of the Fourier transform of data (solid line) and calculated contributions (dotted line) of Pt–O_s shell; (G) k^2-Weighted, phase- and amplitude-corrected, imaginary part and magnitude of the Fourier transform of data (solid line) and calculated contributions (dotted line) of Pt–O_l shell.

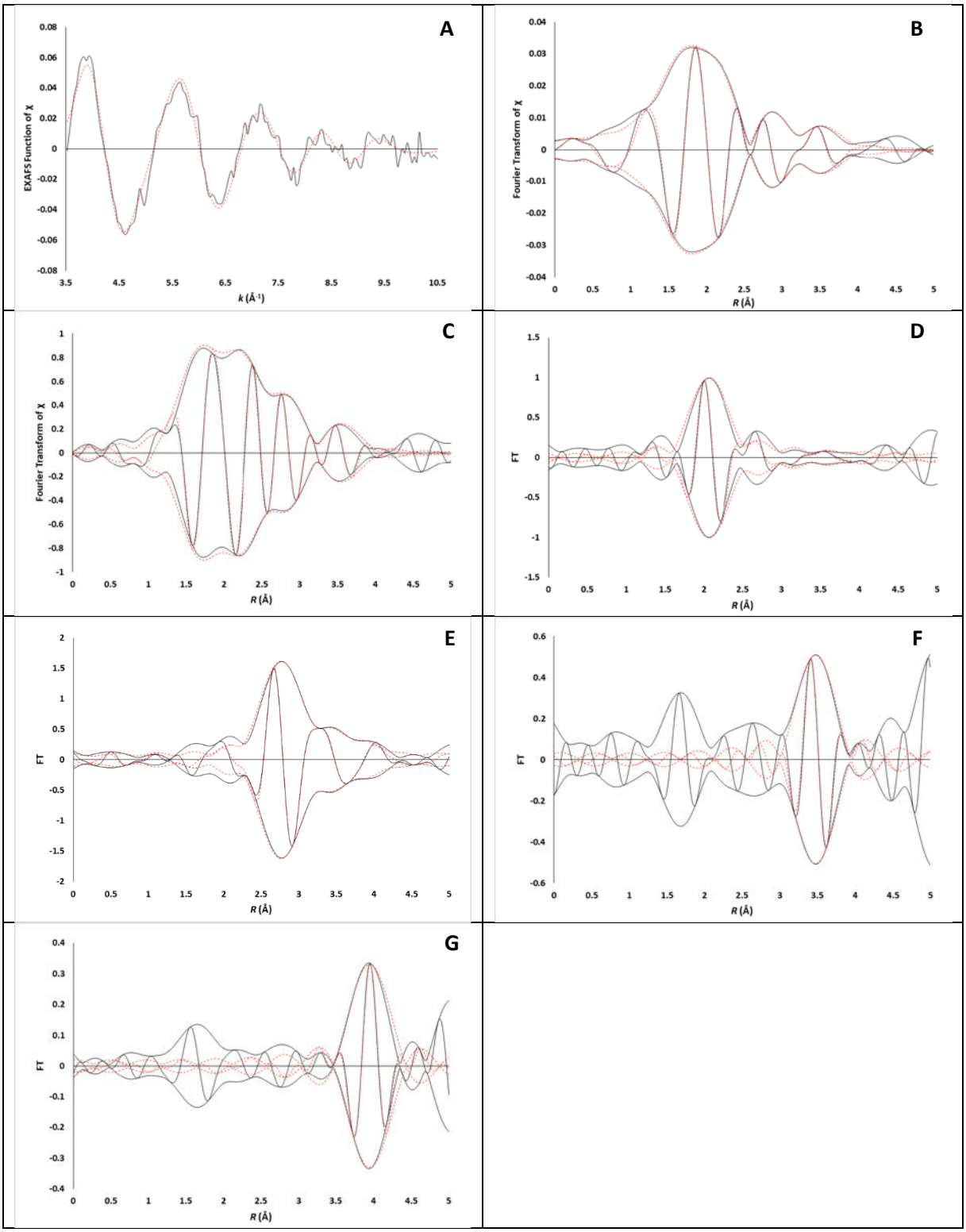

Figure 3A.22. EXAFS data recorded at Pt L3 edge characterizing the supported sample prepared from adsorption of $Pt(acac)_2$ on SAPO-37 in flowing helium at 298 K and 1 bar after expose to hydrogen for 1 h: (A) k^1-Weighted EXAFS function, $k^1(\chi)$ (solid line), and sum of the calculated contributions (dotted line). (B) k^1-Weighted imaginary part and magnitude of the Fourier transform of data (solid line) and sum of the calculated contributions (dotted line). (C) k^3-Weighted imaginary part and magnitude of the

Fourier transform of data (solid line) and sum of the calculated contributions (dotted line). (D) k^2-Weighted, phase- and amplitude-corrected, imaginary part and magnitude of the Fourier Transform of data (solid line) and calculated contributions (dotted line) of Pt–O_{sup} shell; (E) k^2-Weighted, phase- and amplitude-corrected, imaginary part and magnitude of the Fourier transform of data (solid line) and calculated contributions (dotted line) of Pt–Pt shell; (F) k^2-Weighted, phase- and amplitude-corrected, imaginary part and magnitude of the Fourier transform of data (solid line) and calculated contributions (dotted line) of Pt–O_I shell; (G) k^2-Weighted, phase- and amplitude-corrected, imaginary part and magnitude of the Fourier transform of data (solid line) and calculated contributions (dotted line) of Pt–Al shell.

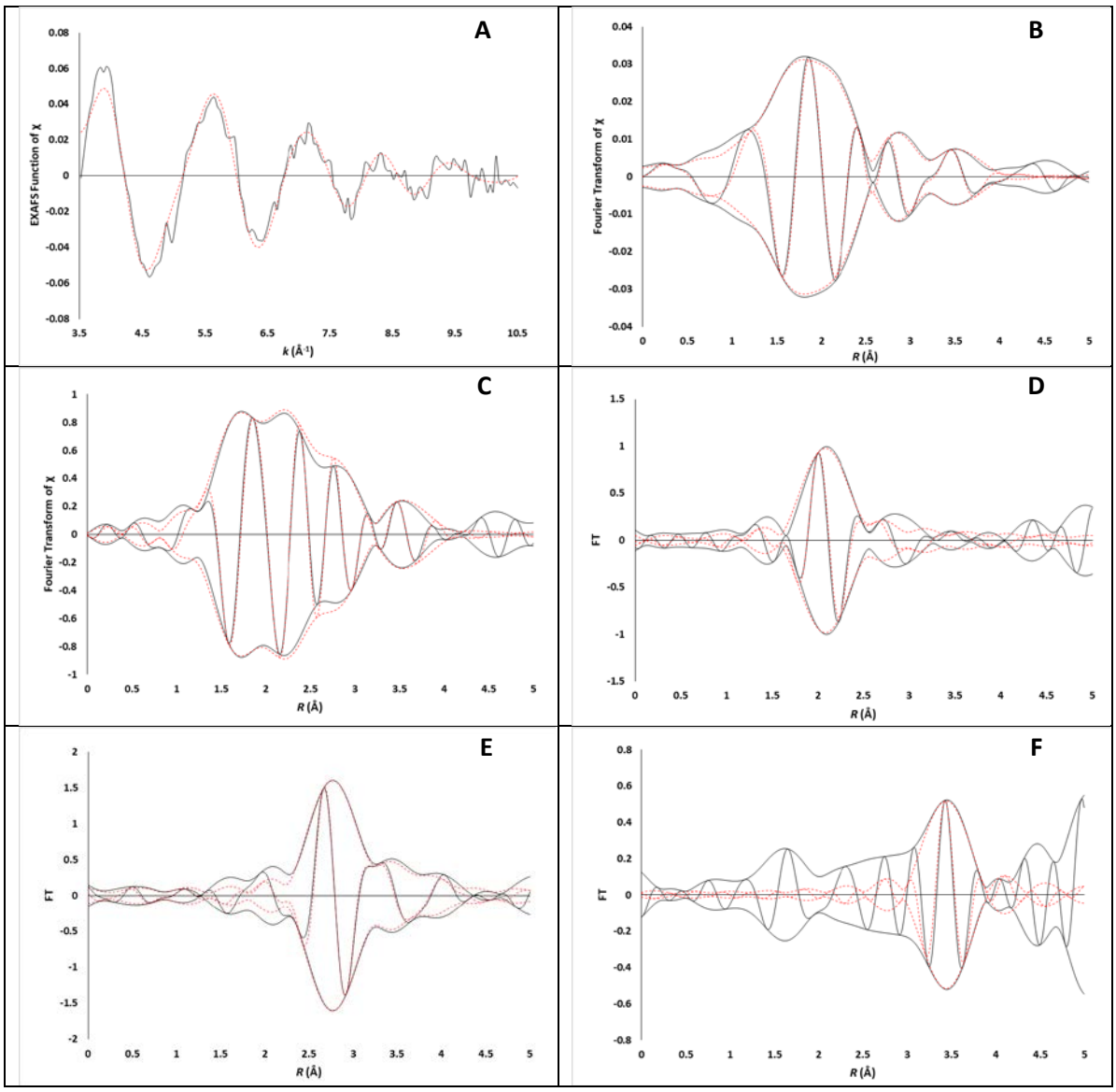

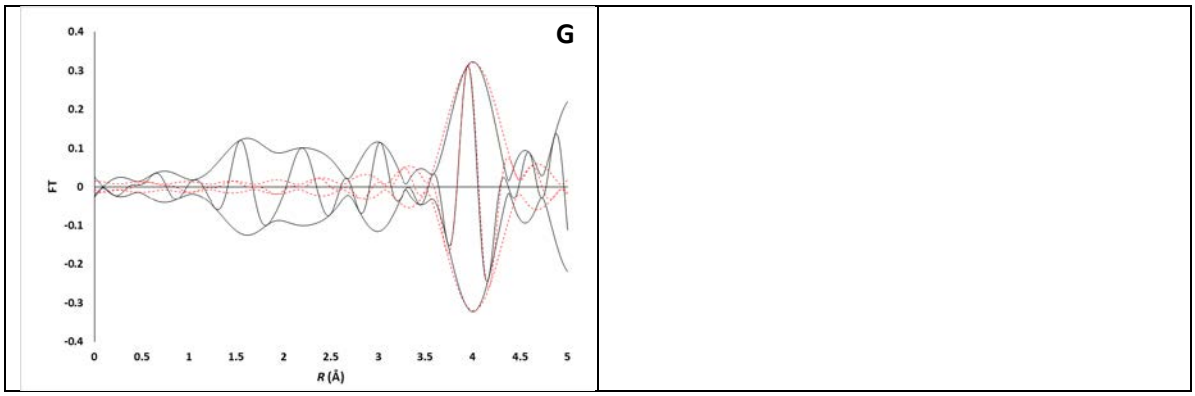

Figure 3A.23. EXAFS data recorded at Pt L3 edge characterizing the supported sample prepared from adsorption of $Pt(acac)_2$ on SAPO-37 in flowing helium at 298 K and 1 bar after expose to hydrogen for 1 h: (A) k^1-Weighted EXAFS function, $k^1(\chi)$ (solid line), and sum of the calculated contributions (dotted line). (B) k^1-Weighted imaginary part and magnitude of the Fourier transform of data (solid line) and sum of the calculated contributions (dotted line). (C) k^3-Weighted imaginary part and magnitude of the Fourier transform of data (solid line) and sum of the calculated contributions (dotted line). (D) k^2-Weighted, phase- and amplitude-corrected, imaginary part and magnitude of the Fourier Transform of data (solid line) and calculated contributions (dotted line) of $Pt–O_{sup}$ shell; (E) k^2-Weighted, phase- and amplitude-corrected, imaginary part and magnitude of the Fourier transform of data (solid line) and calculated contributions (dotted line) of Pt–Pt shell; (F) k^2-Weighted, phase- and amplitude-corrected, imaginary part and magnitude of the Fourier transform of data (solid line) and calculated contributions (dotted line) of $Pt–O_I$ shell; (G) k^2-Weighted, phase- and amplitude-corrected, imaginary part and magnitude of the Fourier transform of data (solid line) and calculated contributions (dotted line) of Pt–Al shell.

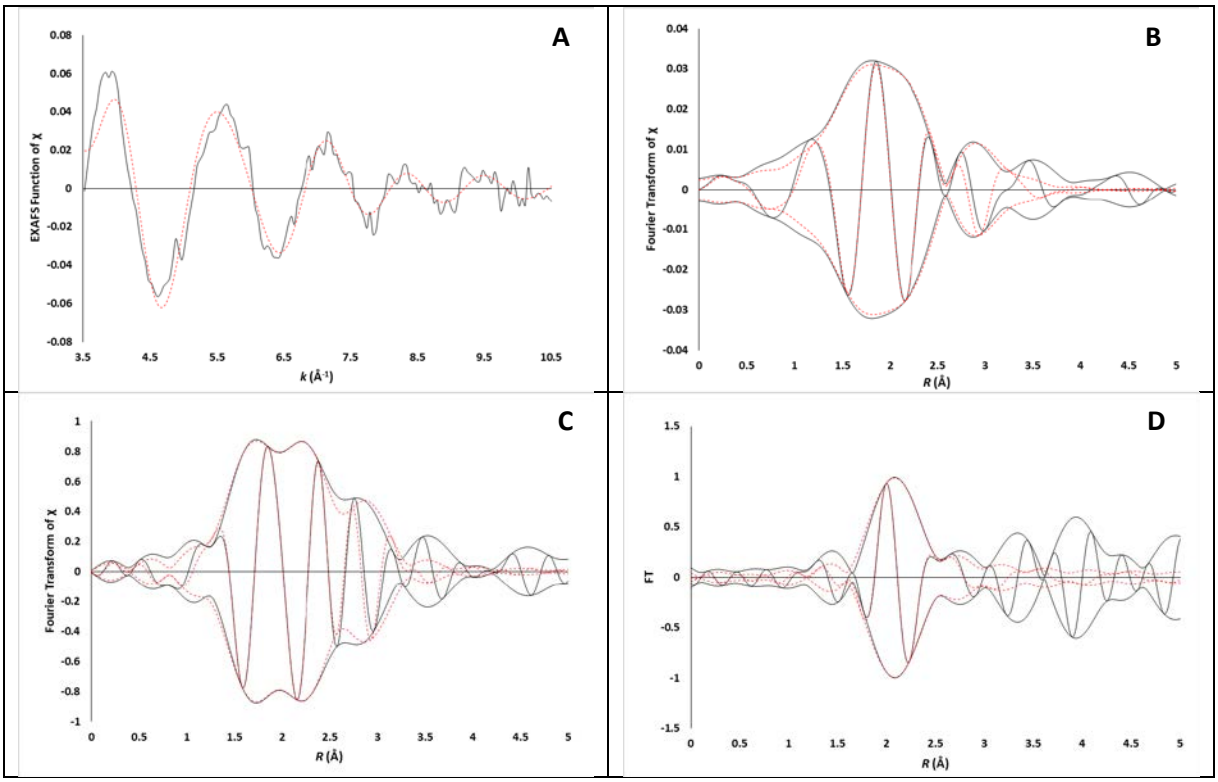

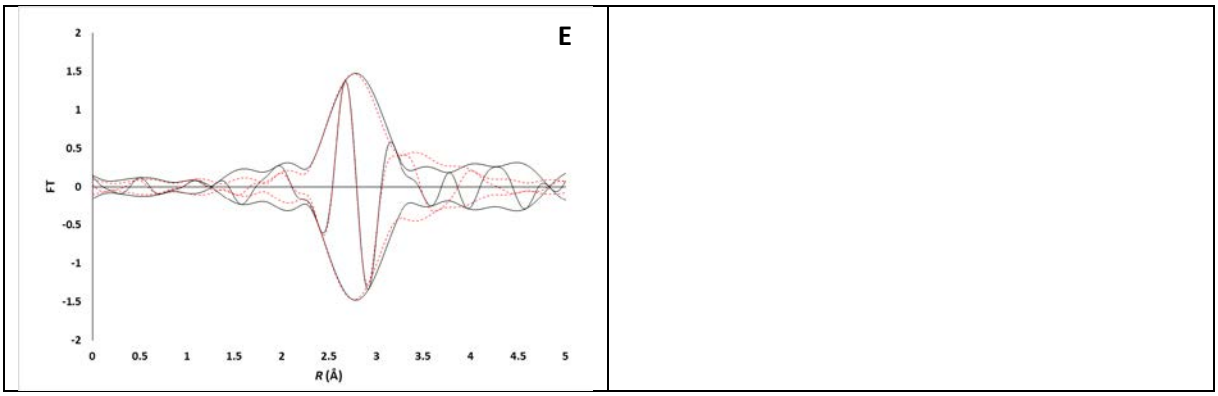

Figure 3A.24. EXAFS data recorded at Pt L3 edge characterizing the supported sample prepared from adsorption of $Pt(acac)_2$ on SAPO-37 in flowing helium at 298 K and 1 bar after expose to hydrogen for 1 h: (A) k^1-Weighted EXAFS function, $k^1(\chi)$ (solid line), and sum of the calculated contributions (dotted line). (B) k^1-Weighted imaginary part and magnitude of the Fourier transform of data (solid line) and sum of the calculated contributions (dotted line). (C) k^3-Weighted imaginary part and magnitude of the Fourier transform of data (solid line) and sum of the calculated contributions (dotted line). (D) k^2-Weighted, phase- and amplitude-corrected, imaginary part and magnitude of the Fourier Transform of data (solid line) and calculated contributions (dotted line) of Pt–O_{sup} shell; (E) k^2-Weighted, phase- and amplitude-corrected, imaginary part and magnitude of the Fourier transform of data (solid line) and calculated contributions (dotted line) of Pt–Pt shell.

References

(1) Hadjiivanov, K. I.; Vayssilov, G. N. Characterization of Oxide Surfaces and Zeolites by Carbon Monoxide as an IR Probe Molecule. *Adv. Catal.* **2002**, *47*, 307–511.

(2) Ding, K.; Gulec, A.; Johnson, A. M.; Schweitzer, N. M.; Stucky, G. D.; Marks, L. D.; Stair, P. C. Identification of Active Sites in CO Oxidation and Water-Gas Shift over Supported Pt Catalysts. *Science.* **2015**, *350*, 189–192.

(3) Chakarova, K.; Mihaylov, M.; Hadjiivanov, K. FTIR Spectroscopic Study of CO Adsorption on Pt-H-ZSM-5. *Micropor. Mesopor.Mater.* **2005**, *81*, 305–312.

(4) Akdogan, Y.; Vogt, C.; Bauer, M.; Bertagnolli, H.; Giurgiu, L.; Roduner, E. Platinum Species in the Pores of NaX, NaY and NaA Zeolites Studied Using EPR, XAS and FTIR Spectroscopies. *Phys. Chem. Chem. Phys.* **2008**, *10*, 2952–2963.

(5) Miessner, H.; Gutschick, D.; Ewald, H.; Müller, H. The Influence of Support on the Geminal

Dicarbonyl Species $Rh^{I}(CO)_2$ on Supported Rhodium Catalysts: An IR Spectroscopic Study. *J. Mol. Catal.* **1986**, *36*, 359–373.

(6) Howard, J.; Lux, P. J.; Yarwood, J. A Fourier-Transform i.r. Study of Ethene Adsorbed on HZSM-5 Zeolite at Low Temperature (295 K). *Zeolites* **1988**, *8*, 427–431.

(7) Perez-Aguilar, J. E.; Chen, C. Y.; Hughes, J. T.; Fang, C. Y.; Gates, B. C. Isostructural Atomically Dispersed Rhodium Catalysts Supported on SAPO-37 and on HY Zeolite. *J. Am. Chem. Soc.* **2020**, *142*, 11474–11485.

(8) Guzman, J.; Anderson, B. G.; Vinod, C. P.; Ramesh, K.; Niemantsverdriet, J. W.; Gates, B. C. Synthesis and Reactivity of Dimethyl Gold Complexes Supported on MgO: Characterization by Infrared and X-Ray Absorption Spectroscopies. *Langmuir* **2005**, *21*, 3675–3683.

(9) Zhou, M.; Crabtree, R. H. C–H Oxidation by Platinum Group Metal Oxo or Peroxo Species. *Chem. Soc. Rev.* **2011**, *40*, 1875–1884.

(10) Davies, M. S.; Hambley, T. W. $[Pt_2Cl_2(\mu_2\text{-}O_2)_2([9]AneN_3)_2]Cl_2$: A Novel Platinum(IV) Dimer with Two Bridging Peroxo Ligands That Provides Insight into the Mechanism of Aerial Oxidation of Platinum(II). *Inorg. Chem.* **1998**, *37*, 5408–5409.

(11) Kistler, J. D.; Chotigkrai, N.; Xu, P.; Enderle, B.; Praserthdam, P.; Chen, C. Y.; Browning, N. D.; Gates, B. C. A Single-Site Platinum CO Oxidation Catalyst in Zeolite KLTL: Microscopic and Spectroscopic Determination of the Locations of the Platinum Atoms. *Angew. Chem. Int. Ed.* **2014**, *53*, 8904–8907.

(12) Zholobenko, V. L.; Lei, G. D.; Carvill, B. T.; Lerner, B. A.; Sachtler, W. M. H. Identification of Isolated Pt Atoms in H-Mordenite. *J. Chem. Soc. Faraday Trans.* **1994**, *90*, 233–238.

(13) Li, G.; Fujimoto, T.; Fukuoka, A. EXAFS and Fourier Transform IR Characterization of Platinum Carbonyl Clusters $[Pt_3(CO)_6]N_2^-$ (n = 3, 4) Encapsulated in NaY Zeolites and Their Effective Catalysis in the CO + NO Reaction. *J. Chem. Soc. Chem. Commun.* **1991**, *3*, 1337–1339.

(14) Liu, Y.; Li, Z.; Yu, Q.; Chen, Y.; Chai, Z.; Zhao, G.; Liu, S.; Cheong, W. C.; Pan, Y.; Zhang, Q.; Gu, L.; Zheng, L.; Wang, Y.; Lu, Y.; Wang, D.; Chen, C.; Peng, Q. A General Strategy for Fabricating Isolated Single Metal Atomic Site Catalysts in Y Zeolite. *J. Am. Chem. Soc.* **2019**, *141*, 9305–9311.

Chapter 4

SAPO-37-Supported Rhodium Clusters[1]

[1]This chapter is in preparation for submission by J. E. Perez-Aguilar, J. T. Hughes, C.-Y. Chen, and B. C. Gates. The original manuscript has been reformatted to fit the requirements of the dissertation

4.1 ABSTRACT

Rhodium diethylene complexes were treated in hydrogen to form tetrarhodium clusters supported on the molecular sieve SAPO-37. The rhodium clusters were characterized by infrared (IR) and extended X-ray absorption fine structure (EXAFS) spectroscopy, with the data indicating an average Rh–Rh coordination number of 3.0 and an average Rh–Rh distance of 2.66 Å. X-ray absorption near edge spectra (XANES) spectra show the transformation of rhodium diethylene complexes to clusters is stoichiometrically simple. As a catalyst, the SAPO-37-supported clusters had a selectivity for hydrogenation in a flow reactor (with a feed H_2:C_2H_4 molar ratio of 1:4) similar to that of DAY zeolite-supported rhodium clusters (and, correspondingly, the SAPO-supported catalyst had a selectivity for ethylene dimerization of approximately 25%). However, the initial room-temperature activity of the SAPO-supported clusters (per rhodium atom) for ethylene conversion in the presence of H_2 was substantially less than that of the zeolite-supported rhodium clusters.

4.2 INTRODUCTION

Zeolites with acidic properties find wide applications as catalysts and supports for metal catalysts. Another class of materials, silicoaluminophosphates (SAPOs), offers good prospects as supports for nearly uniform atomically dispersed supported rhodium and platinum complexes.[1] These microporous, crystalline materials offer many of the advantages of zeolites,[2] potentially remaining stable at higher temperatures than zeolites.[3] Like zeolites, SAPOs are platforms for acidic OH groups on their interior surfaces, and correspondingly they find large-scale applications as acid catalysts.[4]

Atomically dispersed noble metals on solid supports, including zeolites,[5] metal oxides,[6] metal−organic frameworks,[7] and recently SAPOs, have attracted wide attention because they offer new catalytic properties with maximum efficiency in the use of the expensive metals.

The next step beyond these most highly dispersed catalysts would be those incorporating a few metal atoms in clusters on the supports. A Recent report of Fang *et al.*[8] summarizes the synthesis of nearly uniform clusters well approximated as $Rh_4(CO)_{12}$ in the cages of zeolite Y, with the cluster synthesis from a mononuclear precursor being driven by one of the half cycles of the water gas shift reaction. Rhodium clusters on zeolites have been reported to be more selective for hydrogenation versus dimerization than DAY zeolite-supported rhodium diethylene complexes.[9]

Synthesis methods reported by Yang *et al.*[10] have been used to form larger rhodium clusters from atomically dispersed rhodium diethylene complexes, and Serna *et al.*[9] formed a mixture of atomically dispersed rhodium and rhodium clusters in a zeolite. Our broad goals were to investigate a SAPO as a support for rhodium clusters and to assess the uniformity and catalytic properties of the clusters and compare them with those characterizing rhodium in isostructural zeolites as the supports. Here we report how to synthesize uniform, well-defined rhodium clusters on SAPO-37. We show that complexes initially present as $Rh(C_2H_4)_2$ bonded to the SAPO catalyze hydrogenation of ethane and that treatment of the catalyst to make rhodium clusters of only a few atoms each, on average, boosts the activity for dimerization.

Our specific goals were to prepare rhodium clusters on to SAPO-37, to determine the uniformity of the clusters, and to compare their activity and selectivity for ethylene hydrogenation/dimerization to those of SAPO-37-supported rhodium complexes and DAY zeolite-supported rhodium complexes.

4.3 MATERIALS AND METHODS

Synthesis of rhodium clusters on SAPO-37 Details of the sample preparation have been reported.[1] Sample synthesis and handling were carried out using standard moisture and air exclusion techniques. The supported rhodium complex was prepared by bringing the precursor $Rh(C_2H_4)_2$(acac) (6.0 mg, Strem, 99%) (acac is acetylacetonato) in contact with 200.0 mg SAPO-37 slurried in dried and

deoxygenated *n*-pentane (Fisher, 99%). The SAPO was calcined in flowing air (Praxair, 99.5% purity) at 873 K for 6 h and then evacuated for 6 h at 873 K prior to contacting with the precursor. The rhodium content of the resultant powder catalyst was 1.0 wt %. To form rhodium clusters, the SAPO-37-supported sample made from $Rh(C_2H_4)_2(acac)$ was exposed to flowing helium as the temperature was ramped from 298 to 373 K at rate of 5 K min^{-1}. Subsequently, the sample was exposed to a flowing H_2 for 60 min at 1 bar and 373 K, followed by cooling to 298 K. Details of the hydrogen treatment have been reported.[10] The resulting sample was recovered and stored in an argon-filled glovebox. Inductively coupled plasma-mass spectrometry analysis was done to determine the rhodium content of the sample.

Elemental Analysis of the Supported Rhodium Catalyst. The rhodium content of the SAPO-37-supported rhodium sample was determined at the UC Davis Interdisciplinary Center for Plasma Mass Spectrometry on an Agilent Model 7500a, quadrupole-type, inductively coupled plasma mass spectrometer (ICP-MS) (Agilent Technologies, Santa Clara, CA).

Infrared (IR) spectroscopy. A Bruker IFS 66v spectrometer with a room-temperature DTGS detector and a spectral resolution of 2 cm^{-1} was used to collect transmission IR spectra of powder samples. The sample was present in a diffuse reflectance (DRIFTS) cell that also served as a reactor (Harrick Scientific); it was equipped with KBr windows and mounted in a Praying Mantis diffuse reflectance adapter (Harrick Scientific). The DRIFTS cell in the glovebox was loaded with approximately 50 mg of dry KBr powder (Crystal Labs, 7758-02-3), mixed with approximately 20 mg of sample powder. The cell was connected into a flow system that allowed recording of spectra as reactant gases (CO, ^{13}CO, D_2, H_2, and/or ethylene) flowed through the cell at the desired temperature.

X-ray absorption spectroscopy. X-ray absorption spectroscopy (XAS) of the solid samples was carried out at beam line 4-1 of the Stanford Synchrotron Radiation Lightsource (SSRL) at SLAC National Accelerator Laboratory. The storage ring energy and current were 3 GeV and 500 mA, respectively. The double-crystal Si(220) monochromator was detuned by 20% at the Rh K edge. In an argon-filled glovebox

at SSRL, 400 mg of SAPO-37-supported rhodium complex containing 1.0 wt % rhodium was loaded into a transmission and fluorescence X-ray absorption spectroscopy cell/flow reactor designed to accommodate powder samples under vacuum or in reactive atmospheres.[11] The cell window was aligned at a 45° angle relative to the X-ray beam. Transient fluorescence X-ray absorption near edge spectra (XANES) and extended X-ray absorption fine structure (EXAFS) spectra were collected with a Lytle detector for samples in flowing reactive gases. For energy calibration, a rhodium foil mounted downbeam of the sample was scanned simultaneously.

Analysis of the EXAFS data was carried out with Athena of the software package Demeter and with the software XDAP. Athena was used for edge calibration and deglitching and XDAP for background removal, normalization, and conversion of the data into an EXAFS function file. Structural models postulated for the supported rhodium species were compared with the EXAFS data; the models included the plausible contributions Rh–Rh, Rh–O, and Rh–C. Reference files used in the fitting, with backscattering amplitudes and phase shifts for Rh–Rh, Rh–O, Rh–C, and Rh–Al contributions, were calculated with the software FEFF7.0 from crystallographic coordinates of the unit cells of the reference compounds rhodium metal, $Rh(C_2H_4)_2(acac)$, RhO_2, and Rh-Al alloy.[12,13]

Data fitting involved selection from among several plausible structural models that make good chemical sense and fitting to determine structure parameters that were required to have physically and chemically realistic values and appropriate values of goodness of fit—followed by selection of the best-fitting model for each sample. The number of parameters used in the fitting was always less than that justified statistically, calculated on the basis of the Nyquist theorem: $n = 2\Delta k \Delta r/\pi + 2$ (where Δk and Δr, respectively, are the ranges in the wave vector and distance in real space used in the fitting). Data fitting was done iteratively for the candidate models with a difference-file technique by considering each shell individually and the full range over which a satisfactory fit could be obtained for each individual shell to

determine how well each model compared with the data in terms of the overall fit and also the fits of individual shells.

The recommended model representing each sample was chosen as the best-fitting model when the k^1- and k^3-weighted EXAFS data, Fourier-transformed data, and Fourier-transformed data characterizing each shell contribution individually were all in good agreement with the calculated fits. The quality of each fit was evaluated by the value of goodness of fit, defined below:

$$Goodness\ of\ fit = \frac{\nu}{NPTS(\nu - N_{free})} \sum_{i=1}^{NPTS} \left(\frac{\chi_{exp,i} - \chi_{model,i}}{\sigma_{exp,i}} \right)^2$$

where χ_{exp} and χ_{model} are the experimental and calculated EXAFS functions, respectively; σ_{exp} the error in the experimental results; ν the number of independent data points in the fit range; N_{free} the number of free parameters; and NPTS the number of data points in the fit range. The estimates of the error bounds are based on the reported results and statistical analyses; the values are approximate. Complementary information is presented in the Supporting Information, SI.

Catalytic activity measurements. Catalyst performance was tested with samples in a once-through temperature-controlled plug-flow reactor, described elsewhere.[1] The procedures match those reported.[10] The reactant feed gases (H_2, ethylene, and helium (Airgas, all UHP grade)) flowed through a bed of catalyst of known mass (usually in the range of 1.00–15.0 mg) mixed with 1.0 g of inert particles of nonporous α−Al_2O_3 (Sigma-Aldrich, 100–200 mesh) at atmospheric pressure and a temperature of 303 K. A total feed flow rate of 100 mL(NTP) min^{-1} was used in each experiment, with the feed partial pressures (in mbar) being the following: H_2, 50; ethylene, 50; helium, 900 or, alternatively, ethylene, 200; H_2, 50; helium, 750. The effluent stream was analyzed periodically with an online gas chromatograph (Hewlett−Packard HP-6890) equipped with a capillary column (PLOT Alumina "M," 50 m × 0.53 mm) and a flame-ionization detector. The reported catalytic reaction rates per rhodium atom (turnover frequencies, TOF) were calculated from conversions <10%, which were shown to be

differential on the basis of the essentially linear dependence of conversion on inverse space velocity (Figure 4A.1 in the SI). Prior to each catalytic test, the SAPO-37-supported sample initially in the form that was present initially was treated in H_2 to form rhodium clusters (details in Section 2.1).

4.4 RESULTS

Initial SAPO-37-Supported Rhodium Complexes. Structurally well-defined SAPO-37-supported $Rh(C_2H_4)_2$ complexes were synthesized by reaction of $Rh(C_2H_4)_2(acac)$ with calcined SAPO-37, as reported before.[1] An EXAFS-based structural model of the supported species, as has been reported,[1] is summarized in Table 4.1. Elemental analysis showed that the typical sample contained 0.6 ± 0.1 wt%, implying that all of the precursor $Rh(C_2H_4)_2(acac)$ reacted with the SAPO-37 support and was retained by it. This result is consistent with the masses of $Rh(C_2H_4)_2(acac)$ and SAPO used in the synthesis and the inference that all of the precursor $Rh(C_2H_4)_2(acac)$ reacted with the SAPO-37 support.

Tracking Cluster Formation from SAPO-37-Supported Rhodium Complexes in H_2. The reaction of $Rh(C_2H_4)_2(acac)$ with SAPO-37 was accompanied by changes in the IR spectra of SAPO-37 that match previous observations.[1] Spectrum A of Figure 4.1 shows that ethylene ligands were still present on the rhodium after anchoring to the support, indicated by bands in the C–H region (between 2900 and 3150 cm^{-1}) similar to those characterizing HY zeolite-supported rhodium diethylene complexes.[9]

To make rhodium clusters in the support, the temperature of the sample in flowing helium was raised at a rate of 5 K min^{-1} to 373 K, and then the composition of the gas flowing over and through the particles of sample at 373 K was switched from helium to H_2, flowing at 50 mL(NTP) min^{-1} for 1 h. Spectrum B characterizing the sample in helium at room temperature after the exposure to H_2 shows the disappearance of bands characterizing C_2H_4 ligands (at 3086, 3060, and 3015 cm^{-1}) and the concomitant growing of a band at 2091 cm^{-1} [14,15] showing that the initially π-bonded ethylene ligands on the rhodium were replaced. The new band, at 2091 cm^{-1}, is identified as evidence of a rhodium hydride

on the basis of previous reports; Serna *et al.*[15] determined that the band at 2091 cm^{-1} for DAY zeolite-supported rhodium complexes is representative of a rhodium hydride band by exposing the sample to D_2 and observing an Rh–D species, characterized by an IR band at 1486 cm^{-1}. The slight residual band at 2988 cm^{-1} in the spectrum (A, Figure 4.1) matches well with reports of Hacac species on the support surface.[16] Any gas-phase products formed in the reduction (such as ethane) were formed in concentrations too low to observe with the online mass spectrometer.

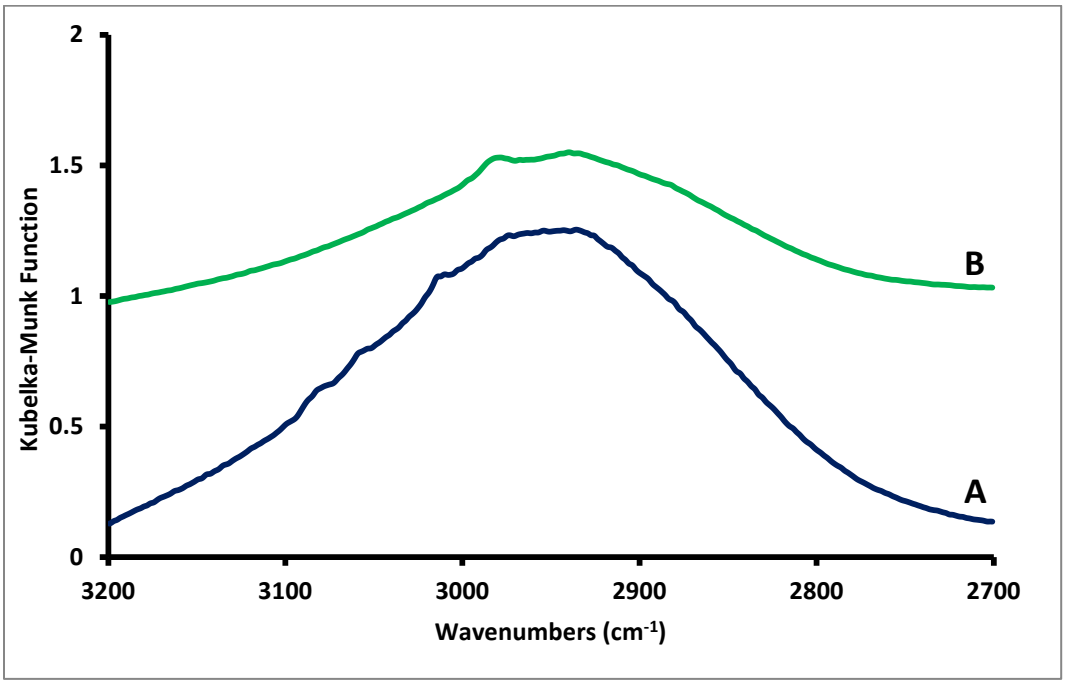

Figure 4.1. DRIFTS spectra in the ν_{CH} region region characterizing the SAPO-37-supported $Rh(C_2H_4)_2$ in (A) flowing He and (B) after the sample had been in contact with flowing H_2 for 1 h at 373 K and 1 bar.

EXAFS data (Table 4.1) characterizing the supported $Rh(C_2H_4)_2$ species show changes in the coordination environments as the sample came in contact with H_2 at 373 K for 60 min. There was a disappearance of the Rh−C contribution, a decrease in the coordination number characterizing the $Rh–O_{support}$ contribution (from 2.1 to 0.9), accompanied by the appearance and growth of a contribution identified as Rh−Rh at a distance of 2.66 Å (from not detectable to a coordination number of nearly 3). These EXAFS data demonstrate the unlinking of the rhodium complex from the support as the Rh atoms migrated and aggregated to form rhodium clusters.

The XANES spectrum of the initial SAPO-37-supported rhodium complexes (Figure 4.2) is consistent with the inference that the initial SAPO-37-supported rhodium diethylene complexes are well represented as a Rh(I) complex, as expected on the basis of XANES and IR data characterizing similar samples, including DAY zeolite-supported rhodium diethylene complexes.[1,17] At 373 K, the initial SAPO-37-supported rhodium complexes when exposed to flowing H_2 at 373 K were reduced, as shown by the decrease in the white line intensity (Figure 4.2). Two isosbestic points, at 25 and 58 eV above the absorption edge (Figure 4.2), indicate the transformation of one species (atomically dispersed) to another, suggesting a near uniformity of the resultant species (clusters), inferred on the basis of the EXAFS data in Table 4.1.[17]

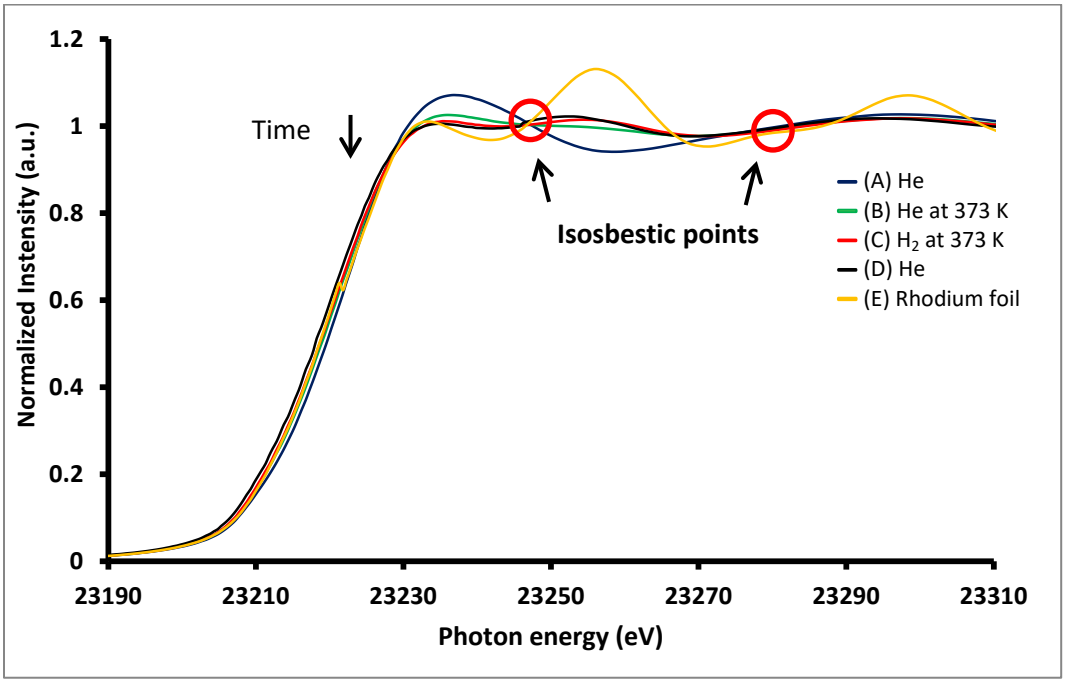

Figure 4.2. Normalized XANES spectra at the Rh K edge characterizing the formation of rhodium clusters from $Rh(C_2H_4)_2$ supported on SAPO-37, as follows: (A) initial rhodium complexes in flowing helium (50.0 mL(NTP) min^{-1}); the sample at 373 K under helium (B); the sample in flowing H_2 (50.0 mL(NTP) min^{-1}) (C); the sample at 298 K in flowing helium (D). Data characterizing rhodium foil are shown for comparison (E).

Thus, the XANES and EXAFS spectra, complementing the IR spectra, indicate the formation of clusters in the support. The Rh–Rh coordination number of nearly 3 indicates, on average, tetrarhodium species (Table 4.1). The decrease in intensity of the white line in the XANES spectra that was observed

when the sample was exposed to H_2 clearly demonstrates that the cluster formation involved the reduction of the rhodium from an initial cationic state (Figure 4.2); the XANES data are not sufficient to determine the exact rhodium oxidation state.

Table 4.1: Structural Models Based on EXAFS Representing $Rh(C_2H_4)_2$ Supported on SAPO-37, and Dealuminated HY Zeolite after Various Treatments.[a] Each Catalyst Contained *approximately* 1.0 wt% Rhodium.

Initial form of catalyst	Treatment conditions	Shell[c]	*N*	*R* (Å)	$10^3 \times \sigma^2$	ΔE_0	Refs
Rh/SAPO-37	Initial species	Rh−C	4.0	2.12	7.5	-7.5	1
		$Rh-O_s$	2.1	2.10	6.3	4.0	
		Rh−Al	1.1	3.10	6.4	-3.0	
Rh/SAPO-37	H_2, 1 bar, 373 K, 60 min	Rh−Rh	3.0	2.66	7.2	2.1	this work
		$Rh-O_s$	0.9	2.13	4.3	3.0	
		Rh−Al	0.6	3.03	5.4	-8.0	
Rh/DAY zeolite	H_2 in flowing He, 1 bar, 373 K, 4 min	Rh−Rh	0.2	2.62	6.5	-0.3	10
		$Rh-O_s$	1.9	2.07	6.9	-4.1	
		Rh−Al	0.9	2.97	1.5	2.4	
		$Rh-O_l$	0.5	3.51	0.8	-8.0	
Rh/DAY zeolite	H_2 in flowing He, 1 bar, 373 K, 60 min	Rh−Rh	4.4	2.67	9.2	4.0	10
		$Rh-O_s$	0.6	2.18	1.6	-7.2	
		Rh−C	*-b*	*-b*	*-b*	*-b*	

[a]Notation: *N*, coordination number; *R*, distance between absorber and backscatterer atoms; $\Delta\sigma^2$, disorder term (Debye–Waller factor); ΔE_0, inner potential correction. Error bounds (accuracies) characterizing the structural parameters determined by EXAFS spectroscopy are estimated to be as follows: *N*, ±20%; *R*, ±0.02 Å; $\Delta\sigma^2$, ±20%; ΔE_0, ±20 %. [b]Contribution not detectable. [c]The subscripts s and l refer to short and long, respectively. Details of the EXAFS fitting are provided in the SI.

Catalytic performance of SAPO-37-supported rhodium clusters. The SAPO-37-supported rhodium clusters formed by exposure of the initial supported rhodium complexes to flowing H_2 for 60 min at 1 bar and 373 K were used as a catalyst for ethylene hydrogenation in a once-through isothermal plug-flow reactor at 303 K and 1 bar. The SAPO-37 alone (with its acidic OH groups) did not have measurable activity for hydrogenation or dimerization under our conditions.[1] Thus, the catalytic activity is attributed to the rhodium clusters. Initial conversions were differential (as shown by the good linear fit to the data showing the initial conversions versus inverse space velocity, Figure 4A.1 in the SI), determining TOF values directly.

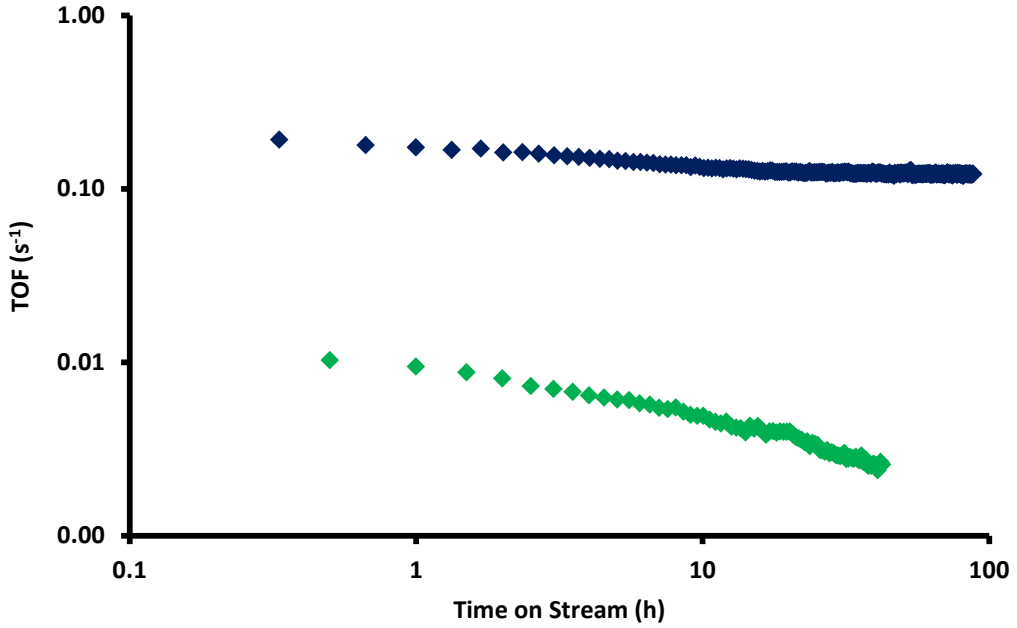

Figure 4.3. Performance of rhodium clusters supported on SAPO-37 for ethylene conversion in the presence of H_2 at 303 K and 1 bar: blue ◆ SAPO-37-supported catalyst (molar H_2:C_2H_4 ratio = 1:1); green ◆ SAPO-37-supported catalyst (feed molar H_2:C_2H_4 ratio = 1:4). Rhodium contents of catalysts were 0.6 ± 0.1 wt%. The values of TOF were determined assuming that each rhodium atom participated in the catalysis. The errors in TOF are estimated to be approximately ± 20%, associated primarily with the error in rhodium content of the catalyst.

The data of Figure 4.3 show how the supported rhodium clusters performed as a catalyst; the initial TOF, determined by extrapolation of the TOF vs. time on stream data to time-on-stream = 0, was found to be 0.12 s^{-1} (calculated on the basis of the presumption that each Rh atom was accessible to reactants) at a H_2:C_2H_4 molar ratio of 1:1 and approximately 0.02 s^{-1} at a H_2:C_2H_4 molar ratio of 1:4.

At a molar H_2:C_2H_4 ratio was 1:1, the SAPO-37-supported rhodium clusters were found to be active and selective for hydrogenation just as the SAPO-37-supported rhodium complexes initially present as atomically dispersed rhodium diethylene complexes.[1] The only products with either rhodium catalyst were ethane, and the activities were 0.12 s^{-1} and 0.13 s^{-1}, respectively (Table 4.2).

At a molar H_2:C_2H_4 ratio was 1:1, the SAPO-37-supported rhodium clusters were found to be more active for hydrogenation than the iridium clusters supported on the metal–organic framework UiO-66 (0.03 s^{-1}).[18] Again, the only product observed with either catalyst was ethane.

When the feed H_2:C_2H_4 ratio was 1:4 (molar), the SAPO-37-supported rhodium clusters were found to be selective for hydrogenation over dimerization—similar to what was reported for DAY zeolite-supported rhodium clusters[10] (Table 4.2). However, the initial TOF of the SAPO-37-supported rhodium clusters was found to be 0.02 s^{-1} which is less than the initial TOF of 0.11 s^{-1} characterizing the reaction on DAY zeolite-supported rhodium clusters[10] (Table 4.2). Details of these and related comparisons are summarized in Table 4.2.

Table 4.2: Catalytic Activities Characterizing Samples Initially Incorporating Metal Complexes Supported on SAPO-37, DAY Zeolite, MgO, and Metal Organic Frameworks (MOFs), after Various Treatments, for Hydrogenation and Dimerization of Ethylene in once-through Flow Reactors. Each Catalyst Contained *approximately* 1.0 wt% Rhodium or Iridium.

Initial form of catalyst	Metal–metal coordination number determined by EXAFS spectroscopy [a]	Initial TOF for ethylene conversion (s^{-1})	Selectivity in ethylene conversion (mol %)					Ref
			ethane	*n*-butane	*trans*-2-butene	1-butene	*cis*-2-butene	
$Rh(C_2H_4)_2$/SAPO-37	3.0	0.19[b]	99.8	0.2				this work
		0.02[d]	76.1	0.6	14.2	3.9	5.2	
	–[c]	0.13	99.6	0.4				1
$Rh(C_2H_4)_2$/DAY zeolite	4.4	0.25[d]	76.9	2.0	12.8	2.9	5.4	10
$Rh(C_2H_4)_2$/DAY zeolite	0.2	0.11[d]	50.3	0.6	26.4	10.4	12.3	10
$Rh(C_2H_4)_2$/DAY zeolite	1.9	0.07[d]	20.4	3.1	76.5[e]			9
$Rh_2(\mu\text{-}OMe)_2(COD)_2$/MgO[f]	1.0	1.1[b]	100	–[c]				19
$Rh(C_2H_4)_2$/DAY zeolite	–[c]	0.10[b]	52.9	1.0	31.3	3.9	10.9	20
		0.11[d]	29.8	0.6	43.2	10.1	16.3	10
$Ir(C_2H_4)_2$/UIO-67	3.0	0.03[b]	99.75	0.05	0.05	0.1	0.05	18
$Ir(CO)_2$/NaY zeolite	1.0	0.029[h]	–[g]					21
	2.9	0.043[h]						
	3.7	0.032[h]						

[a]For the complete set of parameters determined in the EXAFS data fitting, see Table 4.1. As shown in Table 4.1, the Rh–Rh coordination number characterizing the sample after H_2 treatment at 373 K for 60 min; for comparison, the previously reported Rh–Rh coordination number characterizing the sample after treatment in H_2 at 373 K for 60 min and 4 min is also shown. Ir–Ir coordination number are shown for comparison characterizing their respective samples; details of their synthesis are given in references: [9,10, 18,21].

[b]TOFs determined at 303 K and 1.0 bar; feed partial pressures (mbar): C_2H_4, 50; H_2, 50; helium, 900; total flow rate 100 mL(NTP)/min; catalyst mass, 5.0-30.0 mg.

[c]Not detected.

[d]TOFs determined at 298 K and 1.0 bar; feed partial pressures (mbar): C_2H_4, 200; H_2, 50; helium, 750; total flow rate 100 mL(NTP)/min; catalyst mass, 30 mg.

[e]Value reported in reference does not distinguish among the butenes.

[f]OMe = methoxy; COD = cyclooctadienyl.

[g]Not reported.

[h]TOFs determined at 303 K and 1.0 bar; feed partial pressures (mbar): C_2H_4, 155; H_2, 155; helium, 690; total flow range of 27-185 mL(NTP)/min; catalyst mass, 75 mg.

3.4. Deactivation of SAPO-37-supported rhodium clusters. To gain insight into the catalyst activity loss, 20 mg of the catalyst was packed into the DRIFTS cell at 303 K and 1 bar to a flowing stream of C_2H_4 + H_2 at a molar ratio of 4:1. The rhodium clusters were pre-formed on the SAPO-37 prior to reaction conditions. Spectra recorded as the catalytic reactions proceeded (Figure 4A.2 in the SI) show increasing intensities peaks assigned to C−H vibrations (2970−2860 cm^{-1}), assigned to carbonaceous adsorbates or deposits in SAPO (and zeolite) catalysts incorporating supported rhodium complexes that grew after a 24 h exposure.[1] We infer from the spectra that essentially the same carbonaceous adsorbates/deposits formed and interacted with the rhodium, causing catalyst deactivation.

The deactivation of the rhodium clusters matches well with the deactivation of other noble metals on SAPO-37. In previous work it was reported that atomically dispersed rhodium[1] or platinum[22] clusters on SAPO-37 deactivated as a result of the formation of relatively large organic adsorbates/deposits during catalytic hydrogenation (with feeds that were either ethylene-rich or hydrogen-rich). Thus, the deactivation of rhodium clusters on SAPO-37 is as expected for noble metals supported on SAPO-37.

4.5 DISSCUSION

Rhodium Cluster Formation on SAPO-37. Formation of small rhodium clusters in high yields in the pores of DAY zeolite has been reported by Fang *et al.*[8] Fang observed that $Rh_4(CO)_{12}$ formed by reaction of $Rh(CO)_2(acac)$ with OH groups on the surface of DAY zeolite (molar SiO_2/Al_2O_3 ratio of 30:1) as the water-gas shift half reactions took place while. Fang also observed that on HY zeolite (molar SiO_2/Al_2O_3 ratio of 5.2:1) $Rh_6(CO)_{16}$ formed as a major side product. Using IR and EXAFS spectroscopies to characterize his samples, Fang inferred the formation of $Rh_4(CO)_{12}$ on DAY zeolite at a yield of >95%. The synthesis was reported to be the one giving the highest yield of tetrarhodium clusters from rhodium carbonyls. Work by Li *et al.*[21] shows that iridium clusters (represented as Ir_2, Ir_4, and Ir_6) on NaY zeolites can be formed from NaY zeolite-supported iridium dicarbonyl complexes by exposure of the samples to

flowing CO at various temperatures (313 or 448 K). However, the yields of the clusters in the various syntheses were not reported.

Nearly uniform clusters have been reported by Serna *et al.*[9] to form on DAY zeolite supports from rhodium diethylene precursor; the results were obtained in experiments whereby the authors brought atomically dispersed rhodium diethylene complexes on the support in contact with flowing H_2 at 303 K and 1 bar for 1.5 h. They reported a Rh−Rh coordination number of 1.9 for the clusters that formed (Table 4.2) and inferred the presence of extremely small clusters along with unconverted mononuclear rhodium species. Work by Yang *et al.*[10] done with aberration-corrected HAADF-STEM shows that DAY zeolite-supported rhodium diethylene complexes exposed to H_2 at 373 K for 1 h formed rhodium clusters with an average diameter of 0.55 ± 0.10 nm (approximately nine atoms per cluster, on average, if spherical clusters are assumed[10]), which agrees well with the diameter estimated on the basis of their EXAFS data (Table 4.1). They emphasized that single site-isolated Rh atoms were still observed in small numbers along with the clusters, indicating that not all of the rhodium had been converted into clusters during the treatment in H_2. The evidence for the atomically dispersed rhodium was aberration-corrected HAADF-STEM images.

The data reported here show that the atomically dispersed rhodium was similarly converted into rhodium clusters on SAPO-37. The EXAFS data are not sufficient to determine the nuclearities of the clusters, which could have been present in mixtures, but tetrarhodium clusters with tetrahedral frames (as in $Rh_4(CO)_{12}$, which has a Rh−Rh coordination number of 3[8]) and hexarhodium clusters with octahedral frames (as in $Rh_6(CO)_{16}$, which has a Rh−Rh coordination number of 4[23]) are common,[24] and considered more likely to have formed in our samples than rare molecular trirhodium clusters (Rh−Rh coordination number of 2).[25]

Details of the candidate models used in EXAFS data fitting are shown in Table 4A.1 in the SI. The fitting shows that a Rh−Rh coordination number of 3 gives the best-fit model. Alternative models were

considered in the fitting. A model with an Rh−Rh coordination number of 5 (larger than that characterizing hexarhodium in $Rh_6(CO)_{16}$) gives a good overall fit indicated by goodness of fit parameters; however, an unrealistic Debye-Waller factor (higher than 0.01 at room temperature)[17,26,27] of the Rh−Rh contribution found in the fitting was substantially greater than that characterizing the other Rh−O and Rh−Al contributions (Table 4A.1 in the SI). Thus, we rule out the possibility of a high yield of hexarhodium or larger clusters.

In summary, we infer that rhodium clusters that formed on the SAPO were on average approximately tetrarhodium clusters, but the data do not rule out the possible presence of some larger clusters, such as hexarhodium clusters.

Our synthesis conditions were similar to those of Yang *et al.*,[10] but our support (SAPO) was different from Yang's DAY zeolite. However, from the Rh−Rh coordination number determined by EXAFS spectroscopy (3.0 compared to 4.4 in Table 4.1) the clusters formed in our sample were smaller than those reported by Yang *et al.*[10] Thus, we infer the rhodium clusters on the SAPO are slightly smaller in diameter than the 0.55 ± 0.10 nm inferred on the basis of aberration-corrected HAADF-STEM images characterizing the DAY zeolite-supported rhodium clusters.

The isosbestic points in the XANES spectra showing the conversion of SAPO-37-supported atomically dispersed rhodium diethylene complexes to SAPO-37-supported rhodium clusters indicate that this conversion was stoichiometrically simple. The lack of such points in the XANES spectra reported by Serna *et al.*[9] for the conversion of DAY zeolite-supported rhodium diethylene complexes to DAY zeolite-supported rhodium clusters confirms the presence of a mixture of rhodium species in their sample, in contrast to ours.

The white lines of the XANES spectra showing the conversion of SAPO-37-supported atomically dispersed rhodium diethylene complexes to SAPO-37-supported rhodium clusters indicate that the rhodium was reduced when exposed to hydrogen. And when comparing the XANES region of the SAPO-

37-supported rhodium clusters to that characterizing the rhodium foil, we see different features that indicate that the clusters were too small to be considered metallic.

The SAPO pores can provide an environment to accommodate Rh_4 clusters (diameter ≈ 9 Å[28]) (and also Rh_6 clusters (diameter ≈ 10 Å)[8]), a statement that follows from the fact that the SAPO supercage is nearly 13 Å[29] and the SAPO aperture diameter nearly 7.4 Å,[29] values almost the same as those characterizing the isostructural zeolite.[30]

Fang *et al.*[8] reported that to form a high yield of clusters from DAY zeolite-supported rhodium dicarbonyl complexes, several criteria had to be met, as follows: (1) supercages that provide an optimal environment to accommodate Rh_4 clusters (and also Rh_6 clusters) and also small enough to stabilize these clusters by entrapment and (2) a high Si:Al ratio in zeolites for a low surface density of OH groups to favor the selective synthesis of the smaller clusters—because a higher density of the acidic OH groups facilitates the transformation of $Rh_4(CO)_{12}$ to $Rh_6(CO)_{16}$.[8] We suggest that the SAPO superacages provides a nearly optimal environment to accommodate rhodium clusters.

With regard to the surface density of acidic OH groups, the SAPO has a total of more OH groups per unit mass than the zeolite.[31] However, the strengths of the Si−OH−Al Brønsted acid sites on the SAPO are less than those of the Si−OH−Al Brønsted acid sites on the zeolite, as shown by IR spectra.[31] We hypothesize that the difference in the acid strength between the SAPO and the zeolite accounts for the difference in the formation of larger clusters in DAY zeolite-supported rhodium clusters reported by Yang *et al.*[10] (Recall that the EXAFS data show that our clusters were smaller than Yang's.)

However, as EXAFS is an averaging technique, a question remains on whether all the rhodium had been converted into clusters during the treatment in H_2 and small amounts of atomically dispersed rhodium diethylene complexes could have remained unconverted. This question is answered by comparing the activity of the SAPO-37-supprted rhodium clusters to DAY zeolite-supported rhodium clusters reported by Serna *et al.,*[9] as summarized in the next section.

Hydrogenation of Ethylene Catalyzed by SAPO-37-Supported Rhodium Clusters. Under reaction conditions (H_2:C_2H_4 molar ratio of 1:4), the SAPO-37-supported rhodium clusters were active for both hydrogenation and dimerization of ethylene (Table 4.2), and the selectivity was similar to that characterizing the DAY zeolite-supported rhodium clusters reported Yang *et al.*[10] However, we observed activity values different from those reported for DAY zeolite-supported rhodium clusters by Yang *et al.*[10] and Serna *et al.*[9] We observed an initial TOF for ethylene conversion of 0.02 s^{-1} compared to an initial TOF of 0.07 s^{-1} for DAY zeolite-supported rhodium clusters reported by Serna *et al.*[9] and an order magnitude less than an initial TOF of 0.11 s^{-1} for DAY zeolite-supported rhodium clusters reported by Yang *et al.*[10]

Thus, on the basis of catalytic activity for ethylene conversion, the SAPO and zeolite supports are not similar. We rule out any difference in activity due to metal loading because all samples in the comparison contained 0.6 ± 0.1 wt% rhodium. We postulate that our activity difference from that of the catalyst reported by Serna *et al.*[9] was associated with the difference in average cluster sizes and perhaps the fraction of clusters vs. mononuclear species in the separate catalysts. By comparing the average EXAFS Rh–Rh coordination numbers in Table 4.2 (1.9 to 3.0) we suggest that our clusters were less likely than Serna's to have been present in a mixture with smaller rhodium species such as atomically dispersed rhodium. The presumed difference might be an indication of the different chemistries of the SAPO and zeolite supports, such as for example as is reflected in the acid strengths of the OH groups (but more evidence would be needed to test this hypothesis). This hypothesis is bolstered by the differences in selectivity of Serna's catalyst[9] and ours, which his favor dimerization over hydrogenation, in contrast to ours. When comparing our clusters (approximated as tetrarhodium) to those of Yang *et al.*[10], which we infer contained larger clusters (the respective Rh–Rh coordination numbers are 3.0 and 4.4, respectively, Table 4.2); we might further hypothesize that our clusters were less likely than Yang's to include hexarhodium or larger clusters—thus, we hypothesize that our sample was more uniform

structurally than Yang's. However, we recognize that there is no evidence of a trend in catalyst performance with changing average cluster size, as shown by the results of Li *et al.*[21], who asserted that their catalysts incorporated the clusters Ir_2, Ir_4, and Ir_6 on MgO gave no simple explanation for the variation in catalytic performance with cluster size. There is substantial uncertainty in the characterization of the relevant reported samples, and we suggest that the SAPO may provide a greater stability for smaller rhodium clusters than the zeolite. However, we cannot rule out that the rhodium clusters changed under reaction conditions that could lead to the observed differences in activity.

4.6 CONCLUSIONS

In summary, tetrarhodium clusters were formed from isolated rhodium diethylene complexes on SAPO-37 upon exposure to H_2 at 373 K. X-ray absorption spectra indicate an average Rh–Rh coordination number of 3.0 and an average Rh–Rh distance of 2.66 Å. The supported rhodium clusters were found to catalyze ethylene hydrogenation at 303 K at a feed H_2:C_2H_4 molar ratio of 1:4. Their selectivies were similar to those of DAY zeolite-supported rhodium clusters, and their initial room-temperature activities (per rhodium atom) were substantially less than those of the zeolite-supported rhodium clusters.

4.7 ACKNOWLEDGEMENTS

J.T.H. thanks Hong-Xin Li and Phillip Connolly of Zeolyst for their interest and support of this industry-university collaboration. The work was supported by the U.S. Department of Energy (DOE), Office of Science, Basic Energy Sciences (BES), Grant DE-FG02-04ER15513. We thank Chevron for a fellowship supporting J.P.A. We gratefully acknowledge beam time at Beamline 4-1 at the Stanford Synchrotron Radiation Lightsource, supported by the DOE Division of Materials Sciences under Contract DE-AC02-76SF00515 and by the Co-ACCESS program supported by DOE BES Chemical Sciences, Geosciences, and Biosciences Division; we appreciate the help of Ryan Davis, Adam S. Hoffman, and Simon R. Bare at the synchrotron.

4.8 REFERENCES

(1) Perez-Aguilar, J. E.; Chen, C. Y.; Hughes, J. T.; Fang, C. Y.; Gates, B. C. Isostructural Atomically Dispersed Rhodium Catalysts Supported on SAPO-37 and on HY Zeolite. *J. Am. Chem. Soc.* **2020**, *142*, 11474–11485.

(2) Lok, B. M.; Messina, C. A.; Patton, R. L.; Gajek, R. T.; Cannan, T. R.; Flanigen, E. M. Silicoaluminophosphate Molecular Sieves: Another New Class of Microporous Crystalline Inorganic Solids. *J. Am. Chem. Soc.* **1984**, *106*, 6092–6093.

(3) Briend, M.; Peltre, M. J.; Lamy, A.; Man, P. P.; Barthomeuf, D. Dependence of the Acidic Properties of SAPO-37 Molecular Sieve-on Si Content and Heat Treatment. *J. Catal.* **1992**, *138*, 90–100.

(4) Zhong, J.; Han, J.; Wei, Y.; Tian, P.; Guo, X.; Song, C.; Liu, Z. Recent Advances of the Nano-Hierarchical SAPO-34 in the Methanol-to-Olefin (MTO) Reaction and Other Applications. *Catal. Sci. Technol.* **2017**, *7*, 4905–4923.

(5) Liang, A. J.; Bhirud, V. A.; Ehresmann, J. O.; Kletnieks, P. W.; Haw, J. F.; Gates, B. C. A Site-Isolated Rhodium-Diethylene Complex Supported on Highly Dealuminated Y Zeolite: Synthesis and Characterization. *J. Phys. Chem. B* **2005**, *109*, 24236–24243.

(6) Argo, A. M.; Gates, B. C. MgO-Supported Rh_6 and Ir_6: Structural Characterization during the Catalysis of Ethene Hydrogenation. *J. Phys. Chem. B* **2003**, *107*, 5519–5528.

(7) Babucci, M.; Guntida, A.; Gates, B. C. Atomically Dispersed Metals on Well-Defined Supports Including Zeolites and Metal-Organic Frameworks: Structure, Bonding, Reactivity, and Catalysis. *Chem. Rev.* **2020**, *120*, 11956–11985.

(8) Fang, C. Y.; Zhang, S.; Hu, Y.; Vasiliu, M.; Perez-Aguilar, J. E.; Conley, E. T.; Dixon, D. A.; Chen, C. Y.; Gates, B. C. Reversible Metal Aggregation and Redispersion Driven by the Catalytic Water Gas Shift Half-Reactions: Interconversion of Single-Site Rhodium Complexes and Tetrarhodium Clusters in Zeolite HY. *ACS Catal.* **2019**, *9*, 3311–3321.

(9) Serna, P.; Gates, B. C. Zeolite-Supported Rhodium Complexes and Clusters: Switching Catalytic Selectivity by Controlling Structures of Essentially Molecular Species. *J. Am. Chem. Soc.* **2011**, *133*, 4714–4717.

(10) Yang, D.; Xu, P.; Browning, N. D.; Gates, B. C. Tracking Rh Atoms in Zeolite HY: First Steps of Metal Cluster Formation and Influence of Metal Nuclearity on Catalysis of Ethylene Hydrogenation and Ethylene Dimerization. *J. Phys. Chem. Lett.* **2016**, *7*, 2537–2543.

(11) Hoffman, A. S.; Debefve, L. M.; Bendjeriou-Sedjerari, A.; Ouldchikh, S.; Bare, S. R.; Basset, J. M.; Gates, B. C. Transmission and Fluorescence X-ray Absorption Spectroscopy Cell/Flow Reactor for Powder Samples under Vacuum or in Reactive Atmospheres. *Rev. Sci. Instrum.* **2016**, *87*, 073108.

(12) Buhl, M.; Håkansson, M.; Mahmoudkhani, A. H.; Öhrström, L. X-ray Structures and DFT Calculations on Rhodium-Olefin Complexes: Comments on the ^{103}Rh NMR Shift–Stability Correlation. *Organometallics* **2000**, *19*, 5589–5596.

(13) Villars, P.; Calvert, L. D. *Pearson's Handbook of Crystallographic Data for Intermetallic Phases.*; Wiley: Metals Park, 1987.

(14) Liang, A. J.; Craciun, R.; Chen, M.; Kelly, T. G.; Kletnieks, P. W.; Haw, J. F.; Dixon, D. A.; Gates, B. C. Zeolite-Supported Organorhodium Fragments: Essentially Molecular Surface Chemistry Elucidated with Spectroscopy and Theory. *J. Am. Chem. Soc.* **2009**, *131*, 8460–8473.

(15) Serna, P.; Gates, B. C. Zeolite- and MgO-Supported Rhodium Complexes and Rhodium Clusters: Tuning Catalytic Properties to Control Carbon-Carbon vs. Carbon-Hydrogen Bond Formation Reactions of Ethene in the Presence of H2. *J. Catal.* **2013**, *308*, 201–212.

(16) Serna, P.; Yardimci, D.; Kistler, J. D.; Gates, B. C. Formation of Supported Rhodium Clusters from Mononuclear Rhodium Complexes Controlled by the Support and Ligands on Rhodium. *Phys. Chem. Chem. Phys.* **2014**, *16*, 1262–1270.

(17) Liang, A. J.; Gates, B. C. Time-Resolved Structural Characterization of Formation and Break-up of Rhodium Clusters Supported in Highly Dealuminated y Zeolite. *J. Phys. Chem. C* **2008**, *112*, 18039–18049.

(18) Yang, D.; Gaggioli, C. A.; Conley, E.; Babucci, M.; Gagliardi, L.; Gates, B. C. Synthesis and Characterization of Tetrairidium Clusters in the Metal Organic Framework UiO-67: Catalyst for Ethylene Hydrogenation. *J. Catal.* **2020**, *382*, 165–172.

(19) Guan, E.; Gates, B. C. Stable Rhodium Pair Sites on MgO: Influence of Ligands and Rhodium Nuclearity on Catalysis of Ethylene Hydrogenation and H-D Exchange in the Reaction of H_2 with D_2. *ACS Catal.* **2018**, *8*, 482–487.

(20) Bernales, V.; Yang, D.; Yu, J.; Gümüşlu, G.; Cramer, C. J.; Gates, B. C.; Gagliardi, L. Molecular Rhodium Complexes Supported on the Metal-Oxide-like Nodes of Metal Organic Frameworks and on Zeolite HY: Catalysts for Ethylene Hydrogenation and Dimerization. *ACS Appl. Mater. Interf.* **2017**, *9*, 33511–33520.

(21) Li, F.; Gates, B. C. Size-Dependent Catalytic Activity of Zeolite-Supported Iridium Clusters. *J. Phys. Chem. C* **2007**, *111*, 262–267.

(22) To be Published.

(23) Weber, W. A.; Gates, B. C. Hexarhodium Clusters in NaY Zeolite: Characterization by Infrared and Extended X-ray Absorption Fine Structure Spectroscopies. *J. Phys. Chem. B* **1997**, *101*, 10423–10434.

(24) Allian, A. D.; Widjaja, E.; Garland, M. Experimental Raman Spectra of Dilute and Laser-Light-Sensitive $[Rh_4(CO)_9(\mu\text{-}CO)_3]$ and $[(\mu_4\text{-}\eta^2\text{-}3\text{-Hexyne})Rh_4(CO)_8(\mu\text{-}CO)_2]$. Comparison with

Theoretically Predicted Spectra. *Dalt. Trans.* **2006**, 4211–4217.

(25) Fang, L.; Shen, X.; Chen, X.; Lombardi, J. R. Raman Spectra of Rhodium Trimers in Argon Matrices. *J. Chem. Phys.* **2000**, *113*, 7178–7181.

(26) George, G. N.; Hilton, J.; Temple, C.; Prince, R. C.; Rajagopalan, K. V. Structure of the Molybdenum Site of Dimethyl Sulfoxide Reductase. *J. Am. Chem. Soc.* **1999**, *121*, 1256–1266.

(27) Tupy, S. A.; Karim, A. M.; Bagia, C.; Deng, W.; Huang, Y.; Vlachos, D. G.; Chen, J. G. Correlating Ethylene Glycol Reforming Activity with *in Situ* EXAFS Detection of Ni Segregation in Supported NiPt Bimetallic Catalysts. *ACS Catal.* **2012**, *2*, 2290–2296.

(28) Farrugia, L. J. Structural Redetermination of $Rh_4(CO)_{12}$ at 293 and 173 K and Analysis of the Thermal Motion in Relation to the Dynamical Behavior. *J. Clust. Sci.* **2000**, *11*, 39–53.

(29) Martens, J. A.; Grobet, P. J.; Jacobs, P. A. Catalytic Activity and Si, Al, P Ordering in Microporous Silicoaluminophosphates of the SAPO-5, SAPO-11, and SAPO-37 Type. *J. Catal.* **1990**, *126*, 299–305.

(30) Yadav, R.; Sakthivel, A. Silicoaluminophosphate Molecular Sieves as Potential Catalysts for Hydroisomerization of Alkanes and Alkenes. *Appl. Catal. A Gen.* **2014**, *481*, 143–160.

(31) Potter, M. E.; O'Malley, A. J.; Chapman, S.; Kezina, J.; Newland, S. H.; Silverwood, I. P.; Mukhopadhyay, S.; Carravetta, M.; Mezza, T. M.; Parker, S. F.; Catlow, C. R. A.; Raja, R. Understanding the Role of Molecular Diffusion and Catalytic Selectivity in Liquid-Phase Beckmann Rearrangement. *ACS Catal.* **2017**, *7*, 2926–2934.

Chapter 4A

SUPPORTING INFORMATION

for

SAPO-37-Supported Rhodium Clusters [1]

[1]This chapter is in preparation for submission by J. E. Perez-Aguilar, J. T. Hughes, C.-Y. Chen, and B. C. Gates. The original manuscript has been reformatted to fit the requirements of the dissertation

SUPPORTINGUPPORTING DATA

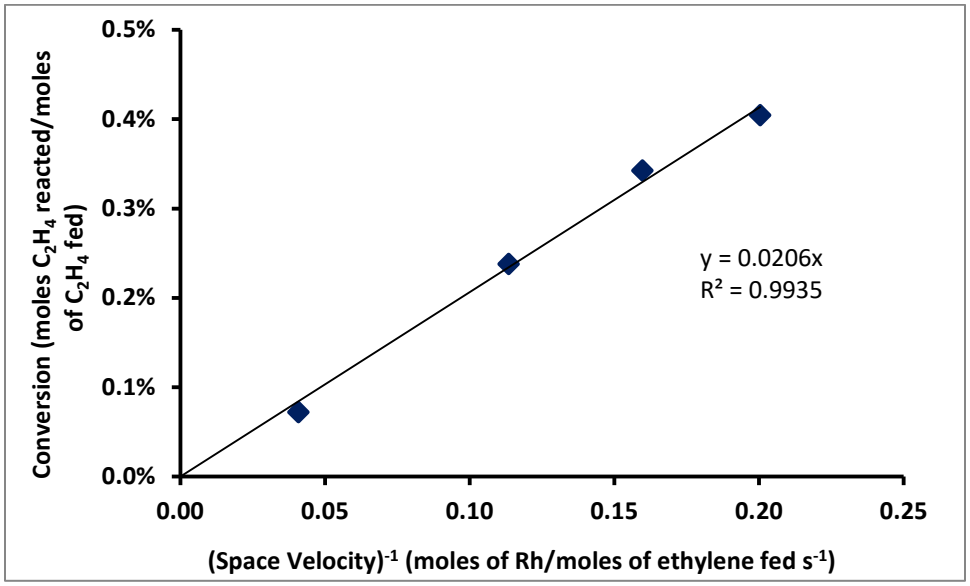

Figure 4A.1. Differential conversion of ethylene; the catalyst was initially present as rhodium clusters supported on SAPO-37. Reaction conditions: feed of H_2 + C_2H_4 at 1:4 molar ratio at 303 K at atmospheric pressure. The linearity of this plot that passes through the origin demonstrates that the data determine rates (TOF values) directly as the slope of the line.

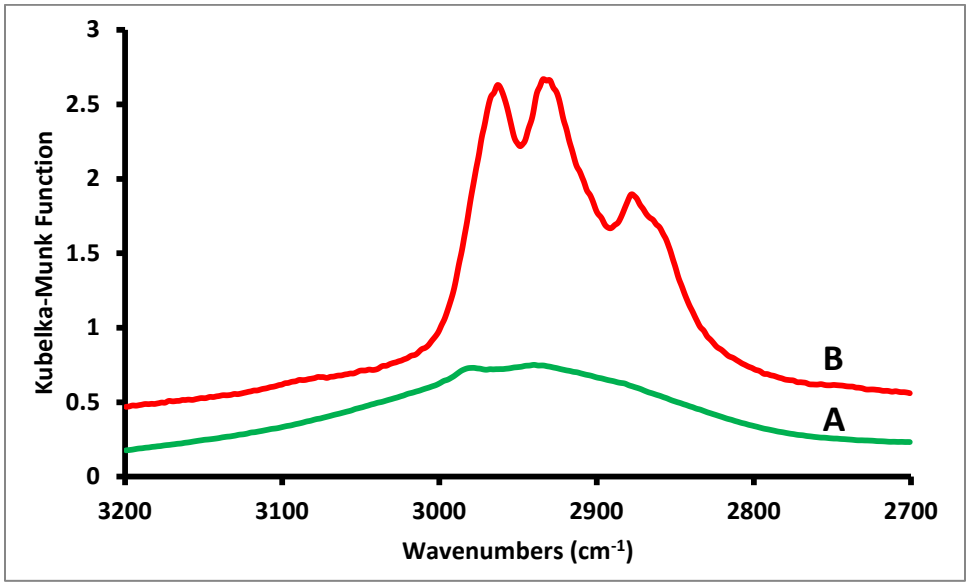

Figure 4A.2. DRIFTS spectra characterizing catalyst: **A**, SAPO-37-supported rhodium clusters in flowing helium (50 mL(NTP)/min) at room temperature after in contact with flowing H_2 for 1 h at 373 K and 1 bar; **B**, same sample under helium after 24 h exposure to reactions conditions (flow rates of 20 mL(NTP)/min of C_2H_4 and 5 mL(NTP)/min of H_2, and 20 mL(NTP)/min of helium) at 303 K).

Table 4A.1. EXAFS models representing the data at the Rh K edge characterizing 1 wt% rhodium supported on SAPO-37. The range in *k* was from 4.0 to 12.0 Å. Error = 0.00041.

Model	Shell	N^a	$10^3 \times \Delta\sigma^2$ (Å^2)[a]	R (Å)[a]	ΔE_0 (eV)[a]	Goodness of Fit
1	Rh	2.1	5.2	2.66	0.4	1.1910
	$O_{support}$	1.1	4.4	2.11	-6.0	
2	Rh	3.0	7.2	2.66	2.1	1.0141
	$O_{support}$	0.9	4.3	2.13	3.0	
	Al	0.6	5.4	3.03	-8.0	
3	Rh	5.0	10.0	2.66	3.4	1.9389
	$O_{support}$	2.0	10.2	2.15	4.0	
	Al	1.6	4.0	3.00	-4.0	

*Denotes best fit model; [a]Notation: *N*, coordination number; *R*, distance between absorber and backscatter atoms; $\Delta\sigma^2$, Debye-Waller/disorder term; ΔE_0, inner potential. Subscripts: Sup, refers to an atom identified to be belonging to the support.

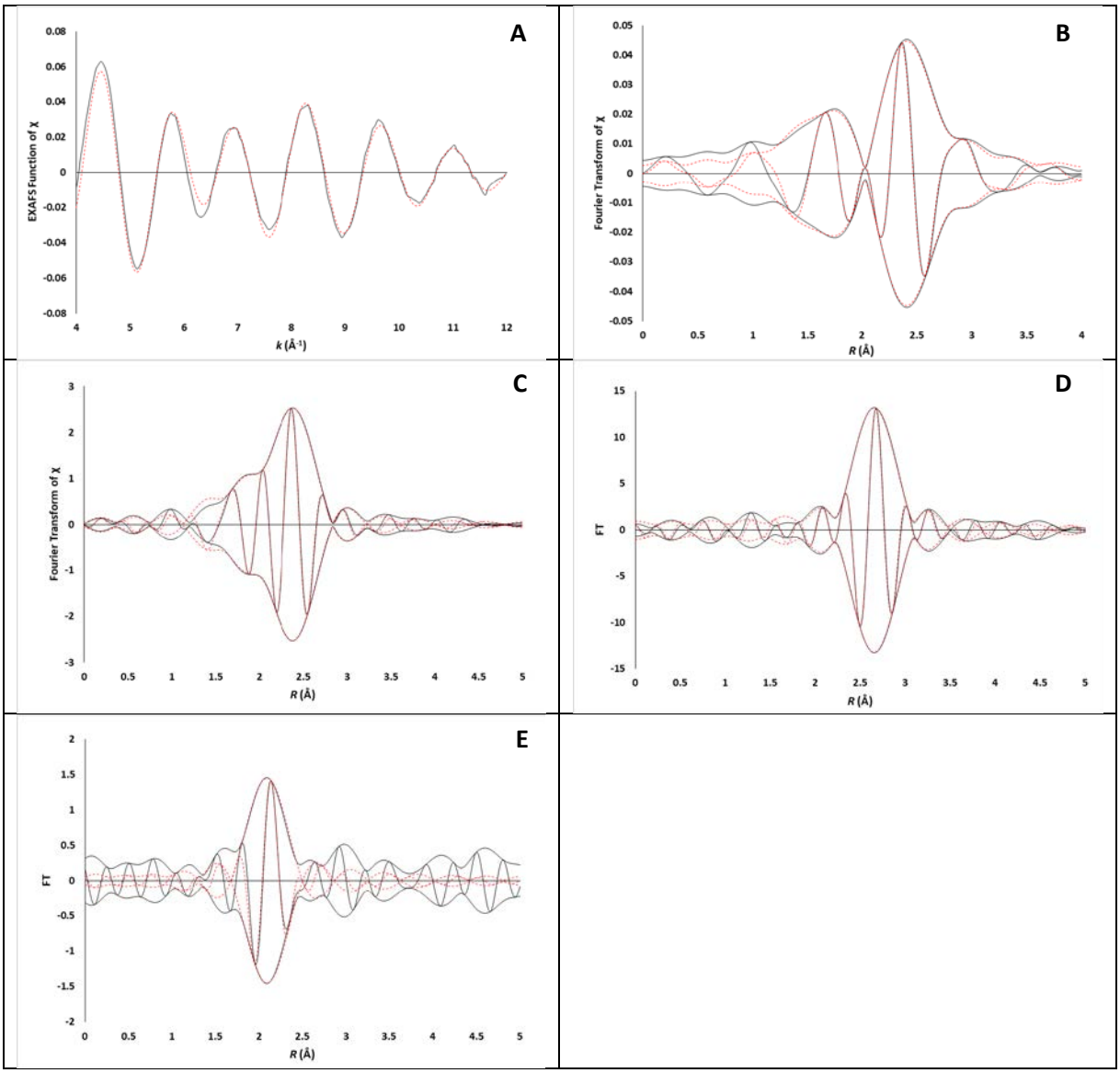

Figure 4A.3. EXAFS data recorded at Rh K edge characterizing the supported sample in flowing helium; the sample was prepared by chemisorption of $Rh(C_2H_4)_2(acac)$ on SAPO-37 exposed to H_2 flowing for 60 min at 373 K and 1 bar: (A) k^1-Weighted EXAFS function, $k^1(\chi)$ (solid line), and sum of the calculated contributions (dotted line). (B) k^1-Weighted imaginary part and magnitude of the Fourier transform of data (solid line) and sum of the calculated contributions (dotted line). (C) k^3-Weighted imaginary part and magnitude of the Fourier transform of data (solid line) and sum of the calculated contributions (dotted line). (D) k^3-Weighted, phase- and amplitude-corrected, imaginary part and magnitude of the Fourier transform of data (solid line) and calculated contributions (dotted line) of Rh–Rh shell. (E) k^2-Weighted, phase- and amplitude-corrected, imaginary part and magnitude of the Fourier transform of data (solid line) and calculated contributions (dotted line) of $Rh–O_{support}$ shell.

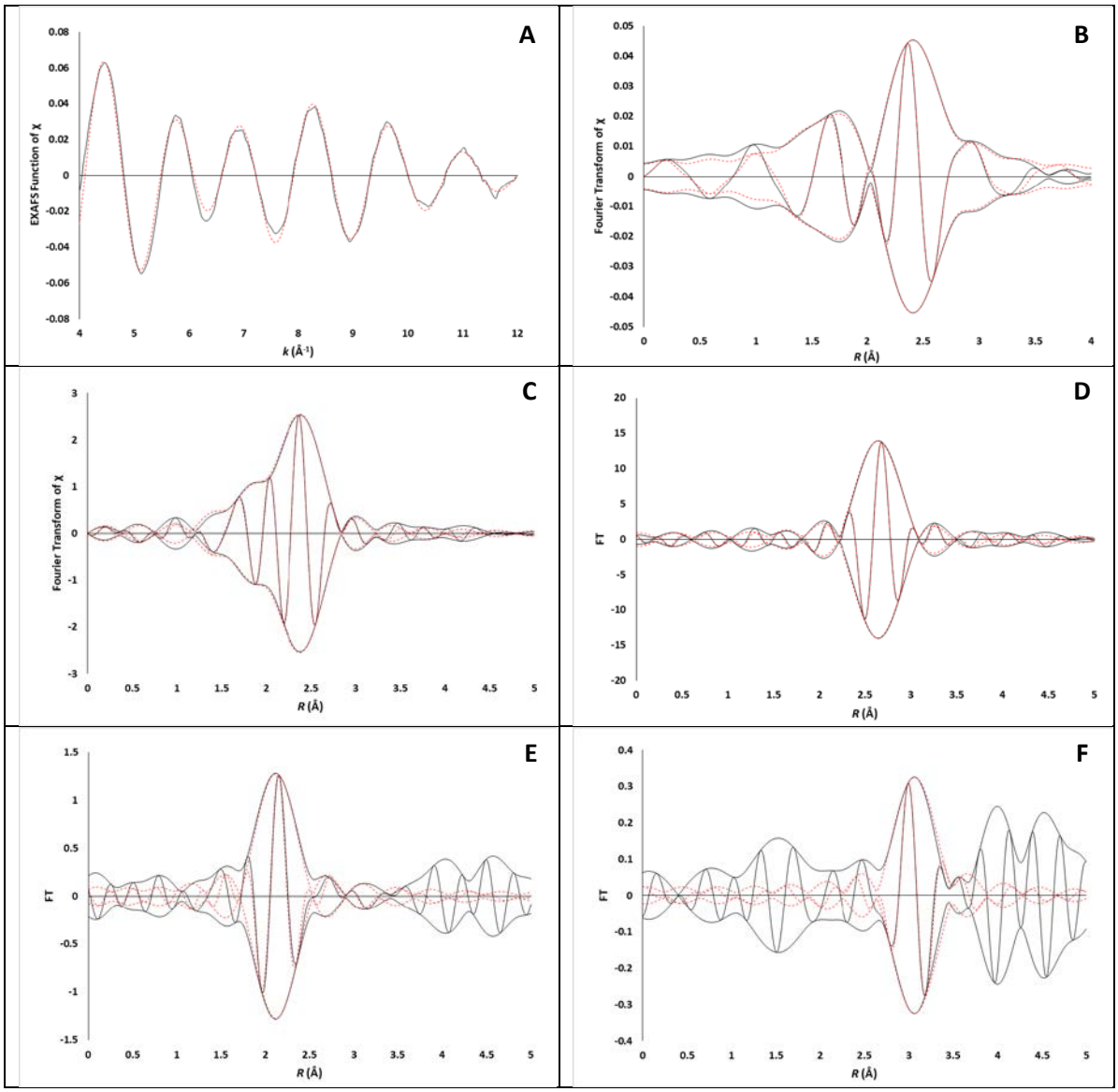

Figure 4A.4. EXAFS data recorded at Rh K edge characterizing the supported sample in flowing helium; the sample was prepared by chemisorption of $Rh(C_2H_4)_2(acac)$ on SAPO-37 that had been exposed to H_2 flowing for 60 min at 373 K and 1 bar: (A) k^1-Weighted EXAFS function, $k^1(\chi)$ (solid line), and sum of the calculated contributions (dotted line). (B) k^1-Weighted imaginary part and magnitude of the Fourier transform of data (solid line) and sum of the calculated contributions (dotted line). (C) k^3-Weighted imaginary part and magnitude of the Fourier transform of data (solid line) and sum of the calculated contributions (dotted line). (D) k^3-Weighted, phase- and amplitude-corrected, imaginary part and magnitude of the Fourier transform of data (solid line) and calculated contributions (dotted line) of Rh–Rh shell. (E) k^2-Weighted, phase- and amplitude-corrected, imaginary part and magnitude of the Fourier transform of data (solid line) and calculated contributions (dotted line) of $Rh–O_{support}$ shell. (F) k^2-Weighted, phase- and amplitude-corrected, imaginary part and magnitude of the Fourier transform of data (solid line) and calculated contributions (dotted line) of Rh–Al shell.

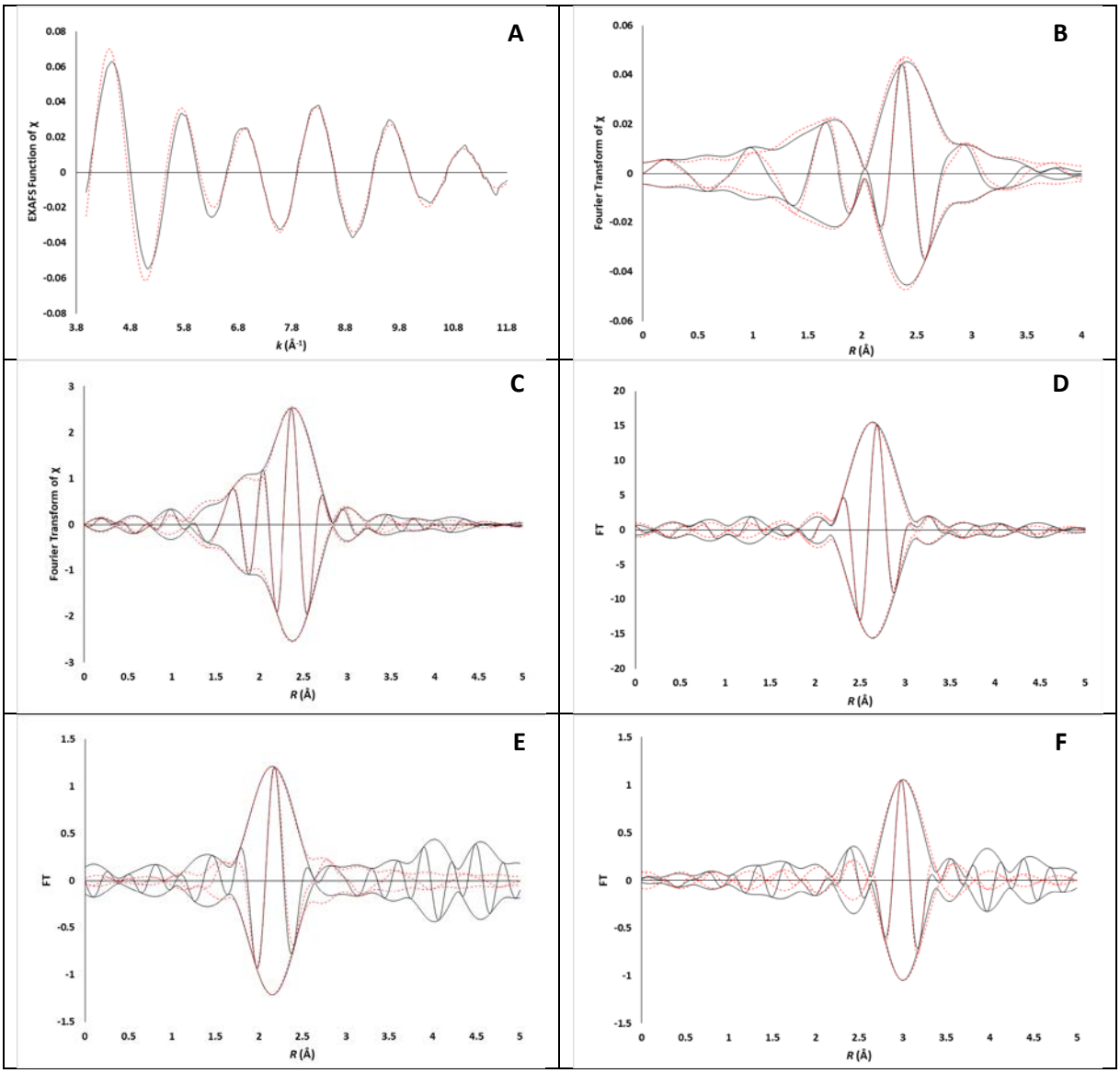

Figure 4A.5. EXAFS data recorded at Rh K edge characterizing the supported sample in flowing helium; the sample was prepared by chemisorption of $Rh(C_2H_4)_2(acac)$ on SAPO-37 subjected to H_2 flow for 60 min at 373 K and 1 bar: (A) k^1-Weighted EXAFS function, $k^1(\chi)$ (solid line), and sum of the calculated contributions (dotted line). (B) k^1-Weighted imaginary part and magnitude of the Fourier transform of data (solid line) and sum of the calculated contributions (dotted line). (C) k^3-Weighted imaginary part and magnitude of the Fourier transform of data (solid line) and sum of the calculated contributions (dotted line). (D) k^3-Weighted, phase- and amplitude-corrected, imaginary part and magnitude of the Fourier transform of data (solid line) and calculated contributions (dotted line) of Rh–Rh shell. (E) k^2-Weighted, phase- and amplitude-corrected, imaginary part and magnitude of the Fourier transform of data (solid line) and calculated contributions (dotted line) of $Rh–O_{support}$ shell. (F) k^2-Weighted, phase- and amplitude-corrected, imaginary part and magnitude of the Fourier transform of data (solid line) and calculated contributions (dotted line) of Rh–Al shell.